DIGITAL FABRICATION OF A TIMBER BRIDGE

Design, optimisation, fabrication and testing at global and connection level

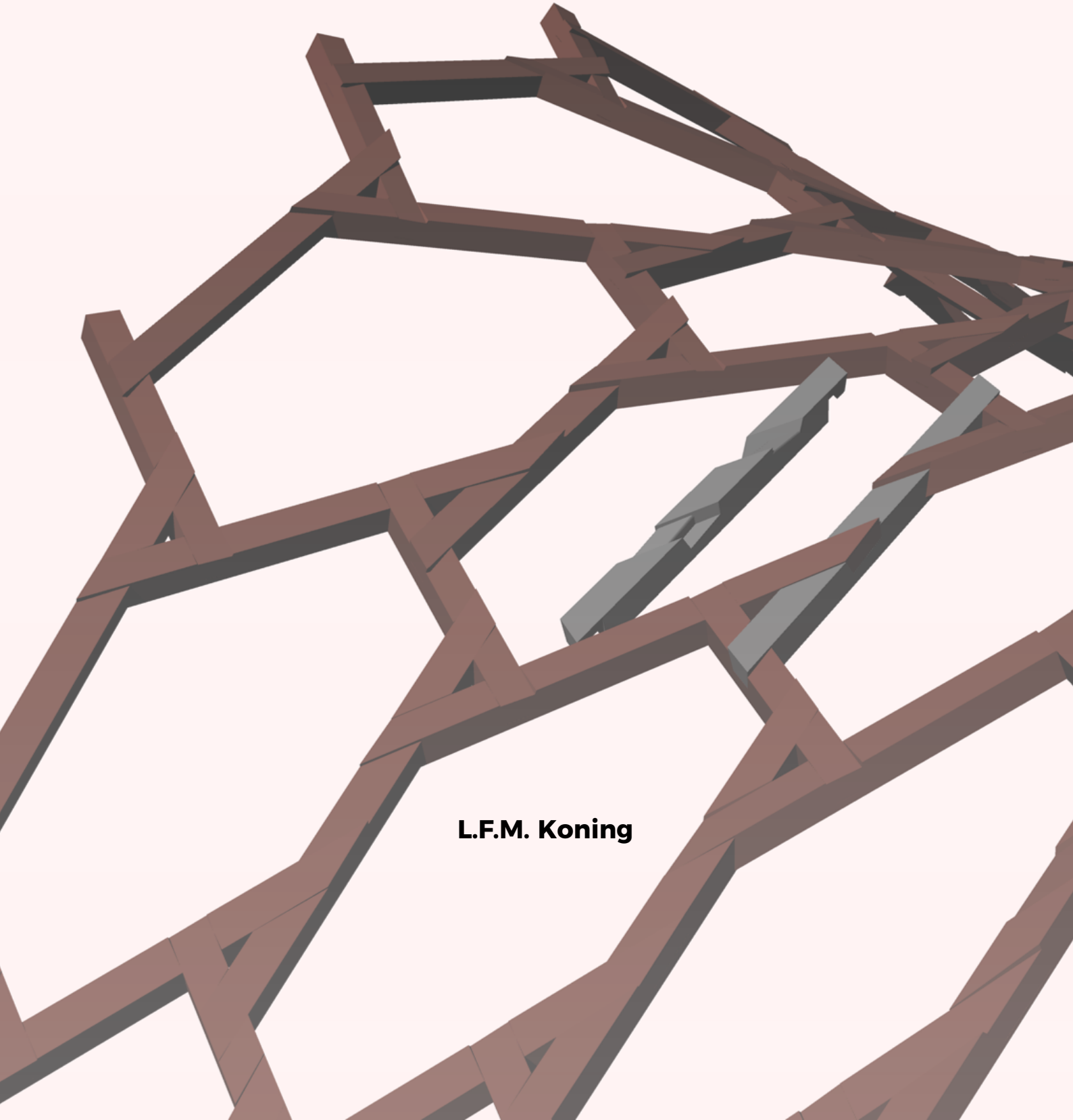

L.F.M. Koning

Digital Fabrication of a Timber Bridge

Design, optimisation, fabrication and testing at global and connection level

by

L.F.M. Koning

Committee:

Prof.dr.ir. J.G. Rots
Dr.ir. M.A.N. Hendriks
Dr.ir. G.J.P. Ravenshorst
ir. S. Joosten (Arup)

Faculty of Civil Engineering and Geosciences
Delft University of Technology

August 27, 2018

ARUP

TU Delft

Preface

This thesis is the result of my Master's Thesis Project with which I will complete my master's degree in Structural Engineering at Delft University of Technology.

The topic of my project has emerged from my interest in structural mechanics, optimisation techniques, parametric design and digital fabrication. After a journey in literature encountering various innovative manufacturing techniques, the trip ended at digital timber fabrication: a fairly unknown fabrication technique which is very appealing for its aesthetics and fitting the current demand for sustainable structures. Excited by projects carried out by research institutes like the Gramazio Kohler group from the ETH, Zürich and the Institute for Computational Design from the university of Stuttgart, I defined my own scope of the project on which I have worked with great pleasure for the past eleven months.

This of course would not have been possible without the help of a group of people. First of all I would like to thank my committee. In particular I would like to acknowledge Stijn Joosten for the daily supervision, the assessment of my work throughout the whole project and his motivational speeches during the stressful days before deadlines. Furthermore, I would like to thank Ir. G.J.P. Ravenshorst for his guidance in the field of timber engineering. My thanks go to Prof.dr.ir. J.G. Rots and Dr.ir. M.A.N. Hendriks for helping me to look at the greater picture and to prevent my Master's Thesis Project from getting the size of a PhD project.

I also woul like to thank Arup for making it possible to do my project in a inspiring work environment. Thanks go to all people working at Arup for giving me support and advise. In specific, I would like to thank Alex Christodoulou for his advice on Grasshopper and for introducing me to Machine Learning.

Additionally, I would like to acknowledge *Wijma Kampen B.V.*, in specific Gertjan Schurman and Peter Zanen, for assessing the feasibility of my connection design and for the production of the test specimens. Furthermore Fred Schilperoort from the Stevin Lab for his guidance during the lab tests. It was a great experience to carry out lab tests and these are of great value for the final result of my project.

Special thanks go to my parents for checking my report for spelling mistakes. Finally, I would like to thank my family and friends for their great support, motivation and love.

Laetitia Koning
Amsterdam, the Netherlands
August 27, 2018

Clarifying Figures

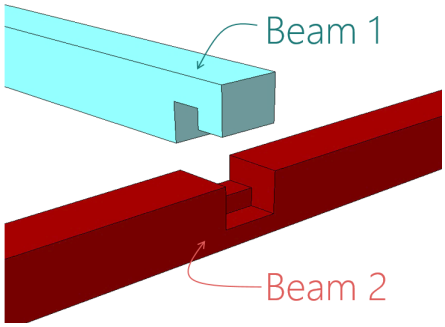

Figure 1: Designation of beam 1 and beam 2 in a connection

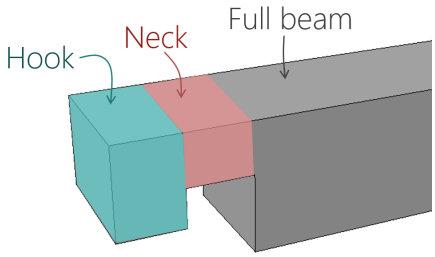

Figure 2: Identification of the different parts of beam 1

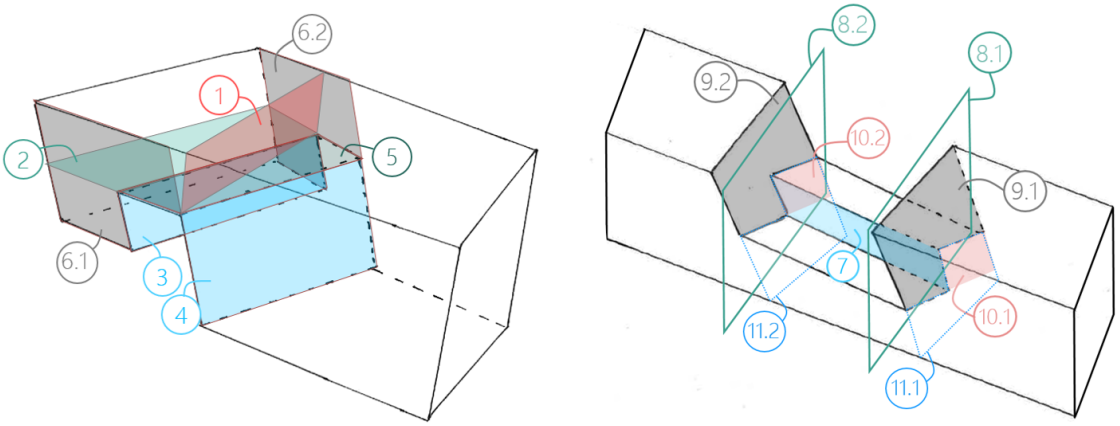

Figure 3: All relevant planes for the stress calculations in the connections

Summary

Currently great steps are taken in the development of new (digital) fabrication techniques and innovative software, enabling to design, check and fabricate structures with large freedom of shape and uniqueness of components in a cost effective way. The new techniques entered the building sector through architectural research institutes, showcasing new possibilities through complex shaped architectural structures like pavilions and art installations. The next step is to apply these new techniques in civil engineering to design structures with a load-bearing function, dealing with outdoor conditions, a large number of load cases and strict safety requirements.

The new digital fabrication techniques can be applied to different materials. In this thesis the focus is on timber. In previous research on robotic timber fabrication, by among others the Gramazio Kohler Research group of the ETH, Zürich and the Institute for Computational Design and Construction of the University of Stuttgart, only limited attention has been payed to the connection design, although the connections are often critical in a structure. Therefore in this research the focus is on the design, optimisation, detailing and testing of the connections.

The thesis examines the topic through a case study: the design of a pedestrian frame bridge made of timber using CNC-milling techniques. Both the global structural level and the connection level are studied and subsequently integrated.

Starting point

Initially, two types of structural systems are explored: a space frame and a gridshell structure. A gridshell was chosen due to its simple connections, ease of construction and therefore better suitability for a digital fabrication and assembly process. In order to further restrict the complexity of the connections, a reciprocal grid is applied: a self-supporting structure in which beams mutually support each other. This type of structure has the advantage that only two beams meet in one node and no bending moments and upward shear forces occur.

Five types of connections are studied: welded steel nodes, 3D printed nodes, connections with fasteners, glued connections and interlocking joints. Although welded steel connections and 3D-printed nodes have a high strength and stiffness, they block the potential to apply a complete digital fabrication and assembly process. Previous research has shown the possibility to apply an entirely robotic construction workflow when simple screwed, nailed or glued connections are applied. However, these simple connections are unsuitable for application in structures with high loads and strict safety regulations. It is therefore decided to apply interlocking joints, also known as Japanese connections, because of their aesthetics, suitability for digital fabrication and higher structural performance compared to conventional screwed or glued connections in digital timber fabrication projects.

Since the bridge will be exposed to outside conditions, a wood type with a high durability class is required. Azobé is chosen by reason of the availability in the Netherlands and adaptability by machines.

A double curved surface is taken as starting point for the shape of the bridge. Both a synclastic and anticlastic surface are considered, see Figure 4. A hexagonal reciprocal grid is applied. In order to create a curved surface with straight beams, the beams should be connected eccentrically. This eccentricity has to be accommodated in the connections.

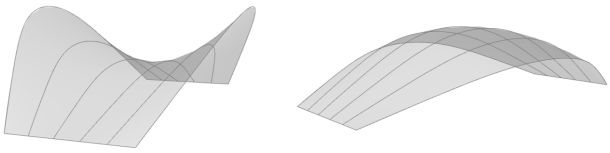

Figure 4: Accuracy vs. level of detail and design freedom

Workflow

Since a gridshell structure is statically indeterminate and the connection design of interlocking joints is integrated in the full beam, the global and connection design are strongly related. Although favourable, designing at both levels simultaneously is difficult due to the lack of starting points. Therefore, an iterative workflow is

applied in which first the global and subsequently the connection design is addressed. Subsequently both are integrated.

Global design

First of all, the geometry of the bridge is created parametrically using the *Grasshopper* plugin for *Rhino* in combination with *Python* on the basis of a set of user input parameters (e.g. span and clearance height), see Figure 5.

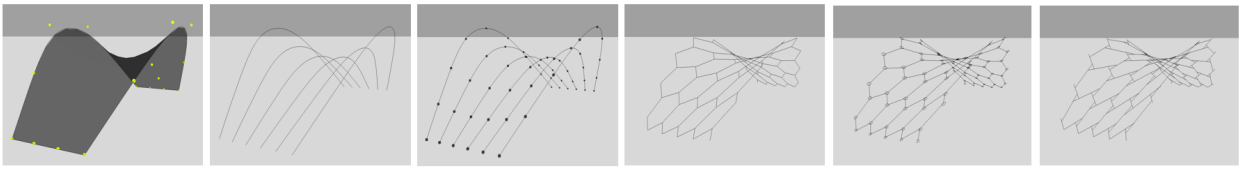

Figure 5: Process of geometry generation

This model is subsequently converted into a structural model using the Finite Element plugin for Grasshopper called *Karamba*. The advantage of using *Grasshopper* together with *Karamba* is that changes can be easily made, allowing analysis of a large number of design alternatives. In this initial design stage, the construction of influence planes is omitted in order to avoid obtaining a computationally intensive model at the expense of design freedom. A set of 12 important load combinations combining dead-, wind- and crowd-load is applied according to NEN-EN 1990 and NEN-EN 1991.

After this, a cross section and shape optimisation are implemented, with the goal to minimise material usage. A *Python* script is written to iteratively determine the minimum cross section sizes, which is necessary for its static indeterminacy. All beams are verified in accordance with NEN-EN 1995-1, considering all 12 load cases. An effective cross sectional area is used for the verification in order to account for the reduced cross section at the location of the connection.

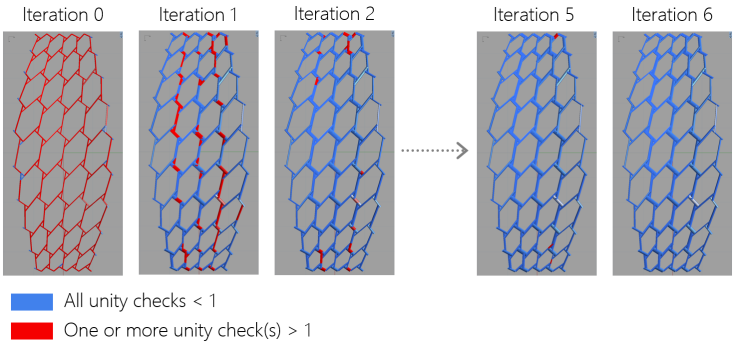

Figure 6: Iterative cross section optimisation

Due to the complex relation between the shape parameters and mass of the structure, an evolutionary solver (*Galapagos*) is used to find the optimal shape. A shortened version of the cross section optimisation loop is integrated in order to effectively approximate the minimum mass of each design alternative.

Connection design

Here, the focus is shifted from the global design to the design of the connection. It is decided to apply a lap joint, see Figure 7a. This type of interlocking joint fulfills all requirements regarding structural performance and design freedom (connection of beams with different sizes at different angles). Furthermore, the connection is feasible for CNC-milling and can accommodate the required eccentricity at the connection to create a double curved surface with straight beams. No additional fastening materials are required, which simplifies assembly of the elements.

As a result of the free-form shape of the bridge, all connections in the structure are different. To avoid designing all connections separately, the design is described in a parametric way. The principal axis of both beams in the connection can be determined by four geometric parameters following from the global model, see Figure 7b. The dimensions and proportions of the connection can be defined by four external dimensions of the beams and three ratio's capturing the size of the notch, see Figure 7c.

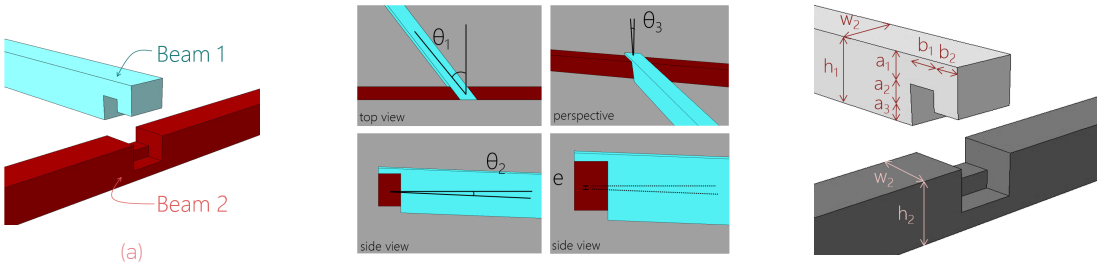

(a) (b) (c)

Figure 7: Lap joint (7a), parameters that are linked to the global design (7b) and dimensional parameters defining the size and proportions of the connection (7c)

Subsequently, the detailing of the connection was examined. A few changes have been made, including slaped and rounded edges, in order to improve the structural performance and serviceability of the connection, see Figure 8. All modifications to the design have been implemented in consultation with a timber producer, *Wijma*, taking into account the possibilities and restrictions of the CNC-milling machine.

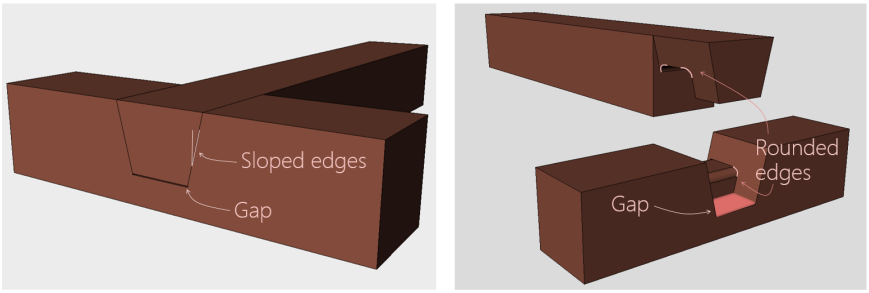

Figure 8: Detailing of the connection design

The next step is the verification of all connections. Although lap joints have already been applied since thousands of years, the knowledge about their structural performance is very limited. Previous research on interlocking joints is often concentrated on detailed numerical analysis of one specific design, resulting in computationally intensive models with limited application for deviating designs. Engineering firms that apply CNC-milling techniques in practice use codes and guidelines that are only valid for standard shapes and conventional building traditions. Both are therefore not suitable for the design of lap joints in a free-form structure, demanding quick calculation methods which are applicable to a large range of design parameters.

Therefore, in this research a simple calculation method is developed in which first all critical planes are assigned and defined in Grasshopper, see Figure 9a. Next, the normal- and shear stresses at the concerning planes are calculated, using the forces from the global *Karamba*-model and dimensions of the planes. All planes are verified for all twelve load combinations according to NEN-EN 1995-1. Additionally, the connection is verified for shear failure along the grain at the corner of the notch, see Figure 9b.

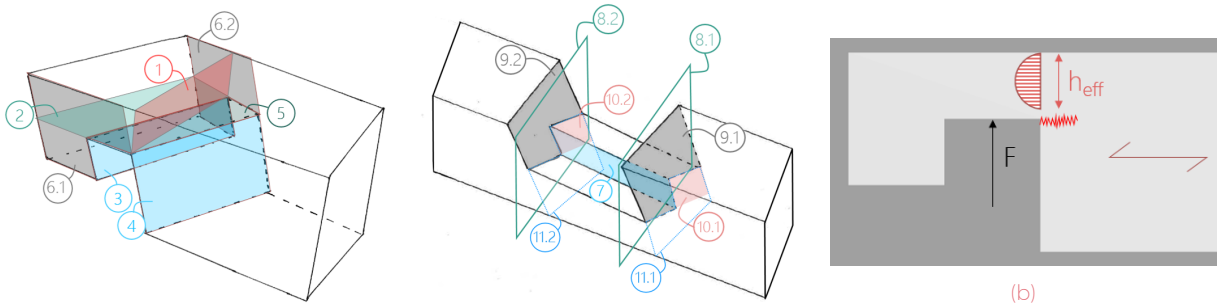

(a) (b)

Figure 9: Relevant planes for stress calculations (9a) and shear failure of the notch along the grain (9b)

Integration

Now that a preliminary global design for the bridge and a parametric definition of the connections is made, the next step is to integrate both designs. The goal is to find optimal dimensions for the connections based on the geometric parameters and the forces of the global model. The optimisation has two objectives:

- The least amount of material usage
- The lowest maximum unity check

Due to the large number of parameters, the complex relation between the parameters, the large number of connections and the statically indeterminacy of the structure, this was a complex task. A way to deal with this is by determining the performance of a large set of possible designs and selecting from this set the best one. Nevertheless, this process is really time consuming. The computation time is reduced by using the result of the cross section optimisation as discussed before as starting point. This eliminates the need to do recalculations to find the force distribution in the statically indeterminate structure.

A way to make a prediction for suitable connection dimensions is by using machine learning. For a set of connections the optimal dimensions are determined by checking a large amount of design alternatives. This data is subsequently used to predict the dimensions of other connections based on the forces in the connection. This gives a better result than using the same dimensions for all connections, without increasing the computation time. Nevertheless, this requires the development of a database with training in- and output, which is time consuming. However, this can be completely automated and therefore carried out outside office hours. It should be decided by the designer if preference is given to spending extra time on the creation of a database of training input in an early design phase, or on finding the right dimensions for the connections that don't fulfil the requirements during the entire design process.

Lab testing of connections

Finally, lab tests were performed to obtain more insight into the failure mechanism with the greatest uncertainty: shear failure of the notched member along the grain, see Figure 10 (left). The Eurocode prescribes a calculation method for the shear capacity of notched members based on the fracture energy of softwood. The tests show that the calculation method does not adequately predict the shear strength of notched members made of Azobé and that therefore additional research on the fracture energy of hardwoods is required to develop a more accurate prediction method.

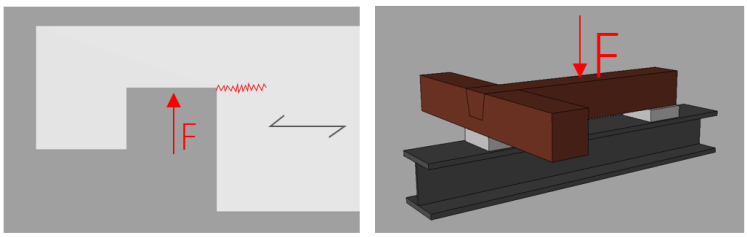

Figure 10: Left: expected location of the crack along the grain due to a shear force *F*. Right: the test setup

Rounded edges and screws were expected to improve the shear capacity. This hypothesis was confirmed by tests. Applying rounded edges with a radius of 10mm instead of sharp edges increases the shear capacity significantly: with a factor 1.6. The increase is even more substantial in case screws are added: a factor 2.2 with sharp and 3.0 with rounded edges, see Figure 11.

Additionally, tests were done with specimens that were first brought to failure and then repaired with screws. The specimens reached approximately the same failure load as the undamaged specimens. This means that the placement of screws is a suitable measurement for repair in case cracks are detected during life-span.

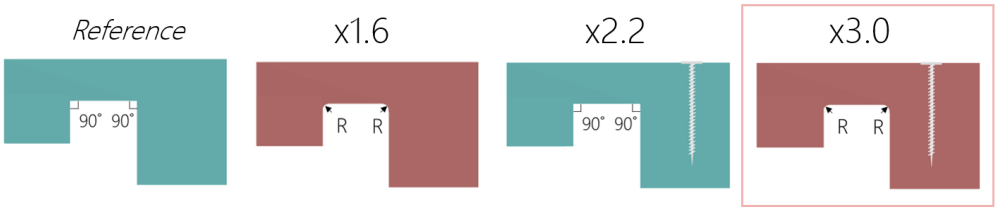

Figure 11: Increase in capacity when applying rounded edges and/or screws

Given the promising test results, it is decided to apply both rounded edges and screws. The calculation model of the connection is updated by multiplying the shear capacity calculated as described above by a multiplication factor that takes into account the increase in the shear capacity. This multiplication factor comes from the test results.

Final design

After completing the described design steps, a first design of the pedestrian bridge is obtained, see Figure 12. The main dimensions of the bridge are:

- Span: 9.4m
- Width of the deck: 2.5m
- Clearance: 1.2m

The bridge is composed of 93 beams which link in 163 connections. The total weight is 2665kg, of which less than 1% steel. The weight of the structure per m^2 bridge deck (excluding the weight of the deck) is $89 kg/m^2$.

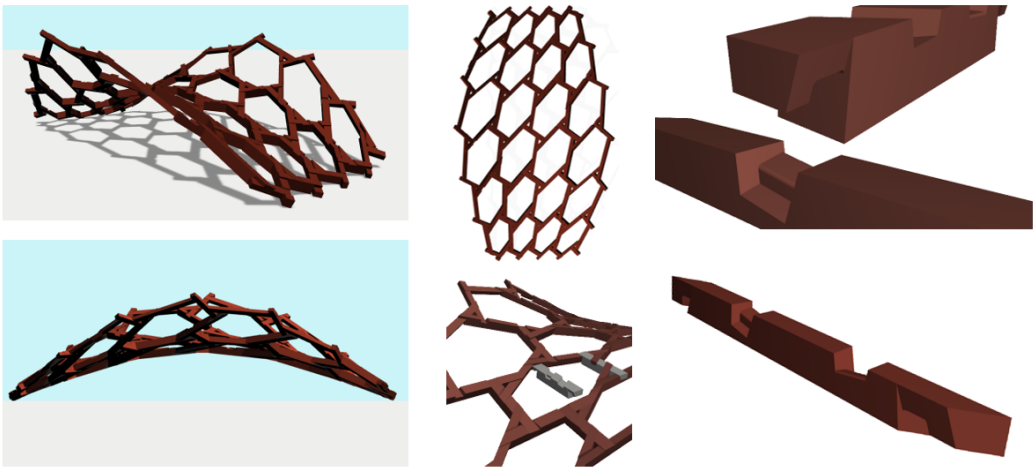

Figure 12: The final design for the case study

Conclusion

The combination of a reciprocal grid and interlocking joints is proven to be particularly suitable digital timber fabrication since a functioning free-form structure can be created without any fasteners. This enables a complete digital fabrication and assembly workflow and limits the use of secondary materials. The uniqueness of all connections and the strong relation between them makes the design process complex. Nevertheless, with the help of design tools like evolutionary solvers and machine learning algorithms it is possible to deal with this complex relation and a large number of parameters.

Lab tests have shown that the verification method for notched members in Eurocode 5 poorly approximates the shear capacity when hardwood is used. Further research on the fracture energy of hardwoods and its dependency on moisture content is required to propose a more suitable method. Tests on specimens with rounded edges and screws as reinforcement have shown a large increase in shear capacity: an increase of a factor 1.6 when only rounded edges are included and a factor 3.0 when both rounded edges and reinforcement are applied. Hence, for notched members it is recommended to always apply rounded edges, preferably in combination with screws.

All in all, this case study shows that it is possible to design a load bearing free-from gridshell timber structure on both global and connection level, using advantages of digital design and fabrication techniques.

Contents

Introduction

1

Introduction

1.1 Introduction

The current way of building is strongly influenced by the conventional way of manufacturing. This has resulted in a standardisation of structural systems, which firmly determines our image of the design of structures like buildings and bridges. Due to the rapid development of innovative (digital) manufacturing techniques, a wide range of new possibilities arises. For this, it will be necessary to revise the current way of building and look for new types of structures, which make effectively use of the benefits and possibilities of the new ways of manufacturing.

Structural optimisation

The great design freedom that is accompanied by the new manufacturing techniques has led to a great amount of research in the field of optimisation tools. Structural optimisation (SO) can broadly be defined as the procedures carried out in order to create an efficient structure. Studies show that SO has great potential. Nevertheless, there are currently still problems in converting the results of SO result into a feasible structural design.

Small scale

The great rise of several 3D printing techniques, like powder bed fusion, direct energy deposition and material jetting, has greatly expanded the design possibilities on small scale. Take for example the structurally optimised node designed by Arup using metal laser sintering (Figure 1.1a) or casting with printed sand mould technique (Figure 1.1b). The design of these nodes is a combination between the results of a topology optimisation and the requirements imposed by the manufacturing technique. However, a drawback of the currently available printing techniques is that the size of the products is limited due to the dimension of available printers. This makes the methods only suitable for products at element level and not (yet) at structure level.

(a) (b)

Figure 1.1: Node printed by laser sintering (1.1a) and casted with a printed sand mould (1.1b)

Large scale

Looking from a broader perspective to digital manufacturing, a field that is undergoing much innovation today is robotic fabrication. Robotic fabrication is currently already extensively used in the automotive industry. Big advantages of robotic fabrication in this industry are for example high efficiency due to short cycle times for

mass-production, higher quality and reliability and the ease of reproduction at different locations. A reason for the technique not to be widely applied in the construction industry yet is due to its unique character of structures in the built environment and the unstructured nature of building sites [46]. However, robotic fabrication also entails plentiful advantages for building structures like a greater design freedom and reduced material use for logistic purposes. In the current built environment, a strong preference is given to repetitive patterns and standardised elements in order to reduce costs, labour and risk of human errors during assembly. Robotic fabrication offers the opportunity to deviate from this while maintaining low operational costs, a limited amount of labour, accuracy and reliability.

Innovations in the field of robotics have triggered several universities and research institutes to do research on the application of robotic fabrication in architecture. The research groups leading in this field are the *Gramazio Kohler Research group* from the ETH, Zürich and the *Institute for Computational Design* from the University of Stuttgart. In Appendix A, a number of notable research projects will be discussed. Despite the enormous progress made in the field of robotic fabrication over the past ten years, there is still a lot of room for improvement, both in the field of automation the design process. The latter being the scope of this project.

1.2 Problem Statement

Research done by several research institutes has shown the great potential of the application of robotics in the fabrication of timber structures, in particular the research carried out by the *Gramazio Kohler research group* from the ETH, Zürich (see Figure 1.2). Up to now, the focus was mainly on architectural components with a limited structural function (only subjected to self-weight loading), built in an indoor (controlled) environment. The next step will be to focus on structures with a structural function, meeting all requirements imposed in the Eurocodes, and move to a complete robotic fabrication on site, allowing for construction on remote places or locations that are hard to reach.

(a) (b) (c)

Figure 1.2: Projects by the Gramazio Kohler research group: *The sequential Structure* (2010) (1.2a), *Complex Timber Structure* (2013) (1.2b) and *Spatial Timber Structure* (2015) (A.11) [63]

In the field of robotic timber fabrication, there has only been a small focus on the connection between the elements; this despite the fact that the connection is often the critical part in timber structures. When only the force distribution and stiffness of the overall structure is considered during a structural optimisation, a non-optimal structure can be obtained with an overestimated strength and stiffness. Therefore, the design of the connections and its structural behaviour must be included into the optimisation procedure for the whole structure. In order to do that, first a suitable connection design should be made that can be fabricated by robots. After this, the node has to be modelled analytically and/or using a FEM-software gaining insight in its structural behaviour. Ideally, the models should then be verified by lab testing. The connection model can subsequently be used as an input for the structural optimisation procedure of the overall structure.

Currently used solutions for complex timber joints

Projects by the ETH on robotic timber fabrication have shown the potential of robotic assembly of complicated 3D-timber connections by applying a bolted connection or a glued connection, see 1.3. However, the strength and stiffness of these connection types are really limited. When designing a structure with a larger force flow through the connections, a more solid connection will be required.

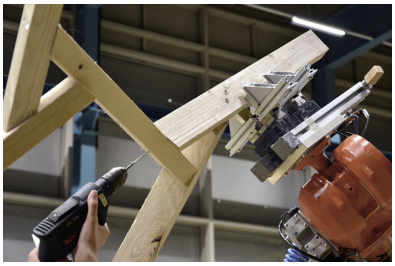

(a)

(b)

Figure 1.3: Bolted connection in the *Complex Timber Structure* (1.3a) and glued connection in the the *Spatial Timber Structure* (1.3b) from the Gramazio Kohler research group [63]

When looking at timber structures manufactured in the conventional way, the most common solution for 3D-connections between timber elements in a free-from structure is a welded steel node which is bolted to the different timber elements, see Figure 1.4. Even though this type of connections provide a considerable higher strength and stiffness, the solutions are expensive and require a lot of labour, especially when every node in the structure is unique.

(a)

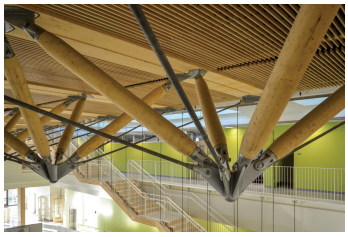

(b)

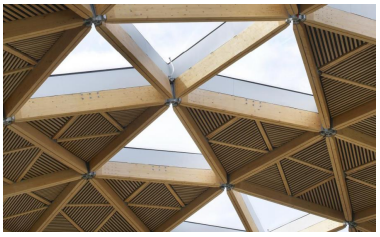

(c)

Figure 1.4: Custom made welded connections in Shigeru Ban's *Cardboard Bridge* [56] (1.4a), Zipper trusses developed by faculty at UMass, Amherst [48] (1.4b) and the University of Exeter Forum, UK [7] (1.4c)

Interlocking joints

An architect that is known for his impressive timber structures is Kengo Kuma. He applies traditional Japanese joinery techniques in modern design, see Figure 1.5. Some other examples of joints from traditional Japanese carpentry are shown in Figure 1.6. The traditional Japanese joinery can be used as a source of inspiration for the connection design due to the purity of the monolithic timber connection: the connections are pure timber on timber connection and gain their strength mainly by interlocking. An advantage of a single material timber connection is that the fabrication of the connection can be integrated into the complete digital fabrication workflow of the complete structure.

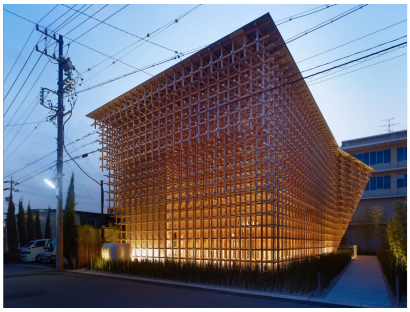

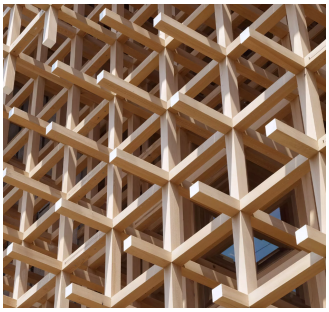

Figure 1.5: *GC Prostho Museum Research Center*, Kasugai-Shi, Japan by Kengo Kuma [20]

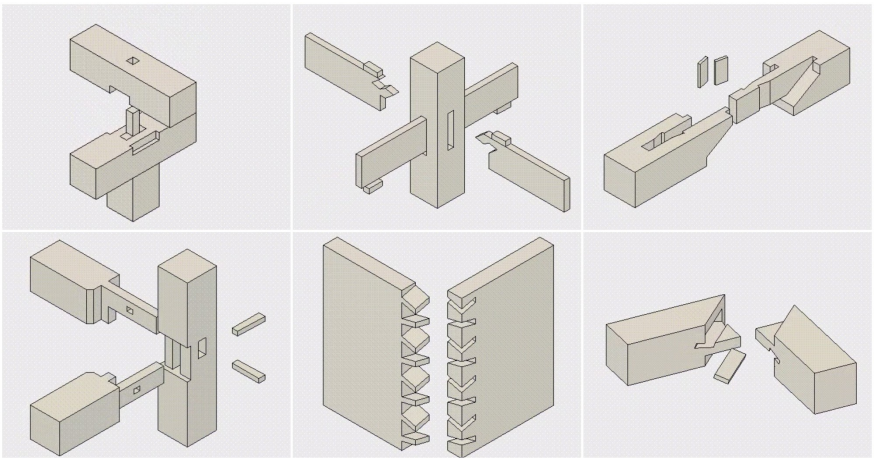

Figure 1.6: Examples of Japanese joinery [32]

1.3 Research question

This research project will focus on the following research question:

How to make a design for a free form timber frame bridge using the advantages of digital fabrication techniques?

Secondary objectives that will be addressed as part of the main research topic are:

- *How to minimise the amount of secondary materials used for connections*
- *How to minimise material usage*
- *How to make an integrated design on global and detail level*
- *How to include the limitations of the digital fabrication process into the design work-flow*

These questions will be dealt with through a case study.

1.4 Case study

The case-study will focus on the structural design of a timber frame bridge for pedestrians. The choice for the design of a bridge is because of its mainly structural vision. In this way, the structural aspects of robotic timber construction can be investigated, rather than the more architectural ones, which have previously been addressed by architectural research groups like the Gramazio Kohler group.

The choice for a timber structure is made foremost because timber can easily be modified and handled by robots. In addition, it's in tune with the desire to use sustainable materials initiated by the growing concern around climate change and the finiteness of resources.

2

Research Approach

The research approach can be split in three parts. The first part is the study phase. This phase consists of a literature review to acquire knowledge about the current state of art in robotic timber fabrication, structural systems and timber connections in frame structures. The second part is the design phase. The design process is an iterative procedure in which consecutively a global design and a connection design for the bridge are made, whereafter both models are integrated, see Figure 2.1. After each iteration, an additional optimisation will be added. The aim is to obtain an integrated design on global and detail level. In the final phase of the research project recommendations are made, conclusions are drawn, the final report is written and a prototype of (a part of) the bridge is made.

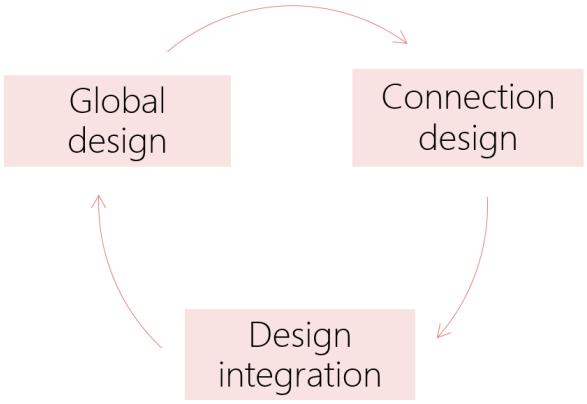

Figure 2.1: Iterative design process

In the next sections a more detailed description of the different phases is given, together with the expected results for each phase.

2.1 Study phase

The study phase consists of a literature review of the current state of art in the field of robotic timber fabrication, different types of timber frame structures and different types of connections. On the basis of this research, a choice will be made for a structural system and type of connection that will be applied in the case study.

2.2 Design phase

As mentioned before, the design process is an iterative procedure in which consecutively the global design and connection design will be optimised and linked to each other.

2.2.1. Global design

Before a design for the connection can be made, there should be a general idea of the required performance of the connection regarding strength, stiffness and geometry. Therefore, the first phase of the bridge design includes the global design of the pedestrian bridge. The first step is to define all loads and load combinations that should be applied to pedestrian bridges according to the Eurocode. Thereafter, all boundary conditions

should be described. In order to verify the structural behaviour of the bridge, a material model should be defined. Furthermore, all requirements regarding the strength and stiffness of the material should be implemented into the calculation software. Finally, after a form study, a preliminary design for the gridshell bridge can be made. In the first design iteration, a cross-section and shape optimisation will be implemented as well. The structural results of the model of this preliminary design will then be used for the design of the connections.

2.2.2. Connection design

Now that a preliminary global design of the bridge is made, the connections between the timber elements can be designed. In order to make sure that a feasible design is obtained, first all design requirements from the global design (both geometric and structural) and the constraints from the CNC milling process should be defined. With this information, a parametric connection design can be made. Thereafter, the strength and stiffness of the connections will be estimated through analytical calculations.

2.2.3. Design integration

The next challenge is to use the geometry and forces from the global model to dimension all individual connections in the bridge. This is complex due to the large number of parameters that define the geometry of the connection. Furthermore, the optimal proportions of the connection are determined by a large number of forces and corresponding unity checks. In this phase of the research, there is a search for a method to deal with this large number of parameters, with eventually the goal to dimension all connections without requiring a long computation time.

2.3 Testing

Since the structural performance of the connections is only verified by means of a simple analytical calculation of the stresses in the critical planes, tests will be carried out to authenticate the calculations. Due to time constraints, only the most critical failure mechanism will be tested: shear failure of the notched member.

2.4 Final phase

In the final phase conclusions are drawn, recommendations formulated and the report finalised. For the final presentation, a case study will be carried out to show the possibilities of the final model.

II

Study Phase

3

Structural System

The aim of the project is to design a timber frame bridge, using the advantages of robotic fabrication techniques. The following two requirements for the structural system are defined:

- Allowing for freedom of shape
- Composed of straight bars (timber beams)

For beam-element based structures a distinction can be made between two types of structures: space frame structures (Figure 3.1a) and grid shell structures (Figure 3.1b). Both type of structures and its advantages and disadvantages will be discussed in the next sections.

(a) (b)

Figure 3.1: The *Palafolls Sports Hall* in Palafolls, Spain (3.1a) [18] and the *Savill Building* in Windsor, England (3.1b) [9]

3.1 Space frame structures

A space frame structure is a lightweight structure containing compression and tension elements which are connected by hinges. In the case that the external loading is applied to the nodes, only axial forces are introduced. Bending moments and shear forces only occur due to self weight loading. In most cases, the term space frame is used for systems with an upper and lower layer of bars (often parallel) with a network of bars in between. Figure 3.2 shows some examples of two-layered structural systems with a repetitive pattern. Usually it is aimed to accomplish a lot of repetition in order to reduce cost and simplify construction. [17]

(a) (b)

Figure 3.2: Two layered systems (3.2a) and different principle shapes (3.2b) [17]

Nowadays, the use of space frame structures in the developed world has diminished because of the high construction costs. Nowadays space frame structures mainly have potential in developing countries because of the high demand for efficient structures due to the high material costs. The application of this type of structures in developed countries has diminished over the past decades due to the increase of labour costs. Though, when applying digital fabrication techniques, a resurgence of space frame structures would be possible. This also fits the growing desire to make efficiently use of materials for increased sustainability.

Figure 3.3 shows an example of a recently built space frame structure designed by the Iraqi-British architect Zaha Hadid, known for her futuristic free-form structures. *The Heydar Aliyev Cultural Center* in Baku, Azerbaijan has a wavelike fluid form, showing the possibility to make free-form structures when applying a space frame.

(a) (b)

Figure 3.3: Heydar Aliyev Cultural Center, Baku, Azerbaijan by Zaha Hadid. Space frame under construction [11] (3.3a) and the final structure including cladding [58] (3.3b)

Another example of a recently built space frame structure is the *Nationaal Militair Museum* in Soesterberg, the Netherlands, see Figure 3.4. Unlike the cultural centre in Baku, the design does not appear highly complex by it's shape. What makes this buildings interesting is the fact that the roof structure is completely optimised for minimum material usage, saving on costs but also on CO2-emission for steel production, processing, transport and assembly.

These two project show the opportunity to both optimise a space frame structure both on global and element level.

(a)

(b)

Figure 3.4: Nationaal Militair Museum in Soesterberg, the Netherlands [40] [52]

3.1.1. Space frame bridges

In general, space frames are mostly used for structures that transfer loads in two directions like for example roof structures.

Figure 3.5 shows the *Cardboard bridge* by Shigeru Ban. The bridge was a temporary structure which was exposed for 2 months during a cultural event close to the famous Roman aquaduct *the Pont du Gard* in France. The bridge spans 20 meters and is built up by 280 coated cardboard tubes connected by steel joints.

(a)

(b)

Figure 3.5: Cardboard bridge by Shigeru Ban [26] [34]

3.1.2. Space frame connections

In order to ensure that the connections between the bars behave like hinges, the joints should have sufficient rotational capacity.

In most cases, steel transition elements are used between the timber bars and joints. Therefore, the solution can be similar to the joints in a structure with steel bars. There is for example a version of the MERO-system (see Figure 3.6) that connects rectangular timber sections. The pieces MERO-bar are pressed into the timber beam and fastened with steel dowels.

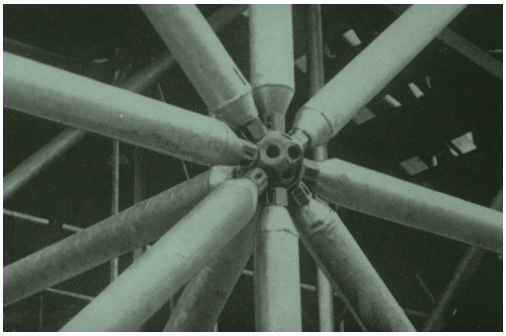

Figure 3.6: MERO System [17]

Figure 3.7 shows an example of another type of joint applied in *The Earth Centre and Solar Canopy* in South Yorkshire, England. A steel transition element is on one side bolted to a steel joint and on the other side to a timber bar.

(a) (b)

Figure 3.7: The Earth Centre and Solar Canopy [55]

When looking to the configurations for two layered space frame systems in Figure 3.2 it can be seen that the minimum amount of bars connecting is four, when applying a grid with two layers of hexagons. Although this type of grid is preferred due to the simplicity of the nodes compared to the other grids, this type of grid is not preferable since both a rectangular and hexagon are not a stable shape. Therefore, the nodes are required to have some moment capacity in order to keep the system stable, leading to bending moments and shear forces in the bar elements as well. When choosing a three-dimensional triangular grid, the minimum number of bars connecting increases to eight.

3.1.3. Advantages and disadvantages of space frames

Disadvantages of space frames are [17]:

- Costs The costs are relatively high compared to other types of structural systems, especially for structures with a small span. The nodes are the most expensive part of the frame. Therefore, reducing the amount of nodes will result in a more economical structure and a shorter erection time.
- Regular Geometry A space frame structure looks really busy. Due to the regular geometry, the structure eyes really dense from certain viewing angles.
- Erection time The number and complexity of joints can lead to a long on site erection time.
- Fire protection Due to the high surface area of the space frame grid elements, it is hard to apply fire protection economically.
- Complexity connections Due to the large number of bars connecting in one point, a complex connection is required. In case of a free-form structure, a high variation in node designs will be required.

Advantages of space frame structures are [17]:

- No bending moments by external forces In case the loads are applied to the nodes, the bars within the space frame only carry axial tension or compression forces since the connections cannot transfer bending moments. Bending moments are only introduced by the the self-weight of the bars.
- Load sharing All elements contribute to the load carrying capacity. In contrast to planar beams or trusses concentrated loads are distributed more evenly trough the structure and to the different supports, resulting in lighter structures and smaller deflections.
- Robustness Failure of one single element does not necessarily lead to collapse of the overall structure. Therefore space frames are considered highly redundant structures.
- Modular components and prefabrication The components of a space frame structure are almost always prefabricated in a factory, leading to a high accuracy and quality. The limited size of the elements leads to easy transportation. Furthermore, depending on the type of connections, the structure could be dis- and re-assembled.

- Regular geometry and simplicity of erection The space frame can be assembled safely close to or at the ground and afterwards jacket into final position. Furthermore, large structures can be assembled in smaller parts on site, limiting disruption of other activities.

- Supporting structures, freedom of placing Within reason, the supports of a space frame can be placed at any node of the grid and at any location in the plan.

3.2 Gridshell structures

A shell structure is a thin, curved plate structure that transmits forces mainly by membrane forces, which are resultants of in-plane normal and shear stresses which are uniformly distributed over the thickness of the shell. In the case of a gridshell, a grid is applied rather than a continuous surface.

A distinction between two types of gridshells can be made:

1. A gridshell built from curved continuous elements like Figure 3.8a

2. A gridshell built from separate straight elements like in Figure 3.8b

The first type of gridshell is not suitable for robotic assembly. Therefore, the focus will be on the second type of gidshell: a shell composed of straight elements which together form a double curved surface.

(a)

(b)

Figure 3.8: *The Toledo Gridshell by Sergio Pone* in the School of Architecture Courtyard in Naples, Italy (3.8a) [61] and *The Marlowe Academy* in Ramsgate, England (3.8b) [13]

Another great example of a lightweight timber gridshell composed of discrete elements is the *SUTD Library Pavilion* located at the Dover Campus in Singapore, see Figure 3.9. The shape of the pavilion follows the thrust-lines in compression, which were derived by using a numerical hanging-chain model. Digital fabrication techniques (CNC-milling) and computational design methods were used to achieve the complex shape and keep the costs low. The structure is composed of:

- 3,008 unique plywood members

- 585 unique sheet-metal tiles

- 3,255 unique plywood spacer blocks

- 192,562 bolts

- 30,039 screws

The structure was pre-assembled by first year SUTD students and after erected on site by the contractor.

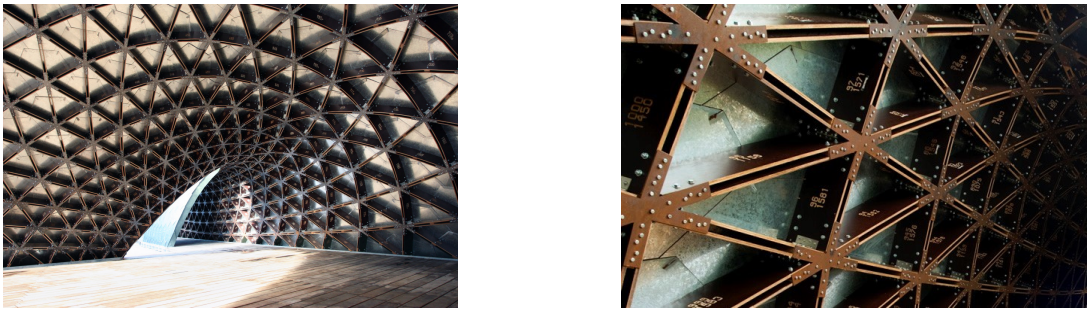

(a) (b)

Figure 3.9: *The SUTD Library Pavilion* located at the Dover Campus, Singapore [31]

3.2.1. Connections in gridshell structures

When considering a free-form gridshell consisting of discontinuous elements, often unique welded steel connections are applied which are bolted to the timber bar elements. Two examples are shown in Figure 3.10 and 3.11.

Figure 3.10 shows the girdshell roof of the *University of Exeter Forum*, England. The roof structure consists of 2000 glulam elements and 162 different steel nodes. 14,724 drawings were produced, containing the detailing of 37,794 (sub)assemblies. This shows the complexity of comprising a free form structure in drawings for fabrication and assembly.

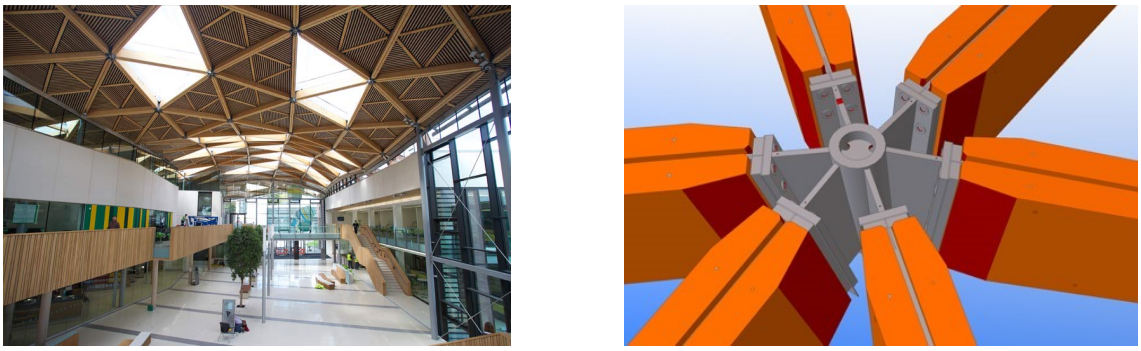

(a) (b)

Figure 3.10: University of Exeter Forum (3.10a) [41] and a *Tekla* model of the node design (3.10b) [59]

Figure 3.11 shows the girdshell roof of the *Herbert Art Gallery & Museum* in Coventry, England. The gridshell is formed by a diagrid of 270 x 142 mm laminated beams. The beams are connected by cast steel spherical nodes (diameter 250mm) with welded plates, enabling connection at different angles.

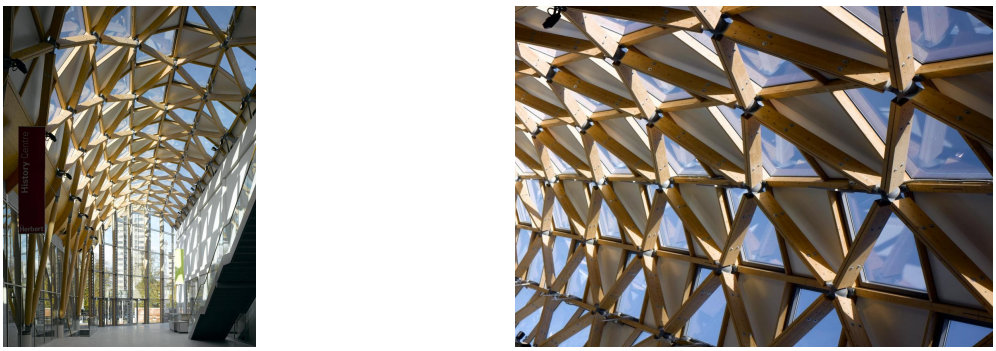

(a) (b)

Figure 3.11: Herbert Art Gallery & Museum in Coventry, England [29]

3.2.2. Reciprocal frame structures

A reciprocal frame structure is a three-dimensional self-supporting structure built up out of beams. Each beam has to both support and be supported by another beam. In order to achieve this, a minimum of three beams is required in order to create a reciprocal (self-supporting) structure. Leonardo Da Vinci already made several architectural designs for reciprocal structures during the Renaissance, see Figure 3.12. Nevertheless, this type of structures only gained popularity recently, due to the development of several computational tools.

(a) (b)

Figure 3.12: Reciprocal bridge design by Leonardo Da Vinci (3.12a) [8] and a model of the bridge (3.12b) [54]

The dome in figure 3.13b is completely constructed without the usage of any fasteners. The loose bars are kept together by gravity. Advantages of reciprocal frames are:

- Built up out of simple (straight) elements
- Great freedom of shape of the final structure
- Rapid construction
- Possibility of dis-assembly and re-assembly (so suitable for temporary structures)

(a) (b)

Figure 3.13: Reciprocal domes [38] [12]

An additional advantage is the simplicity of the joints, especially compared to the joints in space frame structures. Due to the eccentric nature of the connections, only two beams are meeting at one spot. This makes the connections suitable for the application of the Japanese joinery techniques. Nevertheless, the eccentric nature of the joint also has a disadvantage, namely the introduction of bending moments in the beam elements. In order to restrain these bending moments, the eccentricity of the connections should be limited.

A disadvantage of this type of structure is that when one of the bar elements breaks, the whole structure will jeopardise. A bridge structure should have a certain level of robustness in order to prevent progressive collapse due to an (un)identified load situation. In order to achieve this, one of the design strategies shown in Figure 3.14 can be applied.

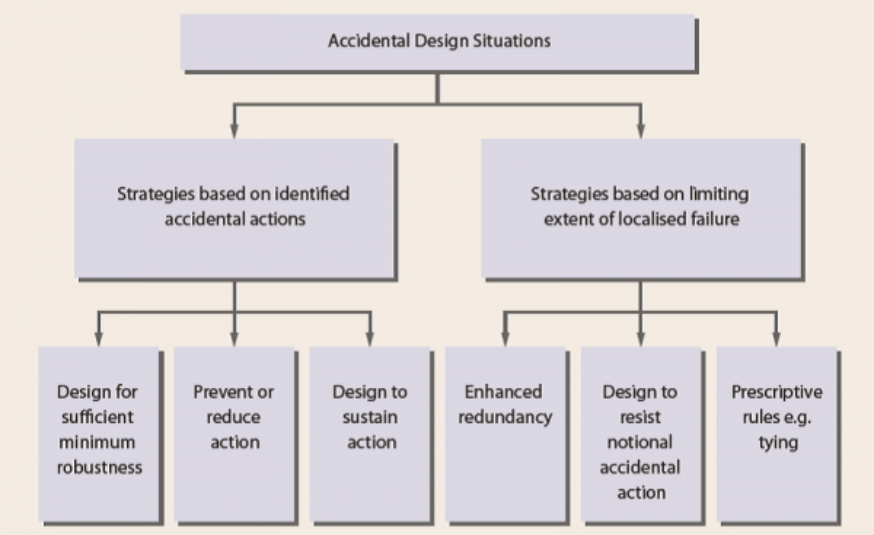

Figure 3.14: Design strategies for accidental design situations [53]

Reciprocal grids

Often, highly symmetric patterns are involved. A number of possible bar grids are shown in Figure B.1

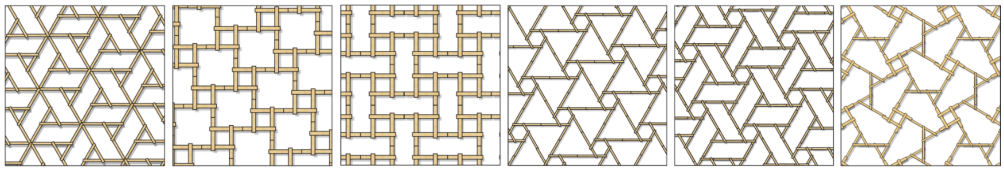

Figure 3.15: Reciprocal grid patterns [51]

By combining the different grid patterns and changing the proportions, different appearances can be obtained, see Figure 3.16

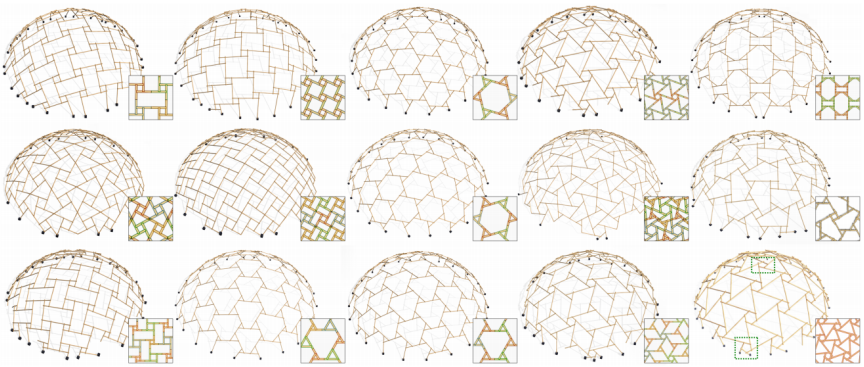

Figure 3.16: Different reciprocal grid patterns mapped on a dome structure [51]

Reciprocal examples

As part of an elective course on digital woodwork as part of the master *Computational Design and Construction* at *Hochschule Ostwestfalen-Lippe*, students had to develop an innovative timber structure inspired by self-supporting, reciprocal systems. Form-finding strategies and understanding of the conditions and constraints related to the digital fabrication technologies were used in the design process. Both the design and 1:1 realisation of the structure using digital fabrication were carried out in four days at the campus of the university.

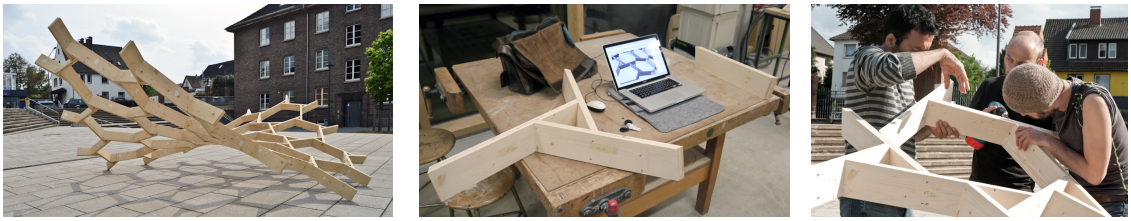

(a) (b) (c)

Figure 3.17: Saddle surface based on a reciprocal frame [33]

3.2.3. Advantages and disadvantages of a gridshell structure

Disadvantages of a gridshell structure are:

- Design freedom In a gridshell structure loads are mainly transferred through in plane forces and scarcely by bending. In order to achieve this, the shape of the structure should be close to the *'surface of trust'*. Deviating from this surface will lead to binding in the frame.
- Erection time The number and complexity of joints can lead to a long on site erection time.
- Redundancy Depending on the kind of grid, there might be a risk for progressive collapse. Especially in case of a reciprocal frame, the redundancy is really low.

Advantages of a gridshell structure are [17]:

- Robustness Failure of one single elements does not necessarily lead to collapse of the overall structure. Therefore space frames are considered highly redundant structures.
- Modular components and prefabrication The components of a gridshell structure are often prefabricated in a factory, leading to a high accuracy and quality. The limited size of the elements leads to easy transportation. Furthermore, depending on the type of connections, the structure could be dis- and re-assembled.
- Regular geometry and simplicity of erection Like space frame structures, gridshells can be assembled safely close to or at the ground and after be jacket into final position. Furthermore, large structures can be assembled in smaller parts on site, limiting disruption of other activities.
- Simplicity of the nodes Compared to multi-layered space frame structures, the nodes in a grid shell are much more simple.

3.3 Conclusion

In order to select one of the two previously mentioned structural systems, both systems are given a score between 1 (bad) and 5 (good) on a few different criteria that are considered essential in the design of a pedestrian bridge, fabricated by robots. The scores are visualised in Figure 3.18.

It can be concluded that, considering the structural performance of the system, a space-frame structure performs better than a gridshell structure. Nevertheless, a gridshell has large advantages regarding fabrication of the nodes and the assembly of the whole structure. When a reciprocal gridshell structure is applied, the complexity of the connections is reduced even more since only two beams meet in one location. This type of structure is therefore really suitable for a completely robotic fabrication and assembly workflow.

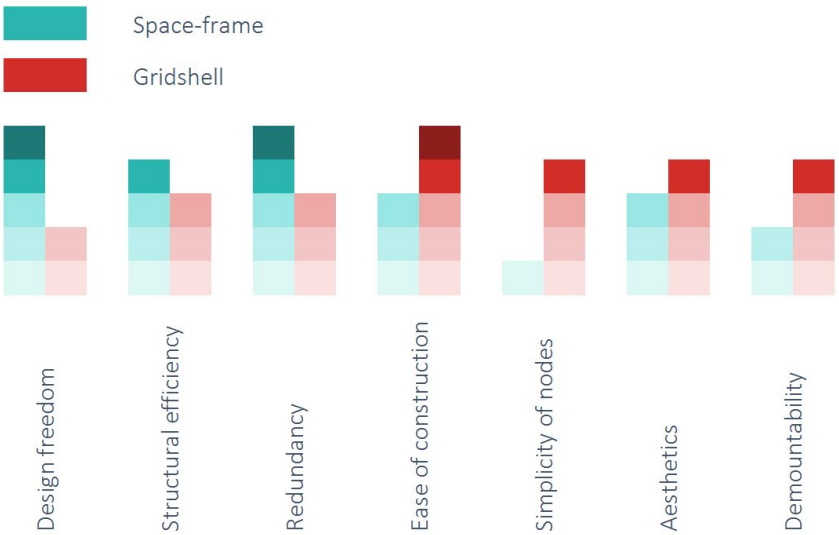

Figure 3.18: Score of the two systems on a few criteria

4

Connections

In the previous sections, several frequently used connection designs have been shown. It could be concluded that the most popular way of connecting timber beams in free form structures is by the application of a welded steel node which is bolted to the timber beams, see for example Figure 3.6, 3.7, 3.10b and 3.11b in Chapter 3 Structural System. In this chapter a distinction will be made between four types of of connections:

- Welded steel nodes
- 3D printed nodes
- Fasteners
- Glued connections
- Interlocking joints

The different types will be briefly discussed in the following sections. Thereafter a choice will be made for one type of connection in a similar way as in Chapter 3 Structural System: a score will be awarded to several criteria that determine the structural performance, reliability, aesthetics and ease of application of the node-type.

4.1 Welded steel nodes

As mentioned before, one of the most popular way of connecting timber elements in a free form structure is by the application of a welded steel node. Some advantages of applying this kind of node are:

- Design freedom Since all nodes are unique and custom made there are not a lot of limitations to the number of bars connecting and the approaching angles.
- Strength & stiffness The nodes have a high strength and stiffness. Therefore not the nodes are usually the critical part in the structure but the timber beams.

Nevertheless, this type of node has also quite some disadvantages:

- Ease of fabrication The fabrication of unique welded steel joints is very labour intensive resulting in high costs and long construction times.
- Aesthetics The application of (relatively big) steel nodes highly influences the appearance of the timber structure.
- Sustainability The application of steel and the welding process decrease the sustainability of the structure
- Weight Welded steel nodes have are heavy and therefore contribute greatly to the self weight of the structure.

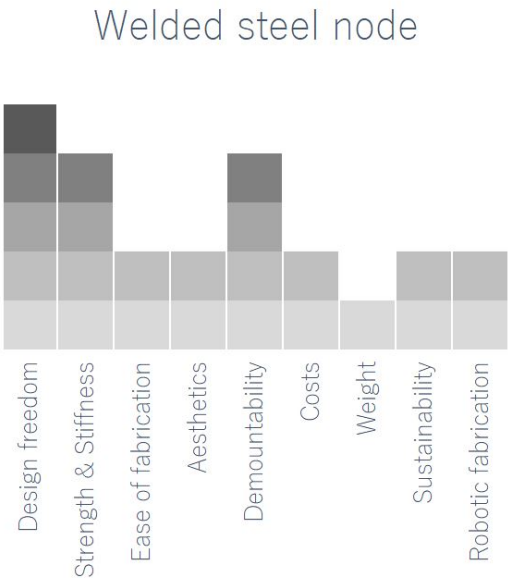

Figure 4.1: Score of the welded steel node on several criteria

4.2 3D printed nodes

A new type of node that is currently in development is the 3D printed node.

Bayu Prayudhi, a former student at the TU Delft, studied in his Master Thesis project called *3F3D: Form Follows Force with 3D printing* the possibility to apply topology optimisation for free-form building envelope designs with the application of additive manufacturing techniques [44]. In order to test his design approach he designed a pavilion-like gridshell timber dome with optimised 3D printed connections. For his prototype he used solid wood as gridshell beams and 3D-printed nodes of carbon fibre reinforced polyester filament. Pictures of his prototype are shown in Figure 4.2.

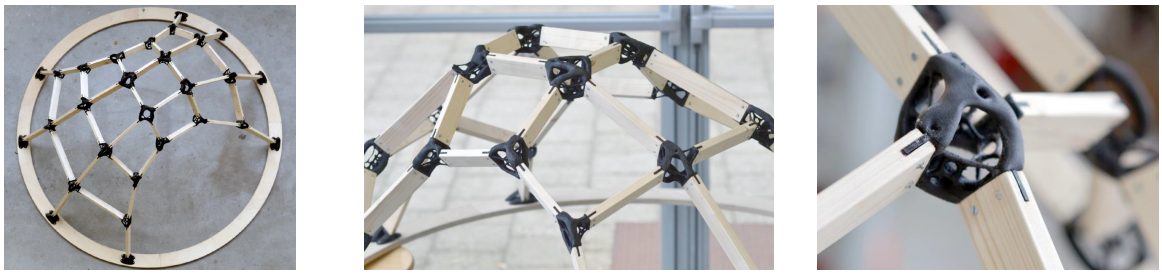

(a) (b) (c)

Figure 4.2: Prototype by Bauy Prayudhi as part of his master thesis *3F3D: Form Follows Force with 3D printing* [**?**]

During the workshop *Intelligent Fabrication 2017 - Digital Bridges* which was discussed in Section A.2, some students also used additive manufacturing techniques to fabricate nodes between timber beam elements. Figure 4.3a shows the bridge and node design made by a group of students using *Grasshopper* software. A scale model (1:10) of the bridge was made during the workshop, including the connections using 3D printing technology, see Figure 4.3b.

If a 3D printed connection is compared to a standard welded steel node, the following advantages can be defined:

- Design freedom The 3D printing technique allows for a high design freedom. Nevertheless, some of the 3D printing techniques that are available at the moment have some limitations regarding the printing angles and minimum material thickness. However, this only influences the design freedom at detail level, not at structure level.
- Strength & stiffness 3D printed nodes have a large design freedom. Therefore the node can be completely be optimised for strength and/or stiffness.

(a) (b)

Figure 4.3: Design and prototype of a timber bridge designed by students as part of the workshop *Intelligent Fabrication 2017 - Digital Bridges* at *Ecole nationale supérieure d'architecture de Versailles* [30]

- Weight When 3D printed nodes are designed according to a topology optimisation, a large decrease of weight can be obtained compared to a welded steel node with a similar strength and stiffness.
- Aesthetics The shape of 3D printed nodes are usually more organic and smooth, leading to a softer appearance than the often rough welded connections.
- Sustainability When the 3D printed node is optimised for minimum material usage, the sustainability of the node is increased compared to welded nodes with respect to usage of finite resource

There are nonetheless also a few disadvantages:

- Simplicity The design process of an optimised 3D printed node is much more complex than for a regular steel node.
- Ease of fabrication The labour required for the production is far less than for a standard welded steel connection. Nonetheless, the process is still time-consuming (depending on the applied technique and material). In the future this might be less of a problem due to an increase of the amount of printers and printer size.
- Cost The most important drawback at the moment are the production costs. Nowadays, the production of a 3D printed node is still considerably larger than a welded connection. At the moment this limits the development and especially the application of 3D printed nodes in construction.

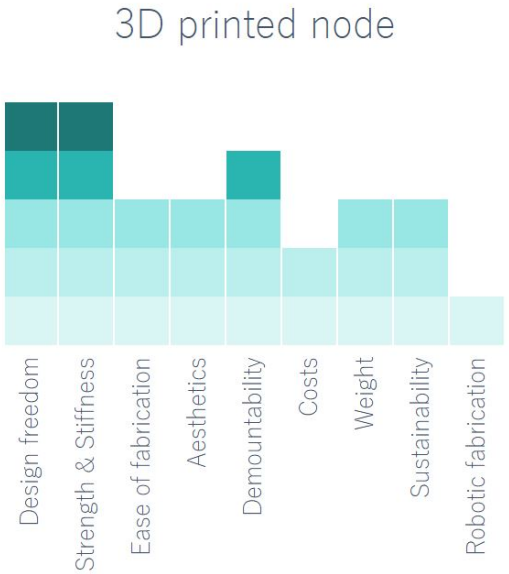

Figure 4.4: Score of the 3D printed node on several criteria

4.3 Connections with fasteners

An example of a gridshell structure with a simple bolted connection is shown in Figure 4.5: *The KREOD Pavilion* in London, England. The designers of the structure were assigned to design a low cost pavilion that was easy and quick to erect. Due to the double curved shape of the pavilion, all connections between the timber elements would have been unique in case that a normal grid structure would have been applied, resulting in really expensive nodes. Therefore the designers decided to apply a reciprocal joining system in which only two bars meet at one spot. In this way they were able to use really simple bolted connections and standard timber beam elements.

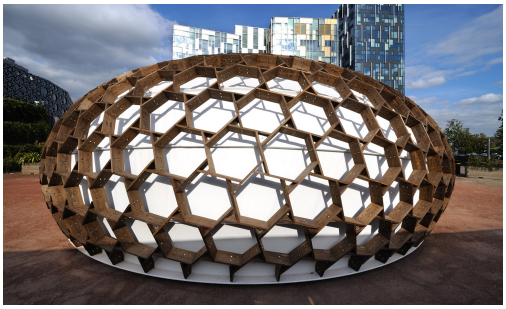

Figure 4.5: The KREOD Pavilion (2012) in London, England [23]

Another example of a gridshell structure with bolted connection is the *Complex Timber Structure* by the *Gramazio Kohler Research group* from the ETH Zürich, discussed in Section A.1.4. Also in this case a reciprocal grid pattern was applied.

These two projects clearly show the limitations of the application of simple bolted connections. First of all, only the connection of a really limited amount of bars in one connection is possible for geometric reasons. Furthermore, a bolted connection has a limited strength and stiffness. A reciprocal grid is therefore suitable since it accomplishes it's stiffness not only from the connection itself but mainly from the triangulation of the bars that it is connecting.

Figure 4.6: Complex Timber Structure by the Gramazio Kohler Research group (2013) [63]

The main advantages of a bolted connection are:

- Cost The connection is cheap to produce.
- Weight Almost no additional weight due for the connection.
- Sustainability Almost no additional material is required.
- Aesthetics

There are nevertheless also two important disadvantages:

- Strength & stiffness The strength and stiffness of the connection type is really limited
- Design freedom Only a limited amount of bars can be joined at one location

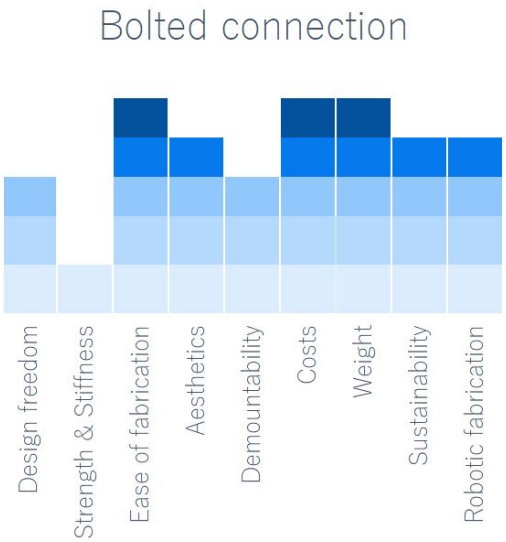

Figure 4.7: Score of the bolted connection on several criteria

4.4 Glued connections

A third type of connection that can be categorised is a glued connection. The Gramazio Kohler research group has experimented with the application of glued connections in the robotic timber fabrication process during the project *Topology optimisation of Spatial Timber Structures (2016)*, see Section A.1.5.

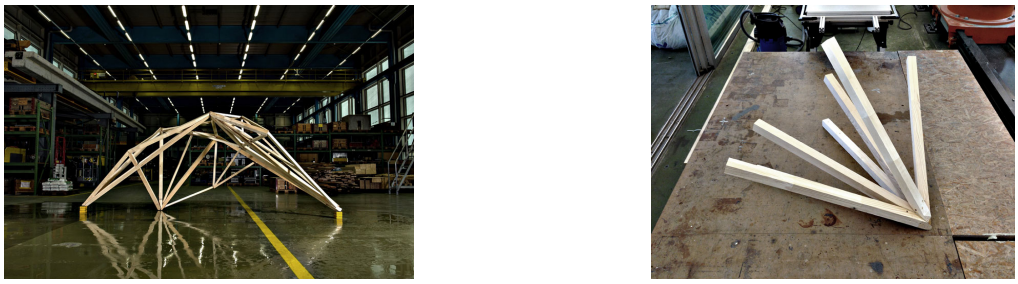

(a) (b)

Figure 4.8: Topology optimisation of Spatial Timber Structures (2015), Zurich [63]

The advantages and disadvantages of glued connections are similar to the ones from connections with fasteners:

Advantages:

- Costs The connection is cheap to produce.
- Weight No additional weight for the connections
- Sustainability Almost no additional material is required.
- Aesthetics

Disadvantages:

- Strength & stiffness The strength and stiffness of the connection type are really low
- Design freedom The more bars are connected at one location, the lower the contact area of the bars, leading to a lower strength and stiffness of the connection

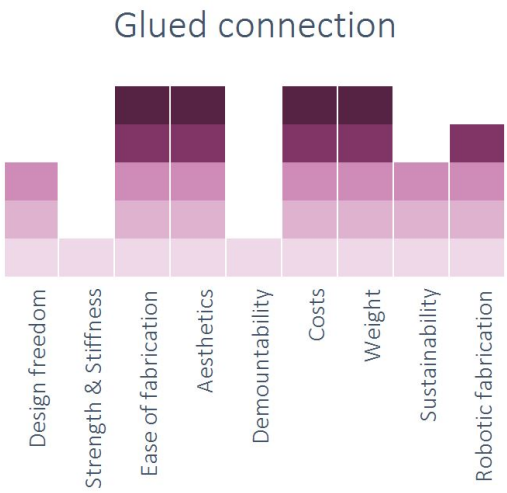

Figure 4.9: Score of the glued connection on several criteria

4.5 Interlocking joints

Wood is one of the oldest building materials, mainly because it is easy to modify and widely available. In the early ages, the development of timber structures was highly influenced by cultural and technical influences and was therefore particular for the region. One of the characteristics of traditional timber joints is demountability, originating from the era of the nomads. Often interlocking joints were applied, which are joints that mainly transfer the load directly through timber surfaces, see for example Figure 4.10. Regularly fasteners were used for reinforcement.

A lot of important knowledge on demountability has gone lost over time. An important reason is the passing of knowledge through hands-on experience and word of mouth to next generations. The transition from a nomad lifestyle to a more sedentary life took away the need for demountability of structures. Together with the development of mechanical fasteners in the Western world like nuts, bolts, beam seats, claw plates, screws, split rings, shear plates, ties, hangers, keys, pints, wedges etc. as result of industrialisation, mechanisation and mass production, this engendered a large decrease of application of demountable joints.

The application of traditional joining types has gone lost because nowadays joints should be designed to allow easy manufacturing for economical considerations. The traditional interlocking joints used to be manufactured manually by highly skilled carpenters. The performance of the joint is very much dependent on the cutting precision. The higher the cutting precision, the lower the installation tolerances can be, resulting in an increase of interface friction and withdraw resistance. In the past, it was really hard to achieve a high accuracy. Nowadays, this could be obtained by applying digital manufacturing techniques. Digital manufacturing techniques could both abate the disincentive regarding the cutting precision, fabrication time and economical considerations. The traditional interlocking joints are designed according to the expertise of carpenters using hand-tools. Since design and manufacturing technique are always inseparable, the geometry of the joints should be adapted to the new digital manufacturing techniques.[25]

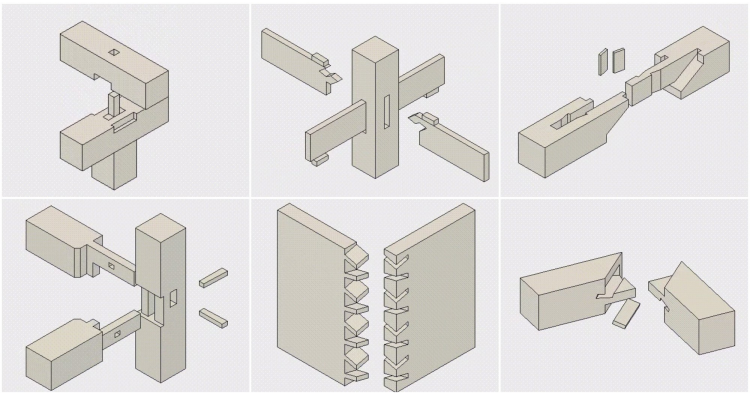

Figure 4.10: Some examples of interlocking joints [22]

Advantages of the application of interlocking joints are:

- Strength & stiffness Compared to a bolted connection,there is made more efficient use of material of the timber beam elements.
- Aesthetics The monolithic character of the connection favours the aesthetics of the structure.
- Demountability Interlocking joints that transfer loads purely by contact without the use of additional fasteners are demountable. This offers the possibility to dis-assemble the structure in case it loses it's function at a certain location and to re-assemble it elsewhere. In addition, it makes the structure suitable to function as a temporary structure.
- Weight Since timber has a high strength over weight ratio compared to steel, a monolithic timber connection is favourable for the weight of the connections and with that the weight of the whole structure.
- Sustainability Apart from fasteners for reinforcement, the interlocking joint enables the construction of a monolithic timber structure. Since timber is a renewable material this is beneficial for the sustainability of the structure.
- Integrated building process Since the digital fabrication of the node can be done on site, the process can be integrated into the robotic fabrication and assembly work flow. Since the structure is monolithic, the building process can be executed by one fabricator. This has multiple advantages, among which are reduced production time, less dependence on other parties and a more clear distribution of responsibility.
- Costs

Disadvantages of interlocking joints are:

- Design freedom Like bolted connections, the number of bars connecting in one point is limited for geometric reasons.
- Strength and stiffness Although the strength and stiffness of an interlocking are higher compared to a bolted connection, they are considerably lower than for a welded or 3D printed steel node.

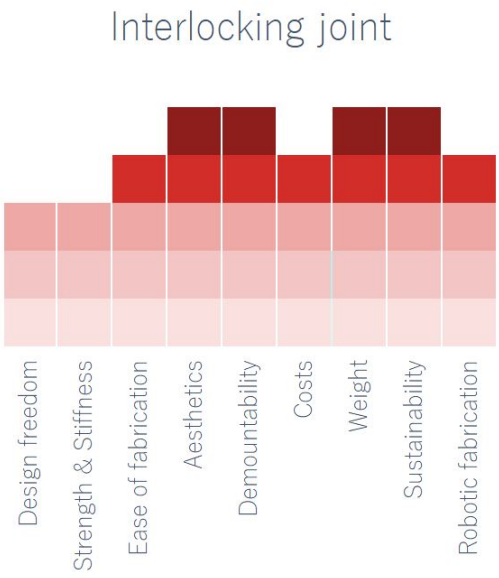

Figure 4.11: Score of the interlocking joint on several criteria

4.6 Conclusion

An overview of the scores of the four different connection types on the designated criteria is shown in Figures 4.12.

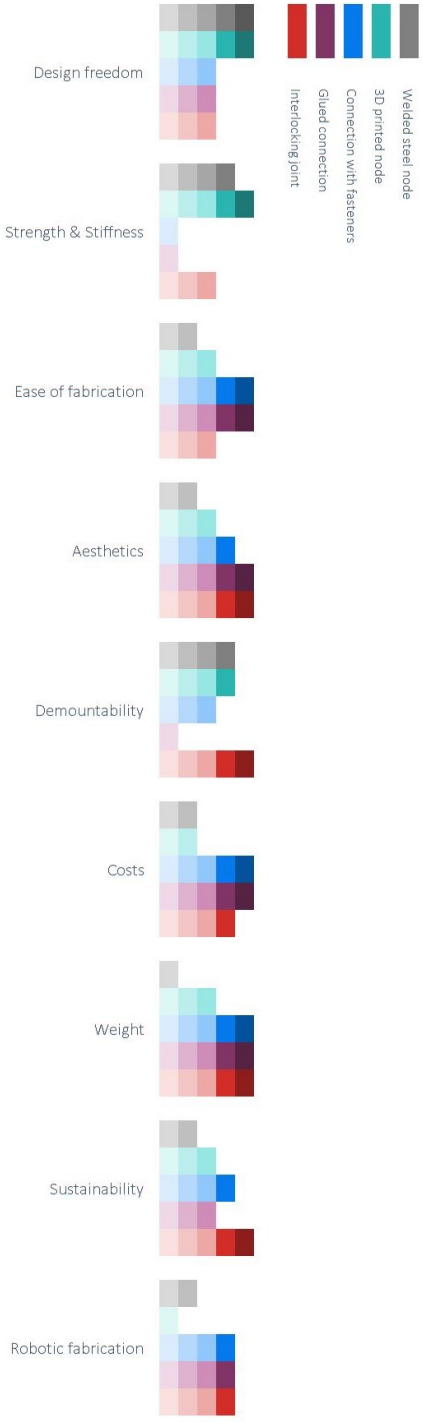

Figure 4.12: Overview of the scores of the five different connection types

It can be concluded that when a connection with a high strength and stiffness is required or a connection that connects a large number of bars at one location, either a welded steel node or 3D printed node is the best option. The application of 3D printed nodes has great potential due to the possibility to optimise the material usage of the node, leading to a decrease in weight and increase of sustainability of the structure. Nevertheless, at the moment the application is still limited due to high costs and lack of regulations regarding the application of additive manufacturing techniques in structures. Furthermore, a complete robotic workflow

including processing of the structural elements and assembly will be excluded when 3D printed nodes are applied.

For structures with a limited amount of bars connecting in one point and a limited stiffness and strength requirement, the application of either a bolted, glued or interlocking joint is favourable due to low costs, low weight and high sustainability. Nowadays, interlocking joints are not commonly applied anymore due labour intensity and high skill requirement of the woodworker. This way of connecting timber beams could make a resurgence, with the availability of new digital manufacturing techniques like wood processing with CNC-milling robots. The interlocking joint holds all advantages of the bolted and glued connection but has a higher strength and stiffness. Furthermore, due to the monolithic character of the joint, the node fabrication can be incorporated into the digital fabrication workflow, which is an important advantage compared to a welded or 3D printed node.

Since this research project focuses on the robotic timber fabrication of a bridge, it has been decided to investigate the application of interlocking joints in the robotic fabrication process.

III

Global Design

5

Starting Points for the Design

After the study phase it was concluded that a grid shell structure will be applied with interlocking joints. This type of structure and connection are suitable to be integrated into a complete digital fabrication workflow. In order to limit the complexity of the connections, it is decided to apply a reciprocal grid. With this type of grid only two connections meet at the same spot. Furthermore, for this type of structure no fasteners are required which makes it very suitable for the application of interlocking joints.

5.1 Grid

A reciprocal structure is a three-dimensional self-supporting structure, see Section 3.2.2. Figure B.1 and 3.16 show a number of examples of reciprocal grid patterns. Since it is out of scope of the project to assess all different types of grids, just one type of grid is picked. For aesthetic reasons it is decided to apply the following grid pattern:

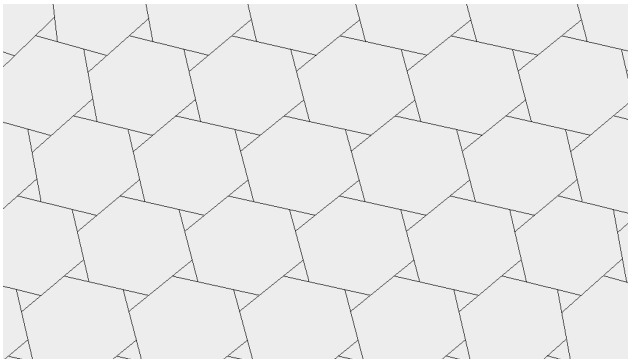

Figure 5.1: The applied reciprocal grid

5.2 Bridge shape

A shell structure is a three-dimensional structure for which the thickness is a lot smaller than its other dimensions. This results in a much larger extensional rigidity than flexural rigidity. Therefore the structure transfers loads mainly by membrane forces (resultants of in-plane normal and shear stresses), rather than bending moments [17]. To enable this, a suitable bridge shape should be chosen. Shell structures are most commonly applied for buildings, but less regularly for bridge structures. The main difference between the function of these type of structures is that the load transfer of roof structures is usually two-directional, while for bridge structures one-directional. An additional requirement for the bridge structure is therefore that the structure must only be supported on two sides. The most straightforward shape that fulfils the requirements (load transfer through membrane forces, only supports on two sides) is an arch structure.

In order to increase the global buckling resistance of the structure and to allow for some bending moments, it is favourable to apply a double curved surface. A double curved surface can either be synclastic (dome shaped) or anticlastic (saddle shaped). Both types are taken into consideration.

Due to time constraints it is not possible to do extensive form study. It is decided to apply the following (parametric) bridge shape:

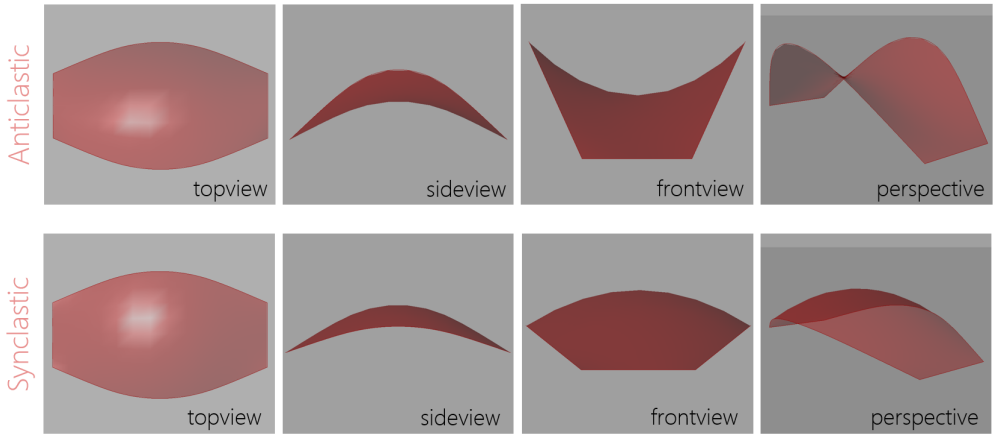

Figure 5.2: Shape of the bridge

To be able to create a curved reciprocal grid shell with straight beam elements, eccentricities at the connections are required. In case of a synclastic shape, the center line of the end of the beams should always be above the center line of the beam it connects to (positive eccentricity), see Figure 5.3 (left). When an anticlastic shape is applied, some of the connections will need to accommodate a positive eccentricity and others a negative eccentricity. This must be taken into account when designing the connection.

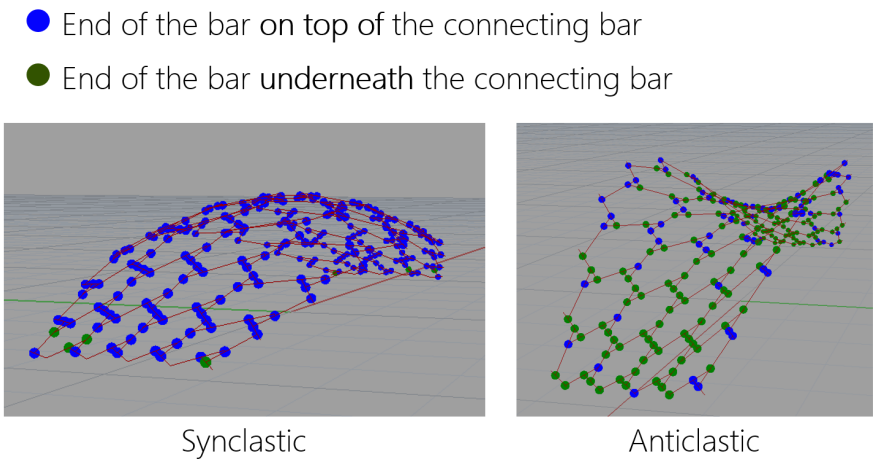

Figure 5.3: Required eccentricities at the connection of beams for a synclastic and an anticlastic bridge shape

5.3 Structural System

The structural system can be modelled as a simply supported beam with two downward point loads, see Figure 5.4. The supports only take a downward load. In all cases, the end of the beams are positioned on top of neighbouring beams. In-between the ends of the beam, the ends of two other beams are on top.

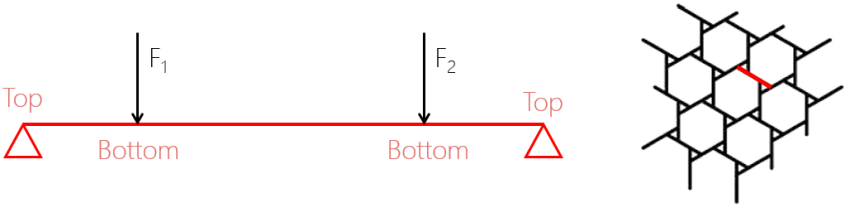

Figure 5.4: Structural System: Model of one single beam

Figure 5.5 shows a physical model of the structural system made of wooden sticks and pins. The beams are not connected by any fasteners. The pinheads enable the transfer of small tension forces in beams. This physical model proved that this reciprocal grid shell system is indeed stable without the use of fasteners.

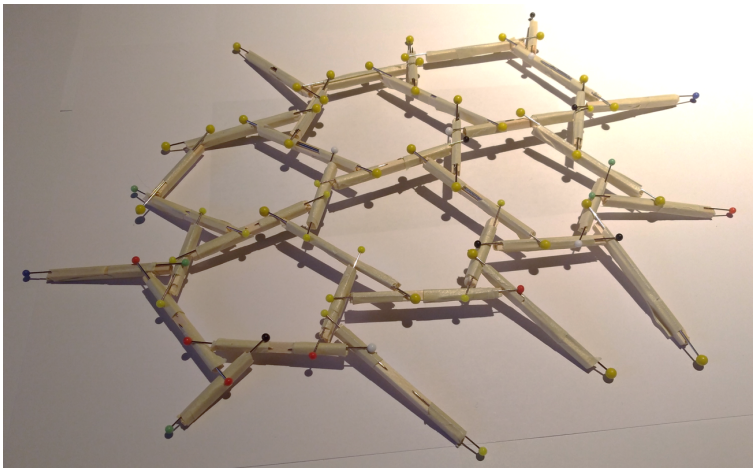

Figure 5.5: Physical model of the structure

To get an idea of the force-flow through this type of structure, a simple model was made, see Figure 5.6. The red arrow shows the applied normal force, *F*.

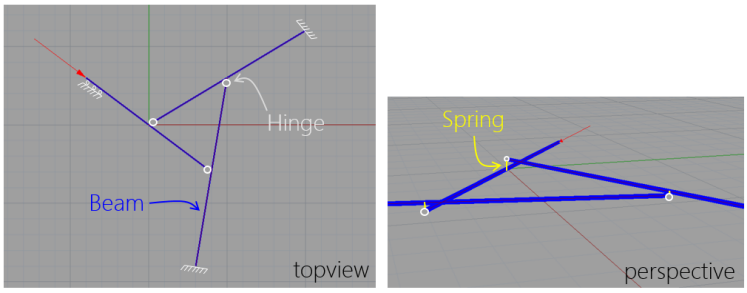

Figure 5.6: Simple model to study the force-flow

The beams are connected by hinges at the end of spring elements. The spring elements are added for two reasons:

- To model the eccentricity at the connections which is necessary to be able to create a curved surface
- To be able to model a non-linear connection: one that can transfer downward but no upward loads

Figure 5.7 shows the internal forces resulting from the external load *F*.

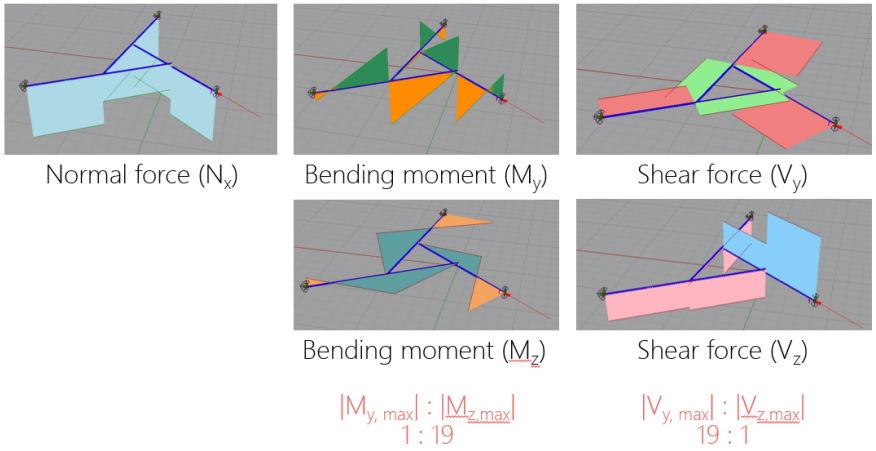

Figure 5.7: Internal forces (normal, shear and bending moments) as result of force *F*

It can be seen that loads are mainly transferred by normal forces. Additionally a considerable bending moment around the z-axis (M_z) and a shear force in y-direction (V_y) is induced. The bending moment around the y-axis (M_y) and a shear force in z-direction (V_z) are less relevant.

6

Loads and Boundary Conditions

This chapter gives an overview of all loads that should be taken into account according to the Eurocode and National Annex. First, an overview is made of all relevant Eurocode chapters (6.1). From this, all loads and load combinations that should be taken into account are defined (6.2). Section 6.4 describes how these loads are applied in the Grasshopper model. Finally, a sensitivity study on support displacements is carried out (6.5).

6.1 Relevant Eurocode chapters

In order to obtain a bridge design that can be considered reliable, the design should fulfil the Eurocodes. Figure 6.1 gives an overview of all existing Eurocodes. The parts that are relevant for the design of a timber bridge are marked pink.

Furthermore, every country has its own national annex with additional rules and guidelines. Below a resume is given of all parts of the Eurocode and National Annex that are consulted:

- **EN 1990: Basis of structural design**
  - *Annex A2: Application on bridges* for additional combinations rules for pedestrian bridges
  - *National Annex to NEN-EN 1990+A1+A1/C2* for load- and combination factors ($\gamma-$ and $\psi-$values)
    - NEN-EN 1990 NB.13 âĂŞ A2.4(B): Partiele factoren
    - (NEN-EN 1990/Tabel NB.17 âĂŞ A2.2: Combinatie factoren
- **EN 1991: Actions on structures**
  - NEN-EN 1991-2+C1:2015: Eurocode 1: Actions on structures - Part 2: Traffic loads on bridges
    - Section 5: Actions on footways, cycle tracks and footbridges
  - NEN EN-1991-1-4: Wind load
    - Section 8: Wind actions on bridges
    - NEN-EN 1991-1-4+A1+C2:2011/NB:2011 (National Annex)
- **EN 1995: Design of timber structures**
  - Table 7.1: Limiting values for deflections for beams, plates and trusses
    - Action: Characteristic traffic load - limiting values: $l/400$
    - Action: Pedestrian load and low traffic load - limiting values: $l/200$
  - NEN-EN 1995-2: Eurocode 5: Design of timer structures - Part 2: Bridges

The relevant rules given in EN 1995-1-1 Section 10 also apply to the structural parts of bridges, with the exception of clauses 10.8 and 10.9.

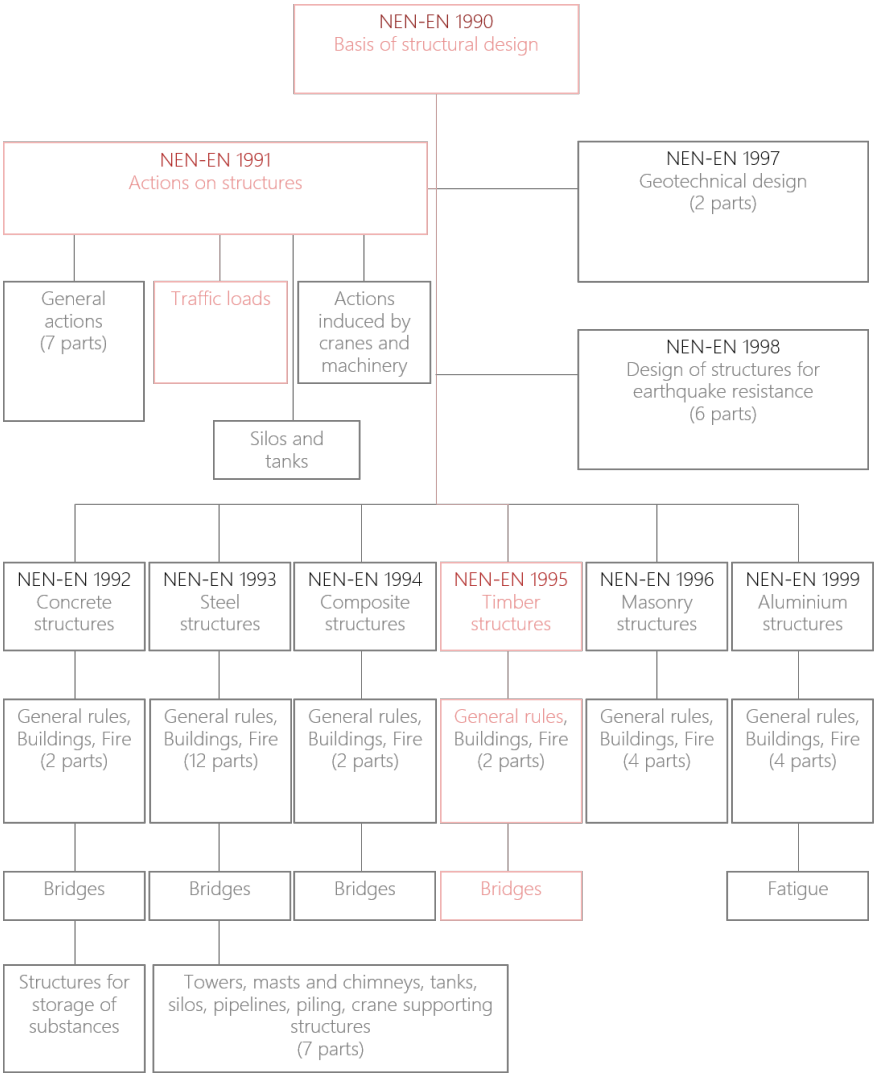

Figure 6.1: Overview Eurocodes

6.2 Loads

The loads can be divided into four groups:

- Permanent actions
  - Dead load
  - Unequal settlements of supports
- Variable actions
  - Traffic loads on bridges
    - Crowd load - uniformly distributed load
    - Crowd load - concentrated load
    - Vehicle loading
  - Wind loading
- Accidental design situations
- Dynamic loading

6.2.1. Permanent actions

Permanent loads that have to be considered are dead load and unequal settlements of supports.

Dead load
The permanent action that has to be taken into account is the self weight of the structure. The self weight of the structure is modelled by a gravitational force with a downward acceleration of 1g, assuming $g = 9.81 m/s^2$.

Settlements of supports
The influence of unequal settlements of the supports can be estimated by imposing a displacement of 10mm per support, acting independently.

6.2.2. Variable actions
The following variable actions

Traffic loads on bridges
Section 5 of Eurocode *NEN-EN 1991-2* is devoted to actions on footways, cycle tracks and footbridges. In this section it is stated that three different load models should be considered:

- A uniformly distributed load, q_{fk}
- A concentrated load, Q_{fvd}
- Loads induced by a service vehicle, Q_{serv}

Crowd load - Uniformly distributed load
A uniformly distributed load of $q_{fk} = 5 kN/m^2$ should be considered for crowd loading. The load should only be applied at unfavourable locations of the influence plane.

Crowd load - Concentrated load
The characteristic value of the concentrated load Q_{fvd} that should be considered amounts 10kN, acting on a square surface of 0.1m x 0.1m.

Additionally, a horizontal load, Q_{flk}, should be considered along the axis of the bridge deck at the height of the wear layer. The characteristic value of this load amounts 10% of the total uniformly distributed load. This horizontal load applies simultaneously with the corresponding vertical load (q_{fk}) and by no means with the concentrated load (Q_{fvk}).

Vehicle loading
It is assumed that no vehicles are allowed to pass the bridge (e.g. ambulances, firetrucks or service vehicles) so therefore Q_{serv} is 0kN.

Wind loading
Wind actions on bridges produce forces on the bridge in the x-, y- and z-direction, see Figure 6.2, where:

x-direction: The direction parallel to the deck width, perpendicular to the span
y-direction: The direction along the span
z-direction: The direction perpendicular to the deck

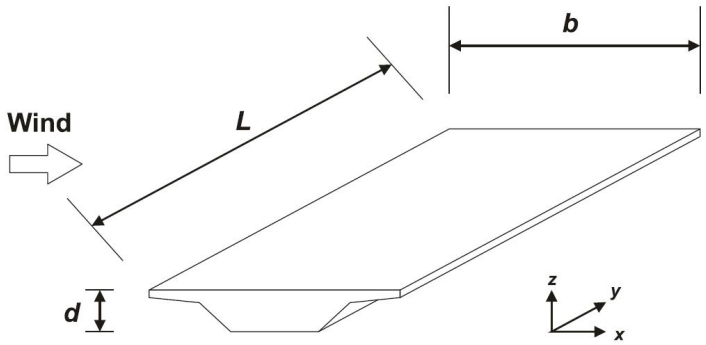

Figure 6.2: Directions of wind actions on bridges (Figure 8.2 of NEN-EN 1991-1-4)

Wind forces on the bridge in x-direction

The wind force, F_w, acting on a bridge structure can be calculated according to a simplified method using Equation 6.1 (NEN-EN 1991-1-4, Section 8.3.2):

$$F_w = \frac{1}{2} \cdot \rho \cdot v_b^2 \cdot C \cdot A_{ref,x} \tag{6.1}$$

Where:

- ρ is the air density, depending on altitude, temperature and barometric pressure to be expected in the region during wind storms. According to the Dutch Annex $\rho = 1.25 kg/m^3$ in the Netherlands
- v_b is the basic wind velocity and can be calculated using Equation 6.2
- C is the wind load factor. $C = c_e \cdot c_{f,x}$, where c_e is the exposure factor, see Equation 6.3
- A_{ref} is the reference area of the structure or structural element (Section 7 or 8 of NEN-EN 1991-1-4)

$$v_b = c_{dir} \cdot c_{season} \cdot v_{b,0} \tag{6.2}$$

Where:

- $v_{b,0}$ is the fundamental value for the basic wind velocity, see Table 6.1. The value depends on the wind area, which can be found in Figure 6.3 for the Netherlands
- c_{dir} is the directional factor and should be taken 1.0 according to the Dutch Annex (NEN-EN 1991-1-4 nb)
- c_{season} is the season factor and should also be taken 1.0 according to the Dutch Annex (NEN-EN 1991-1-4 nb)

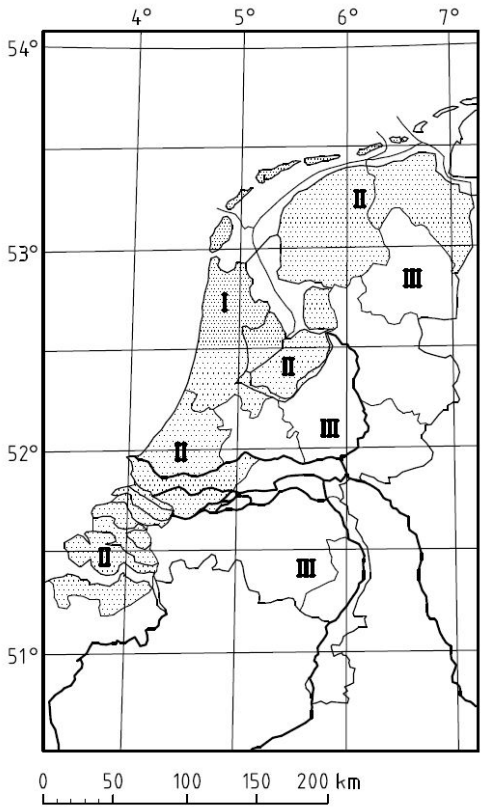

Figure 6.3: Classification of wind areas in the Netherlands according to NEN-EN 1991-1-4

Table 6.1: $v_{b,0}$ in the Netherlands (Table NB.1 from NEN-EN 1991-1-4 nb (Dutch Annex))

Wind area	$v_{b,0}$ $[m/s]$
I	29.5
II	27.0
III	24.5

The exposure factor, $c_e(z)$ can be calculated using the following expression:

$$c_e(z) = \frac{q_p(z)}{q_b} \tag{6.3}$$

Where:

q_b is the peak velocity pressure which can be calculated using Equation 6.5
$q_p(z)$ is the basic velocity pressure given in Equation 6.4 according to Section 4.5 from NEN-EN 1991-1-4. A description of the calculation of the peak velocity value can be found in Appendix F. The peak velocity pressure values for the case that c_o = 1 are given in table 6.2.

$$q_b = \frac{1}{2} \cdot \rho \cdot v_b^2 \tag{6.4}$$

$$q_p(z) = [1 + 7 \cdot I_v(z)] \cdot \frac{1}{2} \cdot \rho \cdot v_m^2(z) \tag{6.5}$$

Where:

ρ is the air density, depending on altitude, temperature and barometric pressure to be expected in the region during wind storms. According to the Dutch Annex $\rho = 1.25 kg/m^3$ in the Netherlands
$I_v(z)$ is the turbulence intensity which can be determined using Equation F.2 in Appendix F
$v_m(z)$ is the mean wind velocity at a height z above the terrain, see Equation F.3

Table 6.2: Peak velocity pressures in case c_o = 1.0 in KN/m^2 according to Table NB.5 of NEN-EN 1991-1-4 nb (Dutch Annex)

Height	**Wind area I**			**Wind area II**			**Wind area III**	
$[m]$	Coastal	Uncultivated	Cultivated	Coastal	Uncultivated	Cultivated	Uncultivated	Cultivated
1	0.93	0.71	0.69	0.78	0.60	0.58	0.49	0.48
2	1.11	0.71	0.69	0.93	0.60	0.58	0.49	0.48
3	1.22	0.71	0.69	1.02	0.60	0.58	0.49	0.48
4	1.30	0.71	0.69	1.09	0.60	0.58	0.49	0.48
5	1.37	0.78	0.69	1.14	0.66	0.58	0.54	0.48
6	1.42	0.84	0.69	1.19	0.71	0.58	0.58	0.48
7	1.47	0.89	0.69	1.23	0.75	0.58	0.62	0.48
8	1.51	0.94	0.73	1.26	0.79	0.62	0.65	0.51
9	1.55	0.98	0.77	1.29	0.82	0.65	0.68	0.53
10	1.58	1.02	0.81	1.32	0.85	0.68	0.70	0.56
15	1.71	1.16	0.96	1.43	0.98	0.80	0.80	0.66
20	1.80	1.27	1.07	1.51	1.07	0.90	0.88	0.74
25	1.88	1.36	1.16	1.57	1.14	0.97	0.94	0.80
30	1.94	1.43	1.23	1.63	1.20	1.03	0.99	0.85
35	2.00	1.50	1.30	1.67	1.25	1.09	1.03	0.89
40	2.04	1.55	1.35	1.71	1.30	1.13	1.07	0.93
45	2.09	1.60	1.40	1.75	1.34	1.17	1.11	0.97
50	2.12	1.65	1.45	1.78	1.38	1.21	1.14	1.00
55	2.16	1.69	1.49	1.81	1.42	1.25	1.17	1.03
60	2.19	1.73	1.53	1.83	1.45	1.28	1.19	1.05
65	2.22	1.76	1.57	1.86	1.48	1.31	1.22	1.08
70	2.25	1.80	1.60	1.88	1.50	1.34	1.24	1.10
75	2.27	1.83	1.63	1.90	1.53	1.37	1.26	1.13
80	2.30	1.86	1.66	1.92	1.55	1.39	1.28	1.15
85	2.32	1.88	1.69	1.94	1.58	1.42	1.30	1.17
90	2.34	1.91	1.72	1.96	1.60	1.44	1.32	1.18
95	2.36	1.93	1.74	1.98	1.62	1.46	1.33	1.20
100	2.38	1.96	1.77	1.99	1.64	1.48	1.35	1.22
110	2.42	2.00	1.81	2.03	1.68	1.52	1.38	1.25
120	2.45	2.04	1.85	2.05	1.71	1.55	1.41	1.28
130	2.48	2.08	1.89	2.08	1.74	1.59	1.44	1.31
140	2.51	2.12	1.93	2.10	1.77	1.62	1.46	1.33
150	2.54	2.15	1.96	2.13	1.80	1.65	1.48	1.35
160	2.56	2.18	2.00	2.15	1.83	1.67	1.50	1.38
170	2.59	2.21	2.03	2.17	1.85	1.70	1.52	1.40
180	2.61	2.24	2.06	2.19	1.88	1.72	1.54	1.42
190	2.63	2.27	2.08	2.20	1.90	1.75	1.56	1.44
200	2.65	2.29	2.11	2.22	1.92	1.77	1.58	1.46

Wind forces on the bridge deck in z-direction

Force coefficients $c_{f,z}$ should be defined for wind actions on the bridge deck in z-direction, both upwards and downwards. According to the Dutch Annex (NEN-EN 1991-1-4 nb), it can be assumed that $c_{f,z} = \pm 0.9$. In the case that the wind action in the z-direction is unfavourable, the load should be combined with wind action in the x-direction.

6.2.3. Accidental design situations

Both bridge deck collision and extraordinary presence of vehicles are not taken into consideration.

6.2.4. Dynamic loading

The relevant eigen-frequencies (for vertical, horizontal and torsional vibrations) of the main supporting structure should be determined. Forces induced by pedestrians with a frequency similar to the eigen-frequency of the bridge can result in resonance and should be taken into consideration during the verification of the limit states concerning vibrations. The effects of pedestrian traffic on the bridge are depending on several factors, for example the number and position of people that are with some probability located at the bridge at the same time, and external factors that are associated with the location of the bridge. In the absence of

significant response of the bridge, a normally walking pedestrian induces simultaneous periodic forces with the following frequencies:

- Vertical direction: 1 to 3Hz
- Horizontal direction: 0.5 to 1.5Hz

Groups of runners can induce a frequency of 3Hz when passing the bridge.

6.3 Load combinations

6.3.1. Load and combination factors

It is assumed that the bridge can be categorised into *Consequence Class (CC) 2*: A structure with medium consequence for loss of human life. Economic, social or environmental consequences are considerable.

Load factors

The following load factors should be applied for a CC2 bridge:

Table 6.3: Table NB.13 - A2.4(B) from NEN-EN 1990 nb: Load factors for road bridges, pedestrian- and cycle bridges STR/GEO (group B)

Name	Equation	Permanent action		Traffic	Wind
		Unfavourable	Favourable		
LC1	6.10a	1.30	0.90	1.35	1.50
LC2	6.10b Traffic leading	1.20	0.90	1.35	1.50
LC3	6.10b Wind leading	1.20	0.90	1.35	1.50

Combination factors

The combination factors (ψ-values) for pedestrian and cycle bridges can be found in Table NB.17 - A2.2 in the dutch annex of *NEN-EN 1990*:

Table 6.4: NEN-EN 1990 Table NB.17-A2.2 - ψ-values for pedestrian and cycle bridges

Name	Equation	Traffic	Wind
C1	6.10a	0.40	0.30
C2	6.10b Traffic leading	1.00	0.30
C3	6.10b Wind leading	0.40	1.00

6.3.2. Ultimate Limit State (ULS)

The following two fundamental load combinations should be taken into account for the Ultimate Limit State (ULS) according to *NEN-EN 1990+A1+A1/C2:2011*, section 6.4.3:

- Equation 6.10a (NEN-EN 1990):

$$\sum_{j\geq 1} \gamma_{G,j} G_{k,j}" + "\gamma_P P" + "\gamma_{Q,1}\psi_{0,1} Q_{k,1}" + "\sum_{i>1} \gamma_{Q,i}\psi_{0,i} Q_{k,i} \tag{6.6}$$

- Equation 6.10b (NEN-EN 1990):

$$\sum_{j\geq 1} \xi_j \gamma_{G,j} G_{k,j}" + "\gamma_P P" + "\gamma_{Q,1} Q_{k,1}" + "\sum_{i>1} \gamma_{Q,i}\psi_{0,i} Q_{k,i} \tag{6.7}$$

6.3.3. Serviceability Limit State (SLS)

Combination of actions for the Serviceability Limit State (SLS) are formulated as follows in *NEN-EN 1990+A1+A1/C2:2011*, section 6.5.3:

- The characteristic combination (eq. 6.14b):

$$\sum_{j\geq 1} G_{k,j}" + "P" + "Q_{k,1}" + "\sum_{i>1} \psi_{0,i} Q_{k,i} \tag{6.8}$$

- The frequent combination (eq. 6.15b):

$$\sum_{j\geq 1} G_{k,j}" + "P" + "\psi_{1,1} Q_{k,1}" + "\sum_{i>1} \psi_{2,i} Q_{k,i} \tag{6.9}$$

6.3.4. Additional combination rules for pedestrian bridges

NEN-EN 1990 Annex A2 comprises additional combination rules for pedestrian bridges. The following paragraphs in Annex A2 are of importance for the design of a footbridge:

Table 6.5: Clauses specific for footbridges in NEN-EN 1990 Annex A2

Clause	**Item**
A.2.2.3(2)	Combination rules for wind and thermal actions
A2.2.3(3)	Combination rules for snow loads and traffic loads
A2.2.3(4)	Combination rules for footbridges protected from bad weather
A2.4.3.2(1)	Comfort criteria for footbridges

In paragraph *A.2.2.3 Combination rules for footbridges* of *NEN-EN 1990 Annex A2* the following is stated:

- The concentrated load Q_{fwk} need not be combined with any other variable actions that are not due to traffic.
- Wind actions and thermal actions need not be taken into account simultaneously unless otherwise specified for local climatic conditions. *(NOTE Depending upon the local climatic conditions a different simultaneity rule for wind and thermal actions may be defined either in the National Annex or for the individual project.)*
- Snow loads need not be combined with groups of loads gr1 and gr2 for footbridges unless otherwise specified for particular geographical areas and certain types of footbridges. *(NOTE Geographical areas, and certain types of footbridges, where snow loads may have to be combined with groups of loads gr1 and gr2 in combinations of actions may be specified in the National Annex.)*
- For footbridges on which pedestrian and cycle traffic is fully protected from all types of bad weather, specific combinations of actions should be defined. *(NOTE Such combinations of actions may be given as appropriate in the National Annex or agreed for the individual project. Combinations of actions similar to those for buildings (see Annex A1), the imposed loads being replaced by the relevant group of loads and the ÏĹ factors for traffic actions being in accordance with Table A2.2, are recommended.)*

Clause *A2.4.3.2 Comfort criteria for footbridges* states comfort criteria should defined in terms of a maximum acceptable acceleration of any part of the bridge deck. The criteria may be defined as appropriate in the National Annex or for the individual project. The following accelerations are recommended maximum values for any part of the deck:

- $0.7 m/s^2$ for vertical vibrations
- $0.2 m/s^2$ for horizontal vibrations during normal use
- $0.4 m/s^2$ for exceptional crowd conditions

A verification of the comfort criteria should be performed in case the fundamental frequency of the deck is less than:

- 5Hz for vertical vibrations
- 2.5Hz for horizontal (lateral) and torsional vibrations

6.4 Application of loads in Grasshopper

6.4.1. Dead load

The *Karamba* plugin for *Grasshopper* has the option to apply a gravity load. This tool applies automatically the dead load in the global z-direction to all structural elements based on the cross-sectional area of the applied cross-sections and the density of the applied material.

6.4.2. Crowd loading

First of all, the relevant load plane should be determined. One way to do this is by using the *Construct Domain* tool in *Grasshopper*. This tool allows you to select a part of a surface. In Figure 6.4 for example only the middle half of the bridge surface is selected.

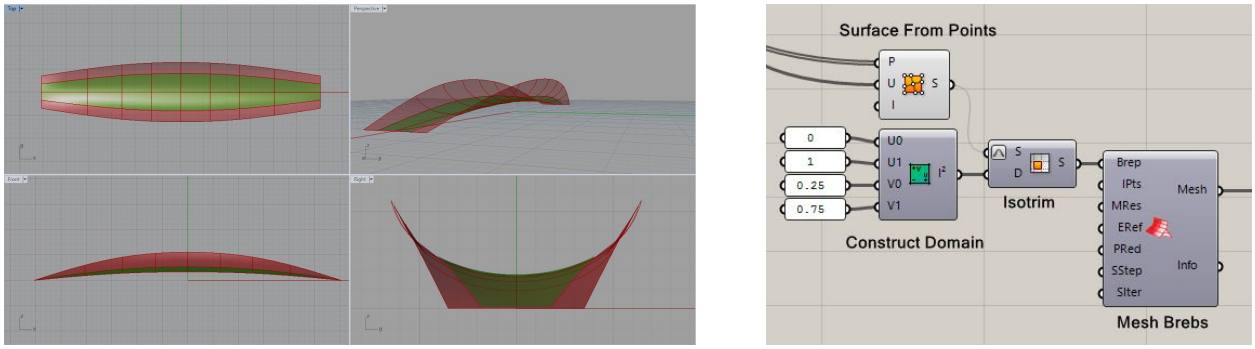

(a) (b)

Figure 6.4: Load plane modelling in Grasshopper

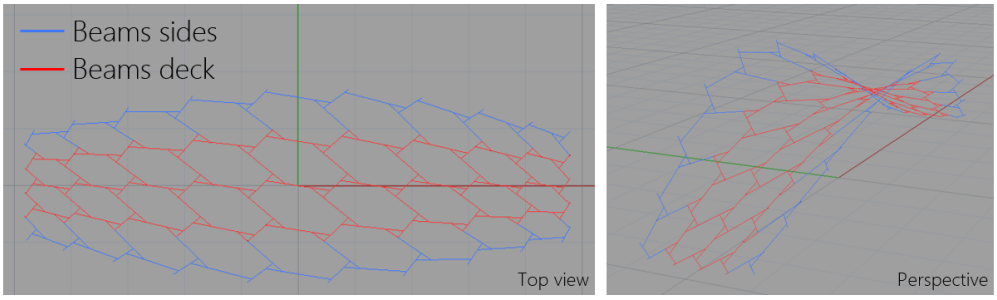

Figure 6.5: Distinction between *Deck beams* and *Side beams*

The area load on the green marked area in Figure 6.4 is converted to point loads at the connections. First, the hexagonal grid is converted to a triangular grid (connecting the centre-points of the hexagons). The area of the triangles in three-dimensional space can be calculated applying:

$$A_\Delta = \frac{1}{2}|\vec{AB} x \vec{AC}| \tag{6.10}$$

Where:

$\vec{AB}$ $= < (x_2 - x_1), (y_2 - y_1), (z_2 - z_1) >$
$\vec{AB}$ $= < (x_3 - x_1), (y_3 - y_1), (z_3 - z_1) >$

For crowd loading the projected area on the xy-plane should be used. Therefore, $z_1 = z_2 = z_3 = 0$ is used for the calculation of the projected area, A_Δ^{xy}. Subsequently, the characteristic crowd load (traffic load), P_T, can be calculated:

$$P_T = A_\Delta^{xy} \cdot q_{fk} \tag{6.11}$$

Where:

q_{fk} is the uniformly distributed crowd load ($q_{fk} = 5 kN/m^2$)

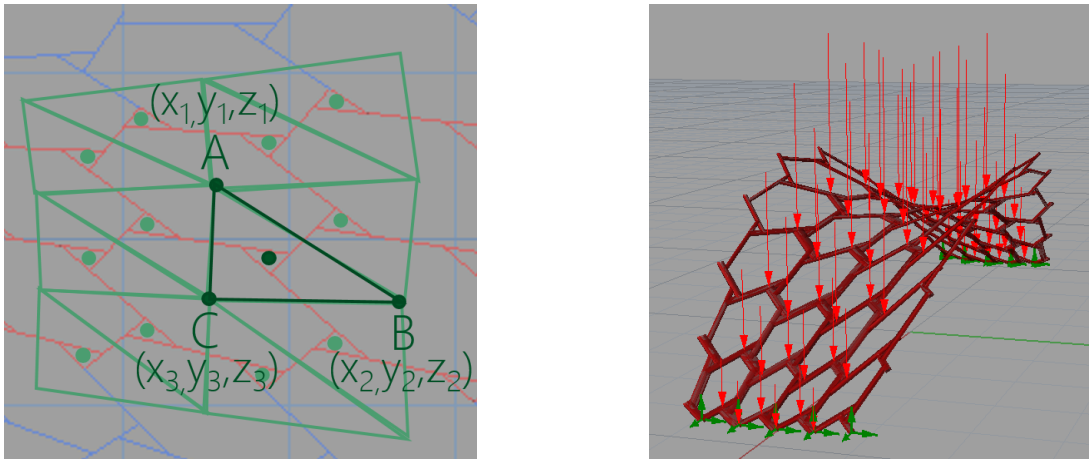

(a) (b)

Figure 6.6: Triangulation for surface load to point load conversion (6.6a) and point load result in Karamba/Grasshopper (6.6b)

6.4.3. Wind loading

The bridge can be divided into two parts: (1) the bridge deck and (2) the sides of the bridge.

Deck

The loads on the deck of the bridge are applied in the same way as the traffic load, that is by converting the surface load to point loads at the connections:

$$P_{w,y} = p_{w,x} \cdot A_{\Delta}^{xz} \tag{6.12}$$

$$P_{w,z} = p_{w,z} \cdot A_{\Delta}^{xy} \tag{6.13}$$

Where:

- A_{Δ}^{xz} is the area of the triangulated surface projected on the xz-plane, which can be calculated using Equation 6.10 using $y_1 = y_2 = y_3 = 0$
- A_{Δ}^{xy} is the area of the triangulated surface projected on the xy-plane
- $p_{w,y}$ is the wind pressure in the global y-direction in $[kN/m^2]$, see Section 6.2.2
- $p_{w,z}$ is the wind pressure in the global z-direction in $[kN/m^2]$, see Section 6.2.2

Sides

The loads at both sides of the bridge are applied as a uniform line-load which can be calculated from the wind pressure and reflected area of the beams. At the moment, the reflected area is not implemented yet, but the height of the beam is used to calculate the line load.

Visualisation of the wind-load

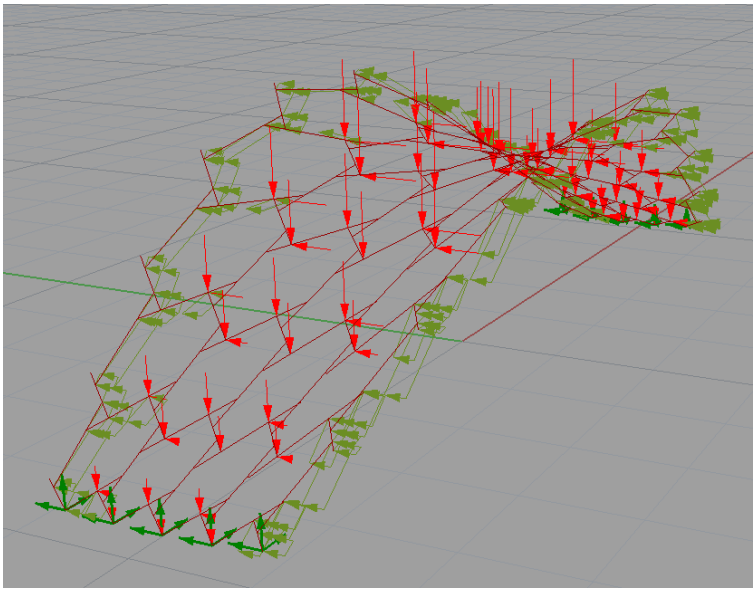

Figure 6.7: Wind-load applied in the Grasshopper/Karamba model

6.4.4. Load combinations

Table 22.1 shows all twelve applied load combinations. The names in the second and third column refer to the load case- and load combinations as described in Table 6.3 and 6.4.

Table 6.6: Applied factors for all load combinations (Combination of load- and combination factors)

Load combination			γ_g	γ_t	$\gamma_{w,v}$	$\gamma_{w,h}$
1	LC1	C1	1.3	0.54	0.45	0.45
2	LC1	C1	1.3	0.54	0.45	-0.45
3	LC1	C1	0.9	0	-0.45	0.45
4	LC1	C1	0.9	0	-0.45	-0.45
5	LC2	C2	1.2	1.35	0.45	0.45
6	LC2	C2	1.2	1.35	0.45	-0.45
7	LC3	C3	1.2	0.54	1.5	1.5
8	LC3	C3	1.2	0.54	1.5	-1.5
9	LC2	C2	0.9	0	-0.45	0.45
10	LC2	C2	0.9	0	-0.45	-0.45
11	LC3	C3	0.9	0	-1.5	1.5
12	LC3	C3	0.9	0	-1.5	-1.5

A negative load factor for the vertical wind load refers to uplift. Figure 6.8 shows load combination 5 (downward wind load) and load combination 11 (uplift).

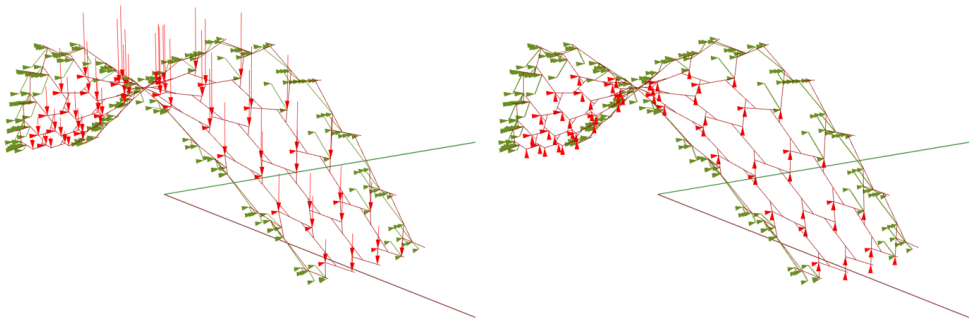

Figure 6.8: Load combination 5 and 11

6.5 Definition of boundary conditions

The boundary conditions can be divided into two groups:

- The geometric boundary conditions, imposing restrictions on the bridge shape
- Support conditions, imposing restrictions on the displacements and rotations at the the supports

6.5.1. Geometric boundary conditions (width/span)

The structure should fulfil a number of geometric boundary conditions that originate from the location of the bridge, see Figure 6.9:

- Dimensions determined by the location of the abutments:
  - Span (S)
  - Height of abutment 1 (H_1)
  - Height of abutment 2 (H_2)
  - Eccentricity of the abutments (e_w)
- Free space for passing traffic:
  - Required free height for passing vehicles (h)
  - Required free width for passing vehicles (w)

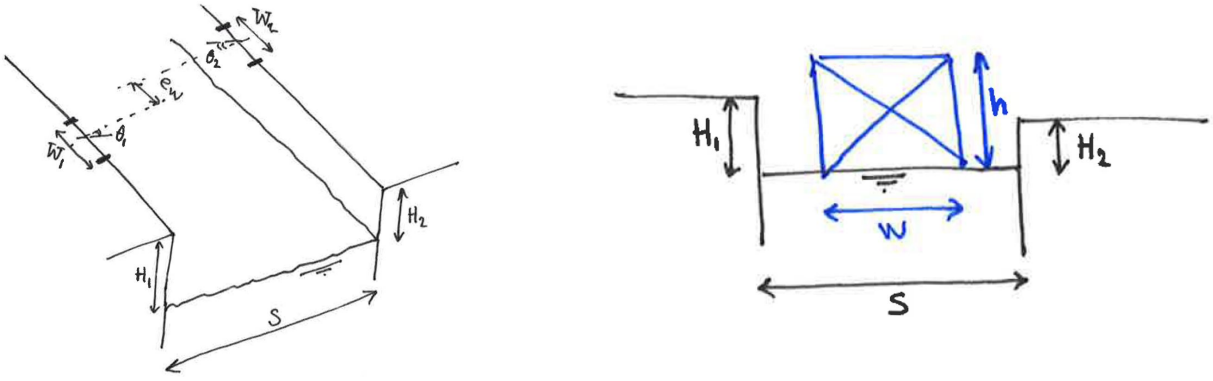

Figure 6.9: Geometric boundary conditions of the bridge

6.5.2. Deformation and rotation constraints

In order to analyse the structural behaviour of the bridge for various support conditions, the bridge is simply supported on one side (Translations constraint in all directions, rotations free) and on the other side simply supported but translations in the x-direction are restricted by means of a horizontal spring, see Figure 6.10 and 6.11.

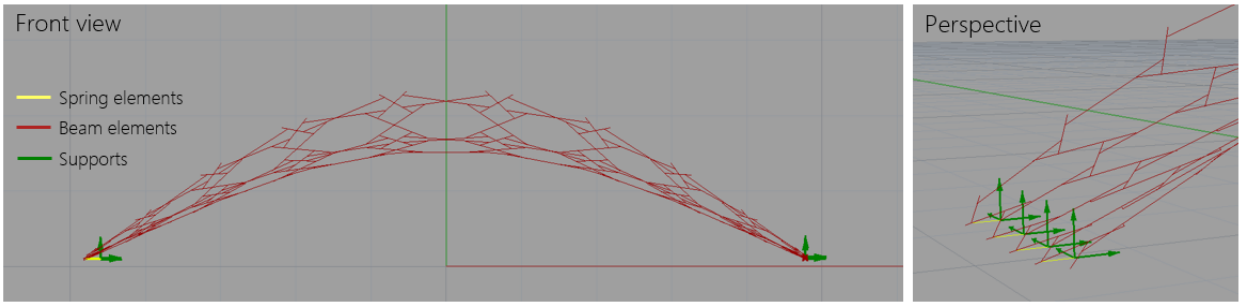

Figure 6.10: Applied constraints in the Grasshopper/Karamba model

For a really high spring stiffness ($k_x \rightarrow \infty$), the support can be considered a hinged support. When assigning a really small stiffness ($k_x \rightarrow 0$), the support approximates a roller support. Hypothetically, the bridge structure will behave like an arch in case when T_x is constraint on both sides ($k_x \rightarrow \infty$) and more like a beam when a roller support is applied ($k_x \rightarrow 0$), see Figure 6.11.

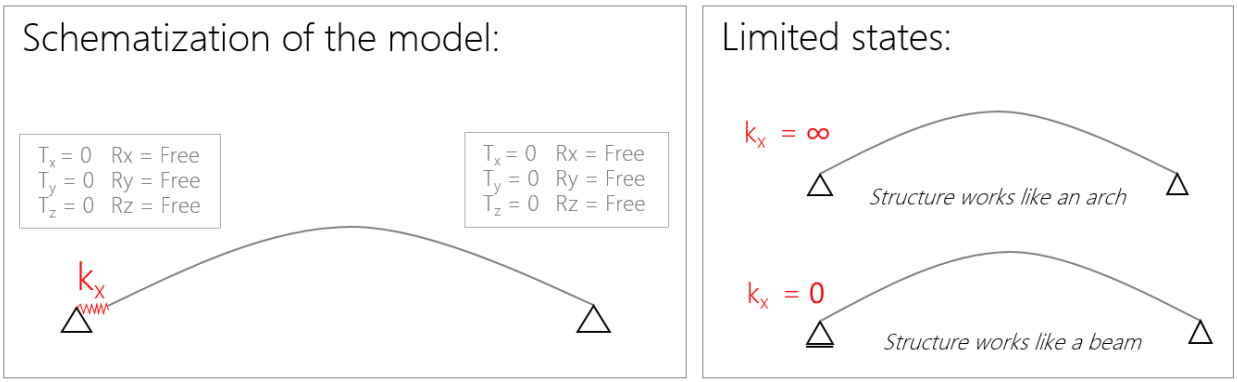

Figure 6.11: Schematization of the support conditions in the model

Figure 6.12 shows the influence of the spring stiffness, k_x, on the maximum normal force (N), shear forces (V_y & V_z) and bending moments (M_y & M_z). The results show that the peak forces and moments decrease for an increasing spring stiffness.

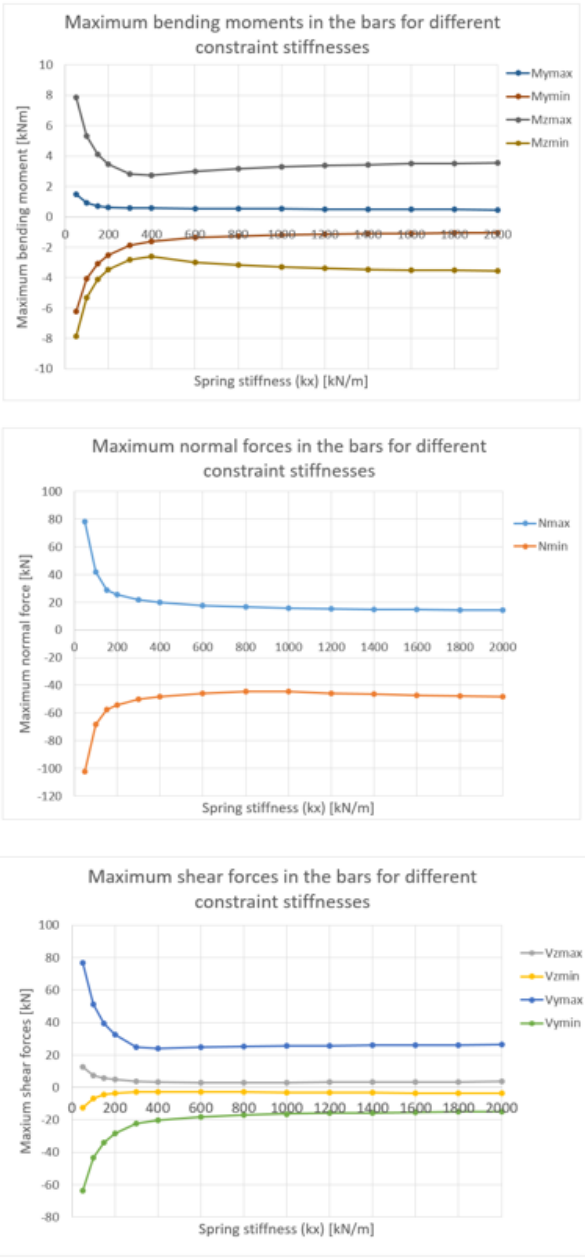

Figure 6.12: Influence of the spring stiffness on the maximum normal force, shear forces and bending moments in the structure

Figure 6.13 shows the bending moments around the local y-axis of the beams and the normal forces (blue = compression, orange = tension) in the structure (for load case 1 (6.10a, see Equation 6.6)) when a spring stiffness $k_x = 0\,kN/m$ and $k_x = 1000\,kN/m$ is applied. The same scale is used for forces/moments in both figures.

The figures show, in accordance with the hypothesis, that the structure works more like a beam when a roller support is applied ($k_x = 0$): the forces are mainly transferred by bending. When a high spring stiffness is applied the structure behaves like an arch and mainly transverses loads by normal forces. This is preferable and therefore it will give preference to apply a support with a stiffness $k_x > 600\,kN/m$ (based on Figure 6.12).

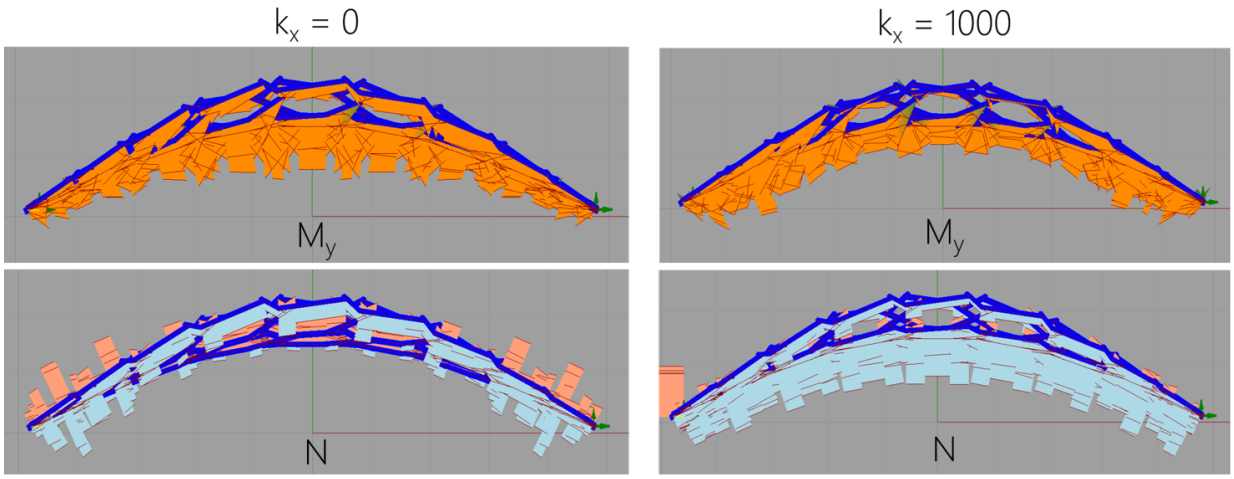

Figure 6.13: Bending moments (M_y) and normal forces (N) in the structure for $k_x = 0 kN/m$ and $k_x = 1000 kN/m$

6.6 Conclusion

The following loads have been applied:

- Dead load
- Traffic load
- Wind load

The loads are combined in twelve load combinations as described in Table 22.1, in accordance with the NEN-EN 1990. Only load cases with traffic loading on the whole deck of the bridge are considered.

A study on the sensitivity of the bridge for displacements at the supports has show that small displacements (smaller than 12 cm), don't have a large influence on the forces in the structure. Therefore, the bridge is modelled to be simply supported on both sides of the bridge ($T_x = T_y = T_z = 0$ and $R_x = R_y = R_z = free$).

7

Timber Properties

Since the bridge will be exposed to outside conditions, a wood type with a high durability class will be required (see Table 12.1). Other requirements are availability in the Netherlands and adaptability of the material by machines. A type of timber that fulfils all these requirements is Azobé, a tropical hardwood originating from West-Africa.

In the next section, the material properties of Azobé will be summarised. Section 7.3 gives an overview of all strength and stiffness requirements for timber structures according to the Eurocode and National Annex. Section 7.4 describes how the properties and requirements subsequently are implemented in the design of the bridge.

7.1 Material properties

7.1.1. Durability class

In NEN-EN 252 and NEN-EN 350-2 a the durability of wood and wood-based materials is classified to attack by decay fungi.

Table 7.1: Durability classes of wood and wood-based materials to attack by decay fungi (NEN-EN 350-1)

Class	Durability
1	Very durable
2	Durable
3	Moderately durable
4	Slightly durable
5	Not durable

Due to the outdoor conditions, a timber type with a high durability class is required. Azobé has a durability class of 1-2 and therefore fulfils this requirement.

7.1.2. Azobé

NEN-EN 1912 Structural Timber - Strength classes - Assignment of visual grades and species gives the following information on the strength class of Azobé:

Strength class:	D70
Grading rule publishing country:	The Netherlands
Grade:	C3 STH
Species commercial name:	Azobé
Source:	West Africa
Botanical identification:	100

Table 7.2: Strength, stiffness and density properties of wood species with strength class D70 according to NEN-EN 338

Strength properties $[N/mm^2]$		
Bending	$f_{m,k}$	70
Tension parallel	$f_{t,0,k}$	42
Tension perpendicular	$f_{t,90,k}$	0.6
Compression parallel	$f_{c,0,k}$	36
Compression perpendicular	$f_{c,90,k}$	12.0
Shear	$f_{v,k}$	5.0
Stiffness properties $[kN/mm^2]$		
Mean modulus of elasticity parallel bending	$E_{m,0,mean}$	20.0
5 percentile modulus of elasticity parallel bending	$E_{m,0,k}$	16.8
Mean modulus of elasticity perpendicular	$E_{m,90,mean}$	1.33
Mean shear modulus	G_{mean}	1.25
Density $[kg/m^3]$		
5 percentile density	ρ_k	1022
Mean density	ρ_{mean}	1074

In research on the mechanical properties of azobé carried out by the TU Delft and TU Munich, a characteristic value of the shear strength of $f_{v,k} = 15.7 N/mm^2$ was found [1]. This is considerably higher than the strength defined in the Eurocode of $5.0 N/mm^2$, for wood species with strength class D70. For the timber calculations carried out for this project, a shear strength of $f_{v,k} = 15.7 N/mm^2$ is assumed.

7.2 Material model

For the structural calculation of the connections, the material is assumed to behave according to linear elasticity theory. Plasticity is not taken into account.

7.3 Strength and stiffness requirements

According to NEN-EN 1995-2 the recommended partial material factor for solid timber and wood-based materials is $\gamma_M = 1.3$. Additionally, a strength modification factor k_{mod} should be applied, depending on the service class and load-duration class. For outside conditions, service class 3 should be applied. The governing load in terms of duration is the wind load, classified as *short-term load duration*. This gives a modification factor $k_{mod} = 0.70$ for solid timber, according to NEN-EN 1995-1-1 (Table 3.1).

The design value of a material property with a characteristic value X_k can be calculated as follows:

$$X_d = k_{mod} \cdot \frac{X_k}{\gamma_M} = 0.70 \cdot \frac{X_k}{1.3} \tag{7.1}$$

7.3.1. Bending

In NEN-EN 1995-1 section 6.1.6 the following two expressions are defined that should be satisfied:

$$\frac{\sigma_{m,y,d}}{f_{m,y,d}} + k_m \frac{\sigma_{m,z,d}}{f_{m,z,d}} \leq 1 \tag{7.2}$$

$$k_m \frac{\sigma_{m,y,d}}{f_{m,y,d}} + \frac{\sigma_{m,z,d}}{f_{m,z,d}} \leq 1 \tag{7.3}$$

Where:

- $\sigma_{m,y,d}$ and $\sigma_{m,z,d}$ are the design bending stresses around the principal axis as shown in Figure 7.4
- $f_{m,y,d}$ and $f_{m,z,d}$ are the corresponding design bending strengths
- k_m is a factor that allows for re-distribution of stresses and effect of inhomogeneities of the material in a cross-section. For rectangular solid timber $k_m = 0.7$

7.3.2. Shear

For shear stresses the following expression should be satisfied:

$$\tau_d \leq f_{v,d} \tag{7.4}$$

Where:

τ_d is the design shear stress

$f_{v,d}$ is the design shear strength for the actual condition

In case of rolling shear, the shear strength is approximately twice the tension strength perpendicular to the grain ($f_{t,90,d}$)

Shear of notched members

Notches and holes in beams considerably reduce the capacity of timber beams. Since the crack propagation from holes or notches is parallel to the grain, the failure is brittle, see Figure 12.8.

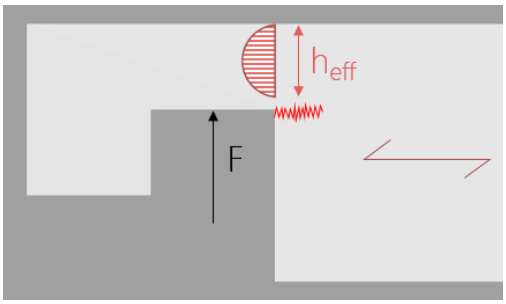

Figure 7.1: Risk for crack at the notch parallel to the grain

When a local failure takes place, the stress will re-distribute during crack propagation. EC 5 specifies rules for the calculation of beams with notches in the National Annex, based on concepts from fracture mechanics. [15]

In NEN-EN 1995-1-1, Section 6.5.2 gives information on how to calculate beams with a notch at the support, like shown in Figure 7.2.

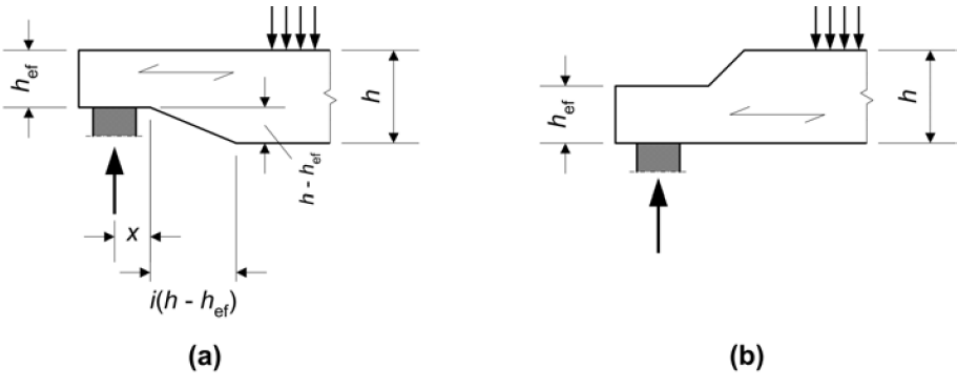

Figure 7.2: Beams with a notch at the end (NEN-EN 1995-1-1)

The following requirement should be met:

$$\tau_d = \frac{1.5V}{bh_{ef}} \leq k_v f_{v,d} \tag{7.5}$$

Where k_v is:

- For beams notched on the same side as the support (Figure 19.1 a)

$$k_v = min \begin{cases} 1 \\ \frac{k_n(1+\frac{1.1i^{1.5}}{\sqrt{h}})}{\sqrt{h}(\sqrt{\alpha(1-\alpha)}+0.8\frac{x}{h}\sqrt{(\frac{1}{\alpha}-\alpha^2)})} \end{cases} \tag{7.6}$$

- For beams notched at the opposite side of the support (Figure 19.1 b)

$$k_v = 1.0 \tag{7.7}$$

Furthermore:

i is the notch inclination (see Figure 19.1 b)
h is the depth of the beam in mm
x is the distance from line of action of the support reaction to the corner of the notch
α the ratio between the effective depth and the real depth ($\alpha = \frac{h_{ef}}{h}$)
k_n

$$= \begin{cases} 4.5, & \text{for LVL} \\ 5, & \text{for solid timber} \\ 6.5, & \text{for glued laminated timber} \end{cases} \tag{7.8}$$

7.3.3. Torsion

For torsion the following expression should be satisfied:

$$\tau_{tor,d} \leq k_{shape} f_{v,d} \tag{7.9}$$

with:

$$k_{shape} = min \begin{cases} 1 + 0.15\frac{h}{b} \\ 2.0 \end{cases} \tag{7.10}$$

Where:

$\tau_{tor,d}$ is the design torsional stress
$f_{v,d}$ is the design shear strength
k_{shape} is the factor depending on the shape of the cross-section, see Equation 7.10
h is the larger cross-sectional dimension
b is the smaller cross-sectional dimension

7.3.4. Stresses under an angle to the grain

Compressive stresses

(NEN-EN 1995-1 p 43) Compressive stresses at an angle α to the grain, see Figure 7.3, should fulfil the following requirement:

$$\sigma_{c,\alpha,d} \leq \frac{f_{c,0,d}}{\frac{f_{c,0,d}}{k_{c,90} f_{c,90,d}} sin^2(\alpha) + cos^2(\alpha)} \tag{7.11}$$

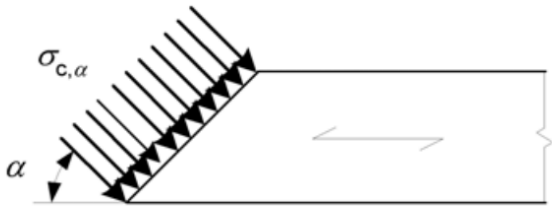

Figure 7.3: Compression stresses at an angle to the grain (NEN-EN 1995-1 Figure 6.7)

Tensile stresses

Although the EC5 does not prescribe how to calculate the capacity of tension forces at an angle to the grain, the National Annex proposes a way to verify it:[15]

$$\sigma_{t,\alpha,d} \leq k_\alpha \cdot f_{t,0,d} = \frac{1}{\frac{f_{t,0,d}}{f_{t,90,d}} \cdot sin^2(\alpha) + \frac{f_{t,0,d}}{f_{v,d}} \cdot sin(\alpha) \cdot cos(\alpha) + cos^2(\alpha)} * f_{t,0,d} \tag{7.12}$$

7.3.5. Combined stresses

Combined bending and axial tension

When combining bending and axial tension, the following two expressions should be satisfied:

$$\frac{\sigma_{t,0,d}}{f_{t,0,d}} + \frac{\sigma_{m,y,d}}{f_{m,y,d}} + k_m \frac{\sigma_{m,z,d}}{f_{m,z,d}} \leq 1 \tag{7.13}$$

$$\frac{\sigma_{t,0,d}}{f_{t,0,d}} + k_m \frac{\sigma_{m,y,d}}{f_{m,y,d}} + \frac{\sigma_{m,z,d}}{f_{m,z,d}} \leq 1 \tag{7.14}$$

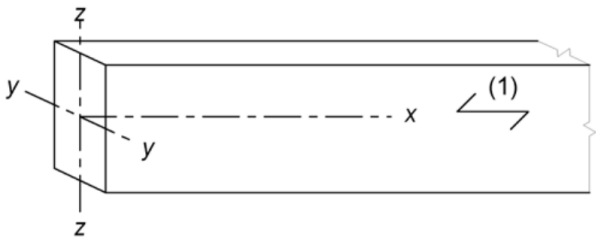

Key:
(1) direction of grain

Figure 7.4: Member axes (NEN-EN 1995-1)

Combined bending and axial compression

When combining bending and axial compression the following two equations should be satisfied:

$$\left(\frac{\sigma_{c,0,d}}{f_{t,0,d}}\right)^2 + \frac{\sigma_{m,y,d}}{f_{m,y,d}} + k_m \frac{\sigma_{m,z,d}}{f_{m,z,d}} \leq 1 \tag{7.15}$$

$$\left(\frac{\sigma_{c,0,d}}{f_{t,0,d}}\right)^2 + k_m \frac{\sigma_{m,y,d}}{f_{m,y,d}} + \frac{\sigma_{m,z,d}}{f_{m,z,d}} \leq 1 \tag{7.16}$$

7.3.6. Stability of members

Due to the really short buckling length of the members, local buckling is disregarded in this first design stage. Although global buckling might be relevant, this is outside scope of the project. It is recommended to carry out a global buckling check in a later design iteration.

7.4 Implementation into GH/Karamba

All verification's of the beams are implemented in the Grasshopper/Karamba model by means of a python script. The verification uses the following results from the Karamba analysis (first order theory for small deformations) for each beam (at the start and end-point):

- Normal force [kN]
- Shear force V_z [kN]
- Shear force V_y [kN]
- Bending moment M_y [kNm]
- Bending moment M_z [kNm]

At the moment, the dimensions of the full sections are used to calculate all stresses. This results in a large underestimation of the stresses since the highest forces are located at the location of the connection, where less material is available. It will be of great importance to integrate the calculation model of the connection, see Chapter 12, inside the verification in the next design step. To get a first impression of the required section size, an effective height of for example $h_{eff} = \frac{1}{2} h_{beam}$ can be used to calculate the stresses.

7.5 Conclusion

For the verification of the timber beams and connections, the following properties are used:

Table 7.3: Strength, stiffness and density properties used for the structural analysis and calculation of relevant Unity Checks

Strength properties $[N/mm^2]$	
$f_{m,0,k}$	70
$f_{m,90,k}$	5.8
$f_{t,0,k}$	42
$f_{t,90,k}$	2.0
$f_{c,0,k}$	36
$f_{c,90,k}$	12.0
$f_{v,k}$	13.9
Stiffness properties $[N/mm^2]$	
$E_{m,0,mean}$	20 000
$E_{m,0,k}$	16 800
$E_{m,90,mean}$	1330
G_{mean}	1250
Density $[kg/m^3]$	
ρ_{mean}	1074

When stresses are applied at an angle to the grain (σ_α), a reduced strength is calculated as described in EC 5 (Equation 7.11 and 7.12).

The following checks are performed:

- Compression stress (under an angle to the grain) (Eq. 7.11)
- Tension stress (under an angle to the grain) (Eq. 7.12)
- Shear stress (Eq. 7.4)
- Combined bending and axial tension (Eq. 7.13 & Eq. 7.14)
- Combined bending and axial compression (Eq. 7.15 & Eq. 7.16)
- Shear capacity of notched members

8

Geometry

In this chapter the procedure of transforming input design parameters to a grid shell consisting of timber beam elements will be shortly described. The process can be divided into three parts, which will be discussed in the following sections:

- Step 1: Convert input parameters to a surface (Section 8.1)
- Step 2: Convert surface to grid-lines (Section 8.2)
- Step 3: Convert grid-lines to beam elements with certain properties (Section 8.3)

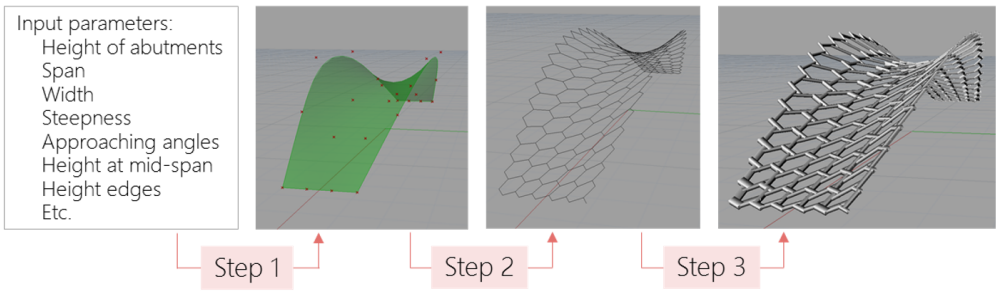

Figure 8.1: Steps in defining the geometry of the structure

8.1 Design parameters to surface

The parameters defining the shape of the bridge can be divided into the following groups:

- Dimensions determined by the location of the abutments (see Section 6.5.1, Figure 6.9)
- Free space for passing traffic (see Section 6.5.1, Figure 6.9)
- User defined parameters influencing the bridge shape, see Figure 8.2 and 8.3:
  - Width of the bridge at the start (w_{start})
  - The approximate width of the bridge at mid-span (w_{top})
  - Approaching angles (θ_1 and θ_2)
  - Minimum/maximum values for the height of the edges ($dh_{top,min}$ and $dh_{top,max}$)
  - Minimum/maximum values for the height of the bridge at mid-span ($h_{mid,min}$ and $h_{mid,max}$)

The surface is generated using the *'Surface From Points*-component in Grasshopper, which creates a NURBS surface from a 3D-grid of points. 24-points are located using the input parameters listed above, shown as yellow dots in Figure 8.2 and 8.3.

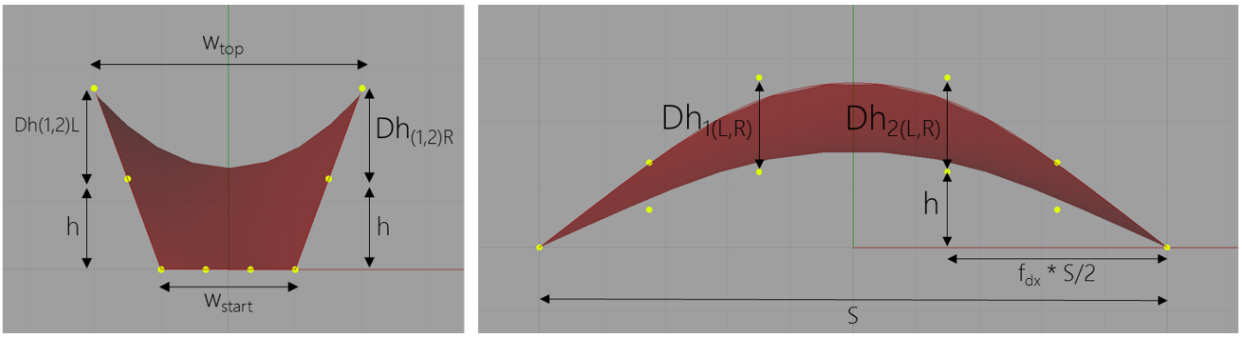

Figure 8.2: Parameters defining the shape of the bridge

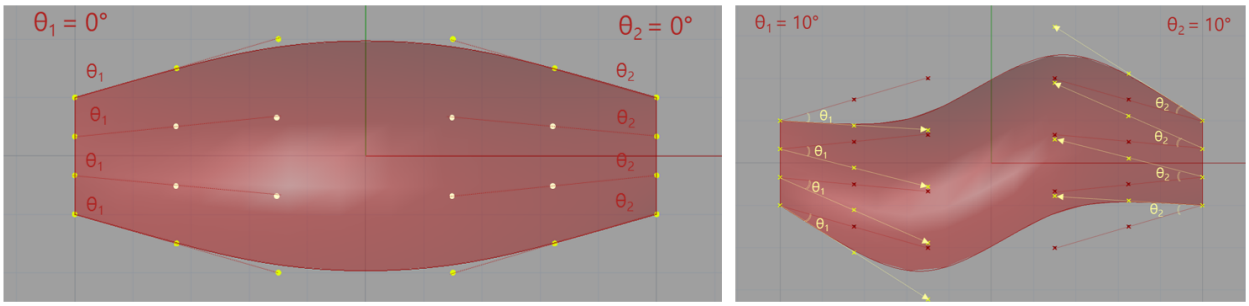

Figure 8.3: Approaching angles

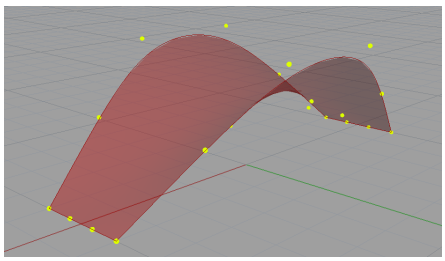

Figure 8.4: 3D view of the bridge surface

8.2 Surface to grid-lines

After the surface is created as discussed above, the surface is meshed using the *'Mesh Surface'* component in Grasshopper. The number of grid-shells in transverse direction, *m*, should be manually defined beforehand. This number could be optimised in a future design stage. The grid-points of the mesh are used to define transverse grid-lines (poly-lines) by interpolation. Next, points are created along the poly-lines, dividing the curve into *n* pieces. These points form a rectangular grid, see Figure 8.5 and 8.6.

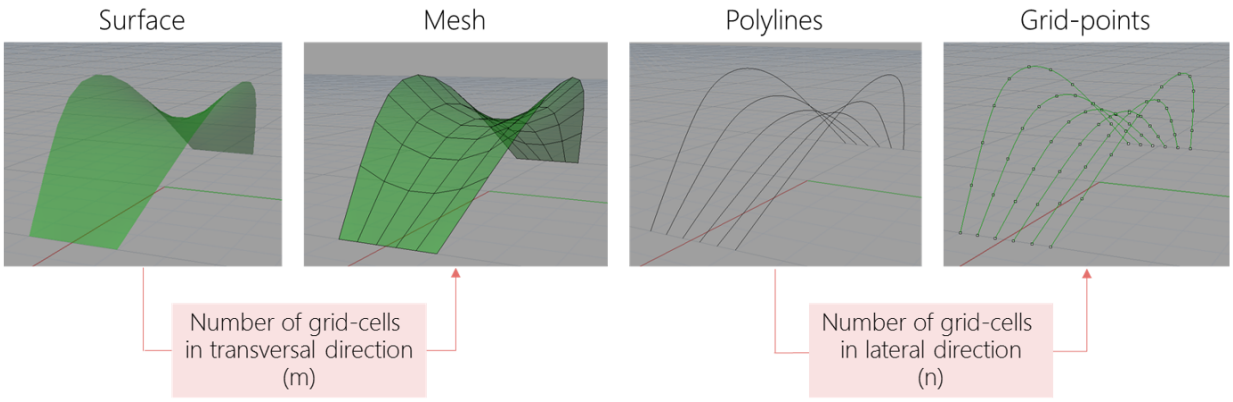

Figure 8.5: Converting a surface into rectangular grid points

Subsequently, the grid is triangulated as shown in Figure 8.6. The centre of the triangles can be calculated as follows:

$$c_1 = \left(\frac{x_1 + x_2 + x_3}{3}, \frac{y_1 + y_2 + y_3}{3}, \frac{z_1 + z_2 + z_3}{3}\right) \tag{8.1}$$

$$c_2 = \left(\frac{x_1 + x_3 + x_4}{3}, \frac{y_1 + y_3 + y_4}{3}, \frac{z_1 + z_3 + z_4}{3}\right) \tag{8.2}$$

Connecting the centre-points results in the hexagonal grid as shown in Figure 8.6. What is still missing is the eccentric connection of the lines.

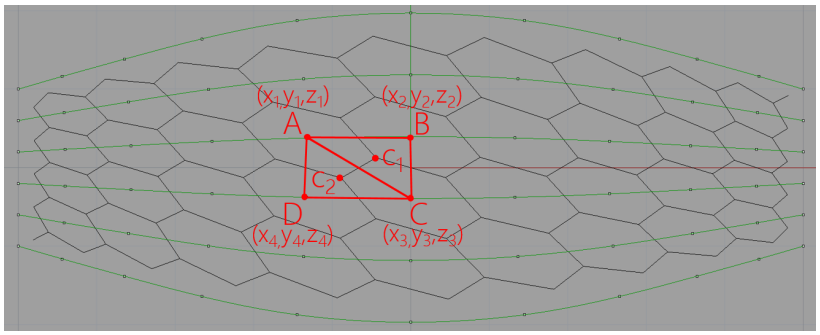

Figure 8.6: Transformation from rectangular grid into a hexagonal grid

In order to induce this eccentricity, first of all circles are defined with a normal vector, $\vec{n}$, perpendicular to the bridge surface, see Figure 8.7. Next, the hexagonal grid-lines are rotated in a way that they are tangential to the circle's perimeter. Thereafter, for each rotated grid-line a plane, $P_\perp$, is defined through the line and perpendicular to the bridge surface, see Figure 8.7 (bottom left). Furthermore, for each grid-line a vector in the direction of the line is defined, $\vec{v_r}\,\|$. Next, on each side of every vector the intersection point of the vector $\vec{v_\|}$ and the neighbouring plane $P_\perp$ is found. Finally these points are connected by lines resulting in the intended grid with eccentric connections.

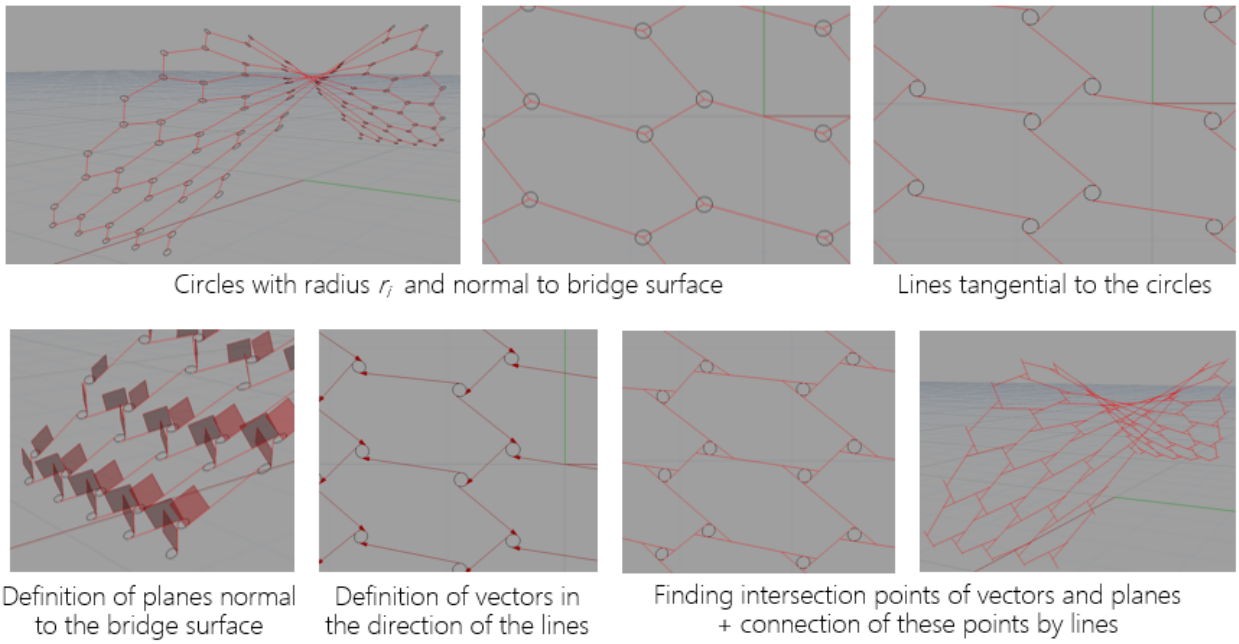

Figure 8.7: Steps undertaken to transform the hexagonal grid into the reciprocal grid pattern

8.3 Grid-lines to beams

Eventually, the grid-lines are converted to beams. This is done using the Grasshopper plugin called *Karamba*. Karamba is a Finite Element program inside the Grasshopper environment. The program enables the conversion of lines into beams when a cross-section is defined, see Figure 8.8.

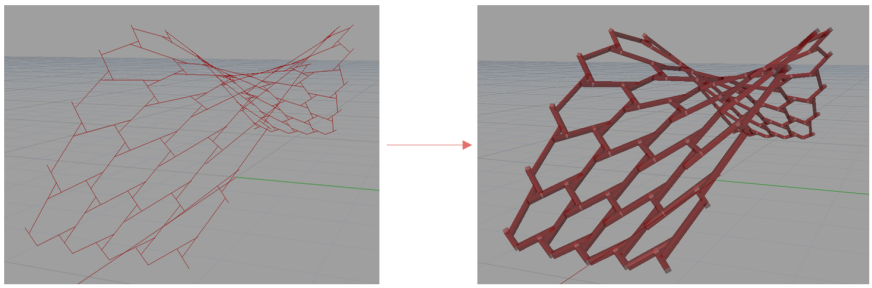

Figure 8.8: Conversion of lines into beams

8.4 Force flow

Figure 8.9, 8.10 and 8.11 show an analysis of the force flow through the structure. On the left, the force distribution in the structure due to a load combination including dead load, wind load and crowd load is shown (Load combination 5, see Table 22.1). On the right, an explanation of the force flow is given on the basis of figures.

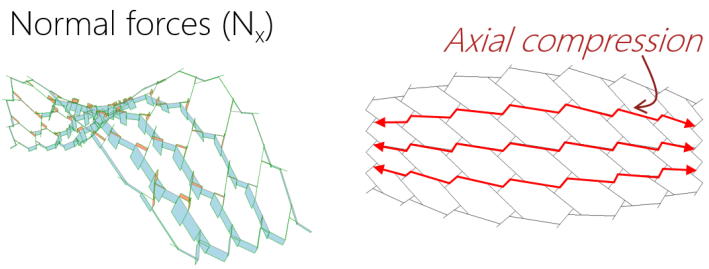

Figure 8.9: Analysis of the normal forces (N_x)

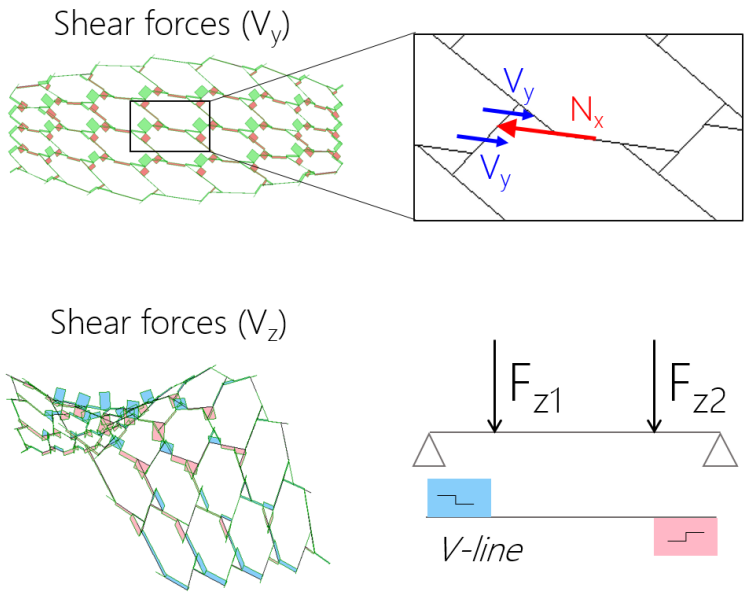

Figure 8.10: Analysis of the shear forces (V_y) and (V_z)

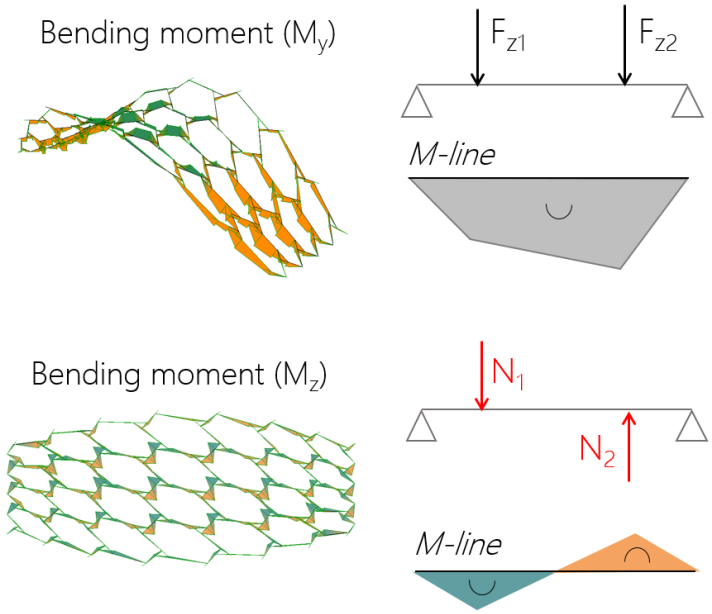

Figure 8.11: Analysis of the bending moments (M_y) and (M_z)

9

Optimisation

This chapter is devoted to the optimisation of the bridge on a global scale. The exact design of the connections is in this stage disregarded. First, a first assessment on the minimum possible section sizes is done (cross-section optimisation) (Section 9.1). The results of this optimisation is subsequently used to determine a favourable bridge shape (Section 9.2). An evolutionary solver (Galapagos) is used to find a favourable bridge shape (optimised for minimal material usage).

9.1 Cross-section optimisation

The first optimisation of the bridge that has been implemented is a cross-section optimisation. Initially, the cross-section optimisation is carried out, independent of the connection design. Since the governing shear forces and bending moments appear at the location of the connection, where less material is available, this optimisation is far from accurate. Therefore it is of great importance that this is taken into account into the next design iteration. A similar optimisation approach can be applied for that. Therefore a short description of the current procedure will be given below.

The applied optimisation loop is shown in Figure 9.2. First of all, the user has to define a the cross section to start the optimisation procedure with and a list of cross sections to choose from. After this the cross section list is sorted based on the cross sectional area. By choosing the cross section with the smallest cross sectional area for every beam, the material usage is minimised. Since multiple cross sections might have the same cross-sectional area (e.g. width x height = 30 x 80 = 80 x 30 = 60 x 40 = 40 x 60 = 2400 mm2), priority is given to beams with an aspect ratio (w/h) close to 1 in order to avoid unnecessary high or wide sections. Figure 9.1 gives a visualisation of the first part of the cross section list including the cross sectional area's.

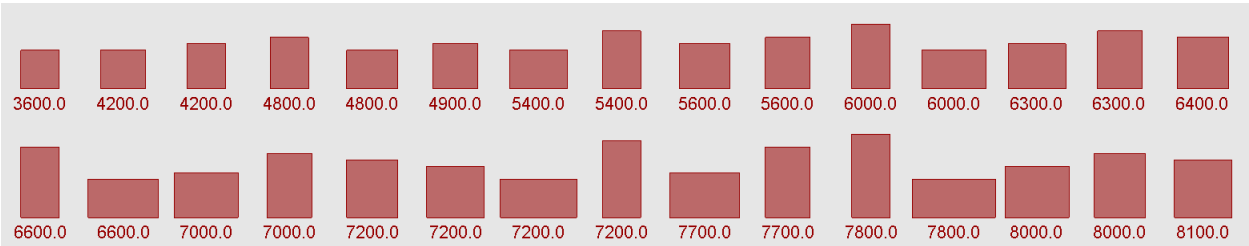

Figure 9.1: Visualisation of the first part of the cross-section list for cross-section optimisation including the cross-sectional area's $[mm^2]$

In order to speed up the optimisation and avoid that it does not converge to a state for which all UC's > 1, the starting point for the cross-section selection process is the list of cross-sections chosen during the previous iteration. The benefit of allowing the selection of a smaller section size could be investigated in future research.

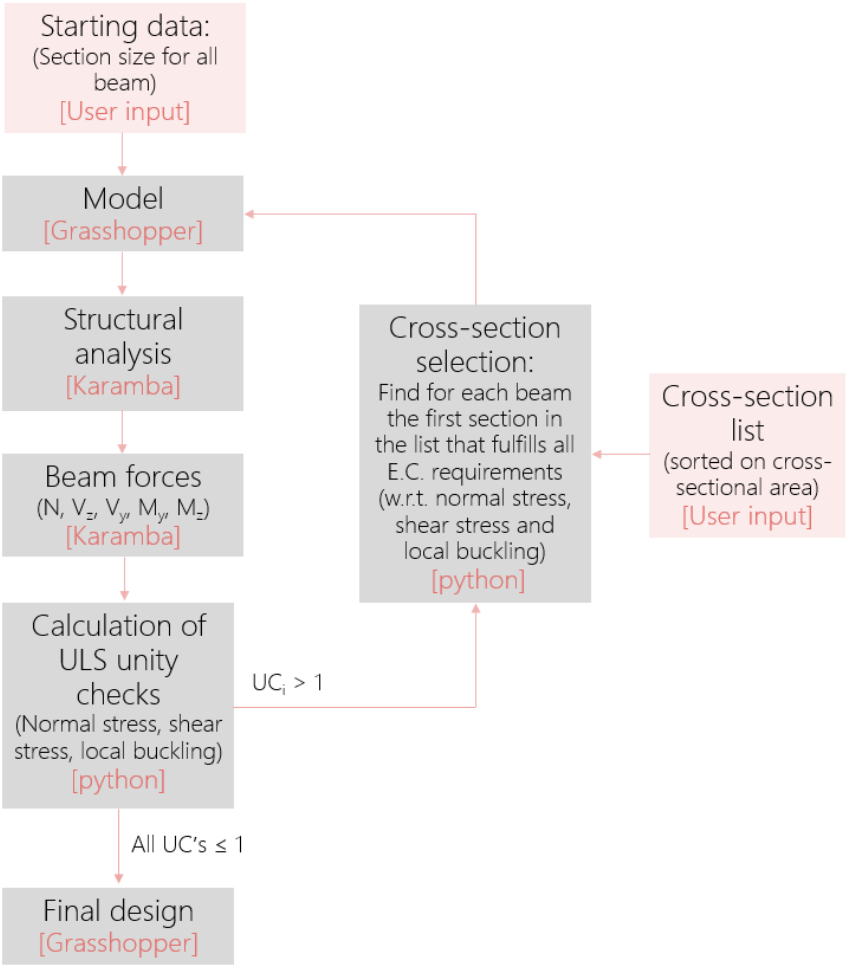

Figure 9.2: Cross-section optimisation procedure

It should be mentioned that for each iteration the unity checks are calculated for all 12 load cases as mentioned in Table 22.1. Figure 9.3 shows, using colour coding, which beams are and are not fulfilling the requirements after each cross-section optimisation iteration. The bridge design has the following details:

Global dimensions

Span:	± 9.5m
Clearance (mid):	± 1.7m
Edge height (mid):	± 0.8m
Width (deck):	± 1.5m
Width (mid):	± 3.3m

Grid

Type	Hexagonal reciprocal grid
Longitudinal divisions	9
Transverse divisions	4

Beams

Maximum beam length:	± 1.2m
Minimum beam length:	± 0.3m
Number of beams:	135
Number of connections:	241

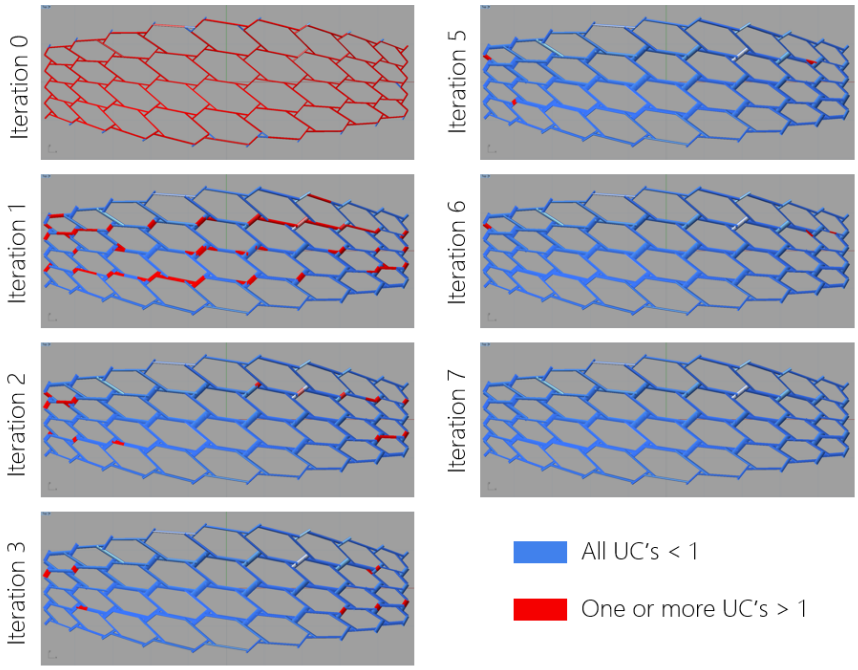

Figure 9.3: Cross-section optimisation (topview)

9.2 Shape optimisation

The second optimisation that is implemented is a shape optimisation. For this, the *Galapagos* optimisation tool in Grasshopper has been used. Galapagos is an Evolutionary Solver. An outline of how this solver works can be found in Section D.2.

9.3 First combined optimisation

In order to get some insight in the optimisation procedure and find possibilities to speed up the shape optimisation procedure, an optimisation has been carried out by varying only two parameters, see Figure 9.4:

- The (approximate) height at midspan (h_{mid})
- The (approximate) height of the edges ($d\,h_{top}$)

The design for both limit values for h_{top} are shown in Figure 9.4.

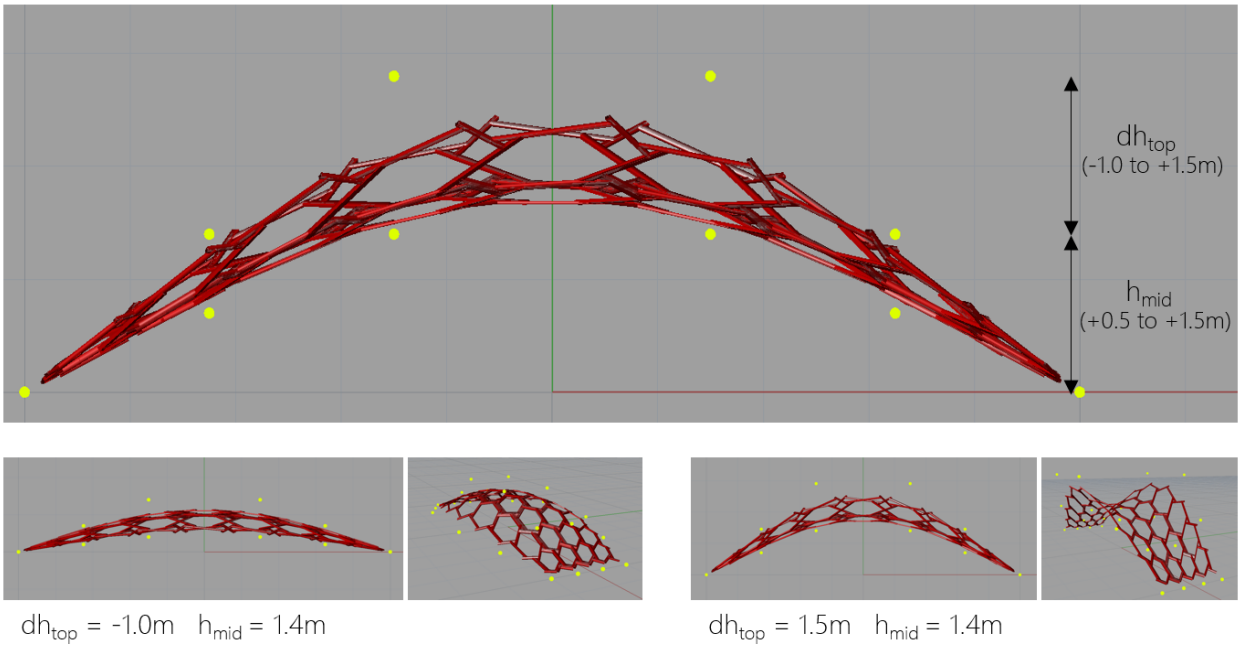

Figure 9.4: Parameters for first optimisation

Number of cross-section optimisation iterations

The speed of the shape optimisation process is governed by the speed of the cross-section optimisation process. Figure 9.5 shows that there is no correlation between the two design parameters h_{mid} and dh_{top}.

Figure 9.5: Number of cross-section optimisation iterations required to obtain a design for which all UC's > 1 for bridge designs with a variable dh_{top} and h_{mid}

In order to evaluate if it is really necessary to run through the cross-section optimisation loop until all unity checks are bigger than 1, the optimisation results are compared with the results when only one cross-section optimisation iteration is done. Figure 9.6 shows that the mass of the structure is slightly lower when only one cross-section optimisation iteration is applied, compared to when the whole loop is completed (until all UC's < 1). Nevertheless, the shape of the 'fitness field' is similar. This suggests that it would be possible to use less cross-section optimisation iterations to get a sufficient result for the optimisation of the bridge shape.

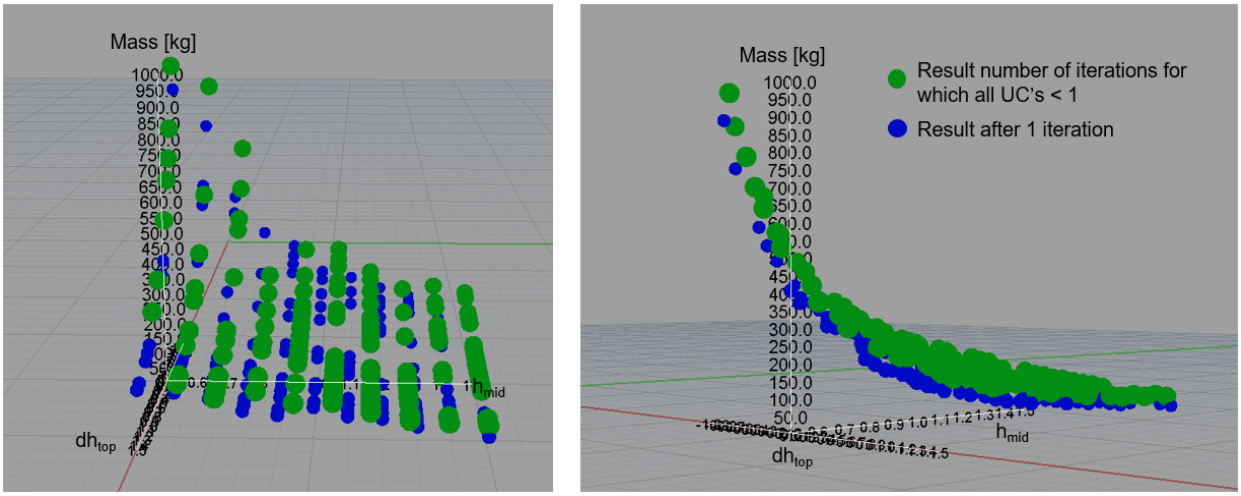

Figure 9.6: Galapagos optimisation results when applying 1 cross-section optimisation iteration (blue) compared to the number of iterations for which all UC's <1 (green)

Figure 9.7 shows for a number of design variants the mass of the structure (9.7a) and error (deviation from the mass of the structure for which all UC's < 1) (9.7b) after each cross-section optimisation iteration. After applying 2 iterations, an error of less than 5% is obtained. After 3 iterations the error is less than 3%.

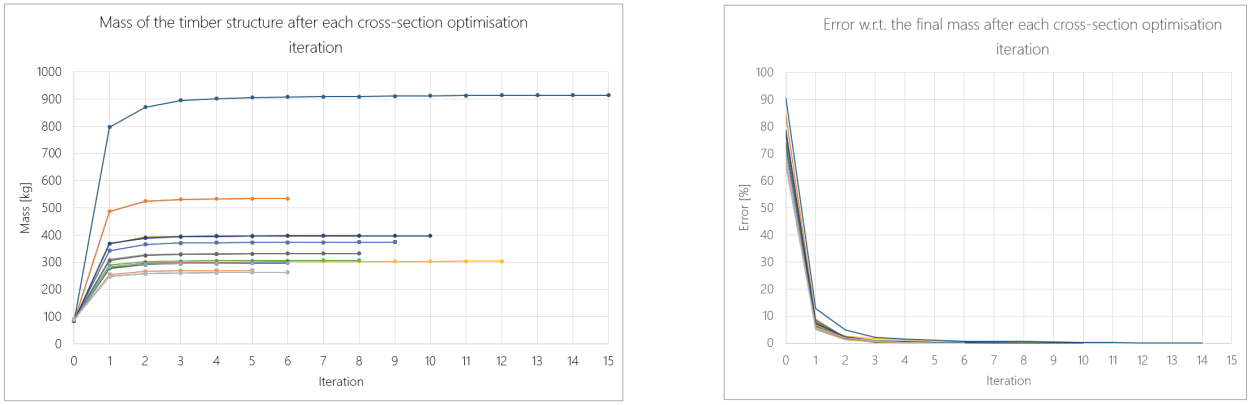

(a) (b)

Figure 9.7: Mass of the timber bridge (9.7a) and error w.r.t. the mass of the structure for which all UC's < 1 (9.7b) after each cross-section optimisation step for a group of bridge shape variants

9.4 Conclusion

A simple way to get a first idea of the minimum section sizes is by giving all beams a small section size to start with and iteratively increase the section-sizes where required. After each iteration the structure has to be analysed to determine the new force distribution in the structure. To take into account the reduced section size at the location of the connection, an effective section height and/or width should be used to calculate the unity checks at the location of the connection.

For the optimisation of the shape of the bridge, an evolutionary solver has been used (Galapagos). The shape of the bridge is optimised for minimum material usage. After each alteration of the shape, the minimum possible section sizes have to be determined as described above. This is a time-consuming process. Nevertheless, the analysis in Section 9.2 has shown that terminating the cross-section optimisation loop after two iterations will provide sufficient results for the shape optimisation for two reasons:

- The preliminary results will give approximately the same fitness-landscape shape as the results at the end of the optimisation loop and therefore the same location of maximum fitness
- After two iterations, the error between the fitness at this point and after finishing the whole loop is smaller than 5%

This reduces the optimisation time significantly without reducing the quality of the results much.

It should be noted that the number of required iterations is dependent on the cross section list. The larger the step size between cross section sizes, the less optimisation iterations are required. The study on the number of required iterations should therefore be redone when changes are made to the cross section list.

IV

Connection Design

10

Connection Design

The first step will be to decide on the type of interlocking joint that will be applied. The connection type should fulfil a set of requirements regarding the structural performance, allowance for design freedom and capabilities for manufacturing and assembly. After the decision for one type of interlocking joint is made, the geometry of the connection will be parametrised with the least amount of parameters. This will be the starting point for the design of every unique connection in the bridge structure.

10.1 Connection type

Appendix B gives a brief outline of interlocking joints that are commonly used in the ancient Japanese architecture. Distinction is made between two types of connections:

- *Tsugite*: splicing joints
- *Shiguchi*: connection joints

Since the length of the beam elements in the reciprocal structure is limited, splicing joints (*Tsugite*) will not be required. Therefore the focus will be on connection joints (*Shiguchi*).

The connection should fulfil the following requirements:

- The connection should allow for:
  - connection at different angles, see Figure 10.1 (left)
  - connection of beams with different section sizes
  - eccentricities between the central axis of the connecting beams, see Figure 10.1 (left)
- The connection should have a resistance to the following forces, see Figure 10.1 (right):
  - Normal forces (both compression and tension)
  - Shear forces (horizontal in two directions, vertical in the direction of gravity)
  - Bending moments at the continuous part of the connection
- The connection should be feasible for CNC-milling

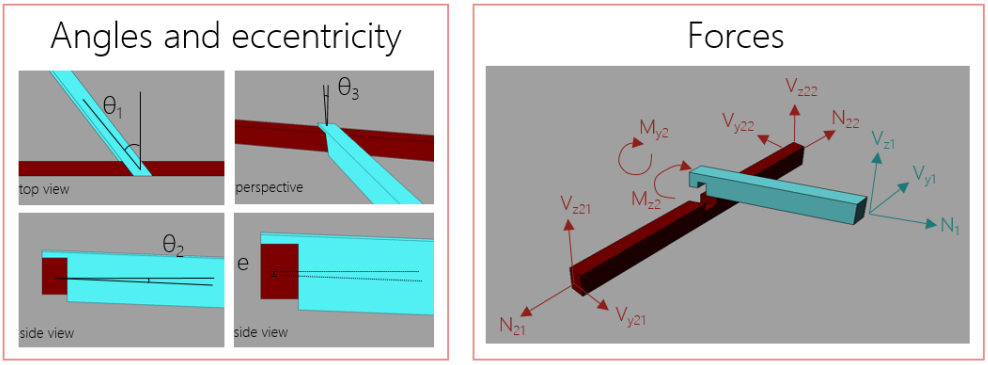

Figure 10.1: Connection requirements: connection at different angles (left) and resistance to normal, shear and bending forces (right)

Furthermore, preferably no fasteners are required. This will simplify the fabrication and assembly process.

Figure B.5 and B.6 in Appendix B show some examples of T-joints. The connections in Figure B.5a have a no or barely resistance to tensile forces in the non-continuous beam.The connections in Figure B.5b all require additional fasteners. The connections in Figure B.6 on the right are also discarded due to lack of resistance to tension forces and shear loading in one direction, respectively.

The two remaining types of connections that fulfil all above mentioned requirements are:

- Type 1: a dovetail joint
- Type 2: a simple lap joint

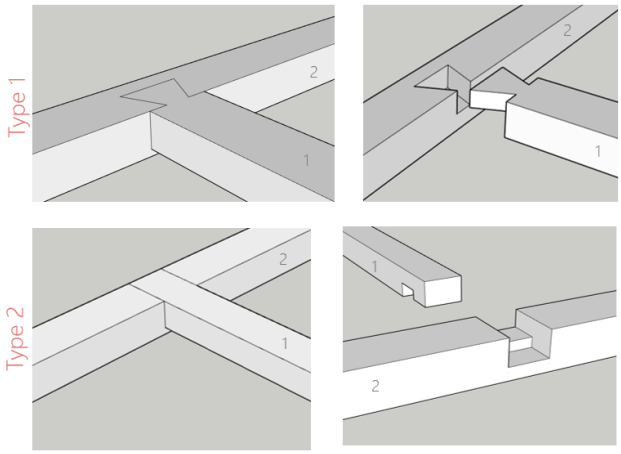

Figure 10.2: Connection Type 1 (dovetail joint) and Type 2 (simple lap joint)

The advantage of Type 1 is that in case of a tension force in beam 1, the connection will be fixated due to the sloped edges. Nevertheless, due to the arching effect, most of the beams are under compression, resulting in loss of the fixation effect.

A disadvantage of connection Type 1 compared to type 2 is the size of the shear plane. Due to the eccentric connection of beams, a normal force in one beam results in an often critical shear force in the connecting beam. This shear force has to be transferred through the red marked areas in Figure 10.3. Due to the sloped edges in connection Type 1, the shear area is significantly reduced, resulting in a smaller shear capacity than connection Type 2.

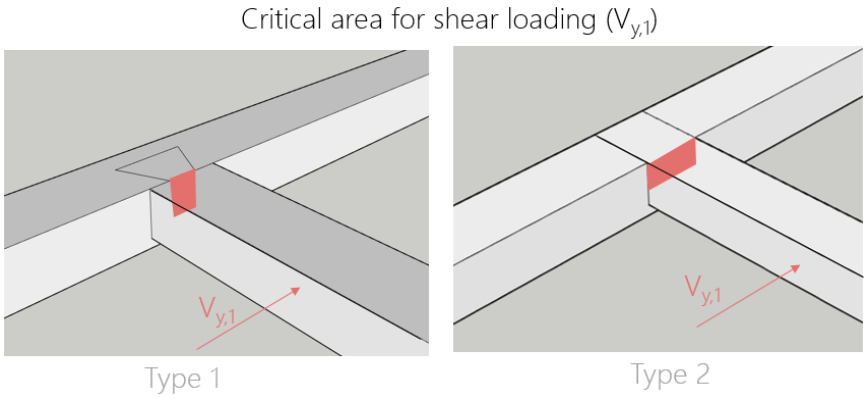

Figure 10.3: Shear plane connection Type 1 and Type 2

A second disadvantage of connection Type 1 is that a problem arises when beams are connecting at an angle, see Figure 10.4. It is preferable to keep the connection design between the dashed lines. Otherwise the beams will have to be adjusted by CNC-milling along the whole length of the beam instead of only at the location of the connection and material will be wasted. This restriction results in the fact that the tension capacity can be low when beams connect at an angle since the slope of the dovetail is on one side almost parallel to the beam.

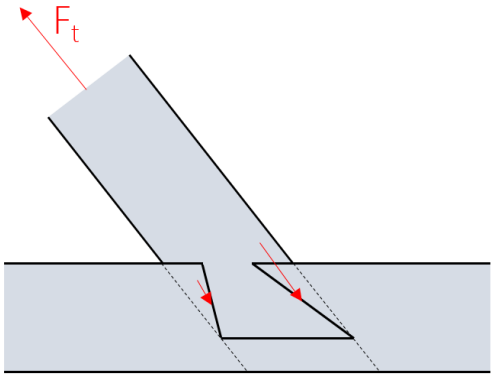

Figure 10.4: Problem with tension capacity when beams meet at an angle (Type 1)

These two disadvantages have led to the decision to continue with connection type 2.

10.2 Parametric definition of the connection dimensions

The design of the connection can be described by four parameters related to the global design (known) and seven parameters defining the internal and external dimensions of the connection (still undetermined). In order to distinguish the two beams meeting in one connection, *beam 1* and *beam 2* are defined as shown in Figure 12.2

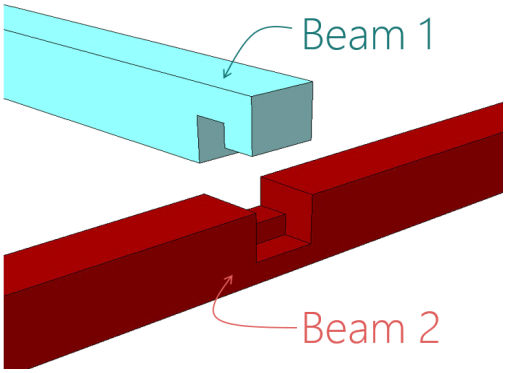

Figure 10.5: Beam 1 and beam 2

Parameters defined by global model

Four parameters can defined from the already known global geometry of the bridge, see Figure 10.6:

- θ_1: The angle between $x_1^{(x2,y2)}$ and y_2 (Where $x_1^{x2,y2}$ is axis x_1 projected on the (x_2, y_2)-plane)
- θ_2: The angle between $x_1^{(y2,z2)}$ and y_2
- θ_3: The angle between $z_1^{(x1,z1)}$ and z_2
- e: The eccentricity between x_1 and x_2

Where (x_1, y_1, z_1) is the local coordinate system of beam 1 and (x_1, y_1, z_1) is the local coordinate system of beam 2. Both local coordinate systems can be extracted from the global model of the bridge.

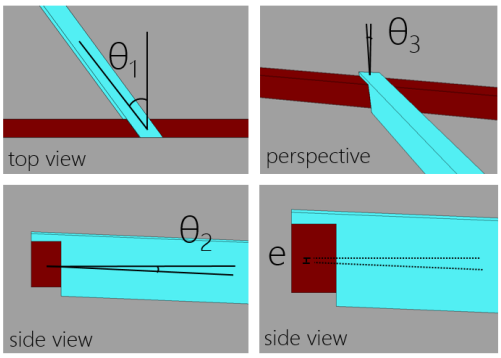

Figure 10.6: Parameters defining the geometry of the connection related to the global geometry of the bridge

When all four parameters are known, the geometry of the connection can be determined and subsequently be applied to the global model, see Figure 10.7.

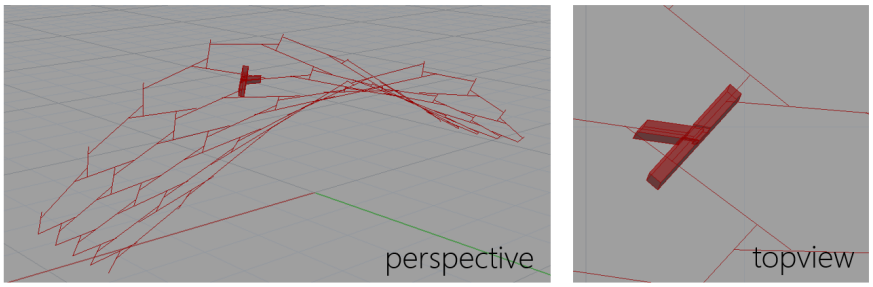

Figure 10.7: Matching global geometry and connection design

Parameters defining the dimensions of the connection

In order to describe the dimensions of the connection 7 parameters are defined, see Figure 10.8 and 10.9:

- Defining the external dimensions:
  - h_1: The height of beam 1
  - w_1: The width of beam 1
  - h_2: The height of beam 2
  - w_2: The width of beam 2
- Defining the internal dimensions:
  - a_1-ratio: The ratio between length a_1 (see Figure 10.8) and the total height of beam 1 (a_1/h_1)
  - a_2-ratio: The ratio between length a_2 (see Figure 10.8) and the total height of beam 1 (a_2/h_1)
  - b_1-ratio: The ratio between length b_1 (see Figure 10.8 and 10.9) and the total width of beam 2 (b_1/w_2)

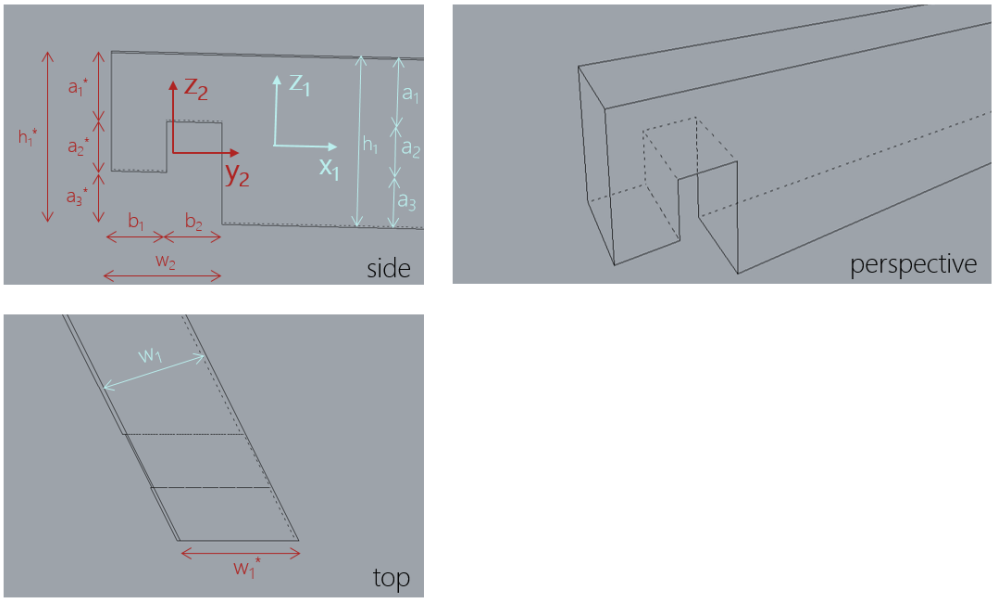

Figure 10.8: Dimensions beam 1

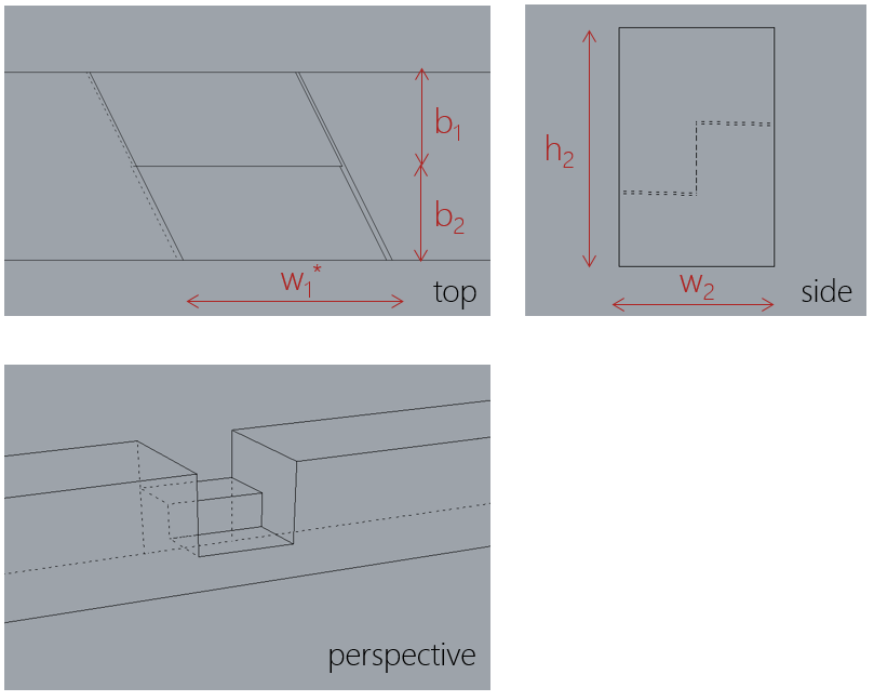

Figure 10.9: Dimensions beam 2

On the basis of those seven parameters plus the four parameters linked to the global design, a design for every (unique) connection in the bridge can be made.

10.3 Conclusion

It is decided to apply a lap joint at the connection. This type of connection fulfils all requirements regarding design freedom (connection of beams with different sizes at different angles) and structural performance. Furthermore, it will be possible to manufacture the connection by means of CNC-milling. No additional fastening materials are required, which simplifies assembly of the elements.

The geometry of the connection can be defined by 4 parameters following from the global model and 7 (yet unknown) parameters defining the dimensions of the connection. The parameters from the global model

are three rotations (θ_1, θ_2 and θ_3) and one eccentricity (e) of beam 1 relative to beam 2, see Figure 10.6. The 7 parameters defining the dimensions of the the connection consist of the four external dimensions of beam 1 and 2 (h_1, w_1, h_2 and w_2) and three ratio's defining the size of the notch (a_1-ratio, a_2-ratio and b_1-ratio).

11

Detailing of connection

This chapter will give a brief overview of decisions made regarding the detailing of the connection. Small adjustments to the connection design are made in order to improve the structural performance and its sensitivity to dimensional deviations due to shrinkage and swelling. For all adjustments made it is verified if the design is feasible for CNC-milling.

11.1 Radii to reduce risk on shear cracks

Members with notches are known for being sensitive to shear cracking. At the transition from the reduced height at the notch to the full member height, a stress peak will appear. This results in a risk for shear cracking parallel to the grain, as shown in Figure 11.1.

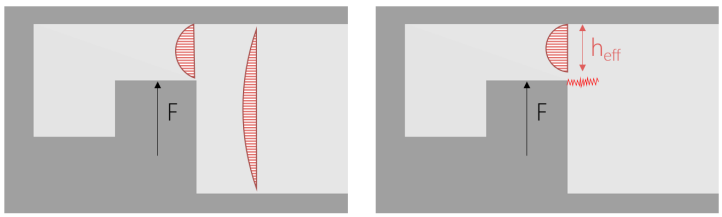

Figure 11.1: Shear crack risk at notches

Therefore, ideally the transition from reduced height to full member height goes gradually. However, full contact is required between beam 1 and 2 to transfer axial compression forces in beam 1. All material that is added to beam 1 to generate a slope for a gradual stress distribution will have to be abstracted from beam 2. This has a negative influence on both the shear and bending capacity of beam 2 at the location of the connection.

A less radical solution is the application of a radius at the location of the stress peaks. Figure 11.2 shows the locations that are prone to shear cracks, together with the favoured radii. Radius 3 (R_3) is not feasible for CNC-milling and is therefore disregarded.

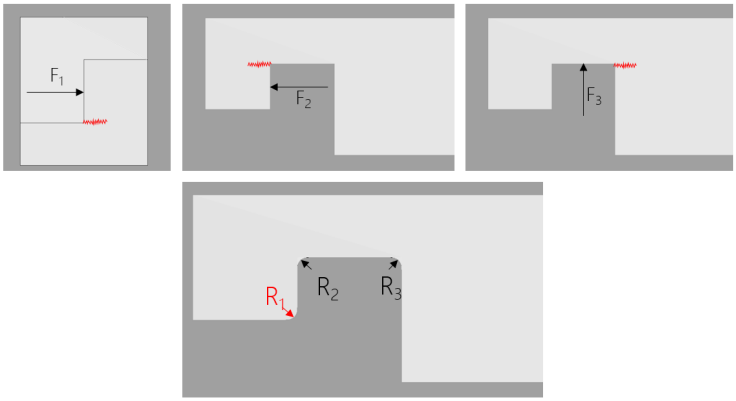

Figure 11.2: Locations prone to shear cracks

11.2 Free space preventing high bending moments

In order to prevent high bending moments at the transition from the notch to full member height, a small free space between beam 1 and beam 2 (1mm) is implemented at the end of beam 1, see Figure 11.3. In this way, the eccentricity of the resultant or the vertical shear force (V_{z1}) is limited.

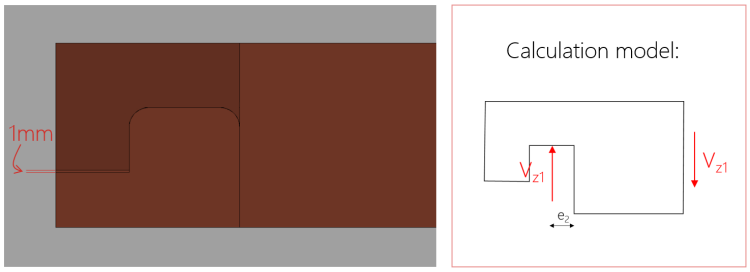

Figure 11.3: Gap between beam 1 and to in order to prevent high bending moments in beam 1

11.3 Sloped edges to allow for dimensional deviations

Timber is a material that is sensitive to changes in moisture content. The material shrinks when the moisture content is decreased. Furthermore, the shrinkage and swelling is smaller parallel to the grain than perpendicular to the grain. This can result in differential swelling and shrinkage at the location of connections where beams with different grain directions meet.

The size of the gap in which beam 1 and 2 connect is defined by the width of beam 1. When both beams will be exposed to moisture, beam 1 (perpendicular to the grain) will swell more than beam 2 (parallel to the grain). This is advantageous when both beams are in position since this will interlock both beams. Nevertheless, when this happens prior to placement, the risk will arise that beam 1 does not fit into the gap, see Figure 11.4 (left).

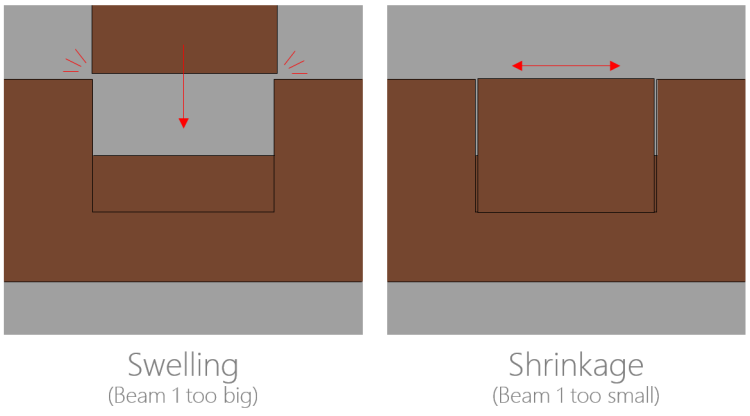

Figure 11.4: Risk for clash when differential swelling occurs prior to placement (left) and for clearance between beam 1 and 2 due to differential shrinkage (right)

Conversely, differential shrinkage can occur when the moisture content decreases. This results in a clearance between both elements, see Figure 11.4 (right). Shear forces, V_y, will first be transferred by friction only. When a certain threshold is reached, the beam 1 will start sliding until contact is made with beam 2. This behaviour is undesirable.

Both the risk for clashes at placement and sliding of the elements can be reduced by applying sloped edges as shown in Figure 11.5a. Currently, a slope of 1:4 is applied. A quantitative study on the differential shrinkage could show if this is a good assumption.

Preferably the beams are only adapted at the location of the connection to save work and time, see Figure 11.5b.

To obtain this, two designs have been made, see Figure 11.6.

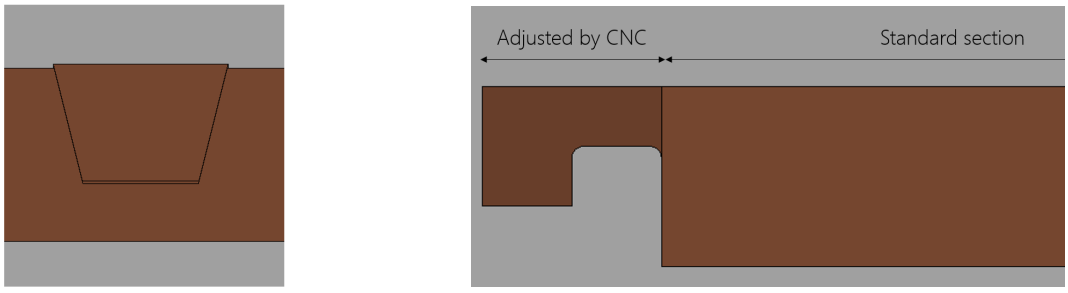

(a) (b)

Figure 11.5: Sloped edges to reduce problems with differential shrinkage/swelling (11.5a) and the adjusted part of the beam (11.5b)

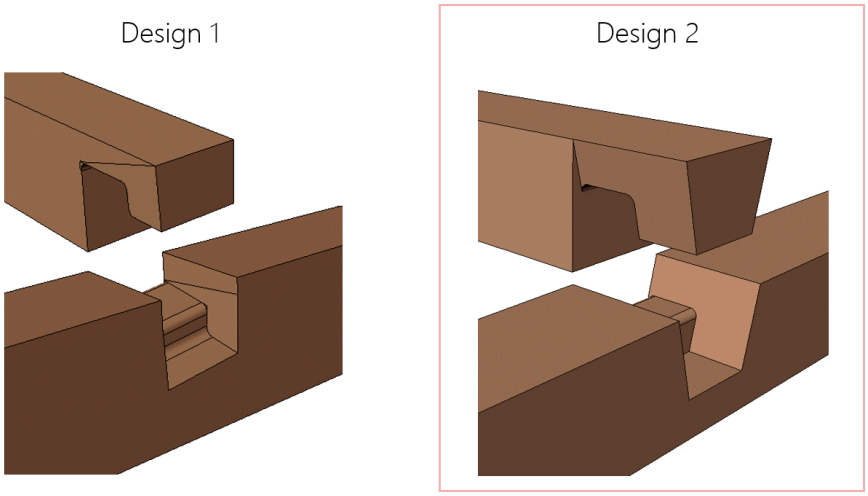

Figure 11.6: Design with slopes 1 & 2

The advantage of design 1 is that there are no extra sharp corners (prone to stress concentrations) added to the design. Nevertheless, for this design the areas marked red in Figure 11.7 are not feasible for CNC-milling. Therefore it is decided to apply design 2.

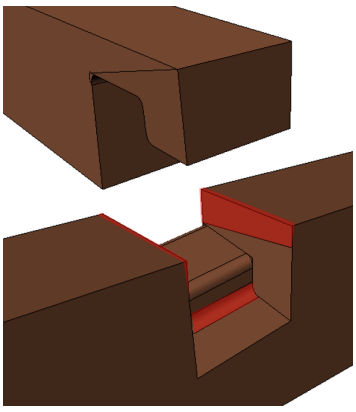

Figure 11.7: Parts of the design that are not feasible for CNC-milling are marked red

11.4 Slopes added for assembly

A first analysis of the assembly of the bridge is carried out. When two beams are placed, the third beam should be rotated into the final position in order to be on top on one beam and below another beam, see Figure 11.8. Figure 11.9 proposes an assembly order.

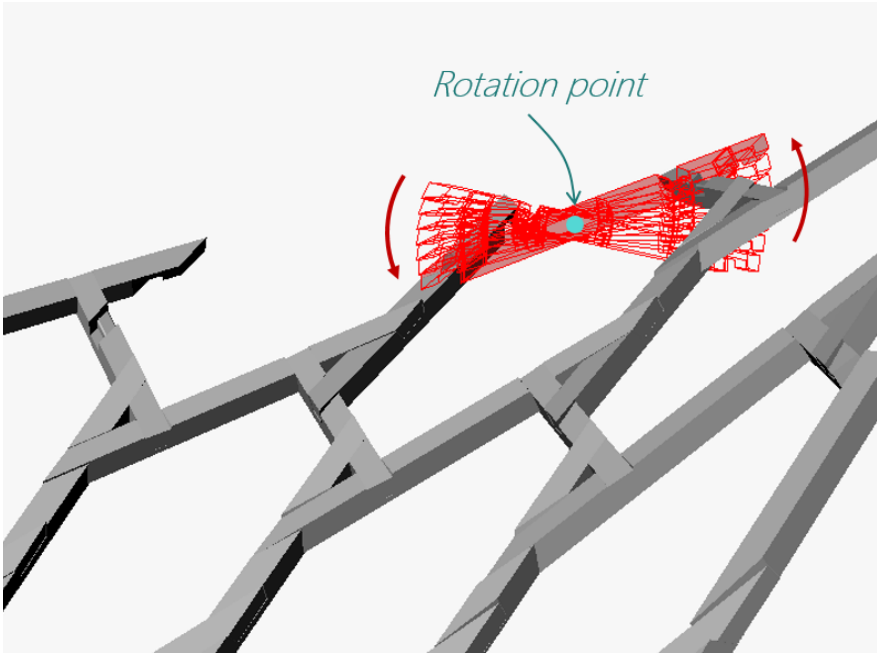

Figure 11.8: The placement of one beam

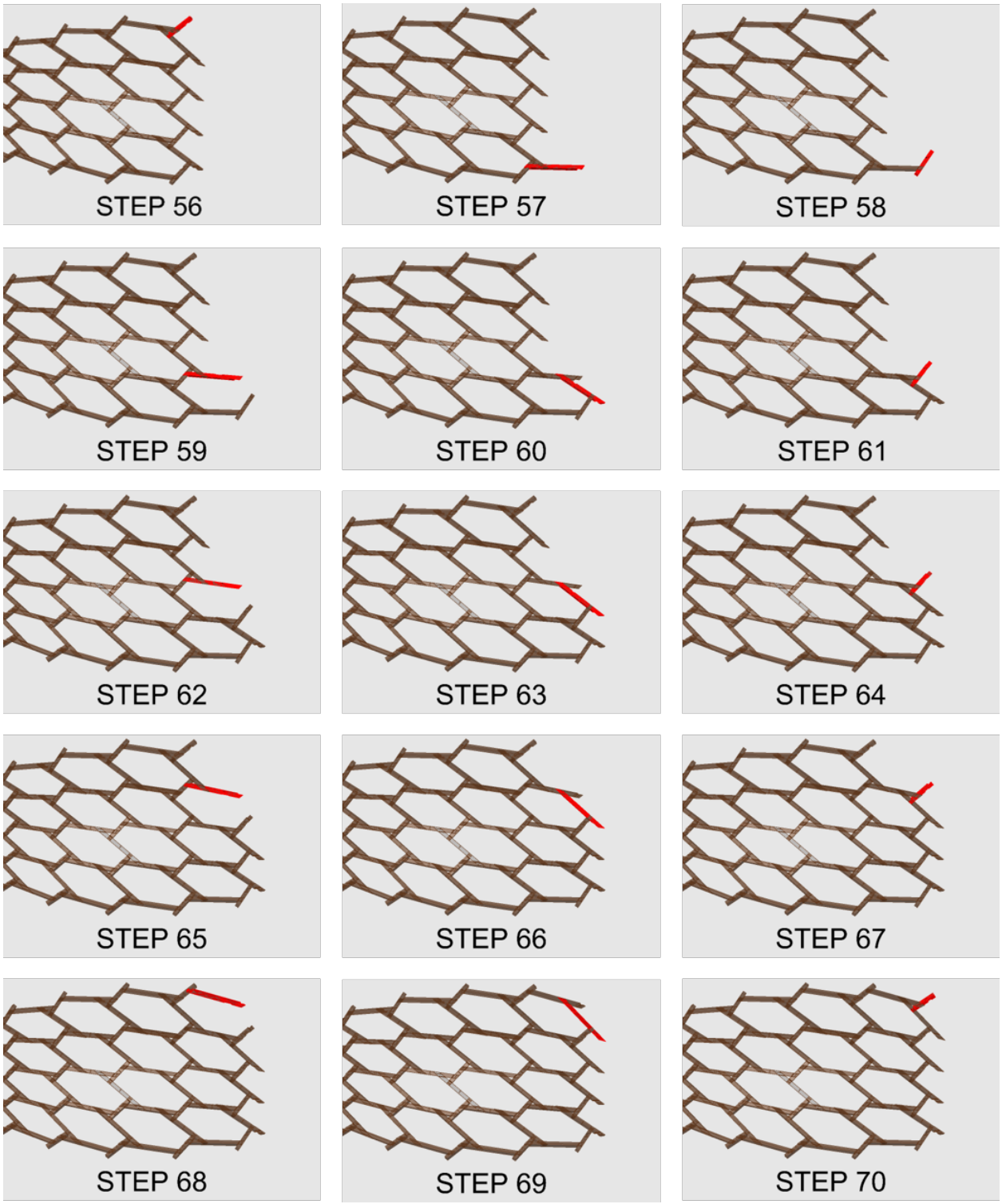

Figure 11.9: Assembly step 56 until 70. Already placed beams are marked brown, new beams are marked red

When the assembly order is known, the rotation point of each beam can be defined, see Figure 11.10.

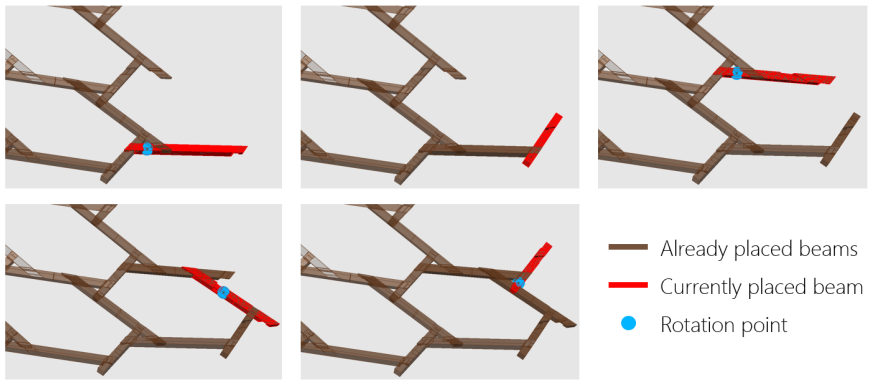

Figure 11.10: Rotation point for assembly of beam step 57 until 61

The clashes that exist during assembly can be tracked down by marking all overlapping volumes while simulating the rotation of the beam, see Figure 11.11.

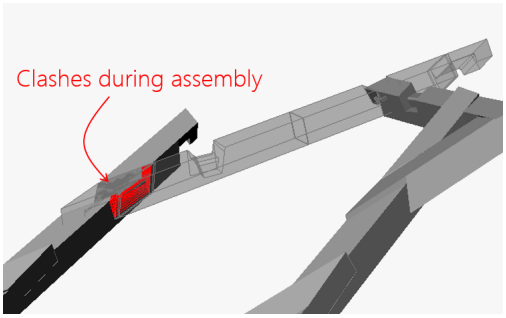

Figure 11.11: Clashes during placement of the beam

The figure shows that there are only clashes at the end part of the beam. The sloped edges that were originally added in order to limit the effects of differential shrinkage and swelling turn out to be favourable for the the assembly process. It should be verified if the gradient of the sloped edge is sufficient in all cases.

In order to prevent the clashes at the end of the beam, the design should be slightly adjusted. The location of the clashes can be defined by two radii, see Figure 11.12 (left). By removing some material from beam 2 and adding material to beam 1, a suitable design for assembly can be obtained, see Figure 11.12 (right).

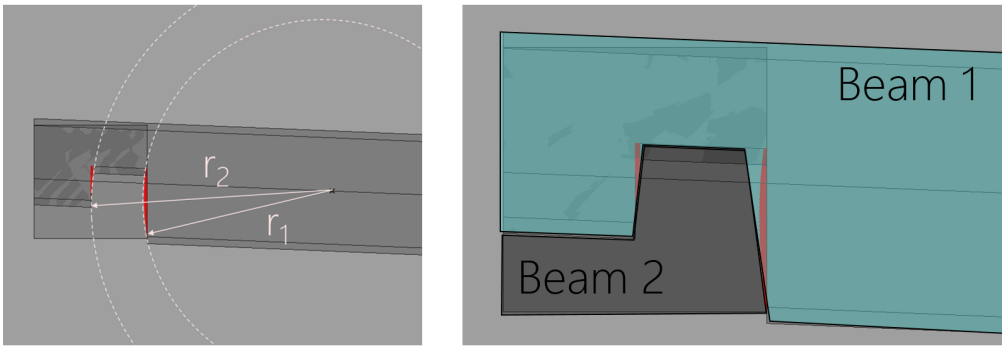

Figure 11.12: Radii defining the clashes (left) and adjusted design for assembly (right)

11.5 Conclusion

In order to improve the structural performance of the connection, two adjustments have been made. First of all, a radius has been added at two locations that are prone to shear cracking, see Figure 11.13a. Note that the same radii will be added for beam 2 so there are no gaps between the two beams. Additionally, a small (1mm) gap is added at the end of the notch in order to limit the bending moments and the transition from the notch to full member height, see Figure 11.13b.

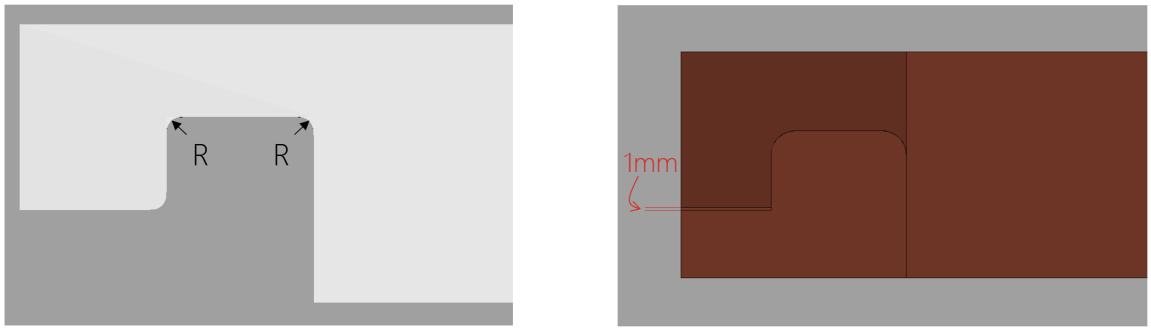

(a) (b)

Figure 11.13: Radii added to lower risk of shear cracking (11.13a) and gap added to lower bending moments (11.13b)

Furthermore, slopes have been added in order to prevent clashes due to differential swelling and movements due to differential shrinkage. Slopes are only added locally at the location of the connection to limit the fabrication time and costs.

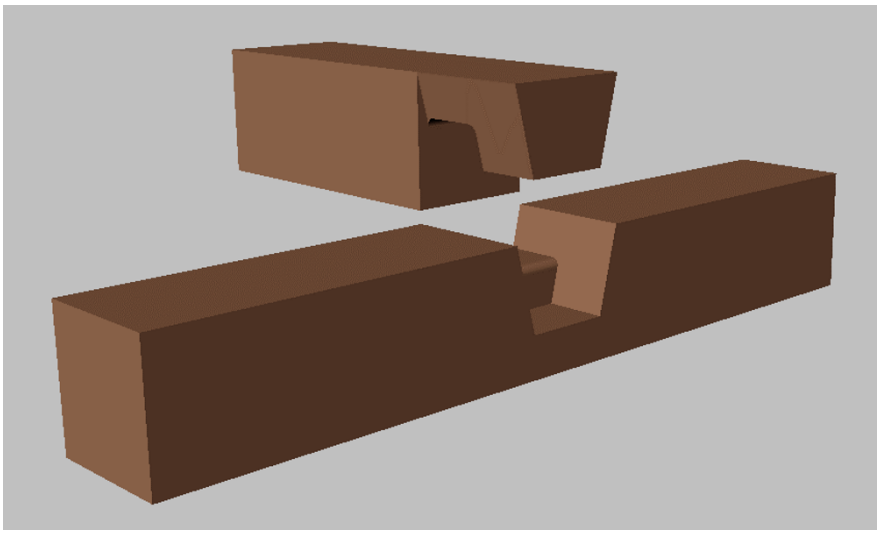

Figure 11.14: Design with added slopes

Finally, adjustments should be made to the design in order enable the assembly process, see Figure 11.15.

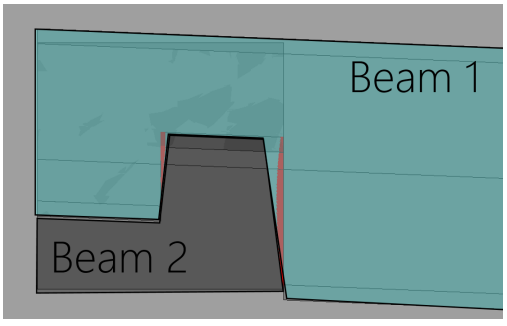

Figure 11.15: Adjusted design for assembly

12

Connection model

12.1 Simplified connection and relevant planes

For the calculation of the connection, a simplified model of the connection is used in which the curved finishings within the connection are disregarded, see Figure 12.1. Furthermore, it is assumed that the connection between two beams has enough rotational capacity to be treated like a hinged connection, resulting in the moment- and shear-distribution shown in Figure 12.1.

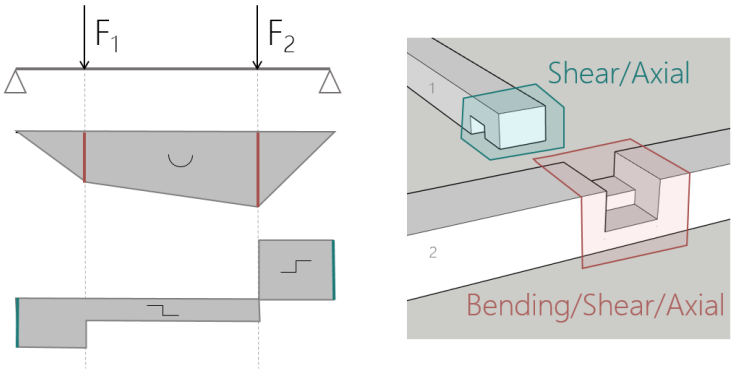

Figure 12.1: Simplified connection model

From this point, the two beams that meet in one connection will be denoted as beam 1 (end-part, lays on top) and beam 2 (mid-part, lays on the bottom), see Figure 12.2.

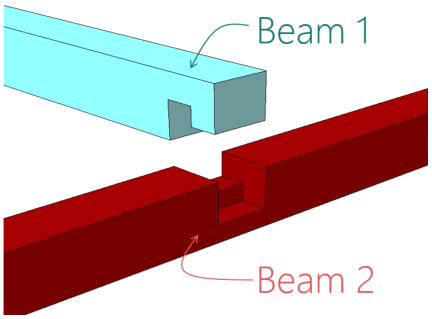

Figure 12.2: Beam 1 and beam 2

Figure 12.3 and 12.4 show all critical planes in beam 1 and beam 2, together with the type of stress the plane is subjected to. For all these planes, the stresses and corresponding unity checks are calculated as described in 12.2

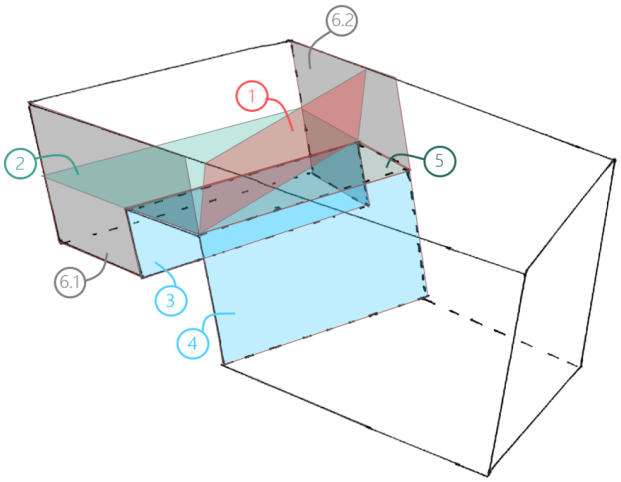

1. Axial + bending + shear
2. Axial + bending + shear
3. Compression (if $N_1 > 0$)
4. Compression (if $N_1 < 0$)
5. Compression
6. Compression

Figure 12.3: Relevant planes beam 1

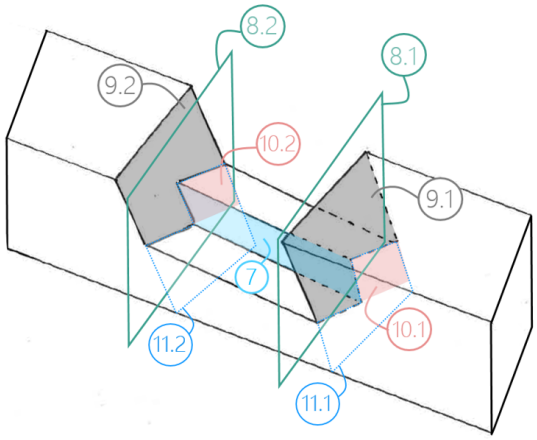

7. Compression (if $N_1 > 0$)
8. Axial + bending + shear
9. Compression
10. Shear + bending
11. Axial + bending + shear

Figure 12.4: Relevant planes beam 2

All relevant geometric properties of the planes (dimensions, I-moduli and center of gravities) are defined by using a grasshopper script, see Figure 12.5.

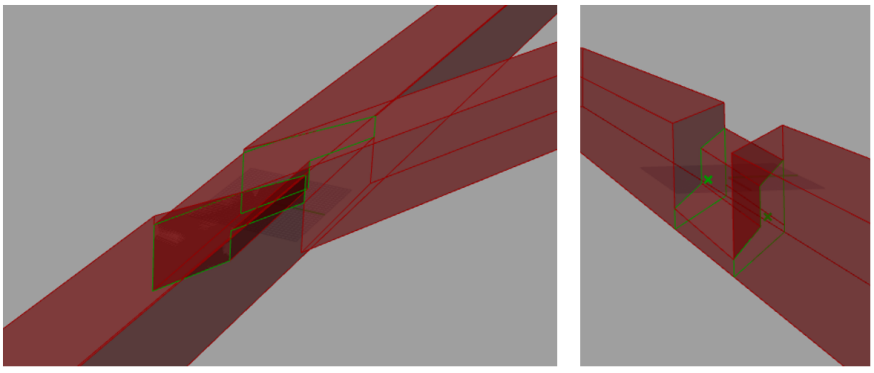

Figure 12.5: Selection of relevant planes in Grasshopper. (Left: Plane 6.1 & 6.2, Right: Plane 11.1 & 11.2 including centre of gravity)

12.2 Stress calculations

Now that the dimensions of all relevant planes are known, the force results from the global (Karamba) model are used to calculate the stresses in all planes.

12.2.1. Stress calculation Plane 1

Bending-, axial- and shear-stresses are introduced in plane 1 by the normal- (N_1) and shear-forces (V_{y1}&V_{z1}) in beam 1.

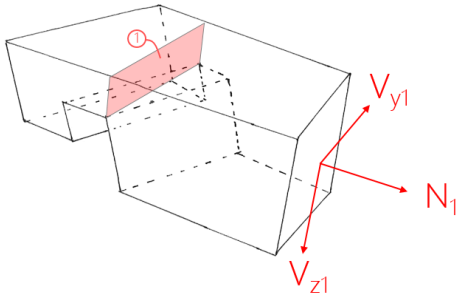

Figure 12.6: Plane 1 and relevant forces

Normal stresses

A distinction should be made between the following two cases:

- $N_1 > 0$ (tension):
  - $\sigma_N = \sigma_{Ax} + \sigma_{M,Vz} + \sigma_{M,N}$
- $N_1 < 0$ (compression):
  - $\sigma_N = \sigma_{M,Vz}$

Where σ_N is the uniformly distributed axial stress due to normal force N_1, $\sigma_{M,Vz}$ is the axial stress caused by the moment due to shear force V_{z1} and $\sigma_{M,N}$ is the axial stress caused by the moment due to normal force N_1, see Figure 12.7.

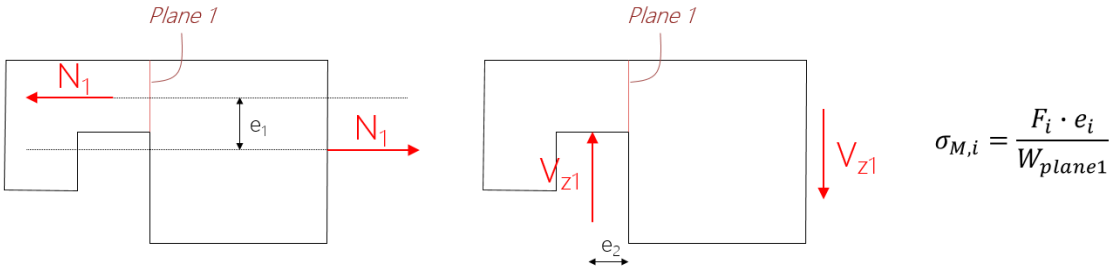

Figure 12.7: Bending moment in plane 1 induced by an axial force (left) and shear force (right) in beam 1

Shear stress

Notches and holes in beams considerably reduce the capacity of timber beams. Since the crack propagation from holes or notches is parallel to the grain, the failure is brittle, see Figure 12.8.

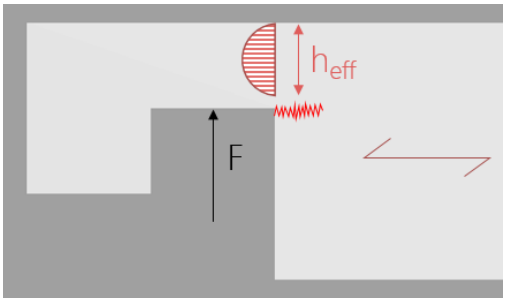

Figure 12.8: Risk for crack at the notch parallel to the grain

When a local failure takes place, the stress will re-distribute during crack propagation. EC 5 specifies rules for the calculation of beams with notches in the National Annex, based on concepts from fracture mechanics. [15]

In NEN-EN 1995-1-1, Section 6.5.2 gives information on how to calculate beams with a notch at the support, like shown in Figure 19.1.

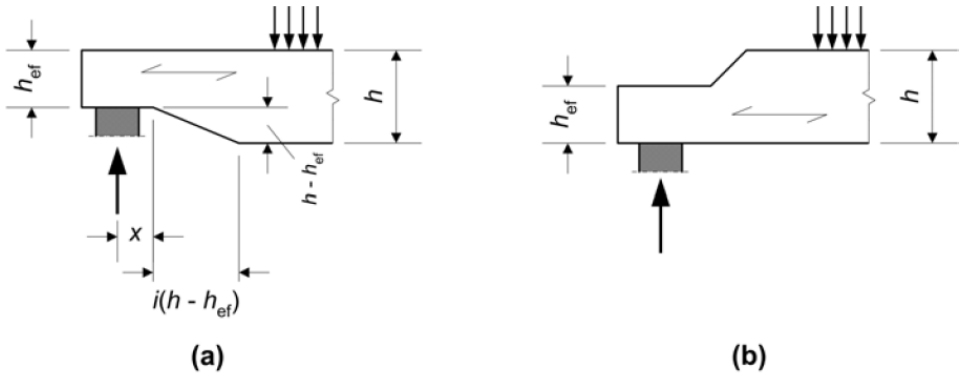

Figure 12.9: Beams with a notch at the end (NEN-EN 1995-1-1)

The following requirement should be met:

$$\tau_d = \frac{1.5V}{bh_{ef}} \leq k_v f_{v,d} \tag{12.1}$$

Where k_v is:

- For beams notched on the same side as the support (Figure 19.1 a)

$$k_v = min \begin{cases} 1 \\ \frac{k_n(1+\frac{1.1i^{1.5}}{\sqrt{h}})}{\sqrt{h}(\sqrt{\alpha(1-\alpha)}+0.8\frac{x}{h}\sqrt{(\frac{1}{\alpha}-\alpha^2)})} \end{cases} \tag{12.2}$$

- For beams notched at the opposite side of the support (Figure 19.1 b)

$$k_v = 1.0 \tag{12.3}$$

Furthermore:

i is the notch inclination (see Figure 19.1 b)
h is the depth of the beam in mm
x is the distance from line of action of the support reaction to the corner of the notch
α the ratio between the effective depth and the real depth ($\alpha = \frac{h_{ef}}{h}$)
k_n

$$= \begin{cases} 4.5, & \text{for LVL} \\ 5, & \text{for solid timber} \\ 6.5, & \text{for glued laminated timber} \end{cases} \tag{12.4}$$

Checks

The following unity checks are calculated:

$$UC_{p1,Ax1} = \begin{cases} \frac{\sigma_N}{f_{t,\alpha,d}} + \frac{\sigma_{M,tot}}{f_{m,d}} & \text{if } N_1 > 0 \\ \frac{\sigma_{M,Vz}}{f_{m,d}} & \text{if } N_1 \leq 0 \end{cases} \tag{12.5}$$

$$UC_{p1,V} = \frac{\tau_z}{(k_v \cdot f_{v,d})} + \frac{\tau_y}{f_{v,d}} \tag{12.6}$$

12.2.2. Stress calculation Plane 2

In case of a tensile normal force in beam 1 ($N_1 > 0$) both normal- and shear stresses are induced in Plane 2, see Figure 12.10.

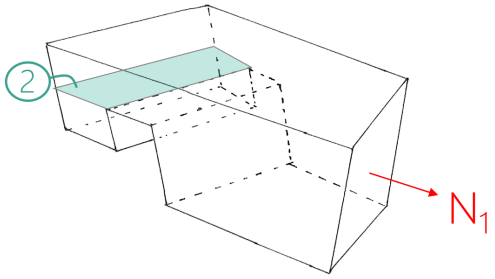

Figure 12.10: Plane 2 and relevant forces

The normal force induces both a shear stress and axial stress due to bending, see Figure 12.14.

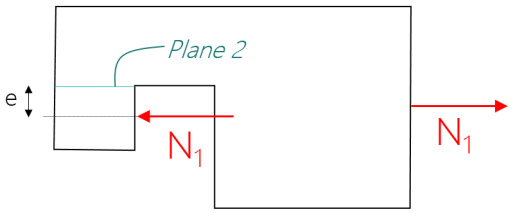

$$\sigma_M = \frac{F \cdot e}{W_{plane2}}$$

Figure 12.11: Bending moment in plane 2 induced by the axial force

The following two unity checks are carried out:

$$UC_{p2,M} = \begin{cases} \frac{\sigma_{M,N}}{f_{m,90,d}} & \text{if } N_1 > 0 \\ 0 & \text{if } N_1 \leq 0 \end{cases} \tag{12.7}$$

$$UC_{p2,V} = \begin{cases} \frac{\tau_y}{f_{v,d}} & \text{if } N_1 > 0 \\ 0 & \text{if } N_1 \leq 0 \end{cases} \tag{12.8}$$

12.2.3. Stress calculation Plane 3, 4, 5, 6, 7 and 9

Plane 3, 4, 5, 6, 7 and 9, see Figure 12.12 are subjected to a normal compressive stress only.

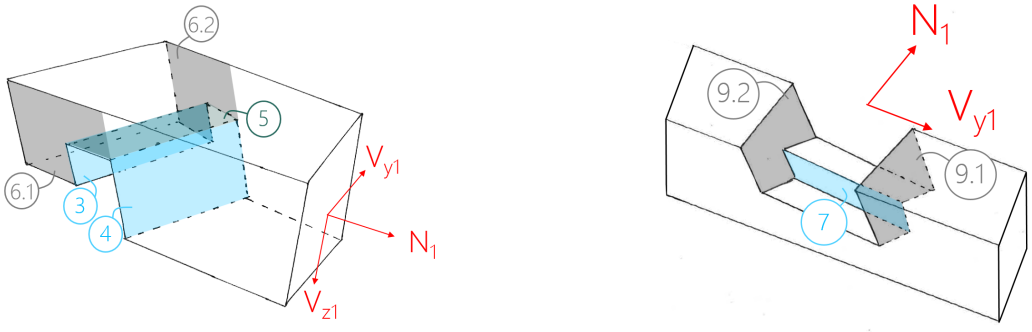

(a) (b)

Figure 12.12: Plane 3, 4, 5 and 6 (12.12a) and plane 7 and 9 (12.12b)

This results in the following checks:

$$UC_{p3,N} = \begin{cases} \frac{\sigma_{c,3}}{f_{c,\alpha,d}} & \text{if } N_1 > 0 \\ 0 & \text{if } N_1 \leq 0 \end{cases} \tag{12.9}$$

Where $\sigma_{c,3} = \frac{N_1}{A_{plane3}}$

$$UC_{p4,N} = \begin{cases} \frac{\sigma_{c,4}}{f_{c,\alpha,d}} & \text{if } N_1 < 0 \\ 0 & \text{if } N_1 \geq 0 \end{cases} \tag{12.10}$$

Where $\sigma_{c,4} = \frac{N_1}{A_{plane4}}$. Plane 4 is the contact area between beam 1 and 2. In some cases this might not correspond to the whole area as marked in Figure 12.12

$$UC_{p5,N} = \frac{\sigma_{c,5}}{f_{c,\alpha,d}} \tag{12.11}$$

Where $\sigma_{c,5} = \frac{V_{z1}}{A_{plane3}}$

$$UC_{p6,N} = \frac{\sigma_{c,6}}{f_{c,\alpha,d}} \tag{12.12}$$

Where $\sigma_{c,6} = \frac{V_{y1}}{A_{plane6,min}}$. $A_{plane6.i}$ is the contact area between beam 1 and 2 at the location of plane 6.1 and 6.2. The minimum of the two is taken, which is a conservative assumption in some cases.

$$UC_{p7,N} = \begin{cases} \frac{\sigma_{c,7}}{f_{c,\alpha,d}} & \text{if } N_1 > 0 \\ 0 & \text{if } N_1 \leq 0 \end{cases} \tag{12.13}$$

Where $\sigma_{c,7} = \frac{N_1}{A_{plane7}}$

$$UC_{p9,N} = \frac{\sigma_{c,9}}{f_{c,\alpha,d}} \tag{12.14}$$

Where $\sigma_{c,9} = \frac{V_{y1}}{A_{plane9,min}}$. $A_{plane9.i}$ is the contact area between beam 1 and 2 at the location of plane 9.1 and 9.2. The minimum of the two is taken, which is a conservative assumption in some cases.

12.2.4. Stress calculation Plane 10

A tensile force in beam 1 results in both bending stresses and shear stresses in Plane 10.1 and 10.2. It is assumed that no shear forces are transferred at the blue-marked plane due to the relatively low capacity in case of rolling shear.

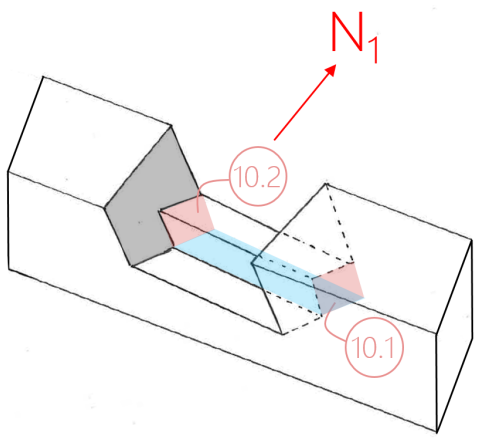

Figure 12.13: Plane 10 and relevant forces

When disregarding the blue-marked area, the following moment line can be obtained:

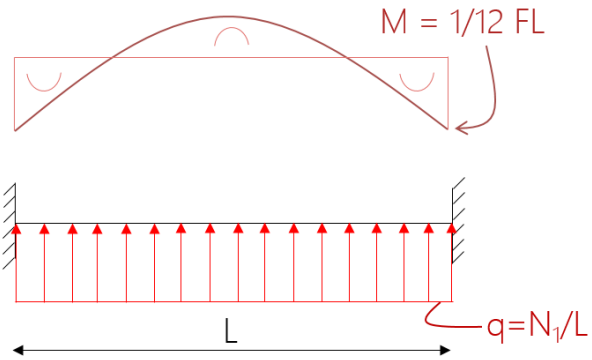

Figure 12.14: Assumed bending moment in plane 10 induced by the axial force N_1

It is assumed that the concerning part is rigidly supported at plane 10.1 and 10.2. This is a conservative assumption which results in a bending moment of M = 1/12FL.

The following two checks are calculated in order to verify Plane 10:

$$UC_{p10,M} = \begin{cases} \frac{\sigma_{M,N}}{f_{m,d}} & \text{if } N_1 > 0 \\ 0 & \text{if } N_1 \leq 0 \end{cases} \tag{12.15}$$

$$UC_{p10,V} = \begin{cases} \frac{\tau_y}{f_{v,d}} & \text{if } N_1 > 0 \\ 0 & \text{if } N_1 \leq 0 \end{cases} \tag{12.16}$$

Where $\tau_y = \frac{3}{2} \frac{\frac{1}{2} \cdot N_1}{A_{plane10}}$

12.2.5. Stress calculation Plane 11

Plane 11.1 and 11.2 are subjected to a normal force, shear forces (y- and z-direction) and bending moments (around the y- and z-axis) acting in beam 2, see Figure 12.15.

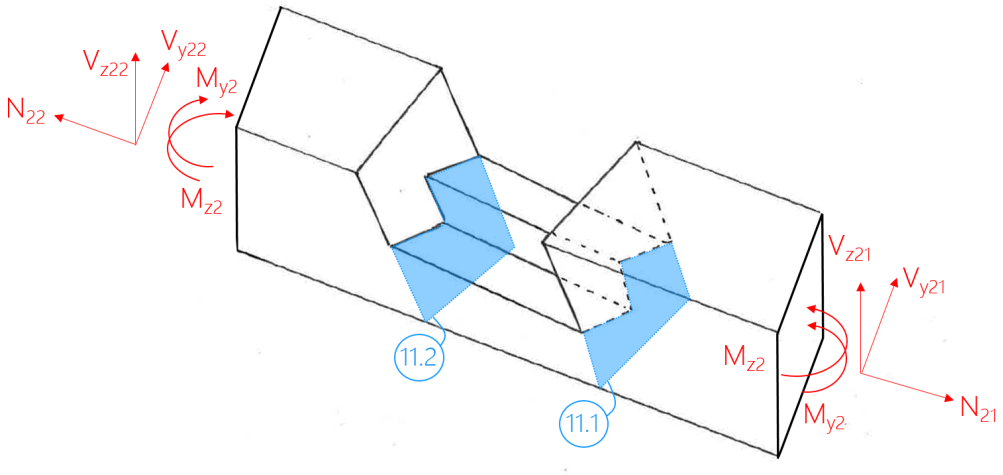

Figure 12.15: Plane 11 and relevant forces

A (conservative) assumption is made that the force acting on both planes (11.1 and 11.2) is the maximum force of the forces on both sides, so:

- $N_2 = [N_{21}, N_{22}]_{max}$
- $V_{y2} = [V_{y21}, V_{y22}]_{max}$
- $V_{z2} = [V_{z21}, V_{z22}]_{max}$

The following dimensions are relevant for the calculation of stresses in Plane 11:

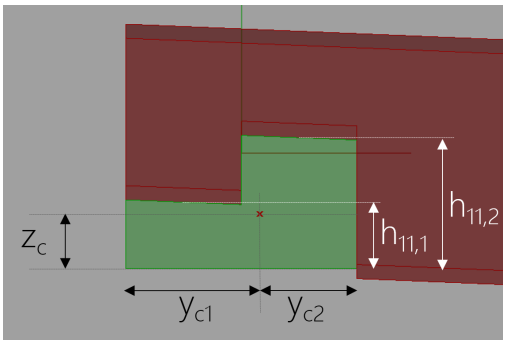

Figure 12.16: Relevant dimensions of Plane 11

Normal stresses

First of all, normal stresses are induced by the normal force in beam 2 (N_2):

$$\sigma_N = \frac{N_2}{A_{plane11}} \tag{12.17}$$

Additionally, normal stresses are induced by bending moments around the y- and z-axis. Two models for the calculation of the stresses due to bending and axial forces in beam 2 are considered, see Figure 12.17. Model 1 disregards the presence of beam 1. The bending moment is transferred through beam 2 only. Model 2 presumes contact between beam 1 and 2 and therefore a transfer of compressive stresses between the beams. Since the stiffness of beam 1 ($E_{m,90,mean} = 1330\,N/mm^2$) is significantly smaller than the stiffness of beam 2 ($E_{m,0,mean} = 20000\,N/mm^2$), the effect of the presence of beam 1 is small. For this reason and simplicity, model 1 is used.

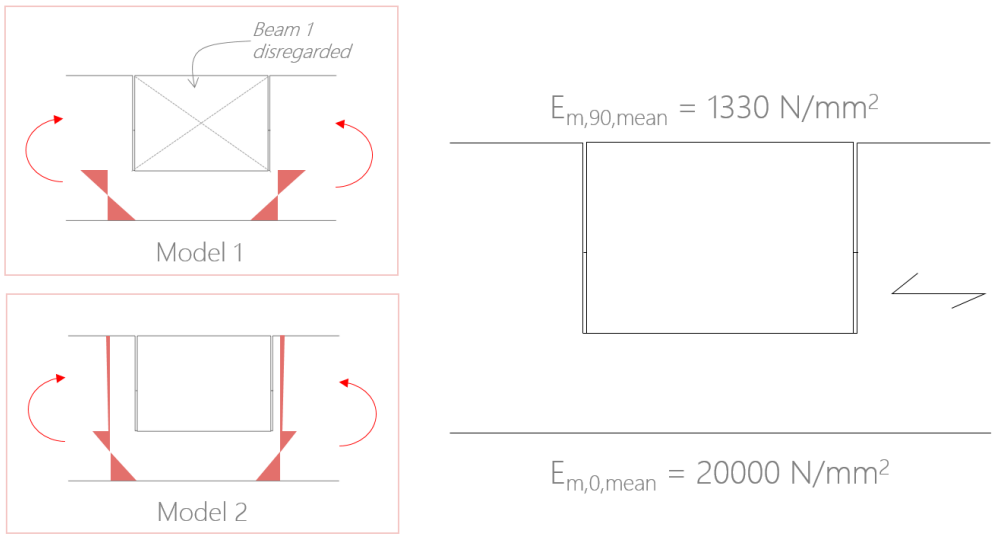

Figure 12.17: Models for stress distribution due to a bending moment M_{y2}

The bending stresses are calculated using the following equation:

$$\sigma_{My} = \frac{M_y \cdot z_{max}}{I_y} \tag{12.18}$$

$$\sigma_{Mz} = \frac{M_z \cdot y_{max}}{I_z} \tag{12.19}$$

Where:

I_y, I_z are defined using Grasshopper

z_{max} is z_c for calculation of tensile stresses and $(h_{11,2} - z_c)$ for calculation of compressive stresses

y_{max} is y_{c1} or y_{c2} depending on the direction of the bending moment and the calculation of tensile or compressive stresses

Shear stresses

The shear stress can be calculated using the following equation:

$$\tau_z = \frac{V_z \cdot S_{a,z}}{I_y \cdot t_y} \tag{12.20}$$

$$\tau_y = \frac{V_y \cdot S_{a,y}}{I_z \cdot t_z} \tag{12.21}$$

It is assumed that $z_c \leq h_{11,1}$. Therefore the static moment, $S_{a,z}$, for a shear force in Z-direction can be calculated accordingly:

$$S_{a,z} = \frac{1}{2} \cdot z_c^2 \cdot w_2 \tag{12.22}$$

Furthermore, the moment of inertia of plane `11` is calculated by Grasshopper. The width, t_y, at the location of maximum shear is the width of beam 2, w_2.

For the static moment $S_{a,y}$ it is assumed that in all cases $y_{c2} \leq \frac{1}{2} w_2$. With this assumption, the static moment can be calculated using the following equation:

$$S_{a,z} = \frac{1}{2} \cdot z_c^2 \cdot w_2 \tag{12.23}$$

The width, t_z, at maximum shear stress is accordingly assumed to be $h_{11,2}$.

Checks

In order to verify beam 2 at Plane `11`, the following three unity checks are calculated:

$$UC_{p11,V} = \frac{\tau_y + \tau_z}{f_{v,d}} \tag{12.24}$$

$$UC_{p11,Ax,c} = -\frac{\sigma_N}{f_{c,0,d}} - \frac{\sigma_{Mz,c}}{f_{m,d}} - \frac{\sigma_{My,c}}{f_{m,d}} \tag{12.25}$$

$$UC_{p11,Ax,t} = \frac{\sigma_N}{f_{c,0,d}} + \frac{\sigma_{Mz,t}}{f_{m,d}} + \frac{\sigma_{My,t}}{f_{m,d}} \tag{12.26}$$

It is hereby assumed that k_m is 1.0 instead of 0.7. This is a conservative assumption.

12.3 Connection in global model

For the first design of the structure, a pure reciprocal structural system is assumed. This means that the beams can only transfer a downward shear force in the local z-direction (direction of the gravitational force).

The geometrical location of the centre-lines of the beams (shown as red lines in Figure 12.18) does not always match the real position of the beam relative to the connecting beam. This is a result of the required eccentricity in the connection in order to obtain a anticlastic (surface curved in opposite ways) shape. The end of the beam is in reality always on top of another beam. However, Figure 12.18 shows two examples of beams where the end of the centre-line of the beam is situated underneath the connecting beam. In order to take this into account, distinction must be made between the following two cases:

- Geometrical location and position of the beam relative to the connecting beam **match** → Transfer **compression** force only
- Geometrical location and position of the beam relative to the connecting beam do **not match** → Transfer **tension** force only

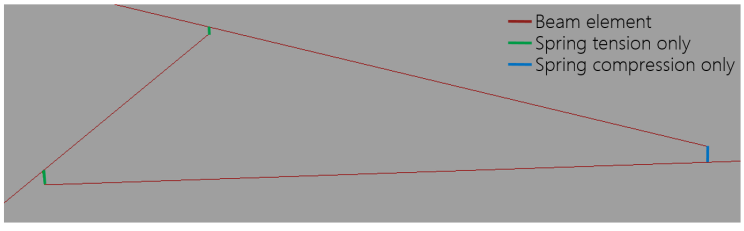

Figure 12.18: Spring elements for modelling of the eccentric, nonlinear connections

The required types of spring elements for two bridge designs are shown in Figure 12.19 and 12.20.

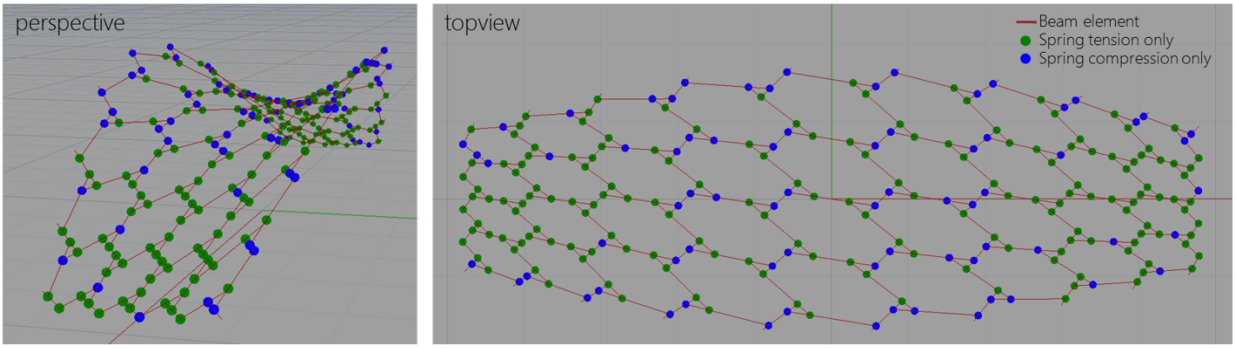

Figure 12.19: Spring elements for modelling of the eccentric, nonlinear connections (anticlastic surface)

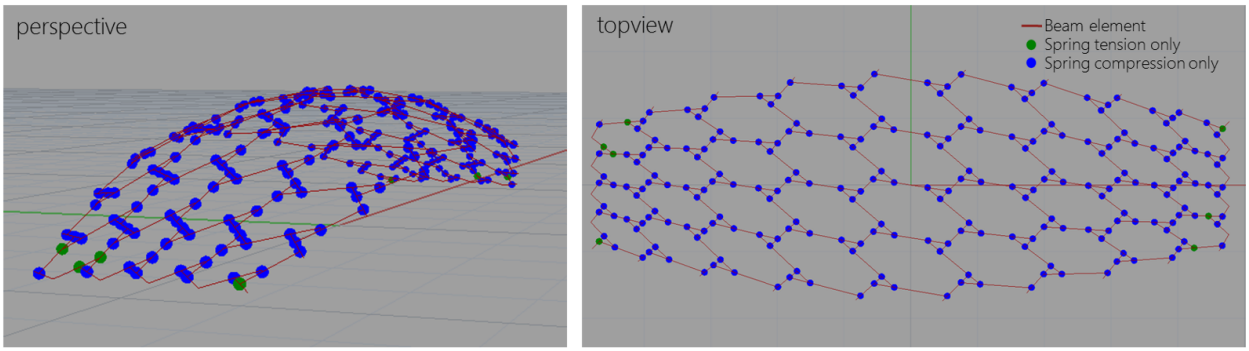

Figure 12.20: Spring elements for modelling of the eccentric, nonlinear connections (synclastic surface)

In order to implement this non-linear behaviour, a non-nonlinear iterative calculation should be applied in which all spring elements which transfer loads they are not supposed to are assigned a 0 stiffness.

12.4 Conclusion

A simple way to verify if the connection fulfils all Eurocode requirements regarding strength is by calculating the stresses in all critical planes.

In case of a simple lap-joint, eleven critical planes can be defined for which normal, bending and/or shear stresses should be calculated:

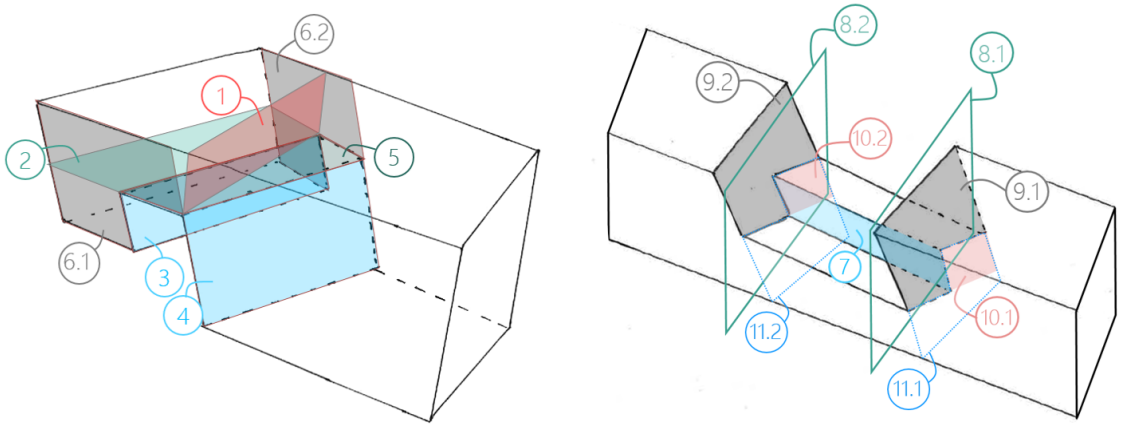

Figure 12.21: Relevant planes for beam 1 (left) and beam 2 (right)

In accordance with Chapter 7, the following unity checks are calculated:

- Normal stress check (tension and compression) (UC_N)
- Shear stress check (combined in y- and z-direction) (UC_V)

- Combined bending and normal stress check (tension and compression) (UC_{Ax})

This leads to following thirteen unity checks for all relevant planes in the simple lap-joint:

Table 12.1: Calculated unity checks in order to verify beam 1 and 2

Beam	Plane	Check	Equation
1	1	$UC_{p1,Ax}$	12.5
		$UC_{p1,V}$	12.6
	2	$UC_{p2,M}$	12.7
		$UC_{p2,V}$	12.8
	3	$UC_{p3,N}$	12.9
	4	$UC_{p4,N}$	12.10
	5	$UC_{p5,N}$	12.11
	6	$UC_{p6,N}$	12.12
2	7	$UC_{p7,N}$	12.13
	10	$UC_{p10,M}$	12.15
	10	$UC_{p10,V}$	12.16
	11	$UC_{p11,V}$	12.24
		$UC_{p11,Ax,c}$	12.25
		$UC_{p11,Ax,t}$	12.26

For the shear capacity of *Plane 1*, the method described in NEN-EN 1995-1-1, Section 6.5.2 for the calculation of notches at supports is applied.

V

Design Integration

13

Complexity and approach

Now that a preliminary design is made for the global design of the bridge and a parametric definition of the connections, the next step is to integrate both designs.

13.1 Complexity of the issue

The challenge is to define the seven parameters defining the dimensions of the connection based on the 4 geometric parameters following from the global model and the internal forces (7 per load case), see Figure 13.1.

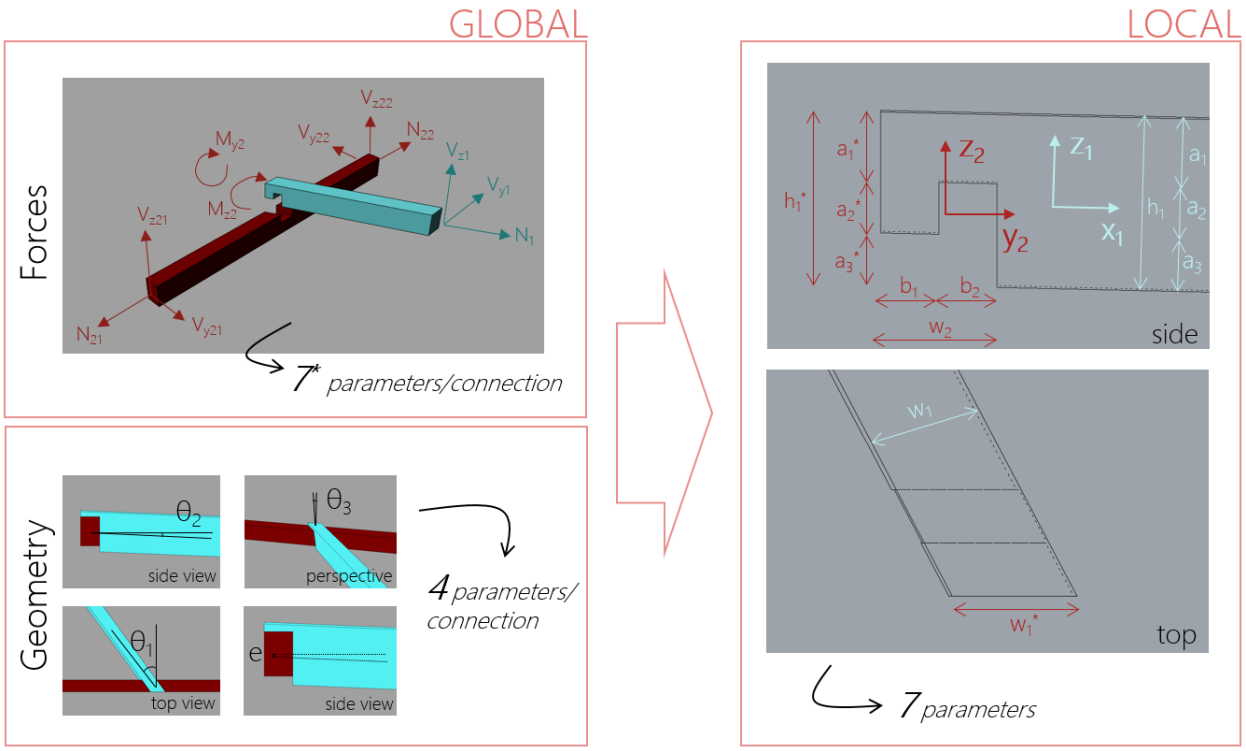

Figure 13.1: Challenge to connect parameters from the global connection to the connection model

The goal is to find the design with the best performance for each unique connection in the structure. The performance of the connection is defined by two factors:

- The least amount of material usage, defined as $((h_1 * w_1) + (h_2 * w_2))_{min}$ (Dominating)
- The design with the best structural performance, defined as the design with the smallest maximum unity check $(UC_{max,i})_{min}$, with $i = 1..13$

Logically, in all cases $(UC_{max,i})_{min}$ should be smaller than 1.0.

This is very complex for four main reasons:

- The **large number of parameters**. This involves both the parameters influencing the optimal design (loads and geometric parameters), as well as the large number of parameters to determine (seven parameters defining the dimensions)

- **Complex relation** between the global- and local parameters. The parameters are linked through the unity checks. A change in one of the dimensional parameters of the connection has an affect on multiple unity checks which are related to multiple forces. This makes it highly complex to directly relate a certain force to a certain dimension. This means that changing the dimension to improve one specific unity check can have a negative influence on other unity checks.

- The **large number of unique connections** in one bridge structure, see Figure 13.2

- The **statically indeterminacy** of the structure makes that the force flow in the structure is influenced by the cross-sectional dimensions of the individual members. This means that when one or more of the cross-section sizes is changed, the forces in the beams have to be re-determined. So the (external) dimensions of all beams are al linked

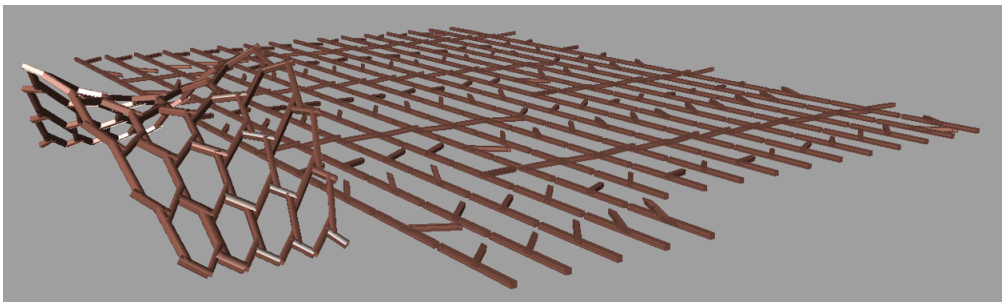

Figure 13.2: Large number of unique connections in one bridge

13.2 Optimisation approach

Since both the seven dimensional parameters (h_1, w_1, h_2, ..., b_1-ratio) and the internal forces ($N_1, V_{y1}, V_{z1}, ..., M_{2z}$) are influencing multiple unity checks, it is hard to predict what favourable dimensions would be. A way to find out is by calculating the unity checks as well as the performance for a great variation of possible dimensional parameters and from this choose the best connection design. This approach is described in Figure 13.3.

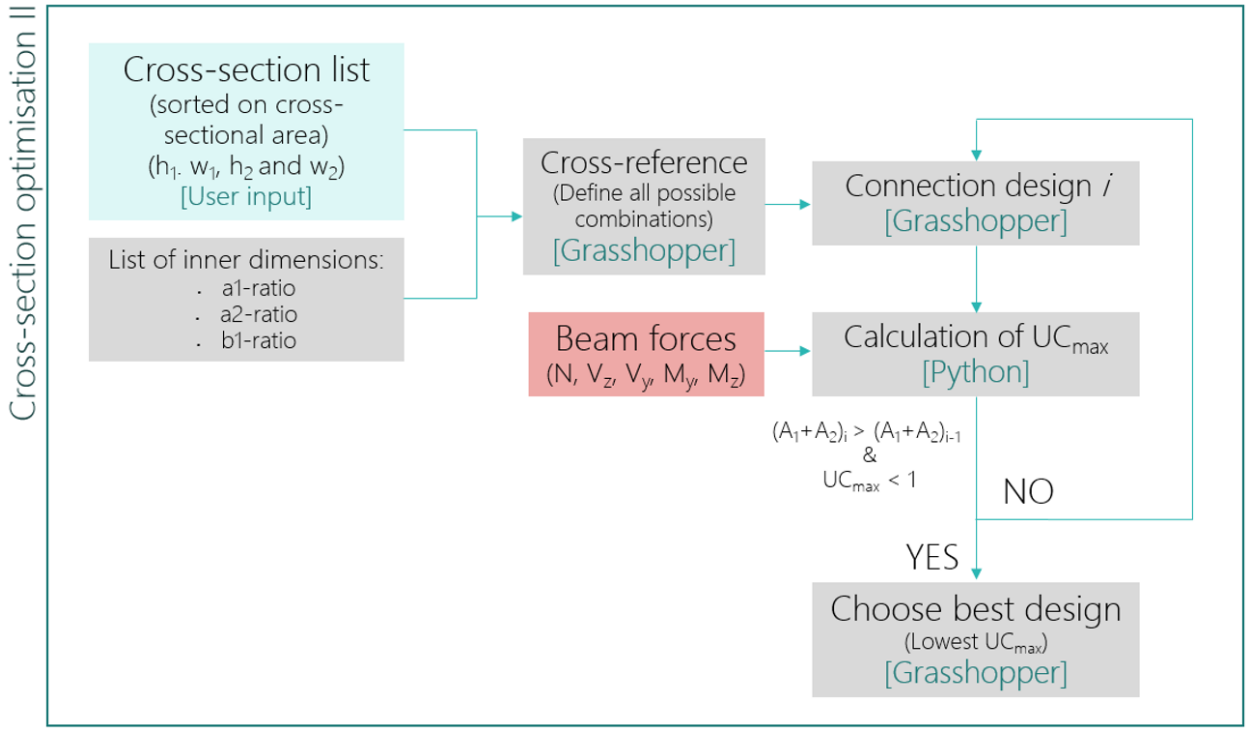

Figure 13.3: Cross-section optimisation II

In order to prevent the evaluation of not relevant designs, the optimisation loop will be aborted once the following two conditions are met:

- The cross-section in the current step is larger than during the cross-section in the previous step ($(A_1 + A_2)_i < (A_1 + A_2)_{i+1}$)
- In one of the previous steps a solution is found for which the maximum unity check is smaller than 1.0 (in other words, a solution that fulfils all EC checks)

Discretization

In order to define a finite number of possible designs, the dimensional parameters are discretized. For the external dimensions only standard section-sizes are used (starting from 100mm (minimum feasible size for CNC-milling), in steps of 50mm). Due to the limited space at the location of a connection, the maximum width of the beam is defined to be 150mm, see Figure 13.4.

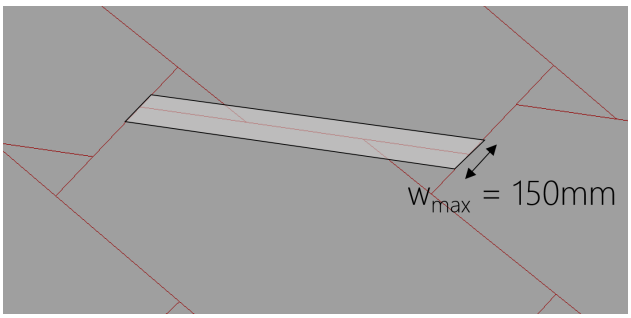

Figure 13.4: Section width restriction

This gives the following possible section sizes:

- h_1 & h_2 = 100, 150, 200, 250, 300mm
- w_1 & w_2 = 100, 150mm

For the ratios defining the proportions within the connection, the discretization comes less natural since in principle a CNC-milling machine or robot could produce every ratio (infinite possible combinations). Therefore, a balance should be found between the performance of the connection found and the time needed for optimisation. Unfortunately, this analysis is not been carried out because of time constraints so the following discretization is applied:

Table 13.1: Discretization of the internal dimensional parameters

Parameter	Minimum value	Maximum value	Step size
a_1-ratio	0.2	0.7	0.1
a_1-ratio	0.2	0.7	0.1
b-ratio	0.2	0.8	0.1

Static indeterminacy

It should be kept in mind that due to static indeterminacy the internal forces in the structure are dependent on the external dimensions of the beam elements (h_1, w_1, h_2 and w_2). Since the optimisation process as described in Figure 13.3 is time-consuming, it is unfavourable to apply a number of iteration steps in order to obtain the actual force distribution in the structure as described in Chapter 9 in Figure 9.2. Therefore, in order to get a reasonable approximation of the force distribution, the force output of *Cross-section optimisation I* (Figure 9.2) is used as input for *Cross-section optimisation II* as marked in red in Figure 13.3. A reduced cross-section size ($\frac{1}{2}h$) is used in this optimisation to consider the change in geometry at the connection.

13.3 Conclusion

The goal is to find the optimal dimensions for each connection, based on two factors:

- The least amount of material usage
- The smallest maximum unity check

Due to the large number of parameters, complex relation between the parameters, large number of connections and the statically indeterminacy of the structure, this is a complex task. A way to deal with this is by checking a large set of possible designs and from this set select the best one. Nevertheless, this process is really time consuming. One way to reduce computation time is to use a simple cross-section optimisation to find the force distribution in the structure. In this way it is omitted that multiple iterations are required to find the force distribution in the statically indeterminate structure. In the next chapter will be evaluated if machine learning could be useful to make a prediction for favourable dimensions.

14

Machine Learning

In this chapter a machine learning will be evaluated as a tool to make a prediction for favourable connection dimensions. First a short introduction on Machine Learning and the used Grasshopper plugin (*Design Space Exploration*) is given. After that research is done on the selection of suitable training input data. Eventually it is verified whether Machine Learning is indeed a suitable method to use or not.

14.1 Introduction to Machine Learning

Driven by the enormous amount of data that is created nowadays, methods are developed for automated data analysis. One of the trending methods is called *Machine Learning*. Machine learning can be defined as a method that can automatically find patterns in a data set and subsequently use these patterns to predict new data. [39] This is shown diagrammatically in Figure 14.1

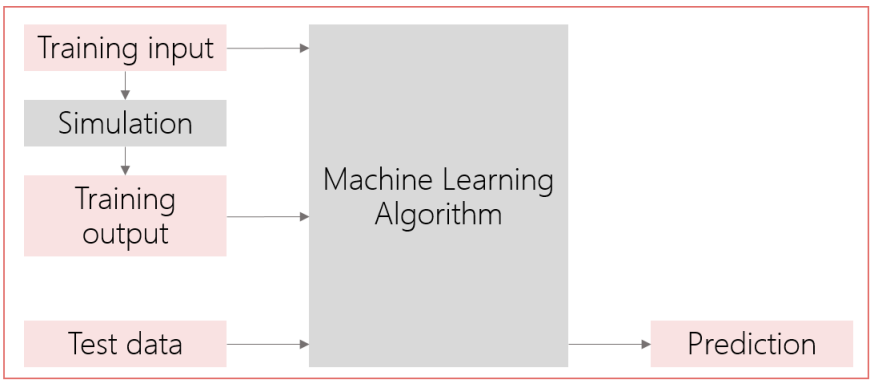

Figure 14.1: Machine learning

14.2 Design Space Exploration (DSE)

Design Space Exploration is a Grasshopper tool developed by the Digital Structures department of MIT. The library provides a set of tools that can be used to explore design spaces and to apply multi-objective optimisation for conceptual design. The tool that is used is called *Tilde (~)*, see Figure 14.2. Based on a design map and its objectives, the algorithm is trained after clicking the *Build*-bottom. After this, instant feedback will be given on the performance of the currently provided set of variables. The tool tries to fit five different *Neural Network* and five different *Random Forest* models to the data. For each model the error is computed, after which the best model is chosen.

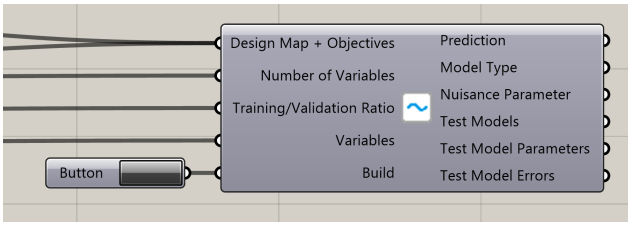

Figure 14.2: Grasshopper component *Tilde* (part from the DSE library)

For validation, the tool requires a training/validation ratio as input. This ratio splits the provided data into two parts. In case a ratio of 0.5 is given, half of the data will be used to train the model. The other half of the data will be used as variables. After training the model, a prediction will be made for this second half, which can be plotted against the real known objective. In this way can be verified if the prediction has sufficient accuracy.

14.2.1. Random Forest algorithm

Random Forest is a supervised learning algorithm. The algorithm first samples fractions of data. On each piece a decision tree is build. Subsequently all predictors are merged. Figure 14.3 shows what a a random forest with two trees would look like. [21] [14]

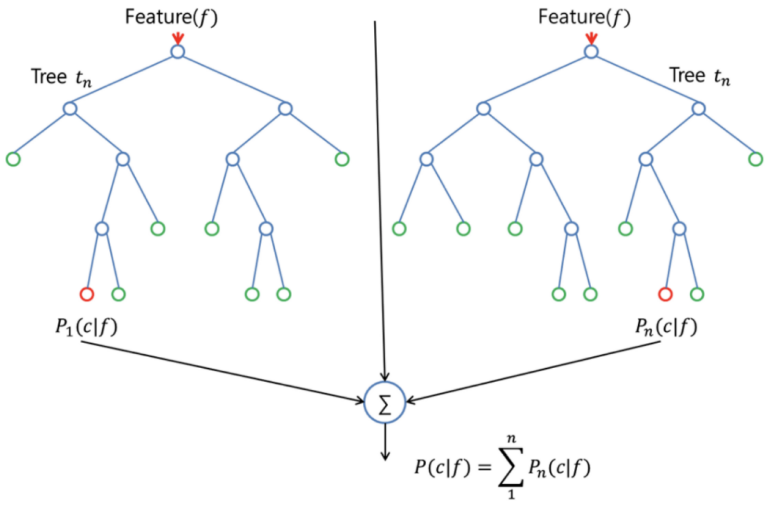

Figure 14.3: Visualisation of a random forest with two trees [21]

Randomness is added by instead of searching for the most important feature while splitting a node, choosing the best feature from a random set of features. This makes the model more stable and the prediction more accurate.

The popularity of the algorithm is due to:

- Simple to use
- High accuracy
- Ability to deal with small sample sizes and high-dimensional feature spaces

14.3 Definition of training input

The goal is to predict the 7 parameters defining the dimensions of a connection based on a set of variables (training input). The connection design is optimised for minimum material usage and best structural performance (smallest unity check). The parameters influencing the unity checks are:

- The four geometric parameters defining the relative positioning of connecting beams (θ_1, θ_2, θ_3 and e)
- The forces the connection is subjected to ($N_1, V_{y1}, V_{z1}, \ldots, Vz22, M_{y2}, M_{z2}$)

The first step is to define the data that are relevant for the prediction of the dimensions. The following decisions have to be made:

- Is it better to use a 'virtual' set of training data or a set of data connected to a *real* connection in the structure?
- Should the geometric parameters be used as training input?
- What forces should be used as training input?
- What load cases should be used to define the training input? Could just one (governing) load case be used or is it better to use the envelope?
- What is the minimum size of the data set to get a sufficiently accurate result?

14.3.1. 'Virtual' vs 'Real' training-set

First of all, an analysis is done to define if it is better to create a virtual training-set or use the data connected to a real occurring connection in a bridge design.

One of the options is to create a 'virtual' training set by defining a range for each parameter ($p_{min} \leq p \leq p_{max}$) and do a discretisation. The set of parameters can subsequently be combined by applying a holistic cross reference: defining all possible combinations of parameters. Nevertheless, this method won't comprise any possible correlations between parameters and therefore includes training sets that are not relevant. In order to verify if this is the case, a study on the correlation between parameters has been done. In order to be able to visualise, three parameters have been plotted in three-dimensional space, see Figure 14.4

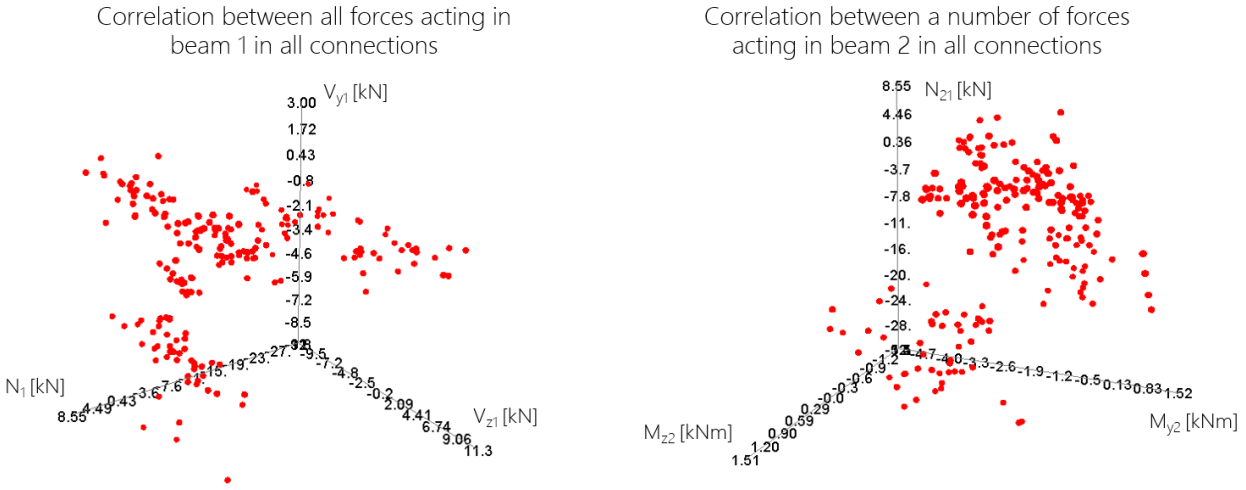

Figure 14.4: Plot of the correlation between forces. Each red dot represents a connection in the bridge structure

It shows that there is indeed a correlation between forces. This means that applying holistic cross reference to the discretised sets of parameters will generate irrelevant combinations of parameters. An easy way to prevent this is by using 'real' occurring sets of parameters that are connected to connections in the structure as a training set. The next question is which connections should be used.

14.3.2. Selection of connections to use to compose a training-set

Three different methods are evaluated to select a limited number of connections in the bridge structure to use as a training set. The first method is to select random connections. When a sufficiently big training-set is used, this method will presumeably comprise the correlation between the different parameters pretty well. Nevertheless, there is a risk that part of the design space won't be covered. A way to make sure that all parts are taken into consideration is by using grouping algorithms. These are algorithms that can group points in a multi-dimensional space based on distance. To enable visualisation, again only three variables (the three forces in beam 1 for each connection in a bridge structure) are plotted in three-dimensional space, see Figure 14.5. For each force, the maximum force occurring in all load cases is used. The reason for this is described in Section 14.3.3.

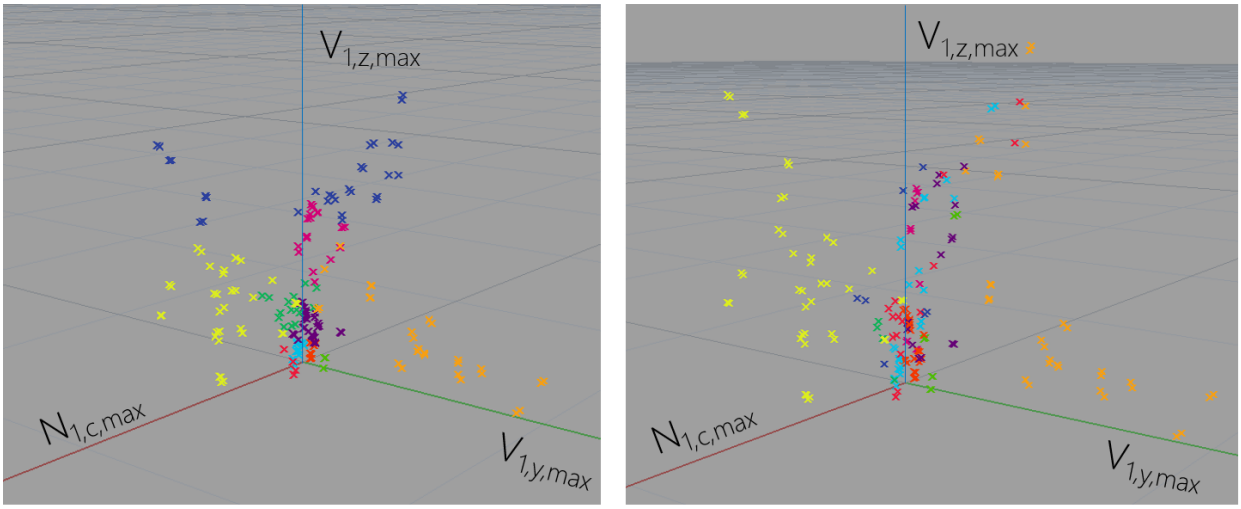

Figure 14.5: Grouping of connections into 10 groups. The figure on the left shows results when the forces are first unitized. For the figure on the left, the actual values of the loads have been used for the grouping process

For the grouping process, the *'k-mean clustering'*-component from the *Owl* plugin for Grasshopper is used. K-means clustering is a method that is used to partition a number of data points into *n* clusters where each point belongs to the cluster with the nearest mean.

For this example, a bridge design with 182 connections is used. The 182 corresponding data points are grouped into 10 groups, each displayed with a different colour in Figure 14.5. To create the grouping as shown on the left, the data points are unitized before applying the grouping algorithm. In other words, all data points are re-mapped from the source domain (e.g. $(N_{1,c,max})_{domain}$ = 0.03 to 15.89kN) to a target domain from 0 to 1. This prevents that differences between parameters with a large domain have a bigger influence on the grouping than parameters with a small domain. In case it is favourable to give certain parameters a bigger importance than others, this can be implemented by applying a weight to each parameter. Since there are large differences between the ranges of the source domains, especially between forces and bending moments, it is preferable to use the unitized values instead of the original values.

Now that the connections are grouped, it should be decided how many and which connections per group should be picked. Two methods are considered:

- Select a certain percentage of each group randomly
- Select a number of connections based on the spread of the group (the larger the spread, the more connections are selected)

The first method is the easiest. The number of connections that should be selected from each group can be calculated as follows:

$$n_i = \frac{N_i}{\sum_{i=0}^{m} N_i} * N, \text{with} i = 0..n_{groups} \tag{14.1}$$

Where:

n_i	is the number of connections selected from group *i*
N_i	is the total number of connections in group *i*
N	is the total amount of connections that should be selected
n_{groups}	is the number of groups

Figure 14.6 shows the result of the selection of connections when 100 out of 182 connections are selected based on the number of connections in one group ($n_{groups} = 10$). Each colour represents a different group.

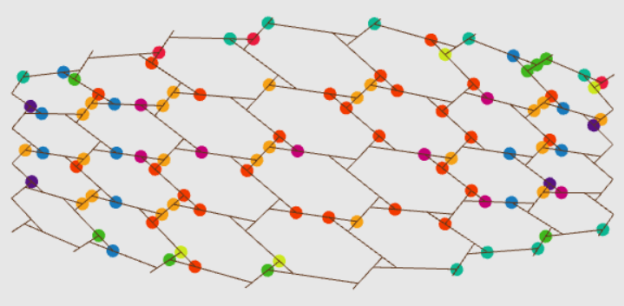

Figure 14.6: Selected connections based on the number of connections in one group. The colours represent the different groups

The second method is more complex. To calculate the distance between points, the *'Nearest Neighbour Number'*-tool of the plugin for Grasshopper called *Dodo* is used. This tool finds *n* nearest neighbours to a coordinate in multi-dimensional space. For every coordinate the distance to its nearest neighbour is calculated. Thereafter, the arithmetic mean of all distances within a group is defined. Finally, the number of connections per group that is selected is defined as follows:

$$n_i = \frac{mean_i}{\sum_{i=0}^{m} mean_i} * N, \text{ with } i = 0..n_{groups} \tag{14.2}$$

Where:

n_i	is the number of connections selected from group i
$mean_i$	is the arithmetic mean of the distances between nearest neighbours in group i
N	is the total amount of connections that should be selected
n_{groups}	is the number of groups

Figure 14.7 shows the result of the selection of connections when 100 out of 182 connections are selected based on the spread within a group ($n_{groups} = 10$).

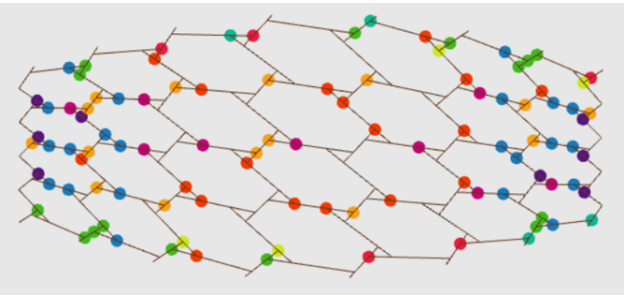

Figure 14.7: Selected connections based on the spread within a group. The colours represent the different groups

Since the same input is used for the grouping in Figure 14.6 and 14.7, the colours are analogous. It shows that connections at corresponding locations in the structure are assigned to the same group. Figure 14.8 shows the selected connections for all three selection methods.

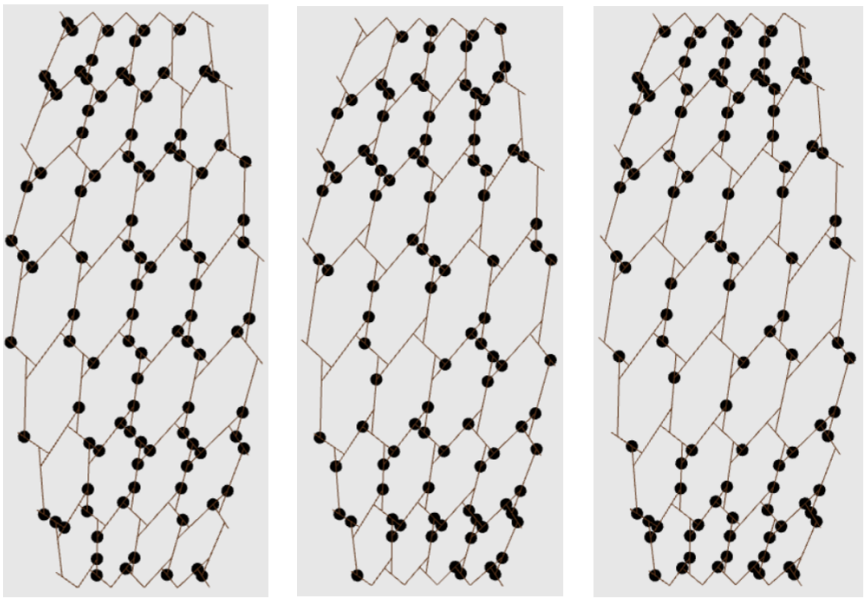

Figure 14.8: Selected connections when applying the 3 different methods

A way to validate the prediction of the machine learning process is by plotting the predicted values against the simulated values. Ideally, the results would lay on the diagonal of the graph where *predicted value = simulated value*. As mentioned in Section 14.2, the DSE tool called *Tilde* requires the input of a *Training/Validation Ratio*. This ratio defines the size of the part of the design space that will be used for the training of the algorithm and which part will be predicted. In this case a *Training/Validation Ratio* of 0.5 is used. The following forces are used as training input: $N_{1,c}$, $N_{1,t}$, V_{y1}, V_{z1}, M_{y2}, M_{z2}. In Section 14.3.3, different combinations of forces as training set are analysed. The goal is to choose the most effective combination.

Figure 14.9 shows graphs of the simulated vs. the predicted value for the three different selection methods. The black dots correspond to the connections that are used as training input and are therefore close to the green diagonal. The blue dots correspond to the connections that are predicted by the machine-learning algorithm without being part of the training input. For all different methods, the mean error of all connections (e_{mean}), the error of the connections that are used as training input (black dots) ($e_{mean,sim}$) and the error of the connections that are predicted (blue dots) ($e_{mean,pred}$) are calculated.

Grouped & selected by spread

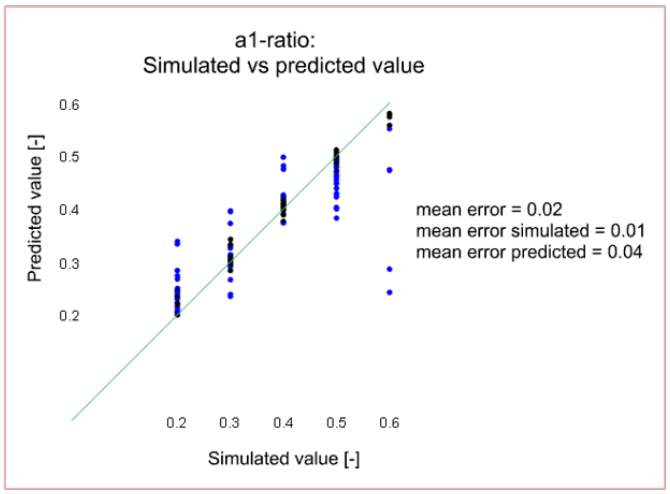

Grouped & selected by percentage

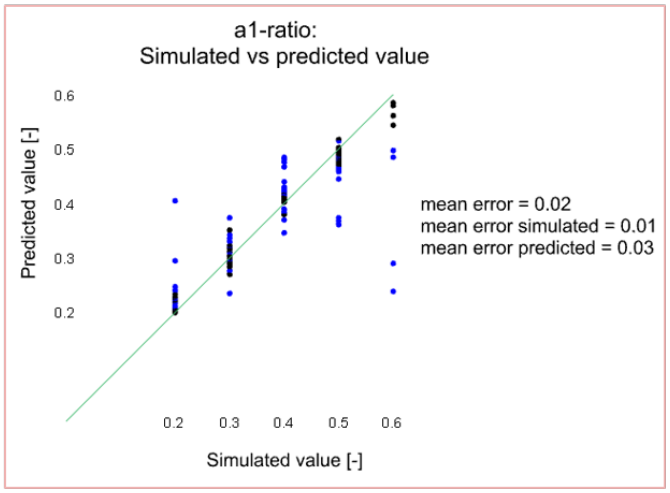

Random connections

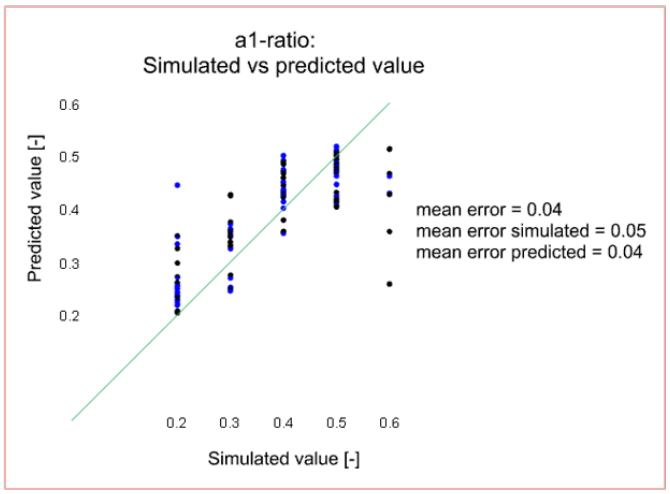

Figure 14.9: Simulated vs. predicted value for the a_1-ratio. Three selection methods are used: grouped & selected by spread, grouped & selected by percentage and random selection of connections

From Figure 14.9 it can be concluded that, in contrast to the expectations, the selection of connections based on the spread within a group does not give the best prediction. Possibly, the reason for this is although the whole design space is comprised best, the focus is too much on less relevant connections. It could be beneficial to include more connections in the training input that are *average* in order to make a better prediction for the majority of the connections than to focus on the exceptional connections.

The second graph shows the results in case per group a certain percentage of connections is selected. In this way it is taken into account that certain groups have a greater importance than others, while maintaining the certainty that the whole design space is captured. This is reflected in the results of the errors. The results are better than the results of the training set selected by spread.

The last graphs shows the results in case a random selection of connections is used as training set. The results are worse than when the connections are selected using a grouping algorithm.

14.3.3. Selection of relevant parameters

This section describes the selection of the right parameters as training input in order to make a good prediction. First, it is considered how to deal with all load cases. Thereafter, a comparison is made of the predictions of six training sets containing different combinations of forces. Finally one training set is selected.

How to deal with load cases

As mentioned before, the connections are optimised for a minimum unity check. 13 unity checks are calculated for all twelve different load cases, combining dead-load, wind-load and crowd-load. The highest unity check of these 13 x 12 unity checks is the governing unity check. The question is which loads to use as training input: all loads of all load cases, a part of the load cases or the envelope of all load cases. Since the maximum unity check is usually caused by the maximum load, it would be evident to use the envelope of all load cases. Nevertheless, some of the unity checks are combined checks (e.g. $\tau = \tau_y + \tau_z$). When using the envelope of the forces for all load cases, it is possible that a prediction is made with forces that are usually not combined in one check. Nevertheless, it is out of scope of this project to analyse other methods.

Limit the number of forces used for the training-set

The second step is to select a limited number of internal forces to use as training input. These are logically the parameters that have the most influence on the seven dimensions that should be determined. The selection of a certain design is based on the set of thirteen unity checks that are calculated for each connection. First an analysis is done to verify which unity checks are usually critical. This could give insight in the most relevant forces and/or geometric dimensions.

For a few connections all possible designs are verified. Every time a unity check is more than 1.0 is counted. In total, the unity check is 88360 times not fulfilled. Figure 14.10 shows the frequency that each individual unity check is not fulfilled, expressed in the percentage of the total amount (88360 times).

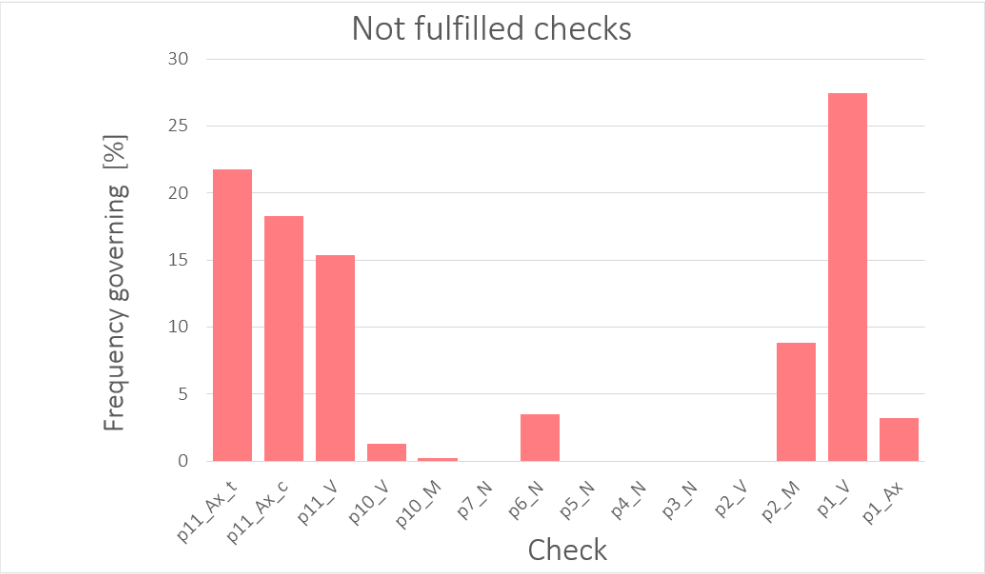

Figure 14.10: Number of times that a certain Unity Check is not fulfilled

The checks that are frequently not fulfilled are shown in Figure 18.2. The following four checks and corresponding forces are most important:

1. Failure of beam one at the transition between the neck and full beam height due to shear loading → V_{y1} & V_{z1}

2. Bending failure of beam 2 at the location of the connection → N_{21}, N_{22}, M_{y2} & M_{z2}

3. Shear failure of beam 2 at the location of the connection → V_{y21}, V_{z21}, V_{y22} & V_{z22}

4. Bending failure of the hook of of beam 1 → $N_{1,tension}$

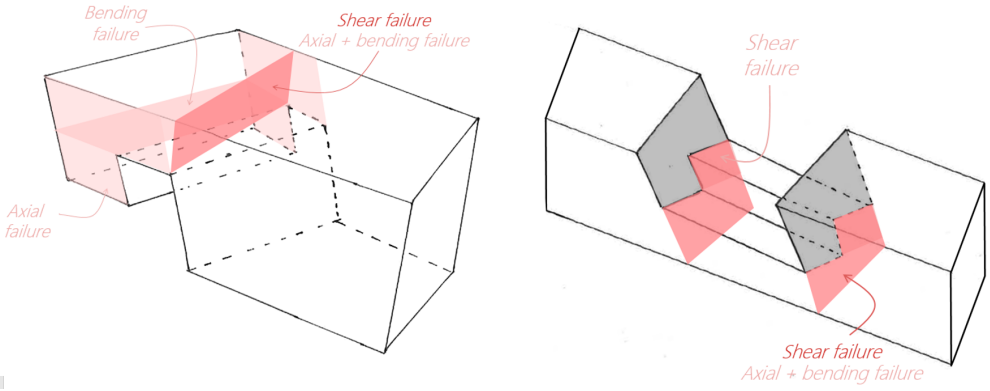

Figure 14.11: Planes that are commonly not fulfilling the requirements

These are basically all forces. Nevertheless, there are forces that are more important than others. For example $V_y > V_z$ and $M_z > M_y$ (in almost all cases). Based on the list above, six combinations of forces are tested as training input, see Table 14.3. The training/validation graphs can be found in Appendix H, Figure H.1, H.2 and H.3.

Table 14.1: Errors of the prediction of the a_1-ratio when using different parameters as training input

	Training input parameters	e_{mean}[%]	$e_{mean,sim}$[%]	$e_{mean,pred}$[%]
1	$V_{y1}, V_{z1}, [N_{21,c}, N_{22,c}]_{max}, M_{y2}, M_{z2}$	0.02	0.01	0.04
2	$N_{1,c}, V_{y1}, V_{z1}, [N_{21,c}, N_{22,c}]_{max}, M_{y2}, M_{z2}$	0.02	0.01	0.03
3	$N_{1,c}, V_{y1}, V_{z1}, M_{y2}, M_{z2}$	0.02	0.00	0.03
4	$N_{1,c}, V_{y1}, V_{z1}, [V_{y,21}, V_{y,22}]_{max}, [V_{z,21}, V_{z,22}]_{max}, M_{y2}, M_{z2}$	0.02	0.01	0.03
5	$N_{1,c}, V_{y1}, V_{z1}, [V_{y,21}, V_{y,22}]_{max}, M_{y2}, M_{z2}$	0.02	0.00	0.03
6	$V_{y1}, V_{z1}, [V_{y,21}, V_{y,22}]_{max}, M_{y2}, M_{z2}$	0.02	0.01	0.04

Table 14.2: Errors of the prediction of the a_2-ratio when using different parameters as training input

	Training input parameters	e_{mean}[%]	$e_{mean,sim}$[%]	$e_{mean,pred}$[%]
1	$V_{y1}, V_{z1}, [N_{21,c}, N_{22,c}]_{max}, M_{y2}, M_{z2}$	0.03	0.02	0.05
2	$N_{1,c}, V_{y1}, V_{z1}, [N_{21,c}, N_{22,c}]_{max}, M_{y2}, M_{z2}$	0.03	0.01	0.05
3	$N_{1,c}, V_{y1}, V_{z1}, M_{y2}, M_{z2}$	0.03	0.01	0.05
4	$N_{1,c}, V_{y1}, V_{z1}, [V_{y,21}, V_{y,22}]_{max}, [V_{z,21}, V_{z,22}]_{max}, M_{y2}, M_{z2}$	0.02	0.00	0.05
5	$N_{1,c}, V_{y1}, V_{z1}, [V_{y,21}, V_{y,22}]_{max}, M_{y2}, M_{z2}$	0.03	0.02	0.05
6	$V_{y1}, V_{z1}, [V_{y,21}, V_{y,22}]_{max}, M_{y2}, M_{z2}$	0.03	0.02	0.05

Table 14.3: Errors of the prediction of the b-ratio when using different parameters as training input

Training input parameters		e_{mean}[%]	$e_{mean,sim}$[%]	$e_{mean,pred}$[%]
1	$V_{y1}, V_{z1}, [N_{21,c}, N_{22,c}]_{max}, M_{y2}, M_{z2}$	0.06	0.02	0.09
2	$N_{1,c}, V_{y1}, V_{z1}, [N_{21,c}, N_{22,c}]_{max}, M_{y2}, M_{z2}$	0.04	0.00	0.07
3	$N_{1,c}, V_{y1}, V_{z1}, M_{y2}, M_{z2}$	0.04	0.00	0.08
4	$N_{1,c}, V_{y1}, V_{z1}, [V_{y,21}, V_{y,22}]_{max}, [V_{z,21}, V_{z,22}]_{max}, M_{y2}, M_{z2}$	0.04	0.00	0.08
5	$N_{1,c}, V_{y1}, V_{z1}, [V_{y,21}, V_{y,22}]_{max}, M_{y2}, M_{z2}$	0.04	0.00	0.08
6	$V_{y1}, V_{z1}, [V_{y,21}, V_{y,22}]_{max}, M_{y2}, M_{z2}$	0.06	0.02	0.09

The error that is most relevant is the error of the predicted values. Table 14.4 shows the predicted errors for the different training input sets for the three dimensional parameters: a_1-ratio, a_2-ratio and b-ratio.

Table 14.4: The mean error of the predicted value of the a_1-ratio, $_2$-ratio and b-ratio when using different parameters as training input

Training input parameters		a_1**-ratio**	a_2**-ratio**	b**-ratio**
1	$V_{y1}, V_{z1}, [N_{21,c}, N_{22,c}]_{max}, M_{y2}, M_{z2}$	0.04	0.05	0.09
2	$N_{1,c}, V_{y1}, V_{z1}, [N_{21,c}, N_{22,c}]_{max}, M_{y2}, M_{z2}$	0.03	0.05	0.07
3	$N_{1,c}, V_{y1}, V_{z1}, M_{y2}, M_{z2}$	0.03	0.05	0.08
4	$N_{1,c}, V_{y1}, V_{z1}, [V_{y,21}, V_{y,22}]_{max}, [V_{z,21}, V_{z,22}]_{max}, M_{y2}, M_{z2}$	0.03	0.05	0.08
5	$N_{1,c}, V_{y1}, V_{z1}, [V_{y,21}, V_{y,22}]_{max}, M_{y2}, M_{z2}$	0.03	0.05	0.08
6	$V_{y1}, V_{z1}, [V_{y,21}, V_{y,22}]_{max}, M_{y2}, M_{z2}$	0.04	0.05	0.09

It can be concluded that the results for all training input sets are really similar. Training input set 2 has the best overall performance and is therefore selected.

14.4 Conclusion

From this chapter it can be concluded that, due to the high correlation between forces occurring in the connections, it is best to use the loads in existing connections as training input, rather than using a virtual training set.

The group of connections that is then used as a training input can best be selected by using a grouping algorithm. This algorithm accumulates connections with similar loads. From each group a number of connections should be selected according to the size of the group.

The connections are optimised for structural performance (lowest maximum unity check). Usually, the maximum unity checks are related to the maximum loads. Therefore way to deal with the large number of load cases is by using the envelope.

Next, the relevant loads should be selected. The performance of six different training input sets is compared. The performances were really similar. The best overall results was obtained when the following set of loads was used as training input: $N_{1,c}, V_{y1}, V_{z1}, [N_{21,c}, N_{22,c}]_{max}, M_{y2}, M_{z2}$.

15

Verification of performance

Now that all dimensional parameters of the connections can be predicted, the performance of the prediction model should be verified. This will be done by implementing all predicted dimensions and calculating the maximum unity checks for the resulting connection designs.

The results will be compared to a design in which all connections have the same dimensions.

15.1 Predicted dimensions compared to average dimensions

15.1.1. Performance using the predicted dimensions using machine learning

First, the optimal dimensional parameters were determined for half of the connections (selected by grouping as described in Section 14.3.2) by applying Cross section optimisation II, see Figure 13.3. After the dimensional parameters of the second half of the connections was predicted using machine learning. Next, the maximum unity check of each connection was calculated. The following results were found:

- Number of connections for which $UC_{max} > 1.0$ = 12 (7%)
- $UC_{max,avg}$: 0.54

15.1.2. Performance when using 'average' dimensions

In order to make a fair comparison, the same connections are selected as the ones that are used as training input for the machine learning algorithm. For this set of connections, the optimisation loop as described in Section 13.2 is run through. After, the average of each parameter is calculated. This results in the following values for the dimensional parameters:

- a_1-ratio = 0.40
- a_2-ratio = 0.30
- b-ratio = 0.38
- h_1 = 100mm
- w_1 = 100mm
- h_2 = 100mm
- w_2 = 100mm

As well as for the design with predicted connections, the maximum unity check for each connection was determined. The following results were found:

- Number of connections for which $UC_{max} > 1.0$ = 36 (20%)
- $UC_{max,avg}$: 0.71

15.1.3. Comparison of performances

The results in the previous show that the performance of the design with individually predicted connections is better than the design with the average connections. The same can be concluded from Figure 15.1, which shows the unity checks for the two different designs. The part of connections that will need to be designed afterwards (due to a UC > 1) is reduced from 20% to 7% when using a random forest algorithm.

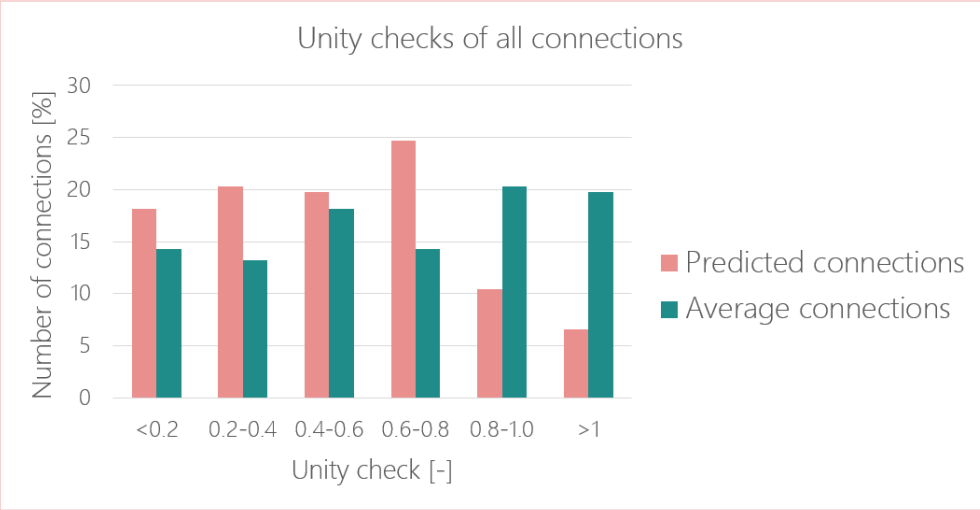

Figure 15.1: Unity checks of all connections when predicting the dimensions (pink) and when using average dimensions (green)

15.2 Conclusion

For the current bridge design and discretisation of the dimensional parameters, the *Cross section optimisation II* (see Figure 13.3) takes approximately four hours to be completed. This means that, when average connections are applied, the dimensions of the remaining 20% of the connections, that do not fulfil the requirements, could be found in around 45 minutes. This is not favourable during the first design stage, in which still a lot of changes in the design are made.

It should be taken into account that the run-time for *Cross section optimisation II* for the current design is relatively short since the smallest section size can be applied to all beams, leading to early abortion of the loop. In case larger section sizes are required, the time will increase significantly (twice as long when all sections are one cross section size bigger).

When using a random forest algorithm, the number of connections that have to be dimensioned afterwards can be reduced to 7%. This percentage might be even more reduced when the size of the training set is increased, another algorithm is used and/or the training input is optimised. The algorithm gives instant feedback (matter of seconds) and therefore does not increase the computation time compared to using averaged values. Nevertheless, first a database of training input should be created by running *Cross section optimisation II* for a large number of connections which are part of a large number of bridge designs. This is really time-consuming. However, the creation of the training data can be automated and therefore be carried out at night or in weekends. Once the data set is created, the design process can be speed up significantly. A decrease in insufficient connections from 20 to 7% already results in a time saving of 35%.

A designer should therefore make the following consideration:

- Apply average dimensions to all connections and apply *Cross section optimisation II* to all connections that don not fulfil the requirements (approximately 20 %)
- Spend time in an early design stage on the creation of a database with training input for a machine learning algorithm, apply dimensions that are predicted by the algorithm and subsequently apply *Cross section optimisation II* to the reduced number of connections that do not fulfil the requirements

In other words, it depends on the designers preference to spend extra time on the creation of a database or on finding the right dimensions for critical connections.

16

Global and Local Geometry

Now that the global and local geometry of the bridge are defined separately, the next step is to combine both to create the final design of the bridge. First, all connections are scaled and located in the right position. Then, all beam parts are combined to form the beams of the bridge. This chapter gives a brief overview of the approach.

16.1 Locating the connections

The connection is modelled in millimetres and the global model in meters. Since Grasshopper only works with numerical values and is not aware of units, the first step is to scale the connection with a factor 0.001 in order to fit into the global model.

All connections are modelled in a local coordinate system (x, y, z) with the origin in the centre of beam 2, x-axis in the direction of beam 2 and the y- and z-direction in the direction of the width and height of the beam, respectively. The next step will be to transfer the coordinate system from the local coordinate system (x, y, z) to the global coordinate system (X_i, Y_i, Z_i) of connection i, see Figure 16.1.

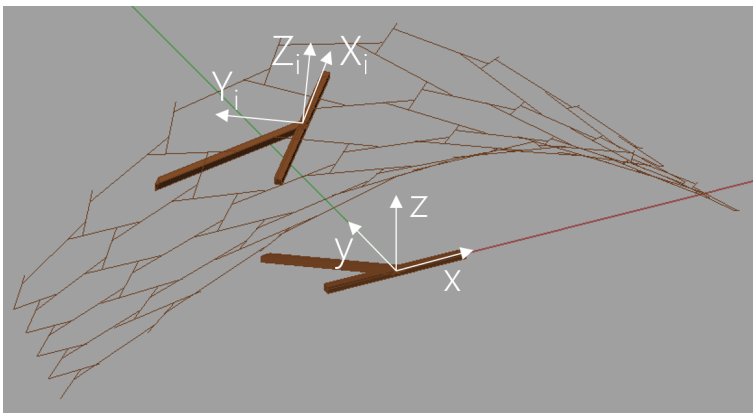

Figure 16.1: Transformation from the local coordinate system (x, y, z) to the global coordinate system of the connection (X_i, Y_i, Z_i)

16.2 Combining connection parts to create beams

Now that all connections are located in the right position, the next step is to combine connection parts to create continuous beams. Each beam has four connections involved: two end parts (Beam 1) and two mid parts (Beam 2), see Figure 16.2.

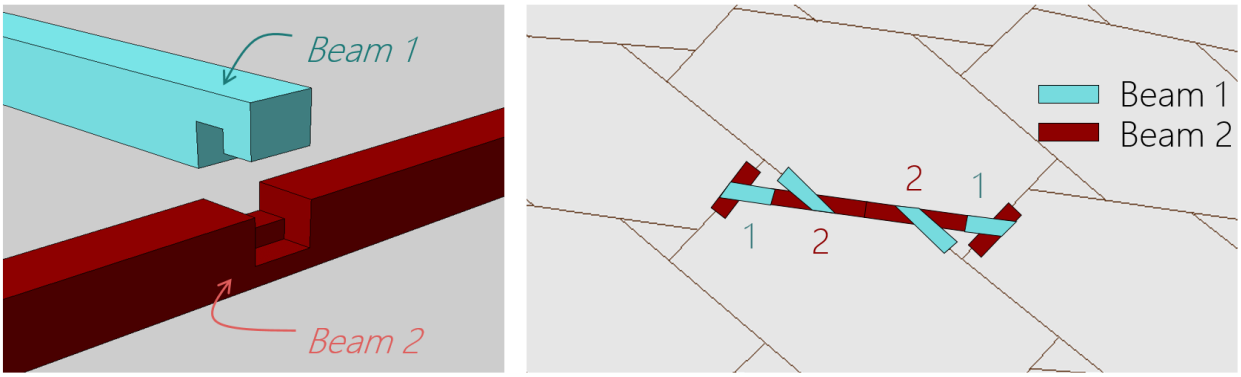

Figure 16.2: Combining connection parts to beams

As can be seen in Figure 16.1, the length of the beams in the connections are initially modelled with with a length of 2 meters. A decision has to be made regarding the location of the connection between connecting beam parts. The connection should be made at a location where the section has the full cross-section, so not at a location that is CNC-milled. It is decided to create the connection between the two mid-parts at the point between the origin of the beam parts, see Figure 16.3. Due to limited space between the end- and mid-parts, the connection is made as shown in Figure 16.3: parallel to Beam 2, at a distance of 6mm. In this way the connection between two parts is always made at a location where the beam has its full cross-section.

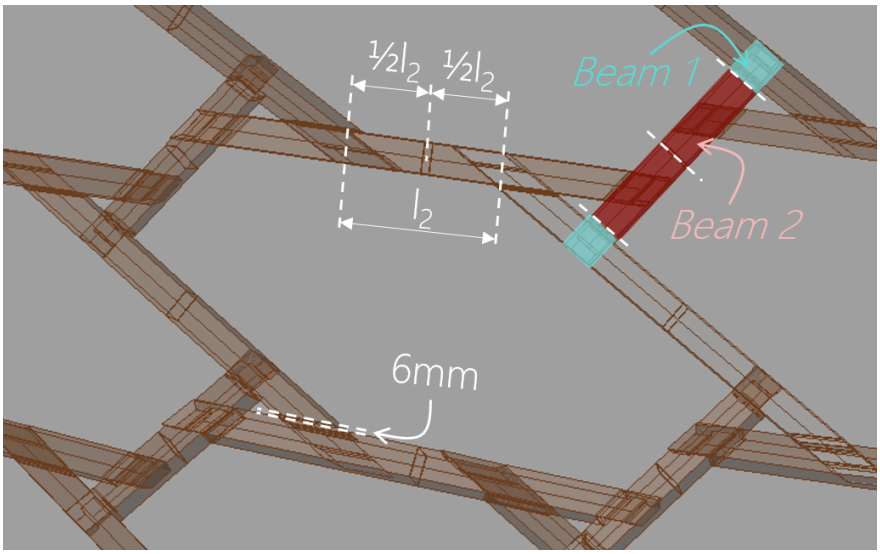

Figure 16.3: Location of the connection between different beam parts

Once all beams are connected as described above, the design of all beams is completed.

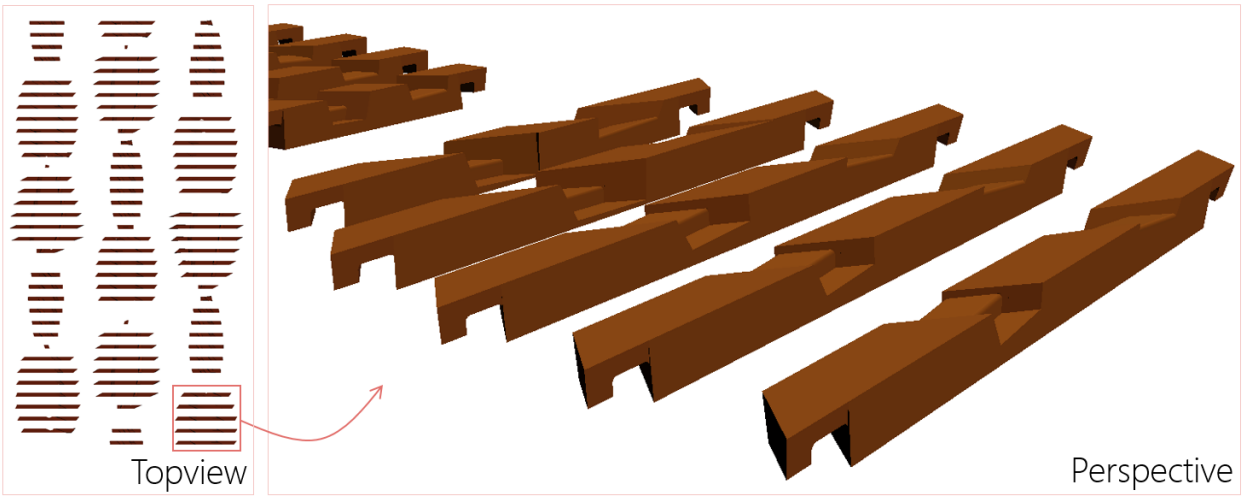

Figure 16.4: Design of the complete beams

17

Workflow

After running through one complete design iteration, consecutively focusing on the global design, connection design and integration of both, conclusions can be drawn regarding the workflow for the design of structures using the advantages of digital fabrication techniques. The main advantage of digital fabrication that is addressed is the great design freedom, accompanied by the following improtant benefits:

- The possibility to design free form structures
- The possibility to optimise individual elements in the structure

However, this larger design freedom also entails a difficulty: the design process becomes more complex.

Design workflow

Digital fabrication is often associated with design without limitations. Nevertheless, every type of manufacturing has its restrictions. The first step is therefore to define the possibilities and limitations in order to make optimum use of the fabrication technique and to prevent ending up with an unworkable design. Both limitations of the fabrication technique used for production of individual elements and limitations during assembly should be incorporated into the design.

Subsequently it is important to designate all aspects that have to be designed and optimised. For example the shape of the structure, grid layout, connection design, cross section sizes etc.. Ideally all aspects would be designed and optimised simultaneously since they are all interdependent. However this is complicated due to a lack of starting points. Furthermore, including too much detail in an early design stage is at the expense of design freedom, see Figure 17.1. The more detail is added to the design, the more computationally intensive the model(s) get. This makes it time consuming to make changes and therefore hard to check a large number of design alternatives. For these two reasons it is preferable to subdivide the design process into a couple of major design steps, addressing different design aspects or optimisation procedures which can be performed either independently or consecutively.

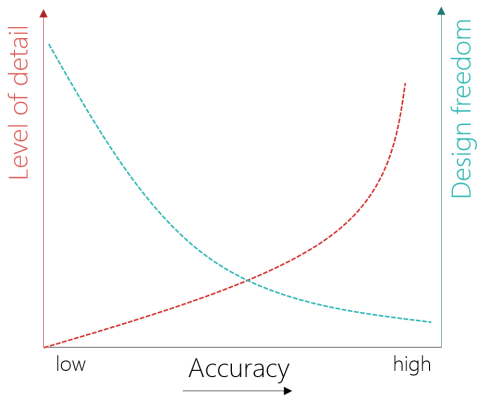

Figure 17.1: Accuracy vs. level of detail and design freedom

When a structure composed of beam and (integrated) connection elements is to be designed (e.g. gridshell, truss or space frame structure), an effective way of dealing with all designated design steps is by applying

an iterative workflow in which first a feature of the global design of the bridge and subsequently a detail of the connection design is addressed. After this both designs have to be integrated, see Figure 17.2a. An additional design aspect or optimisation is added during each iteration, thereby increasing the level of detail and accuracy. The goal is to address as many aspects as possible at the beginning of the design process, when the design freedom is still large.

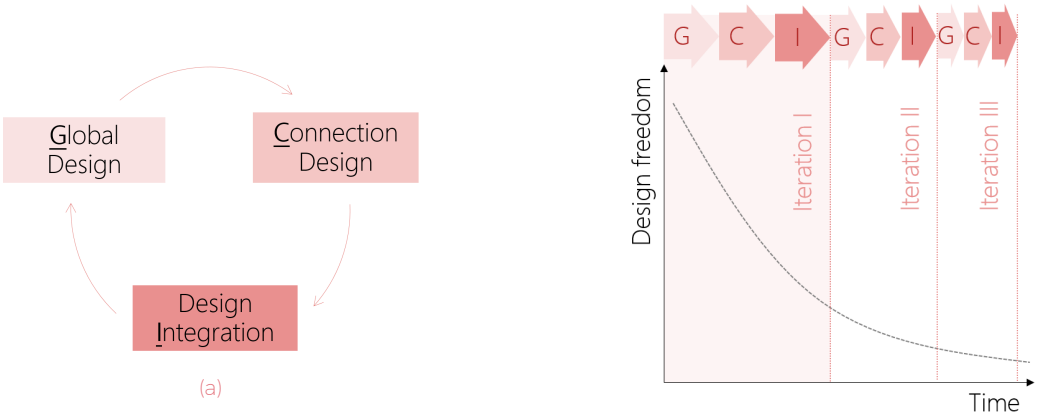

Figure 17.2: Iterative design workflow (17.2a) and accuracy vs. design freedom including design phases (17.2b)

Assumptions and simplifications

To allow for the assessment of a large number of different design alternatives in this first design stage, it is important to have a fast model. To achieve this, assumptions should be made and simplifications applied. For every assumption the level of accuracy should be examined. In case an assumption is conservative, the deviation from reality is related to a loss of gain. When a non-conservative assumption is made, the assumption is associated with risk and requires more attention. Figure 17.3 shows a decision tree for the implementation of assumptions and simplifications.

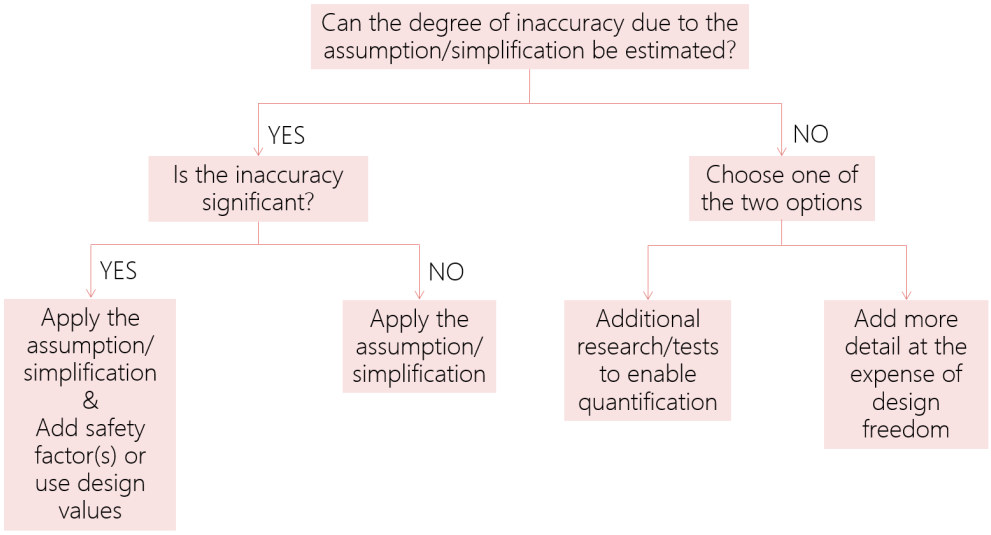

Figure 17.3: Decision tree for application of an assumption or simplification

It is of great importance that after implementation of an assumption/simplification, the quality of the model is evaluated. This could be done by doing hand-calculations, calculating unity checks and/or using engineering judgement. Summarising, the following steps should be undertaken for each design step:

1. Define goal of the design step
2. Determine possible assumptions/simplifications to confine the complexity of the design step

3. Examine the loss of accuracy due to the assumptions/simplifications. If necessary add safety factors and/or use design values. If there is too much uncertainty regarding the accuracy of the assumption, additional research should be done (literature or testing) or it should be considered to abandon the assumption and increase the level of detail, see Figure 17.3

4. Assess the quality of the simplified model

Optimisation methods

In some cases it is simple to develop custom-made scripts directly linking the design parameters to the fitness (design objective). An example is a cross section optimisation where the forces in the structure are linked to the minimum section sizes through the Eurocode checks. Nevertheless, for other optimisation objectives it is complex to uncover such a relation. In that case optimisation algorithms (eg. evolutionary algorithms) offer a solution. Despite the good performance of algorithms, these are a kind of black box due to lack of transparency and limited possibility for adaptability. It is therefore important to verify if the optimisation process is performing as expected and is converging towards a global optimum, not a local optimum.

Moreover, in all cases it is advisable to evaluate the necessity to absolutely reach the optimum. In some cases it might be sufficient to prematurely abort the optimisation process. A study on the quality of the result v.s. the number of optimisation steps/iterations can clarify this. Early termination can speed up the design process considerably, enabling assessment of more design alternatives within the same time span.

VI

Lab Testing

18

Test Setup

In contrast with the behaviour of steel, there are still a lot of uncertainties with respect to the behaviour of timber. The great variation in timber species, the homogeneity and the orthotropy of the material make it hard to predict both the resistance and stress distribution within the material and deformation behaviour. In this research the focus is on strength calculations. In a follow-up study it would be interesting to focus on the deformation behaviour of the connections and overall structure.

18.1 Wijma Kampen B.V.

Wijma is a timber producer situated in Kampen, the Netherlands. The firm focuses on sustainable harvesting and processing of tropical hardwoods, like Azobé. The company mainly carries out projects in the geo-, road- and hydraulic engineering sector (e.g. mooring piles, ducdalphes, wooden bridges and lock gates). Figure 18.1 shows pictures made at the the firm in Kampen:

Figure 18.1: Wijma Kampen. Top: (part of a) lock gate, fabricated by CNC-milling. Bottom: timber stock and CNC-milling machine

Wijma offered to share thoughts regarding the detailing of the connections, check the feasibility of the design for CNC-milling and produce a number of test specimens.

18.2 Selection of the strength test

A selection of three test setups is made based on uncertainty in the verification of the failure mechanism and the relevance of the failure mechanism for the determination of the dimensions of the connection. Based on

the analysis of the most common failure mechanisms carried out in Section 14.3.3, the following planes are most relevant:

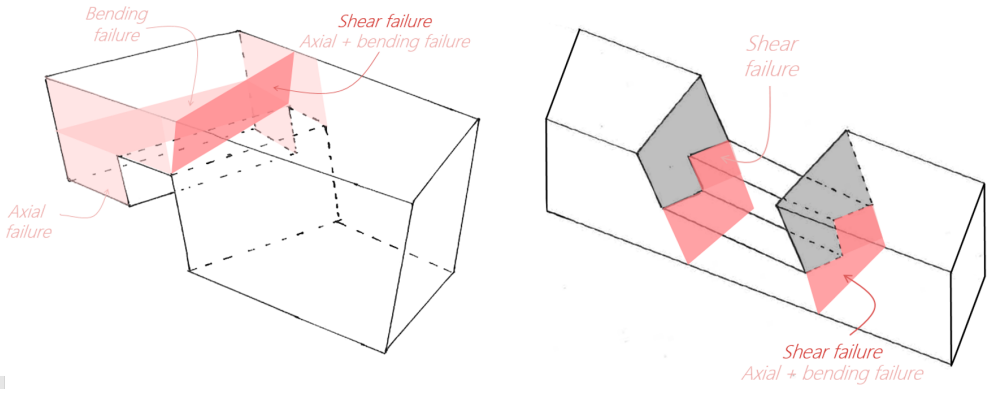

Figure 18.2: Planes that are critical

Three failure mechanisms that are commonly not fulfilling the requirements and have a large degree of uncertainty are:

- Cracking failure next to the notch of Beam 1
- Bending failure (perpendicular to the grain) of the hook (see Figure 2)
- Bending failure of beam 2 at the location of the connection

18.2.1. Cracking failure of the notched beam

Cracking failure due to shear loading is often the critical failure mechanism for notched members. The Eurocode describes a verification method for notched members based on linear crack growth, using the fracture energy of European softwoods. In the Eurocode, the verification is disguised as a regular shear stress check (assuming a parabolic shear distribution at the neck of beam 1 as shown in Figure 18.3a) by the introduction of factor k_v:

$$\tau_d = \frac{1.5V}{bh_{ef}} \leq k_v f_{v,d} \tag{18.1}$$

Nevertheless, in reality the cracking failure is not related to the parabolic shear stress and shear strength but to the stiffnesses (E_x and G_{xy}) and fracture energy ($G_{f,y}$) of the timber. The stiffness values and fracture energy of softwood (Spruce) are included in factor k_v (through another factor: k_n). Since the fracture energy of hardwoods is unknown, the method might not be suitable for hardwoods like Azobé.

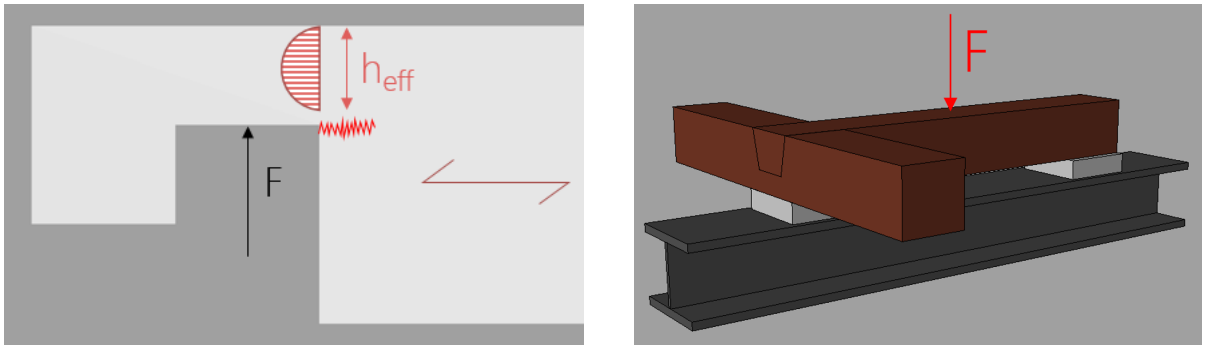

(a) (b)

Figure 18.3: Shear failure of the notch along the grain (18.3a) and setup test 1 (18.3b)

18.2.2. Bending failure of the end of the notch

The second failure mechanism is bending failure of the end of the notch. A tension force in Beam 1 will result in a compression force at the end of the notch as shown in Figure 18.4a. This force induces a bending

moment, associated with a tension force perpendicular to the grain. There is a high uncertainty regarding the tension resistance perpendicular to the grain.

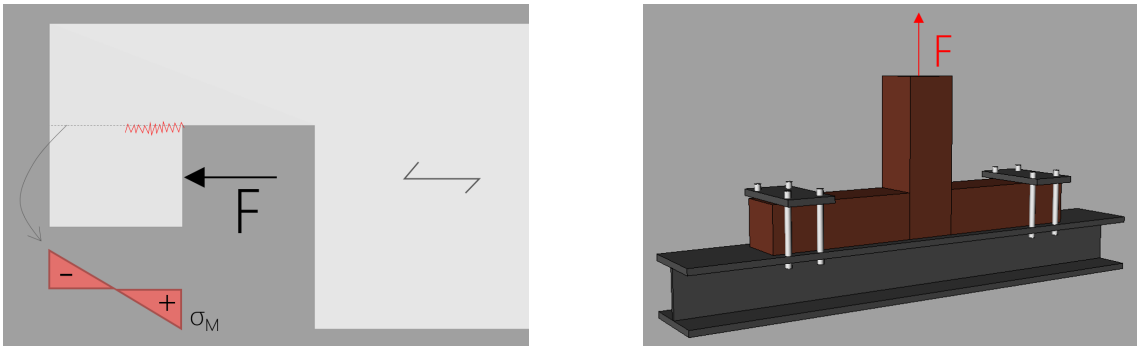

(a) (b)

Figure 18.4: Bending failure of the end of the notch due to bending stress perpendicular to the grain (18.4a) and setup test 2 (18.4b)

18.2.3. Bending failure of beam 2

As described in Section 12.2.5, it should be decided if the presence of beam 1 should be taken into account or not, for the calculation of the bending moment resistance at the location of the connection. Since the elastic modulus of Beam 1 (perpendicular to the grain, $E_{90} = 1330\,N/mm^2$) is significantly smaller than the elastic modulus of Beam 2 (parallel to the grain, $E_0 = 20000\,N/mm^2$) it has been assumed that the presence of Beam 1 can be disregarded. Nevertheless, to verify the anisotropic behaviour and the behaviour of the complex shape of Beam 2 at the location of the connection when subjected to bending (*Plane 11*), tests could be carried out.

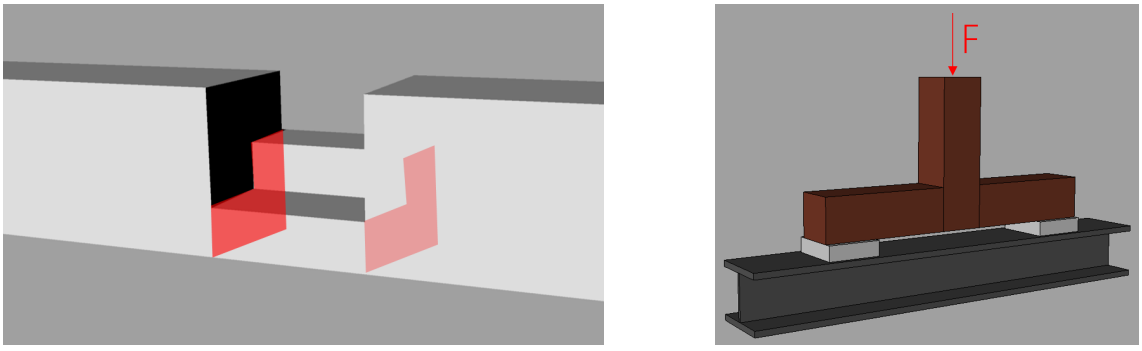

(a) (b)

Figure 18.5: Critical planes for bending failure of Beam 2 (18.5a) and setup test 3 (18.5b)

18.2.4. Selection

Due to time constraints only one test type will be carried out. The disadvantage of test number 2 (bending failure of the end of the notch) is that a large spread in results due to the large deviations in strength perpendicular to the grain is expected. For this reason a large number of tests is necessary to draw conclusions. However, the number of available test specimens is limited.

Due to the higher uncertainty, wider applicability and the suitability within the scope of research at the timber section at the TU Delft, it has been decided to focus on cracking failure of the notched member due to shear loading.

18.3 Goal of the test

The goal of the test is to get insight in the structural behaviour of notched members. The test should first of all give insight in the capacity of the specific connection in order to be able to dimension the design. The calculation can be compared to the EC5 in order to evaluate its applicability.

As mentioned before, notches considerably lower the capacity of timber beams due to stress concentrations at the corner of the notch and tensile stresses acting in the weak direction of the timber. Therefore, the effect of two measures to increase the capacity is evaluated.

First of all, the influence of the application of rounded edges at the locations that are prone to shear cracking is evaluated. A radius of 10mm is applied.

In order to both increase the capacity and prevent brittle failure it is advisable to apply reinforcement. This can be done by applying either internal- or external reinforcement [15]:

- Internal reinforcements:
  - Glued-in threaded rods
  - Glued-in rebars
  - Fully threaded wood screws
- External reinforcements:
  - Glued-on plywood,
  - Glued-on LVL,
  - Glued-on boards,
  - Punched metal plate fasteners.

For this research it is decided to apply fully threaded wood screws due to its easy application and therefore possible integration within a completely digital fabrication workflow.

Six types of specimens are tested, see Figure 18.6

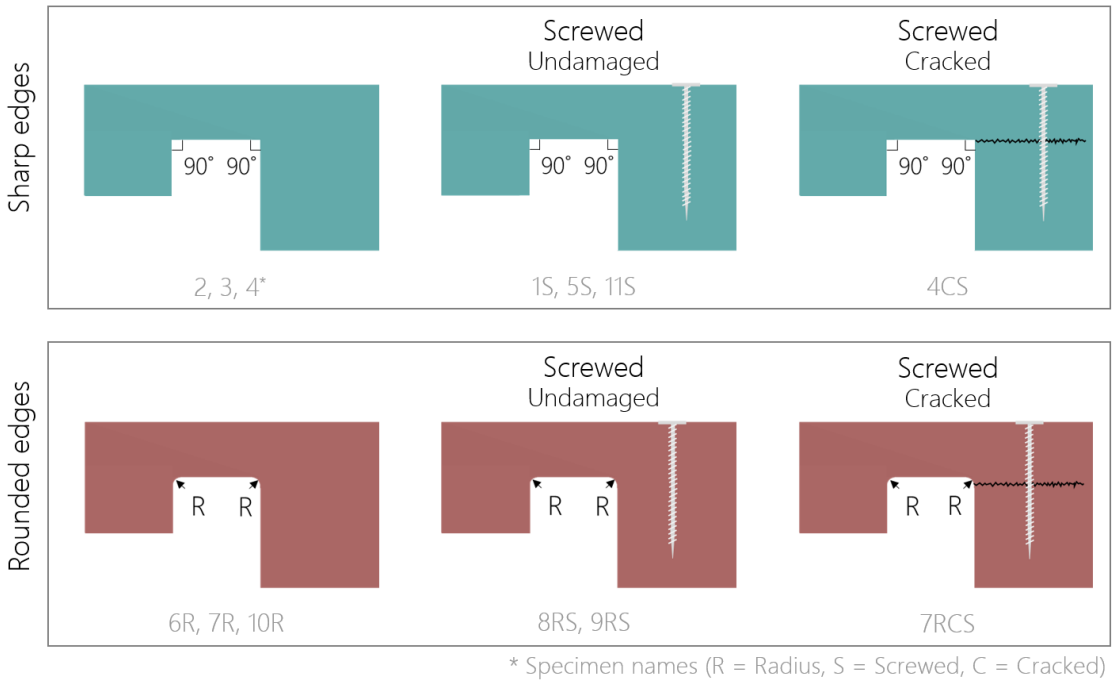

Figure 18.6: The six different types of test specimens: specimens with sharp edges (#), sharp edges and screws (#S), cracked specimen with sharp edges and screws (#CS) and specimens with rounded edges (#R), rounded edges and screws (#RS) and cracked specimen with sharp edges and screws (#RCS)

Two types of tests will be done with reinforced members:

- Testing of undamaged specimens: Specimen 5S, 11S (sharp edges), 8RS and 9RS (rounded edges) will be tested when still intact. In this way the combined effect of the timber and screws can be examined.
- Testing of cracked specimens: After specimen 4 and 7R are brought to collapse, screws will be placed. In this way the effect of the screws itself can be examined.

18.4 Test setup

18.4.1. Dimensions of the test specimens

Figure 18.7 shows the outer dimensions of the test specimens. Both connecting beams have a cross-sectional size of 95x95mm. The lengths of the beams are:

- $L_{Beam1} = 600mm$
- $L_{Beam2} = 400mm$

Both beams meet at an angle of 90 degrees, without eccentricity ($\theta_1 = \theta_2 = \theta_3 = e = 0$)

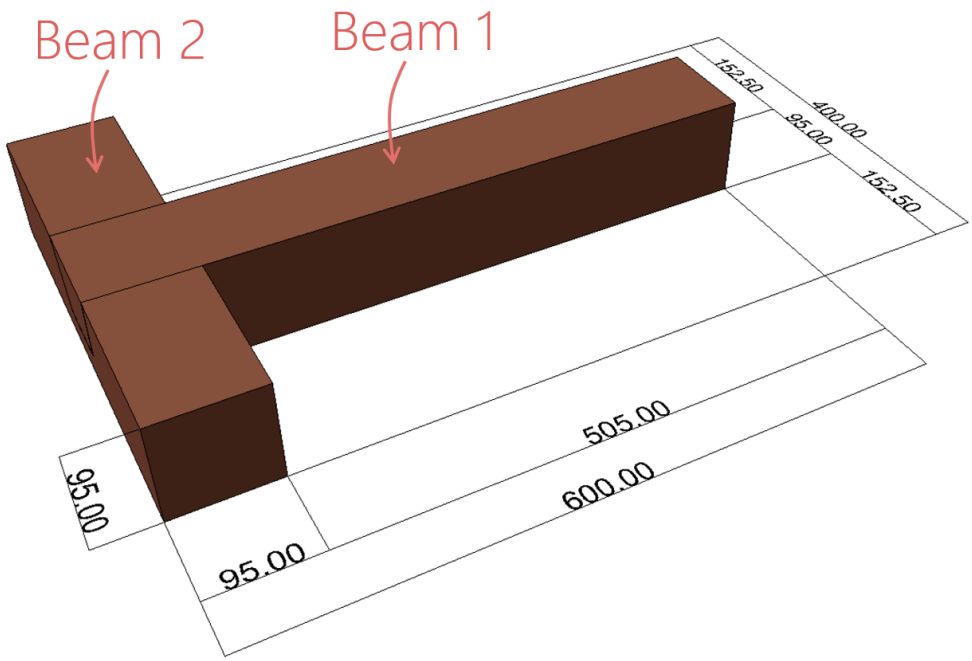

Figure 18.7: Outer dimensions of the whole connection

Figure 18.8 shows the geometric parameters defining the dimensions of beam 1. As discussed in Section 10.2, the *internal* dimensions can be expressed through 3 ratios:

- a_1-ratio: The ratio between length a_1 and the total height of beam 1 (a_1/h_1)
- a_2-ratio: The ratio between length a_2 and the total height of beam 1 (a_2/h_1)
- b_1-ratio: The ratio between length b_1 and the total width of beam 2

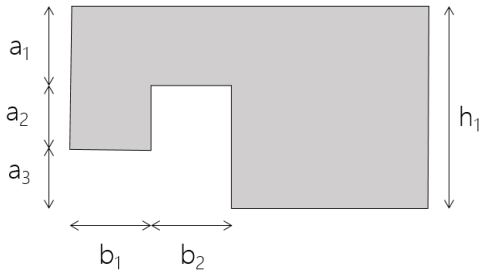

Figure 18.8: Geometric parameters of beam 1

The following seven parameters are chosen:

- a_1-ratio = 0.35

- a_2-ratio = 0.35
- b-ratio = 0.4
- $h_1 = w_1 = h_2 = w_2$ = 95mm

This results in the dimension as shown in Figure 18.9 and 18.10. The dimensions of the test specimens are identical, except for the lack of the radius (R = 10mm) in the specimens with sharp edges.

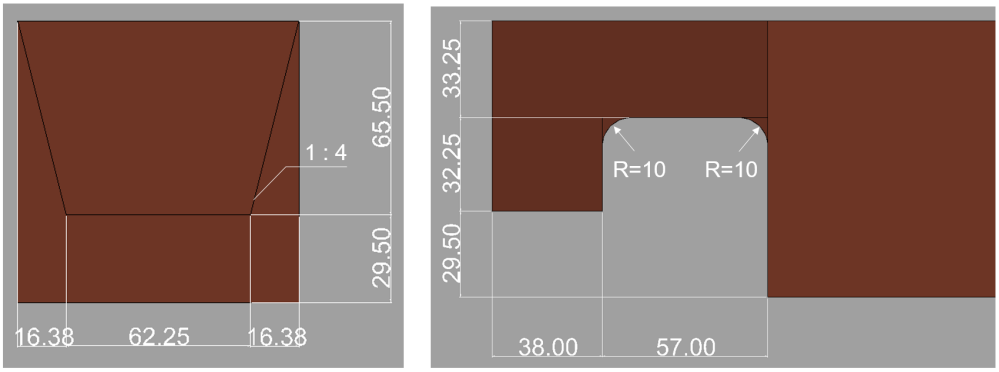

Figure 18.9: Dimensions of Beam 1 at the location of the connection

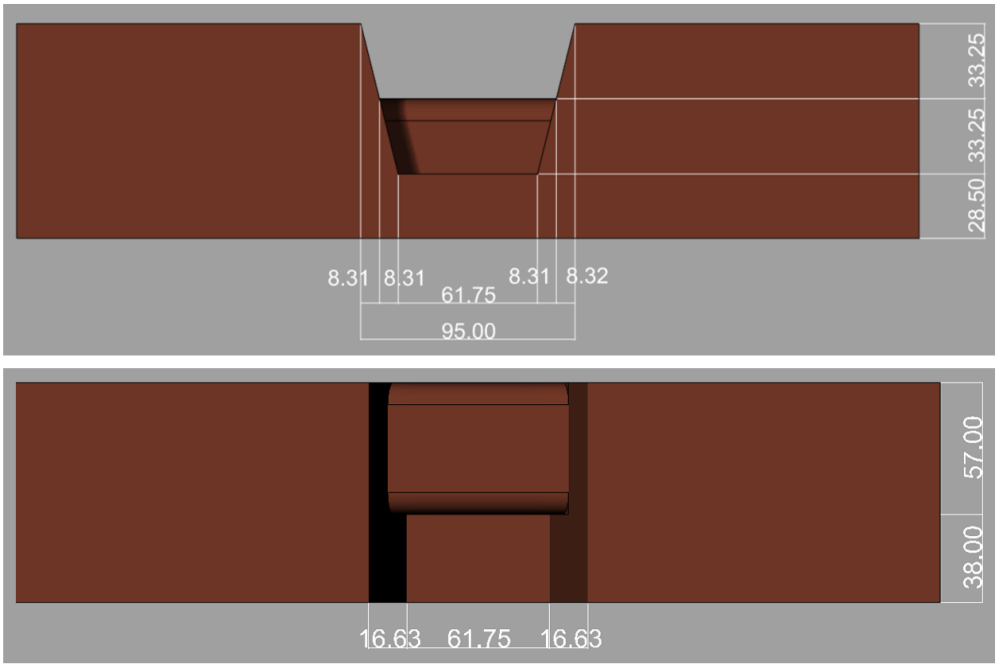

Figure 18.10: Dimensions of Beam 2 at the location of the connection

Position of the screws

Part of the specimens will be reinforced by three screws. The specifications of the screws that are used for the tests are:

- Brand: Rothoblaas
- Type: HTS
- Screw head: TX20
- Length: 70mm
- Diameter of the outer tread: 5mm

- Inner thread: ± 3.3mm

The position of the screws is shown in Figure 18.11. An edge distance of $4 \cdot D = 20\,mm$ is assumed, resulting in a spacing of $S = 27.5mm$. Before placement of screws, three holes are pre-drilled with a depth of 55mm and a diameter of 3.5mm.

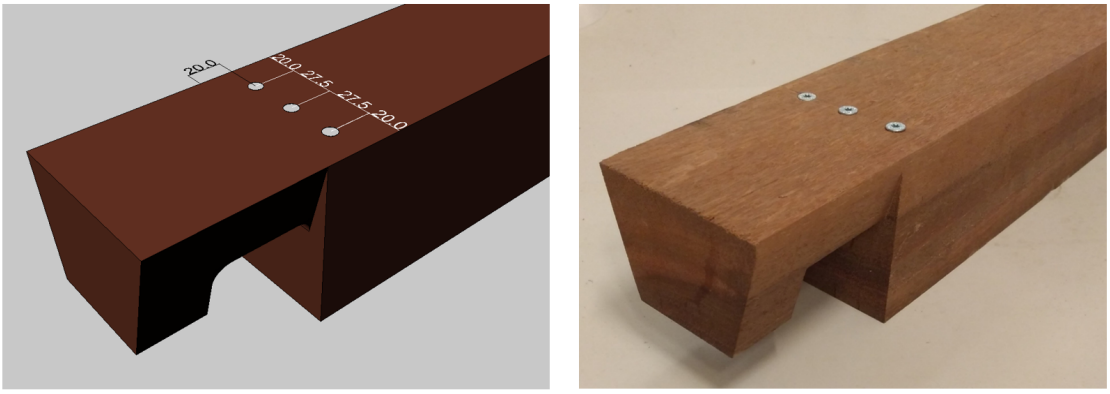

Figure 18.11: The position of the screws. Left: modelled position, right: actual specimen

18.4.2. Layout of the test setup

Figure 18.12 shows a 3D-view of the modelled and actual test setup. Figure 18.13 shows the side-view of the setup, including the location of the supports and load.

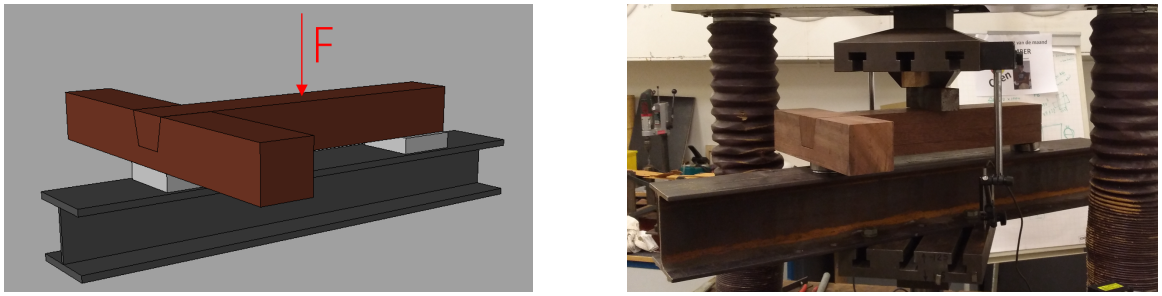

(a) (b)

Figure 18.12: 3D model of the test setup (18.12a) and the actual setup (18.12b)

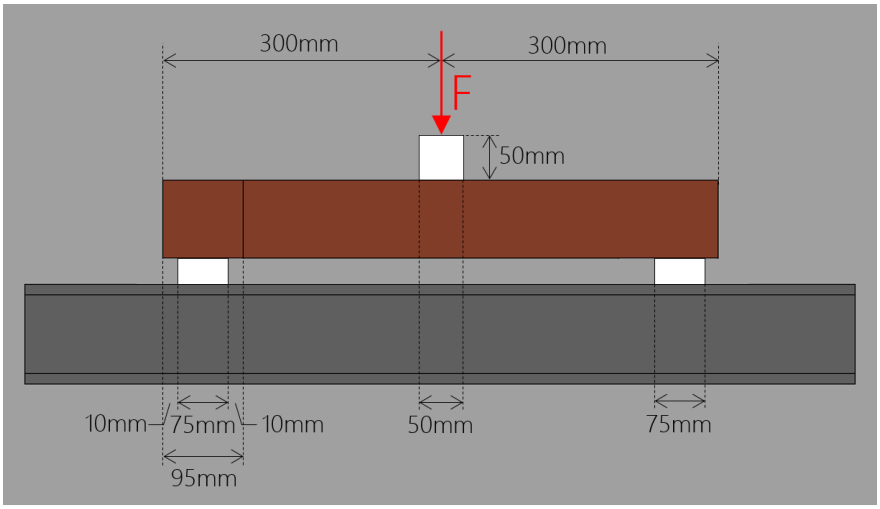

Figure 18.13: Dimensions of the test setup

As shown in Figure 18.12b and 18.13, the load is applied at the centre of beam 1. The load is transferred from the testing machine to the test specimen through a steel strip with a width and height of 50mm. The specimen has pinned supports on both sides. The supports do not constrain any of the three rotations in space, see Figure 18.14. This type of support prevents the development of torsion stresses in the specimen.

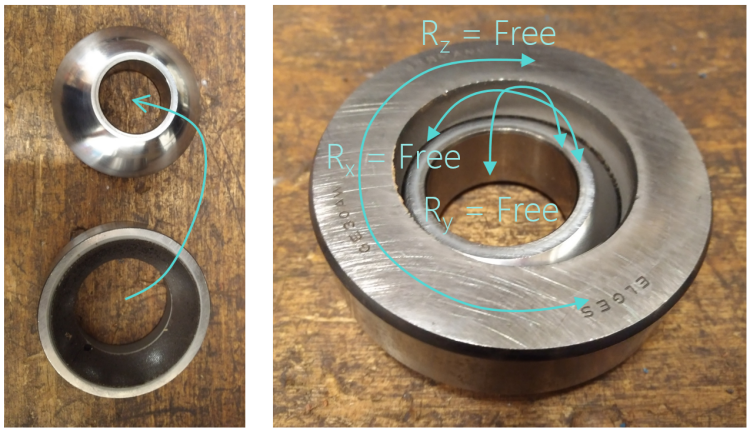

Figure 18.14: Pinned support that does not constrain any of the 3 rotations ($R_x = R_y = R_z =$ Free)

18.4.3. Measurements

The goal of the test is to determine the failure load. Therefore, only the displacements at the centre of the beam are measured (at the location of the load). The displacements are measured by three devices:

- **S01**: The displacement measured by the testing machine
- **OS01**: The displacement between the top and bottom of the machine on side 1, see Figure 18.15
- **OS02**: The displacement between the top and bottom of the machine on side 2

The displacements measured by the machine (*S01*) are the displacements of the weight inside the machine. At a force of approximately 6kN the weight will settle. This will be observed in the force-displacement graphs. For this reason additionally two measuring tools are installed, measuring the displacement between the top and the bottom of the testing machine.

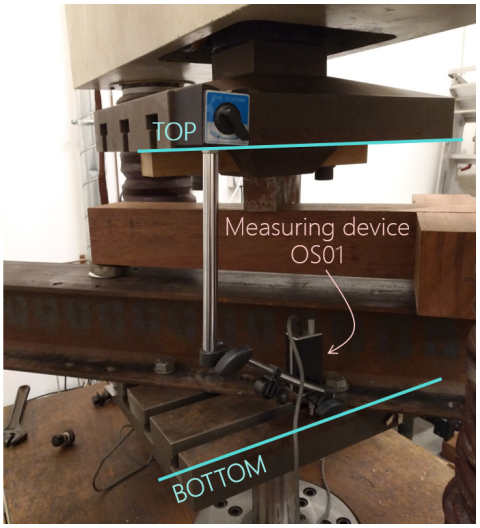

Figure 18.15: Measurement device OS01

19

Hypothesis Lab Tests

In this section, an prediction of the failure load of the specimens, as well as the maximum displacement will be made.

For the estimation of deflections and the maximum load, not the characteristic values but the average values of the stiffness should be used. Research done by G.J.P. Ravenshorst on *Species ind pendent strength grading of structural timber* gives a mean modulus of elasticity of $20900\,N/mm^2$ for Azobé with strength grade D70.[3]

All values are related to Azobé with a moisture content of 12%. Nevertheless, the specimens that are used for the test were kept wet while stored during the days before the tests. Therefore, all specimens had a moisture content (*m.c.*) higher than the fibre saturation point ($> 25\%$), see Section 20.1. A method described by G.J.P. Ravenshorst to convert the modulus of elasticity at a moisture content of 12% ($E_{12\%}$) to another moisture content (E_{mc}) is by using the following equation:

$$E_{mc} = E_{12\%} \cdot (1 - k_{mc} \frac{min(mc; 25.0) - 12}{13}) \tag{19.1}$$

$k_{mc} = 0.13$ is assumed to be a conservative assumption. Since for all specimens $mc > 25.0\%$, the following modulus of elasticity is obtained:

$$E_{>25\%} = 20900 \cdot (1 - 0.13 \frac{25 - 12}{13}) = 18200\,N/mm^2 \tag{19.2}$$

19.1 Prediction of failure loads

19.1.1. Capacity of specimens with sharp edges

The shear capacity of notched members is described in Eurocode 5 (NEN-EN 1995-1-1, section 6.5.2).

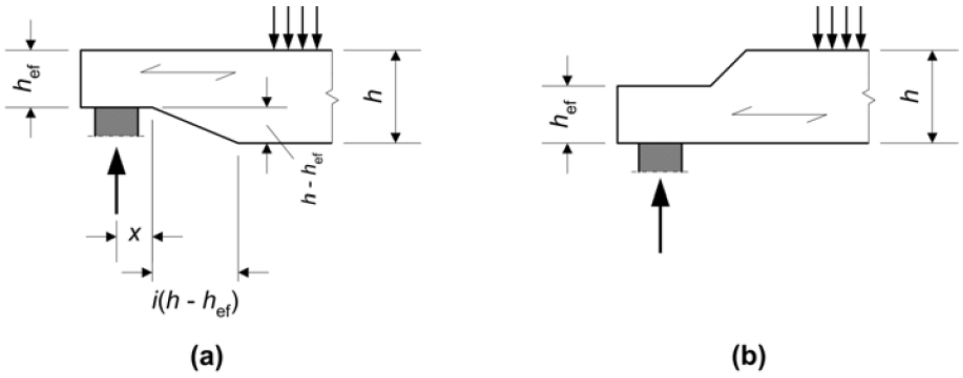

Figure 19.1: Beams with a notch at the end (NEN-EN 1995-1-1)

The check is disguised as a maximum shear stress check at the narrow part of the beam, see Equation 19.3:

$$\tau_d = \frac{1.5V}{bh_{ef}} \leq k_v f_{v,d} \tag{19.3}$$

The reduction factor k_v includes the fracture energy theory and can be calculated using the following expression: Where k_v for beams notched on the same side as the support (Figure 19.1 a) is:

$$k_v = min \begin{cases} 1 \\ \frac{k_n(1+\frac{1.1i^{1.5}}{\sqrt{h}})}{\sqrt{h}(\sqrt{\alpha(1-\alpha)}+0.8\frac{x}{h}\sqrt{(\frac{1}{\alpha}-\alpha^2)})} \end{cases} \tag{19.4}$$

Where:

- i the notch inclination. In this case $i = 0$
- h depth of the beam in mm, so $h = h_1 = 95mm$
- x the distance from line of action of the support reaction to the corner of the notch: $x = \frac{1}{2}(1 - b_{ratio}) \cdot w_2 = \frac{1}{2}(1 - 0.4) \cdot 95 = 28.5mm$
- α the ratio between the effective depth and the real depth ($\alpha = \frac{h_{ef}}{h}$) = a_1-ratio = 0.35
- k_n is 5 for solid timber

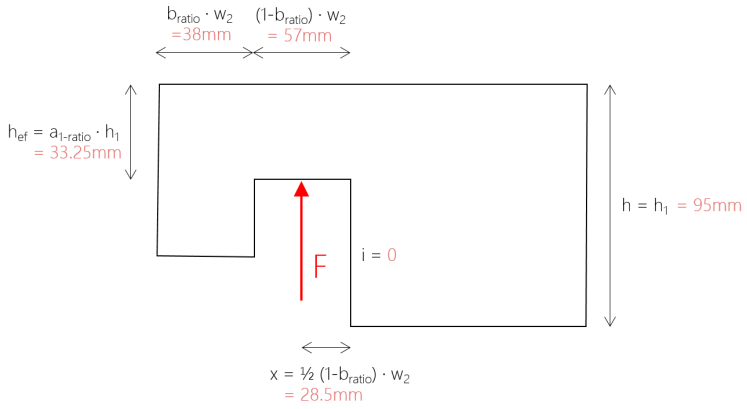

Figure 19.2: The relevant dimensions to determine the factor k_v

The Eurocode prescribes to use $k_n = 5$ for solid timber. This factor includes the stiffness, shear strength and fracture energy of softwood (spruce) and is therefore potentially not applicable for hardwoods like Azobé. In order to find out which value to use for k_n, the original formula based on the fracture energy as developed by Gustafsson [2] is examined, see Equation 19.5.

$$\frac{V_f}{b\alpha d} = \frac{\sqrt{\frac{G_{f,y}}{d}}}{\sqrt{\frac{0.6(\alpha-\alpha^2)}{G_{xy}}} + \beta\sqrt{\frac{6(\frac{1}{\alpha}-\alpha^2)}{E_x}}} \tag{19.5}$$

Where:

- $G_{f,y}$ fracture energy. $G_{f,y} = 1.420 Nmm/mm$ is assumed for Azobé (see Equation 19.14)
- d depth of the beam in mm, so $h = h_1 = 95mm$
- b width of the beam, $b = 95mm$
- α the ratio between the effective depth and the real depth ($\alpha = \frac{h_{ef}}{h}$) = a_1-ratio = 0.35 [-]
- $beta$ the ratio between the distance the support and end of the notch and the total height of the beam, so $\beta = \frac{1}{2}(1 - b\text{-ratio}) \cdot \frac{w_2}{h_1} = \frac{1}{2}(1 - 0.4) \cdot \frac{95}{95} = 0.3$ [-]
- E_x modulus of elasticity parallel to the grain. For Azobé $E_{x,mean} = 18200 N/mm^2$
- G_{xy} shear modulus in $[N/mm^2]$ and can be derived from the modulus of elasticity: $G_{xy} = \frac{E_x}{16}$. For Azobé $G_{xy,mean} = 1138 N/mm^2$

Combining Equation 19.3 and 19.5 gives:

$$k_v = \frac{1.5}{f_{v,d}} \cdot \frac{V_f}{b\alpha d} = \frac{1.5}{f_{v,d}} \cdot \frac{\sqrt{\frac{G_{f,y}}{d}}}{\sqrt{\frac{0.6(\alpha-\alpha^2)}{G_{xy}}} + \beta\sqrt{\frac{6(\frac{1}{\alpha}-\alpha^2)}{E_x}}} \tag{19.6}$$

Rewriting the equation and applying the assumption that $E_x/G_{xy} = 16$ gives:

$$k_v = \frac{1.5}{f_{v,d}} \cdot \frac{\sqrt{\frac{E_x G_{f,y}}{d}}}{\sqrt{\frac{0.6(\alpha-\alpha^2)E_x}{G_{xy}}} + \beta\sqrt{6(\frac{1}{\alpha}-\alpha^2)\frac{E_x}{E_x}}} = \frac{1.5}{f_{v,d}} \cdot \frac{\sqrt{\frac{E_x G_{f,y}}{d}}}{\sqrt{0.6(\alpha-\alpha^2)\cdot 16} + \beta\sqrt{6(\frac{1}{\alpha}-\alpha^2)\cdot 1}} \tag{19.7}$$

$$= 1.5 \cdot \frac{\sqrt{\frac{E_x G_{f,y}}{f_{v,d}^2 d}}}{\sqrt{9.6(\alpha - \alpha^2)} + \beta\sqrt{6(\frac{1}{\alpha} - \alpha^2)}} = 1.5 \cdot \frac{\sqrt{\frac{E_x G_{f,y}}{f_{v,d}^2 d}}}{3.10\sqrt{(\alpha - \alpha^2)} + 2.45 \cdot \beta\sqrt{(\frac{1}{\alpha} - \alpha^2)}} \tag{19.8}$$

$$= 1.5 \cdot \frac{\frac{1}{3}\sqrt{\frac{E_x G_{f,y}}{f_{v,d}^2 d}}}{1 \cdot \sqrt{(\alpha - \alpha^2)} + 0.8 \cdot \beta\sqrt{(\frac{1}{\alpha} - \alpha^2)}} = 1.5 \cdot \frac{\frac{1}{3}\sqrt{\frac{E_x G_{f,y}}{f_{v,d}^2}}}{\sqrt{d}(\sqrt{(\alpha - \alpha^2)} + 0.8 \cdot \beta\sqrt{(\frac{1}{\alpha} - \alpha^2)})} \tag{19.9}$$

This gives:

$$k_v = 1.5 \cdot \frac{k_n}{\sqrt{(\alpha - \alpha^2)} + 0.8 \cdot \beta\sqrt{(\frac{1}{\alpha} - \alpha^2)}} \tag{19.10}$$

With:

$$k_n = \frac{1}{3}\sqrt{\frac{E_x G_{f,y}}{f_{v,d}^2}} \tag{19.11}$$

When comparing this to the Eurocode equations (Equation 19.3 and C.23) it can be seen that the factor 1.5 in Equation 19.10 is not taken into account in the Eurocode. For this reason, it is decided to use the original equation for the fracture energy as stated in Equation 19.5. For the sake of clarity, the equation is repeated here:

$$\frac{V_f}{b\alpha d} = \frac{\sqrt{\frac{G_{f,y}}{d}}}{\sqrt{\frac{0.6(\alpha - \alpha^2)}{G_{xy}}} + \beta\sqrt{\frac{6(\frac{1}{\alpha} - \alpha^2)}{E_x}}} \tag{19.12}$$

According to the master thesis work by K. Moerkbeek [37] and J.R. van Otterloo [62], the fracture energy for hardwoods can be better expressed using the following equation:

$$G_{f,y} = 5.36373 \cdot 10^{-4} \cdot \rho + 4.1504 \cdot 10^{-5} \cdot E_0 \tag{19.13}$$

For Azobé, this would result in a fracture energy of $1.34 Nmm^2/mm$:

$$G_{f,y} = 5.36373 \cdot 10^{-4} \cdot 1100 + 4.1504 \cdot 10^{-5} \cdot 18200 = 1.34 Nmm^2/mm \tag{19.14}$$

It should be noted that this equation is based on tests on specimens with a moisture content below the fibre saturation point. The actual fracture energy of the specimens used for the tests might therefore deviate from the value calculated with Equation 19.14.

Assuming $G_{f,y} = 1.34 Nmm^2/mm$, the following shear capacity is obtained:

$$V_f = 95 \cdot 0.35 \cdot 95 \cdot \frac{\sqrt{\frac{1.34}{95}}}{\sqrt{\frac{0.6(0.35 - 0.35^2)}{1138}} + 0.3\sqrt{\frac{6(\frac{1}{0.35} - 0.35^2)}{18200}}} = 18.8 kN \tag{19.15}$$

The shear force is half of the applied load on the test specimen. This results in a maximum load of $F = 37.6 kN$.

19.1.2. Expected effect of applying rounded edges

The application of rounded edges instead of sharp edges hypothetically results in a shift of the crack location downwards, as shown in figure 19.3 [5]. Additionally, the transition from full member height to the neck is slightly more gradually, leading to a reduction of the the peak stress.

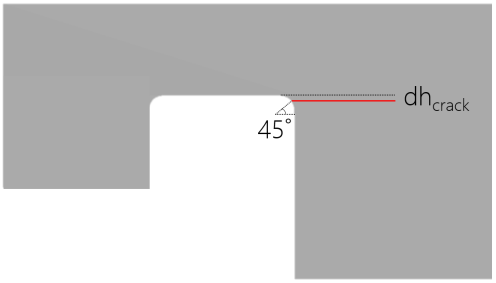

Figure 19.3: Expected shift of the location of the crack when applying rounded edges

The effect of the shift crack height can be determined by changing the α factor in Gustafsson's equation (Equation 19.12). The shift dh_{crack} is calculated as follows:

$$dh_{crack} = r(1 - sin(45)) = 10(1 - sin(45)) = 3mm \tag{19.16}$$

This gives a new alpha factor of $\alpha* = \frac{\alpha \cdot h + dh_{crack}}{h} = \frac{0.35 \cdot 95 + 3}{95} = 0.38$. Applying this new α-value in Equation 19.12 gives an increase in shear capacity of 10% (V = 20.7kN).

This does not take into account the effect of the more gradual stress distribution.

19.1.3. Expected effect of applying screws

The capacity of notched beams has been studied by various authors, based on analysis by means of finite element models, lab testing and fracture mechanics. In the late 1980's an approach was developed by Gustafsson based on fracture mechanics. This approach is later included in EC5. In time, more research is done on reinforced notched members. Nevertheless, no calculation methods for reinforced members are included in EC5. However, approaches to calculate the force in the reinforcement are given in the German standard (DIN 1052:2008) and a number of handbooks (e.g. APA). This method will be used to predict the increase in capacity of the test specimens with 3 screws.

It is assumed that the beam fails according to Mode I crack opening, see Figure 19.4.

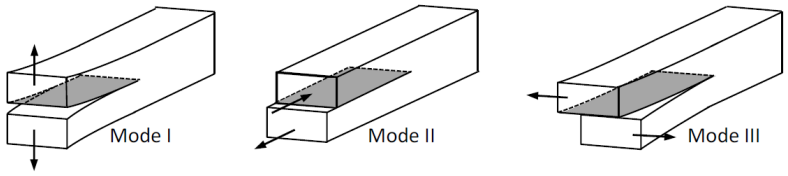

Figure 19.4: The three different kinds of crack opening in fracture mechanics [15]

At the corner of the notch, tensile stresses will occur perpendicular to the grain. This method assumes that the entire tensile force has to be taken by the reinforcement only. The tensile strength perpendicular to the grain of the timber is disregarded. For this reason, the tensile force in the reinforcement $F_{t,90}$ can be set equal to the integration of shear stresses below the depth of the notch:

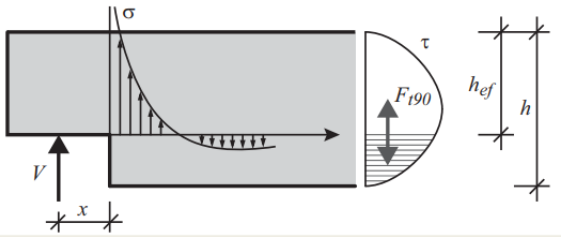

Figure 19.5: Assumed stress distribution and part of the shear stress that should be taken by the reinforcement [28]

The parabolic shear stress distribution can be defined as follows:

$$\tau(x) = \frac{4\tau_{max}x}{h}(1 - \frac{x}{h}) \tag{19.17}$$

Where x runs from the bottom of the full beam to the top of the full beam, see Figure 19.6.

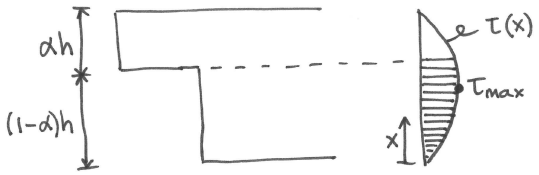

Figure 19.6: Shear stress distribution and relevant dimensions

Taking the integral of the shear stress for the part below the corner of the notch and multiplying this by the width of the beam b gives the force that should be taken by the screws:

$$F_{t,90} = b\int_0^{h(1-\alpha)} \tau(x)dx = \frac{4b\tau_{max}}{h}\left[\frac{1}{2}x^2 - \frac{1}{3}\frac{x^3}{h}\right]_0^{h(1-\alpha)} = 4bh\tau_{max}\left(\frac{1}{2}(1-\alpha)^2 - \frac{1}{3}(1-\alpha)^3\right) \tag{19.18}$$

The maximum shear stress can be calculated using the following equation:

$$\tau_{max} = \frac{3}{2}\frac{V}{bh} \tag{19.19}$$

The German National Annex prescribes a modification of 1.3 to take into account the orthotropy of the material and notch length. This gives:

$$F_{t,90} = 4bh\frac{3}{2}\frac{1.3V}{bh}\left(\frac{1}{2}(1-\alpha)^2 - \frac{1}{3}(1-\alpha)^3\right) = 1.3V\left[3(1-\alpha)^2 - 2(1-\alpha)^3\right] \tag{19.20}$$

The next step is to determine the withdrawal capacity of the screws. Unfortunately, EC5 only states a calculation method that can be applied to screws with a outer diameter larger than 6mm. Furthermore, the equations are based on tests carried out on softwoods. In the next paragraphs, the withdrawal strength is calculated using a few different methods found in literature which will subsequently be compared.

NEN-EN 1995-1-1=2005

NEN-EN 1995-1-1=2005, section 8.7.2 gives the following equation to calculate the withdrawal capacity of connections with axially loaded screws:

$$F_{ax,\alpha,R} = n_{ef}(\pi d l_{ef})^{0.8} f_{ax,\alpha} \tag{19.21}$$

Where:

$F_{ax,\alpha,R}$	withdrawal capacity of the connection at an angle α to the grain
n_{ef}	effective number of screws ($n_{ef} = n^{0.9} = 3^{0.9} = 2.69$)
d	outer diameter measured on the threaded part ($d = 5mm$)
l_{ef}	pointside penetration length of the threaded part minus one screw diameter
$f_{ax,\alpha}$	withdrawal strength at an angle α to the grain

The effective length l_{ef} is measured on the test specimen to be approximately 25mm, see Figure 19.7.

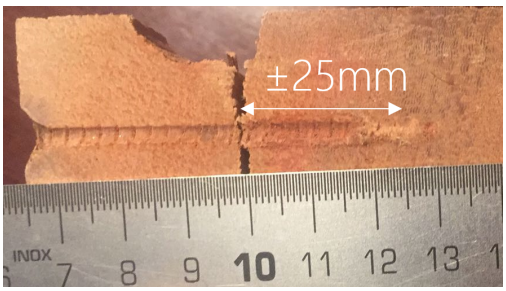

Figure 19.7: Effective withdrawal length measured on the test specimen

The EC5 (2004) gives the following equation to calculate the withdrawal strength $f_{ax,\alpha}$:

$$f_{ax,\alpha,k} = \frac{f_{ax,k}}{sin^2(\alpha) + 1.5cos^2(\alpha)} = \frac{3.6 \cdot 10^{-3}\rho_k^{1.5}}{sin^2(\alpha) + 1.5cos^2(\alpha)} \tag{19.22}$$

Using the mean value for the density (instead of the characteristic value) $\rho_{mean} = 1050kg/m^3$, this gives $f_{ax} = 122.5N/mm^2$. Using equation 19.25 gives a withdrawal capacity $F_{ax,R1} = 39.2kN$.

NEN-EN 1995-1-1=2011

The newer version of the EC (2011) gives a different calculation method than the EC5 from 2005. The new code distinguishes between connections with screws that meet the following two requirements, and connections that do not:

- $6mm \leq d \leq 12mm$
- $0.6 \leq d_1/d \leq 0.75$

In case they do not, the withdrawal strength strength can be calculated using the following equation:

$$F_{ax,\alpha,R} = \frac{n_{ef} f_{ax} d l_{ef} k_d}{1.2cos^2(\alpha) + sin^2(\alpha)} \cdot (\frac{\rho_k}{\rho_a})^{0.8} \tag{19.23}$$

Where $f_{ax,k}$ is the characteristic withdrawal parameter perpendicular to the grain which should be determined by tests according EN 14592 for the associated density ρ_a. Since the diameter of the screws that are used for the tests is 5mm, it would be required to perform lab tests in order to define the right withdrawal parameter. Since this is out of the scope of the project, the equations that are suitable for diameters between 6 and 12mm will be used to get an indication of the order of magnitude. The following equation is stated in NEN-EN 1995-1-1 (2011) to calculate the withdrawal strength:

$$f_{ax,k} = 0.52 d^{-0.5} l_{ef}^{-0.1} \rho_k^{0.8} \tag{19.24}$$

Where all parameters are mentioned before in the calculation according to the NEN-EN 1995-1-1=2005 ($d = 5mm, l_{ef} = 25mm, \rho_{mean} = 1050 kg/m^3$). This gives $f_{ax} = 44 N/mm^2$. Subsequently, the withdrawal capacity can be calculated:

$$F_{ax,\alpha,R} = \frac{n_{ef} f_{ax} d l_{ef} k_d}{1.2cos^2(\alpha) + sin^2(\alpha)} \tag{19.25}$$

With:

$$k_d = min \begin{cases} \frac{d}{8} \\ 1 \end{cases} \tag{19.26}$$

This results in a withdrawal capacity of $F_{ax,R3} = 9.2 kN$.

Capacity of Rothoblaas screws according to the ETA

The ETA has published a assessment of Rothoblaas' self-tapping screws in *European Technical Assessment ETA-11/0030 of 2016-04-07* [6]. In this report, the following equation to determine the withdrawal capacity of fully threaded screws is given:

$$F_{ax,\alpha,Rk} = \frac{n_e f \cdot 11.7 \cdot d \cdot l_{ef}}{1.2 \cdot cos^2(\alpha) + sin^2(\alpha)} \cdot (\frac{\rho}{350})^{0.8} \tag{19.27}$$

The equation is based on EN 1995-1-1:2008 and it should be noted that the equation is meant for screws in softwood. Filling in the equation gives $F_{ax,R2} = 9.5 kN$.

Eckelman equation

In research carried out by M.A. Taj, S.K. Najafi and G. Ebrahimi on the *Withdrawal and lateral resistance of wood screw in beech, hornbeam and poplar*, two expressions to calculate the withdrawal capacity of screws were compared [57]:

- The expression given in the NDS (*National Design Specification for Wood Construction*):

$$W = 98.1 G^2 D L \tag{19.28}$$

Where:

W	withdrawal capacity of the wood screw $[N]$
G	specific gravity of wood (oven dried) $[-]$
D	The shank diameter of the screw $[mm]$

- The expression given by Eckelman:

$$W = 4.06 D (L - D)^{\frac{3}{4}} \sigma_S \tag{19.29}$$

Where:

W	withdrawal capacity of the wood screw $[kg]$
D	shank diameter of the screw $[cm]$
L	threaded portion of screw in the wood $[cm]$
σ_s	shear strength parallel to the grain of the wood $[kg/cm^2]$

A comparison of test results to the ultimate withdrawal resistance calculated with the above mentioned expressions showed that the Eckelman equation gives the best prediction [57]. Given that $D = 0.5cm, L = 2.5cm$ and $\sigma_S = 16.2 N/mm^2 = 165.2 kg/cm^2$, the withdrawal capacity according to the Eckelman equation is $W = 845 kg = 8287 N$. Assuming an effective number of screws of $n_{ef} = 2.69$ gives $F_{ax,R4} = 22.3 kN$

For comparison, the withdrawal capacity is also calculated according to the NDS (Equation 19.28). Using $G = \frac{\rho_{timber}}{\rho_{H2O}} = 1050/1000 = 1.05$, $D = 5mm$ and L = $25mm$ gives $W = 13.52 kN$. Assuming an effective number of screws of $n_{ef} = 2.69$ gives $F_{ax,R5} = 36.4 kN$

Canadian timber design codes

In research carried out by S. Kennedy, A. Salenikovich, W. Munoz and M. Mohammad called *Design equation for withdrawal resistance of threaded fasteners in the Canadian timber design code* five calculation methods from the Canadian, the American *National Design Specification for Wood Construction* (NDS) and two other research studies are evaluated by comparing the predicted values to test data. Below, the withdrawal capacity will be calculated using all five methods. The following parameters are relevant:

$P_{rw,avg}$	average withdrawal resistance $[N]$
P_{rw}	the specific withdrawal resistance $[N]$
d	the fastener nominal diameter $[mm]$ ($d = 5mm$)
G_0	the measured relative density based on oven-dry mass and volume $[-]$ (it is assumed that $G_0 = G = 1.05$)
G	the mean relative density for the species or species group based on oven-dry mass and volume $[-]$ ($G = 1.05$)
L	the length of penetration in the wood specimen $[mm]$ ($L = 25mm$)
n_{ef}	the effective number of screws $[-]$ ($n_{ef} = 2.69$)

- CSA O86-09 equation for wood-screws

$$P_{rw,avg} = 112 d^{0.82} G_0^{1.77} L \tag{19.30}$$

  - $P_{rw,avg} = 11.4kN$
  - $F_{ax,R6} = n_{ef} P_{rw,avg} = 30.7kN$

- NDS-2012 equation for lag screws

$$P_{rw,avg} = 116 d^{0.75} G_0^{1.5} L \tag{19.31}$$

  - $P_{rw,avg} = 10.4kN$
  - $F_{ax,R7} = n_{ef} P_{rw,avg} = 28.1kN$

- NDS-2012 equation for wood screws

$$P_{rw,avg} = 98 d G_0^2 L \tag{19.32}$$

  - $P_{rw,avg} = 13.5kN$
  - $F_{ax,R8} = n_{ef} P_{rw,avg} = 36.3kN$

- McLain equation for lag screws

$$P_{rw,avg} = 165 d^{0.61} G_0^{1.35} L \tag{19.33}$$

  - $P_{rw,avg} = 11.8kN$
  - $F_{ax,R9} = n_{ef} P_{rw,avg} = 31.6kN$

- MHBH equation for lag screws

$$P_{rw,avg} = 110 d^{0.75} G_0^{1.5} L \tag{19.34}$$

  - $P_{rw,avg} = 9.7kN$
  - $F_{ax,R10} = n_{ef} P_{rw,avg} = 26.0kN$

Overview of results

The withdrawal strengths calculated with the methods as described in the previous sections are shown in a bar chart in Figure 19.8.

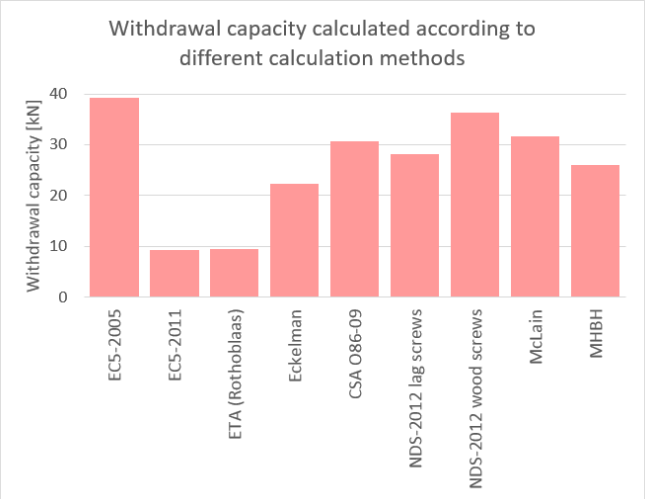

Figure 19.8: Withdrawal strength according to several methods

The really low strengths according to the EC5 (2011) and the ETA (for Rothoblaas screws) are remarkable. In the EC5 (2011), the applicability of the used equations was limited to certain diameter sizes. Since the diameter of the screws that are used for the tests did not fulfil this requirement, this could explain the deviation from other methods. The low strength value provided by the ETA could be explained by the fact that the equation is meant for screws in softwood and might therefore not be applicable in case hardwood is applied.

The remaining methods give strength values in the range from 26 to 39.2kN, with a mean of 30.6kN. This value will be used to predict the strength of the reinforced test specimens.

Prediction shear capacity of the reinforced specimens

As mentioned before in Equation 19.20, the shear strength of reinforced notched beams can be estimated using the following expression as determined by Henrici and stated in the Eurocode:

$$V_{Henrici} = \frac{F_{t,90}}{1.3 \cdot [3(1-\alpha)^2 - 2(1-\alpha)^3]} \tag{19.35}$$

Assuming $F_{t,90} = 30.6kN$ and $\alpha = 0.35$ gives $V_{Henrici} = 32.8kN$. Figure 19.9 shows a comparison of the estimated capacities with test results.

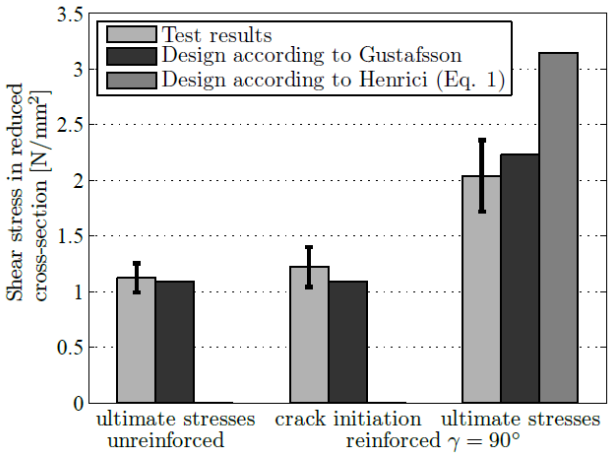

Figure 19.9: Comparison of estimated capacities with test results as part of the research by R. Jockwer, A. Frangi, E. Serrano and R. Steiger [2]

The diagram shows that the ultimate stresses are estimated with a factor of approximately 1.5 when the expression developed by Henrici is used (Equation 19.35). This would mean that the strength of the tests specimens is approximately $V_{predicted} = V_{Henrici}/1.5 = 21.9kN$.

19.1.4. Summary

Table 19.1 summarises the predictions made:

Table 19.1: Predicted shear strength values

Type of test	Critical shear force [kN]	Factor [-]
Sharp, no screws	18.8	1.0
Rounded, no screws	20.7	1.1
Sharp, with screws	21.9	1.2

The expected increase in capacity when applying rounded edges is 10%. An increase of 20% is predicted when screws are applied.

19.2 Prediction of deflections

In order to determine the required height of the supports, the deflections at mid-span should be determined. The bending moment depends on the exact distance between the supports. A conservative assumption is that this length $L = L_{beam1} = 600mm$. For specimens with sharp edges, the expected failure load is 37.6kN. This gives the following bending moment:

$$M_{mid} = \frac{1}{4}FL = \frac{1}{4} \cdot 37.6 \cdot 0.6 = 6.6kNm \tag{19.36}$$

The following approximation of the deflection is made:

$$I = \frac{1}{12}w_1 h_1^3 = \frac{1}{12} \cdot 95 \cdot 95^3 = 6.79 \cdot 10^6 mm^4 \tag{19.37}$$

$$\delta_{mid} = \frac{1}{48}\frac{FL^3}{E_{avg}I} = \frac{1}{48}\frac{37.6 \cdot 10^3 \cdot 600^3}{1.82 \cdot 10^4 \cdot 6.79 \cdot 10^6} = 1.37mm \tag{19.38}$$

For this calculation, it is assumed that there are no deflections at the supports. At a certain point, a crack will appear at the notch, resulting in an additional deflection of the beam. When this crack propagates, the deflection will likewise increase. Since the capacity of the beam decreases during crack propagation, the force applied on the beam will decrease as well. At a certain point, brittle failure is expected where the beam will split along the grain.

19.3 Expected load-displacement graph

Since the failure is parallel to the grain, brittle failure is expected. Figure 19.10 shows the expected load-displacement graph.

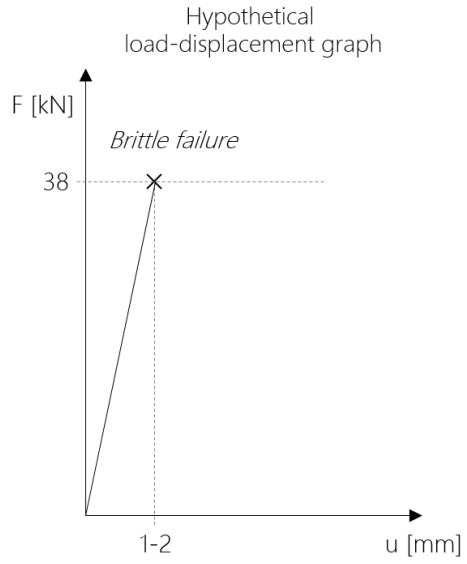

Figure 19.10: Hypothetical load-displacement graph

20

Test Results

20.1 Results of the tests without screws

In the next sections, the test results will be presented by means of force-displacement curves and pictures of the failure mechanisms of the different types of specimens.

20.1.1. Specimens with sharp edges

Figure 20.1 shows the force-displacement curves of the three specimens with sharp edges (specimen 2, 3 and 4). The slopes (and therefore the elasticity) as well as the failure load of all three specimens are similar. The jump in the curve from specimen 2 is the result of the correction applied to the measurement data from measuring device S01 (settlement of the weight). Measuring devices OS01 and OS02 were placed after testing specimen 2. For the other curves, the data from device OS01 was used.

Assuming that half of the load is transferred to the connection, the following mean value and standard deviation are found:

- $\mu_{Fv} = 10.51 kN$
- $s_{Fv} = 0.27 kN$

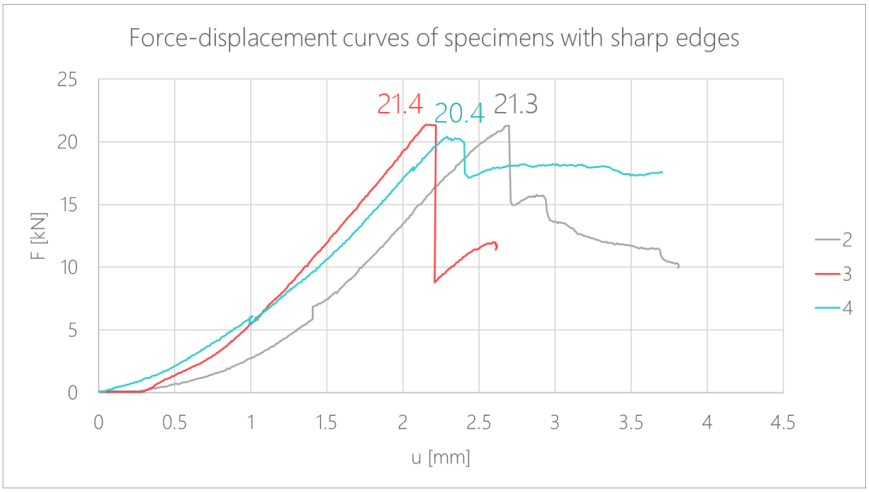

Figure 20.1: Force-displacement curves of the specimens with sharp edges including the maximum values (Specimen 2, 3 and 4)

In all three cases, the beam split exactly at the top of the notch as marked red in Figure 20.2 (top left). In longitudinal direction the crack follows the direction of the fibres.

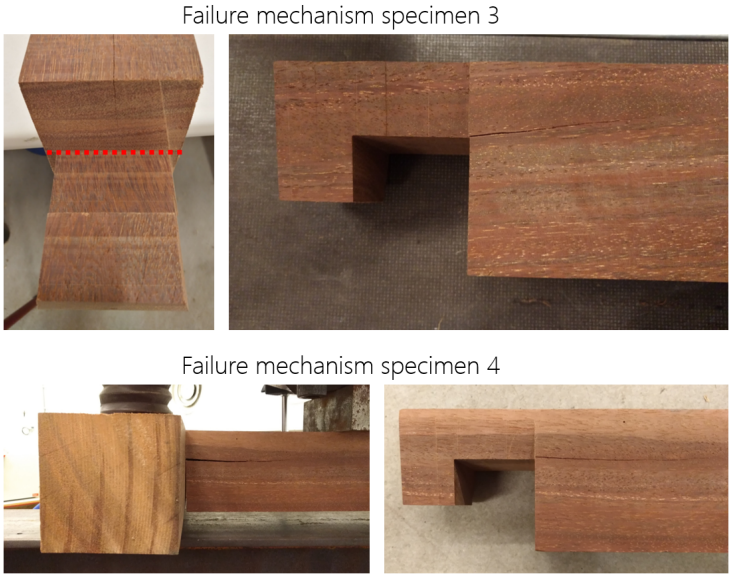

Figure 20.2: Failure mechanism of the specimens with sharp edges (specimen 3 and 4)

20.1.2. Specimens with rounded edges

Figure 20.3 shows the force-displacement curves of the three specimens with rounded edges (specimen 6R, 7R and 10R). Again the slopes as well as the failure load of all three specimens are very similar.

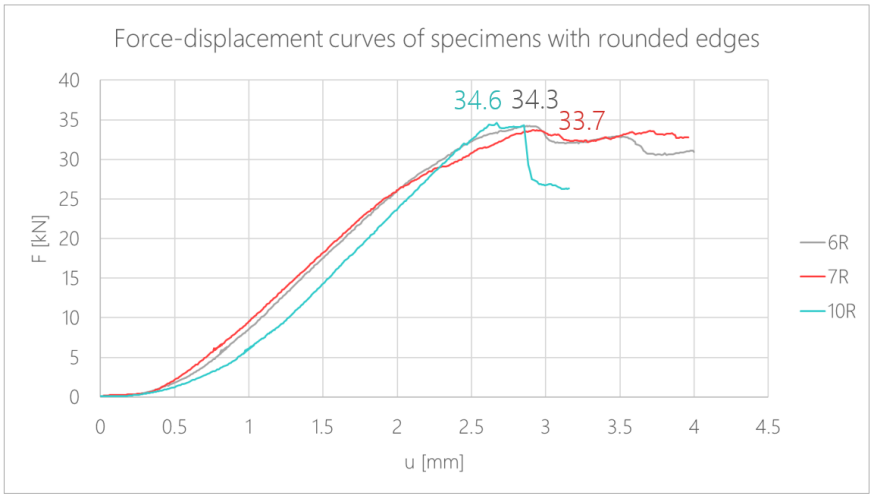

Figure 20.3: Force-displacement curves of the specimens with rounded edges including the maximum values (Specimen 6R, 7R and 10R)

The following mean value and standard deviation are found for the shear capacity of beam 1:

- $\mu_{Fv} = 17.10 kN$
- $s_{Fv} = 0.22 kN$

The shear capacity is 1.6 times larger than the shear capacity of the specimens with sharp edges.

In contrast to the specimens with sharp edges, the start of the crack at the notch is more arbitrary, see Figure 20.4. In longitudinal direction the crack still follows the direction of the fibres.

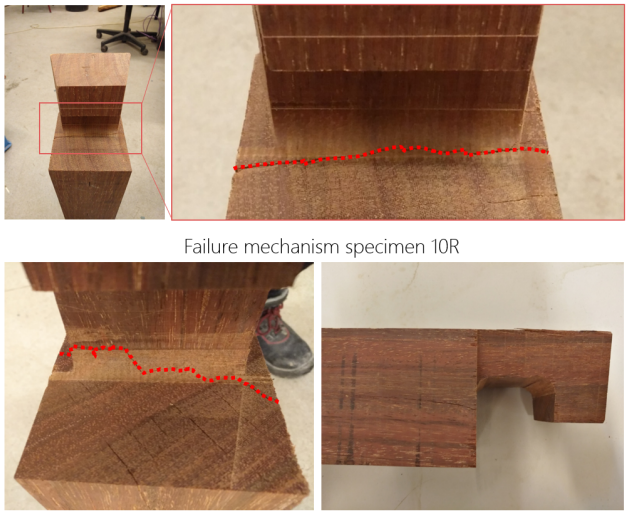

Figure 20.4: Failure mechanism of the specimens with rounded edges (specimen 6R and 10R)

20.2 Results of the tests with screws

As mentioned in Section 18.3, two types of tests are done (with undamaged members (dark coloured curves) and cracked members (light coloured curves). The results are shown in Figure 20.5.

Excluding the specimens that were tested before, the following mean values and standard deviations for the shear force in the connection ($\frac{1}{2}F$) are obtained:

- With sharp edges:
  - $\mu_{Fv,sharp} = 23.10\,kN$
  - $s_{Fv,sharp} = 1.58\,kN$
- With rounded edges:
  - $\mu_{Fv,rounded} = 31.14\,kN$
  - $s_{Fv,rounded} = 3.73\,kN$

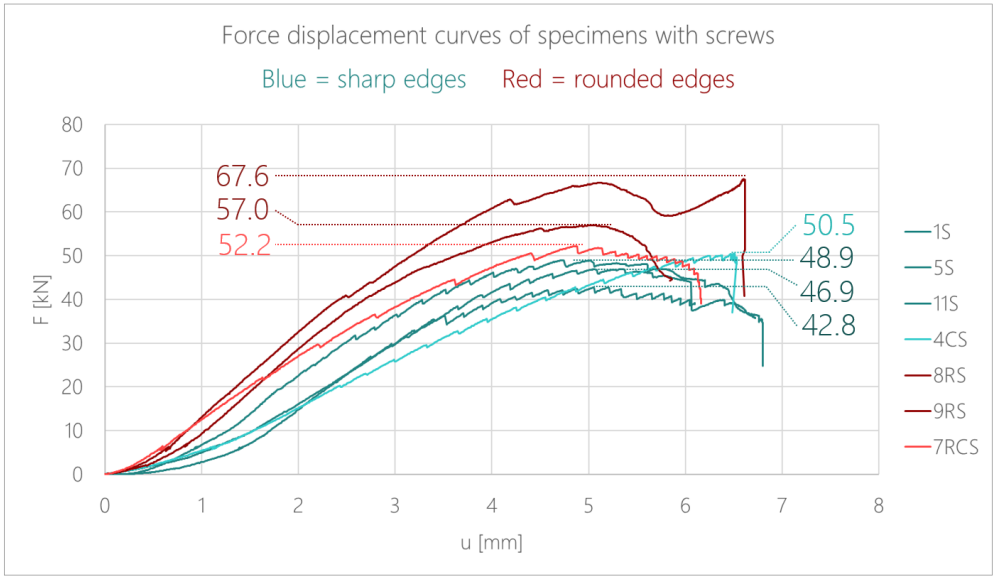

Figure 20.5: Force-displacement curves of the specimens with screws including the maximum values (Specimen 2, 3 and 4)

For safety reasons the tests were aborted before the capacity completely dropped due the occurrence of large rotations, see Figure 20.6.

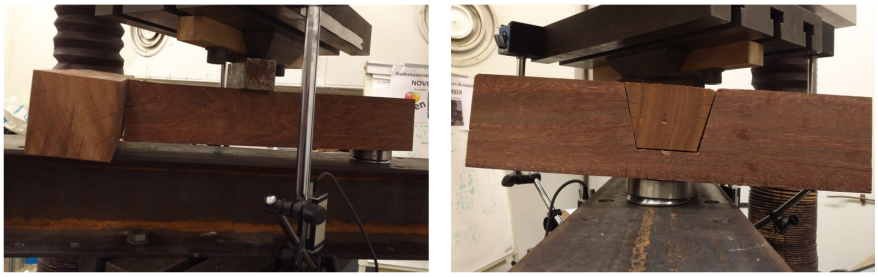

Figure 20.6: Rotation and torsion of the specimen when a large force was applied (specimen 7RCS)

Figure 20.7 and 20.8 show reinforced specimens with sharp (11S) and rounded (8RS) edges during, shortly after and a few minutes after testing. It can be seen that the failure mechanisms are similar to the ones of the specimens without screws (sharp edges: straight along the notch, rounded edges: arbitrary course). The major differences are the larger size of the gap and longer length of the crack. The high shear strenth of specimen *8RS* could be explained by the curved course of the crack, see Figure 20.8. Since the fibre direction is not completely horizontal, the fibres are loaded at a slight angle to the grain, resulting in a higher strength.

During loading shortly after loading Few minutes after loading

Figure 20.7: Failure mechanism of a specimen with sharp edges and reinforced with screws (specimen 11S)

During loading shortly after loading Few minutes after loading

Figure 20.8: Failure mechanism of a specimen with rounded edges and reinforced with screws (specimen 8RS)

In order to get insight into the behaviour of the screws, for two of the specimens (11S and 8RS), the screws were removed and the beam cut through at the former location of the screws, see Figure 20.9. No damage to the screws was detected. From the large diameter of the screw hole below the crack it can be concluded that pull out of the screws occurs. At the top, small slip is observed. This can explain the stepped course of the force-displacement curves. Likely each step results from a (number of) fibre(s) tipping over the thread.

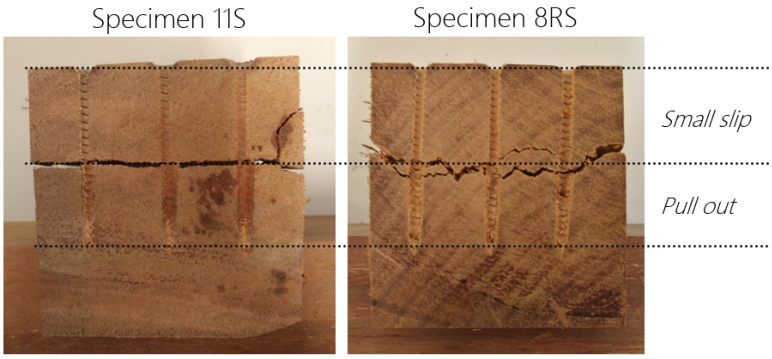

Figure 20.9: Failure mechanism of the screws: pull out below and small slip above the crack

20.3 Moisture content

The test specimens were kept wet between the day of production and the day of testing (21-6-2018). After testing, from each test specimen a sample with a width of approximately 2cm was cut, just after the location of cracking, see figure 20.10.

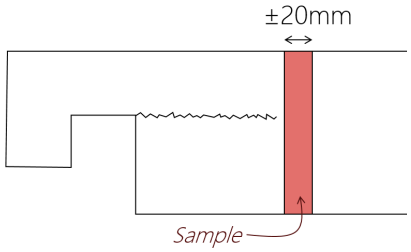

Figure 20.10: Sample for moisture content measurement

Subsequently, the samples were weighted directly after cutting on the day of testing (20-6-2018). After they were placed in an oven and weighted again on 21-6-2018 and 25-6-2018. The mass of the samples at the day of testing (m_u) and the oven dry wood at 25-6-2018 (m_{dtr} are used to calculated the moisture content of the specimens during testing, using the following equation:

$$u = \frac{m_u - m_{dtr}}{m_{dtr}} \cdot 100 \tag{20.1}$$

Where:

u	is the moisture content of the wood [%]
m_u	is the mass of the moist wood [g]
m_{dtr}	is the mass of the oven-dry wood [g]

Table 20.1: Mass of the samples during before, during and after drying and moisture content

Specimen	**Weight [g]**			**Moisture content [%]**
	20-6-2018	21-6-2018	25-6-2018	
1S	251.2	184.9	184.5	36.2
2	243.4	182.2	181.7	33.9
3	208.3	147.7	147.6	41.1
4CS	196.9	143.0	142.8	37.9
5S	227.8	160.8	160.6	41.8
6R	225.7	177.2	176.6	27.8
7RCS	241.8	176.9	175.9	37.4
8RS	210.9	163.3	162.7	29.6
9RS	221.4	164.1	163.4	35.5
10R	227.2	162.2	161.8	40.4
11S	214.7	153.7	153.4	39.9

21

Test Evaluation, Conclusions and Recommendations

21.1 Evaluation

In Chapter 19, an estimation of the shear capacity for three types of tests was made. Table 21.1 shows both the tested and predicted values.

Table 21.1: Tested and predicted shear capacity

Type	**Critical shear force [kN]**	
	Tested	Predicted
Sharp, no screws	10.51	18.8
Rounded, no screws	17.10	20.7
Sharp, with screws	23.10	21.9
Rounded, with screws	31.14	-

It can be seen that especially the capacity of the specimens with sharp edges was significantly overestimated. In this section, a few possible reasons for the deviation between tested and predicted values are summoned.

21.1.1. Shift of the supporting point due to rotations

One possible reason is the shift of the supporting point due to rotations of both beam 1 and 2 during loading As earlier shown in Figure 20.6, large rotations occurred during testing, especially in case of the specimens with screws :

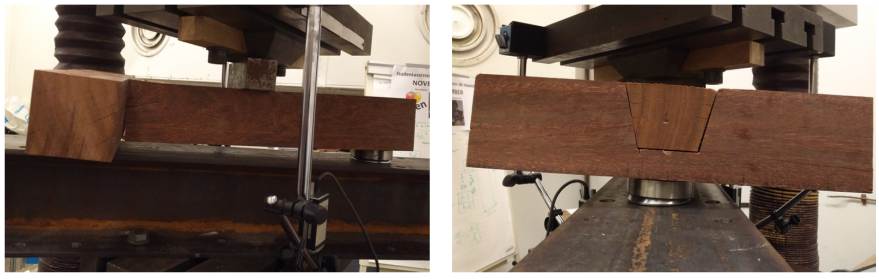

Figure 21.1: Rotation and torsion of the specimen when a large force was applied (specimen 7RCS)

This could have lead to a shift of the supporting point due to the eccentric point of application of the load with respect to the support as shown in Figure 21.2.

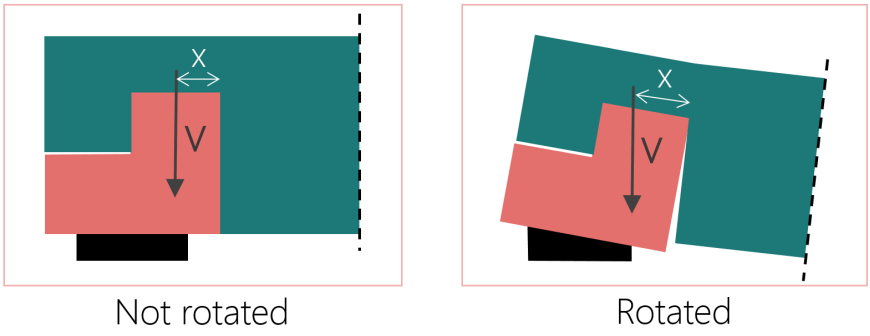

Figure 21.2: Shift of the supporting point due to rotations at the support

In order to make a safe estimation of the point of application of the load, the worst case scenario could be assumed: $x_{max} = b_2 = (1 - b_{1-ratio}) \cdot w_2 = 0.6 \cdot 95 = 57mm$ (instead of x = 28.5mm). This would result in the following shear capacity, using Equation 19.12 in Section 19:

$$V_f = \frac{(b\alpha d)\cdot\sqrt{\frac{G_{f,y}}{d}}}{\sqrt{\frac{0.6(\alpha-\alpha^2)}{G_{xy}}} + \beta\sqrt{\frac{6(\frac{1}{\alpha}-\alpha^2)}{E_x}}} = \frac{(95 \cdot 0.35 \cdot 95)\sqrt{\frac{1.34}{95}}}{\sqrt{\frac{0.6(0.35-0.35^2)}{1138}} + 0.6\sqrt{\frac{6(\frac{1}{0.35}-0.35^2)}{18200}}} = 13.0kN \tag{21.1}$$

21.1.2. Moisture content

Another reason could be that the equation used to calculate the fracture energy is not applicable for timber with a high moisture content. Since it is an empirical equation, it is hard to trace the effect. Additional tests could give more insight in the dependency between fracture energy and moisture content.

21.1.3. Crack width

For the prediction of the effect of the rounded edges a shift of the crack downwards was assumed. When looking at the failure mechanism of the test-specimens, it can be concluded that this was a good assumption. In some cases the shift was even larger than expected. Something that was not taken into account is the increase in crack width. The specimens with sharp edges have a completely straight crack along the notch, with a width equal to the width of the beam. The course of the crack in specimens with rounded edges is more random and has therefore a length larger than the width of the specimen requiring more energy to initiate the crack, see Figure 21.3. This will lead to a higher capacity than calculated with Gustafsson's equation (Equation 19.12).

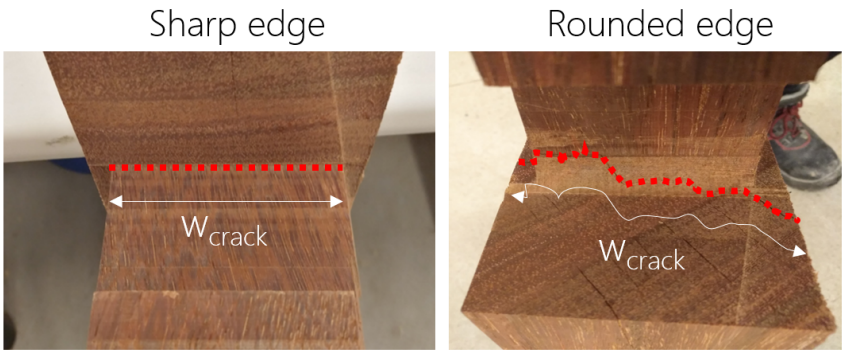

Figure 21.3: Increase in crack width when applying rounded edges

21.2 Conclusions

Figure 21.4 and Table 21.3 summarise all test results.

Table 21.2: Mean values and standard deviations of the different types of test specimens

Type	μ **[kN]**	s **[kN]**	**Factor [-]**
Sharp, no screws	10.51	0.27	1.0
Rounded, no screws	17.10	0.22	1.6
Sharp, with screws	23.10	1.58	2.2
Rounded, with screws	31.14	3.73	3.0

When comparing the test result to the predicted value using Gustaffson's equation is not really exact in predicting the shear capacity of notched members made of Azobé. The number of test specimens is too small to get complete clarity about the reason for this deviation. Additional tests on the the fracture energy of hardwood and it's dependency on the moisture content of the wood could give more insight.

The factor in the right column of Table 21.3 indicates the increase in capacity when adjustments are made to the most simple design: no screws and sharp edges. By applying rounded edges instead of sharp edges, the shear capacity of the connection is increased by a factor of 1.6. This is the result of the shift of the crack downwards. Furthermore, the rounded edges prevent the occurrence of very local peak stresses. This results in a longer crack path at the edge, associated with a larger shear capacity. An even higher capacity is achieved when the beam is reinforced by placing screws just after the notch. An increase in shear capacity with a factor 2.2 (sharp edges) and 3.0 (with rounded edges) is obtained. It is therefore recommended to always apply rounded edges, since a higher capacity is obtained without increasing the costs and fabrication time. The application of screws, on the other hand, makes the fabrication process more complicated. The possible material savings due to the increase in capacity should therefore be weighed against the increase in fabrication costs and time. This applies to all types of structures with notched members, including for example lock gates or timber roof structures.

Capacities in the same order of magnitude are found when the screws are placed after a crack is developed. This means that the placement of screws is a suitable measurement for repair in case cracks are detected during life-span.

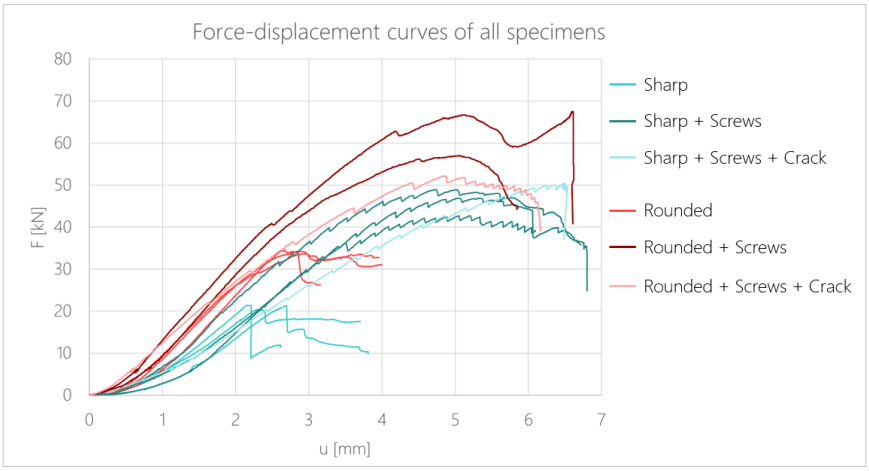

Figure 21.4: Force-displacement curves for all specimens

21.3 Recommendations

21.3.1. Future tests

Given the big differences in results between the different type of specimens, it would be interesting to do a variant study. The following parameters could be varied:

- The radius
- Regarding the screws:
  - Screw diameter
  - Screw length
  - Number of screws

- Location of the screws (edge distance)

Moreover, currently the proportions and size of the test specimens are kept constant. A ratio of 0.35 between the narrow part and full cross-section height was applied. It would be interesting to perform similar tests with different ratios.

Bending moment capacity of the hook of beam 1

The results of the test show a large increase of capacity when screws are applied. This measure could also be used to increase the bending moment capacity of the hook of beam 1, as discussed in section 18.2.2. The horizontal load on the hook results in a bending moment, associated with a compression and tension stress in the hook, see Figure 21.5 (left). When a screw is placed, (part of) the tension stress can be taken by the screw. This is a way to deal with the great uncertainty regarding the tensile strength perpendicular to the grain.

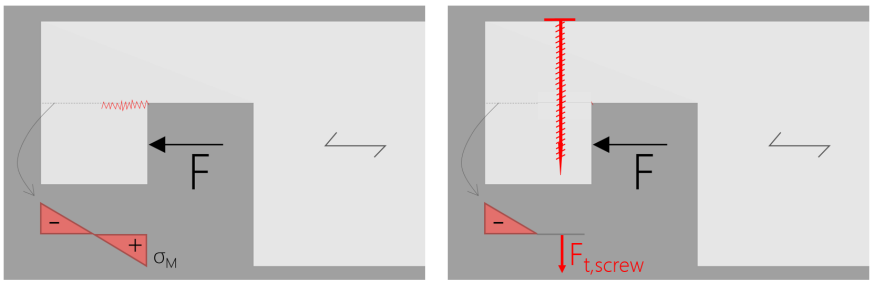

Without screw With screw

Figure 21.5: Stress distribution in the hook of beam 1 with and without screws

21.4 Adjustments to calculation model of the connection

For now it will be assumed that the capacity can be calculated using the equation using the fracture energy, using 5% values for the stiffnesses.

$$\frac{V_f}{b\alpha d} = \frac{\sqrt{\frac{G_{f,y,d}}{d}}}{\sqrt{\frac{0.6(\alpha-\alpha^2)}{G_{xy,d}}} + \beta\sqrt{\frac{6(\frac{1}{\alpha}-\alpha^2)}{E_{x,d}}}} \tag{21.2}$$

Where:

- $G_{f,y,k}$ is the fracture energy. $G_{f,y,k} = 1.29 N mm/mm$ is assumed for Azobé (see Equation 19.14, using $E_{x,k} = 16800 N/mm^2$ as calculated below)
- d is the depth of the beam in mm (h_1)
- b is the width of the beam (w_1)
- α the ratio between the effective depth and the real depth (a_1-ratio) [-]
- $beta$ is the ratio between the distance the support and end of the notch and the total height of the beam. As described in Section 21.1.1, the supporting point might shift to the end of the neck of the beam. A save assumption will therefore be made: $beta = (1 - b_{1,ratio})$
- $E_{x,k}$ is the modulus of elasticity parallel to the grain. For é $E_{x,k} = 16800 N/mm^2$
- $G_{xy,d}$ is the shear modulus in $[N/mm^2]$. $G_{xy,k} = \frac{E_{x,k}}{16} = 1050 N/mm^2$

Calculation of characteristic multiplication factor

From the tests could be concluded that the capacity is 3 times higher when rounded edges and three screws are applied. In order to embed some safety, the characteristic value should be determined. The characteristic value (5-percentile) of the multiplication factor can be determine by first calculating the characteristic value of the capacity for all four types of tests and subsequently recalculating the multiplication factor from this.

The strength parameters are assumed to be logarithmically normally distributed, in accordance with *NEN-EN 14358 Timber structures - Calculation and verification of characteristic values*. First, the mean value $\bar{y}$ and standard deviation s_y can be calculated using the following equations:

$$\bar{y} = \frac{1}{n}\sum_{i=1}^{n} ln(m_i) \tag{21.3}$$

$$s_y = max \begin{cases} \sqrt{\frac{1}{n-1} \sum_{i=1}^{n} (ln(m_i) - \bar{y})^2} \\ 0.05 \end{cases} \tag{21.4}$$

Where n is the number of test specimens and m_i is the strength parameter or resistance following from test specimen i. Subsequently, the 5-percentile of the sample can be calculated:

$$m_k = exp(\bar{y} - k_s(n) s_y) \tag{21.5}$$

Where:

$$k_s(n) = \frac{6.5n + 6}{3.7n - 3} \tag{21.6}$$

In case of 3 test specimens, this gives $k_s(3) = 3.15$. Using the test data for the four types of test specimens gives the following values for the characteristic strength parameters:

Table 21.3: Characteristic strenght parameters for the four types of test specimens

Type	m **[kN]**	m_k **[kN]**	**Factor [-]**
Sharp, no screws	10.51	9.0	1.0
Rounded, no screws	17.10	14.6	1.6
Sharp, with screws	23.10	18.5	2.1
Rounded, with screws	31.14	19.4	2.2

It is decided to both apply rounded edges and screws. The capacity that will be used is therefore:

$$V_d = k_{RS} \cdot V_f = 2.2 \cdot V_f \tag{21.7}$$

Where V_f is the shear capacity calculated with Equation 21.2 and $k_{RS} = 2.2$ the multiplication factor calculated from the characteristic strength values when both rounded edges and screws are applied.

VII

Case Study

22

Final Design

22.1 Starting points

Location

The location for which the bridge is designed is *The Green Village* in Delft (Van der Broekweg 4, Delft). The Green Village is a plot of land located at the campus of the TU Delft without governmental land-use planning. This simplifies the contracting process and therefore speeds up the realisation of projects. This plot of land is used to show innovative projects, developed at the TU Delft, see Figure 22.1. Currently there is already one pedestrian access bridge made of glass. The timber bridge could be placed next to it to show the possibilities of construction with different materials.

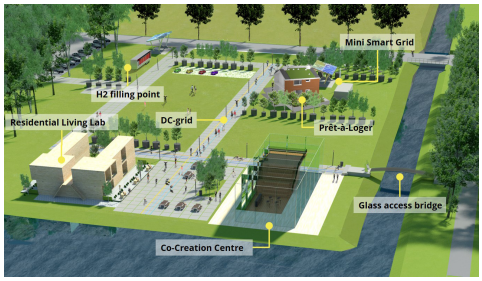

Figure 22.1: Impression of The Green Village [19]

Geometric boundary conditions

The required span of the bridge is approximately 10m. Since there is already another access bridge, a width of 2.5m is assumed to be sufficient. Because there is no traffic on the water, there are no requirements regarding the minimum clearance height. Furthermore, the abutments are at equal height and in line (no eccentricity).

Grid

Chosen is for a grid with the following details, see Figure 22.2:

Number of divisions in longitudinal direction (n)	6
Number of divisions in transverse direction (m)	4
Radius circumscribed circle of small triangles	70 to 120 mm

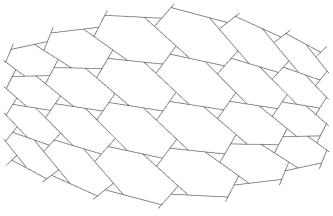

Figure 22.2: Applied grid

22.2 Adjustment of load cases

An adjustment has been made to the set of load cases. Instead of load case 1 till 4 as discussed in Table 22.1, a set of four asymmetric load cases have been applied. In each load case the crowd load is only applied on half of the bridge deck, see Figure 22.3.

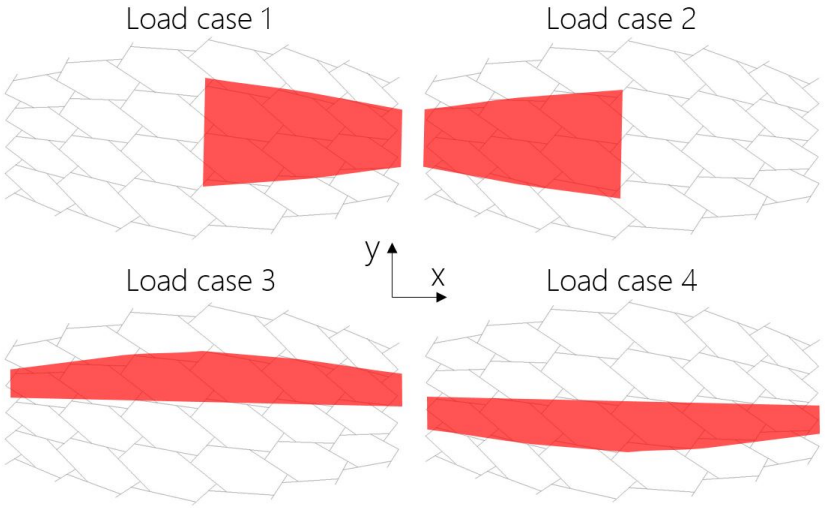

Figure 22.3: Location of the traffic load in adjusted load case 1 until 4

The following factors are used for all load combinations:

Table 22.1: Applied factors for all load combinations (Combination of load- and combination factors)

Load combination			γ_g	γ_t	$\gamma_{w,v}$	$\gamma_{w,h}$
1	LC2	C2	1.2	1.35	0.45	0.45
2	LC2	C2	1.2	1.35	0.45	-0.45
3	LC2	C2	1.2	1.35	0.45	0.45
4	LC2	C2	1.2	1.35	0.45	-0.45
5	LC2	C2	1.2	1.35	0.45	0.45
6	LC2	C2	1.2	1.35	0.45	-0.45
7	LC3	C3	1.2	0.54	1.5	1.5
8	LC3	C3	1.2	0.54	1.5	-1.5
9	LC2	C2	0.9	0	-0.45	0.45
10	LC2	C2	0.9	0	-0.45	-0.45
11	LC3	C3	0.9	0	-1.5	1.5
12	LC3	C3	0.9	0	-1.5	-1.5

22.3 Cross-section and shape optimisation

Cross section table

A cross-section table with standard section sizes from timber producer *Wijma* is used for the first cross-section optimisation as described in Section 9.1, Figure 9.2. The minimum standard section size that is feasible for CNC-milling is 95x95mm. The first thirty section sizes in the cross-section table are visualised in Figure 22.4

Figure 22.4: Standard cross-section sizes that are used for the cross-section optimisation

When using this cross-section table, a problem is encountered. A design is obtained in which beams with really different sizes connect, see Figure 22.5. This is unfavourable for the connection design.

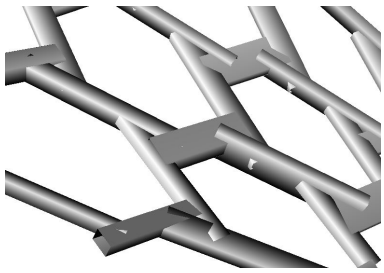

Figure 22.5: Problem with large differences between section sizes of connecting beams

For this reason it is decided to adjust the section table to allow only for beams with a small difference between height and width ($|w - h|_{max} = 100mm$). This gives the following cross-section table:

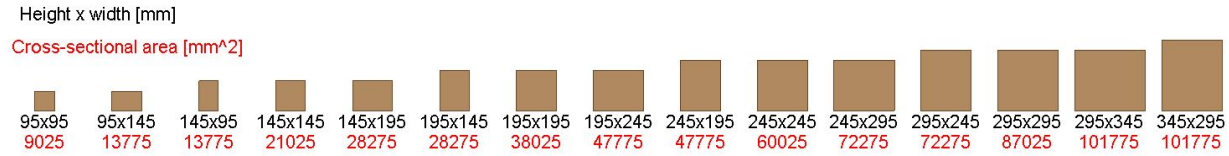

Figure 22.6: Updated cross-section sizes that are used for the cross-section optimisation

Shape optimisation

As described in Section 9.2, the shape of the bridge is optimised by varying two parameters: the height of the bridge at mid-span (h_{mid}) and the height (or depth) of the edges (dh_{top}). The following range for both parameters is analysed:

- $0.0m \leq h_{mid} \leq 1.0m$, step size = 0.1m
- $-1.0m \leq dh_{top} \leq +2.5m$, step size = 0.1m

Figure 22.7 shows a view different designs and their location in the design space.

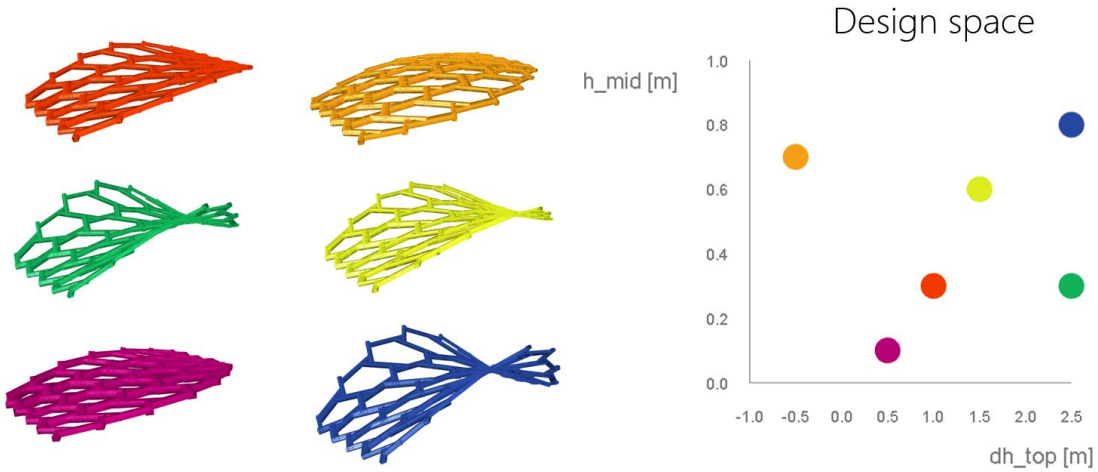

Figure 22.7: Six design options and their location in the design space

The shape optimisation is carried out using the evolutionary solver *Galapagos*. The structure is optimised for minimum material usage (minimum mass). The following fitness landscape is obtained:

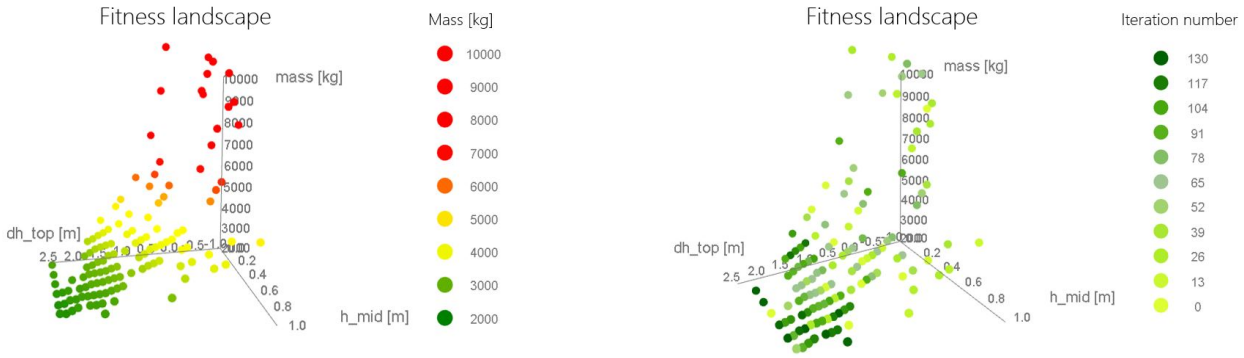

Figure 22.8: The fitness landscape after analysis of 130 designs using Galapagos

The figure on the right shows the iteration number using colour coding. It can be concluded that the algorithm works effectively since over time more designs in the area with a high fitness (low mass) are analysed (dark green). It is clear that a design with both a high h_{mid} and dh_{top} is favourable. The design with the smallest mass that was found after 130 iteration has the following details:

- h_{mid} = 0.7m
- dh_{top} = 2.5m
- Mass = 2665kg

Figure 22.9 shows the design with the smallest mass, found after 103 iterations.

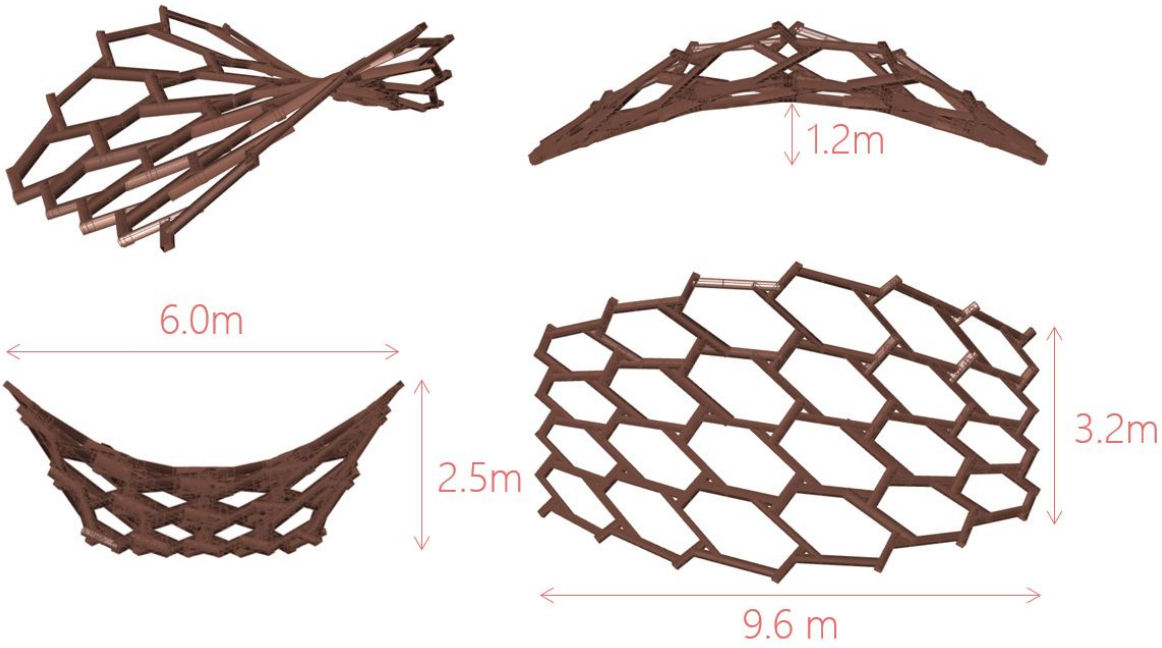

Figure 22.9: Design with the smallest mass found after 130 iterations

The bridge has the following details: Some specifications of the bridge are:

Global dimensions	
Span:	± 9.4m
Clearance (mid):	± 1.2m
Edge height (mid):	± 1.3m
Width (deck):	± 2.5m
Width (mid):	± 6.0m
Weight of the structure	
Weight of the timber	± 2665kg
Weight of the steel (screws)	± 5kg
Grid	
Type	Hexagonal reciprocal grid
Longitudinal divisions	6
Transverse divisions	4
Beams	
Maximum beam length:	± 2.0m
Minimum beam length:	± 0.5m
Number of beams:	93
Number of connections:	163

22.4 Forces in the global design

Figure 22.10 gives an overview of the maximum shear forces, bending moments and normal forces in the structure following from the analysis by *Karamba*.

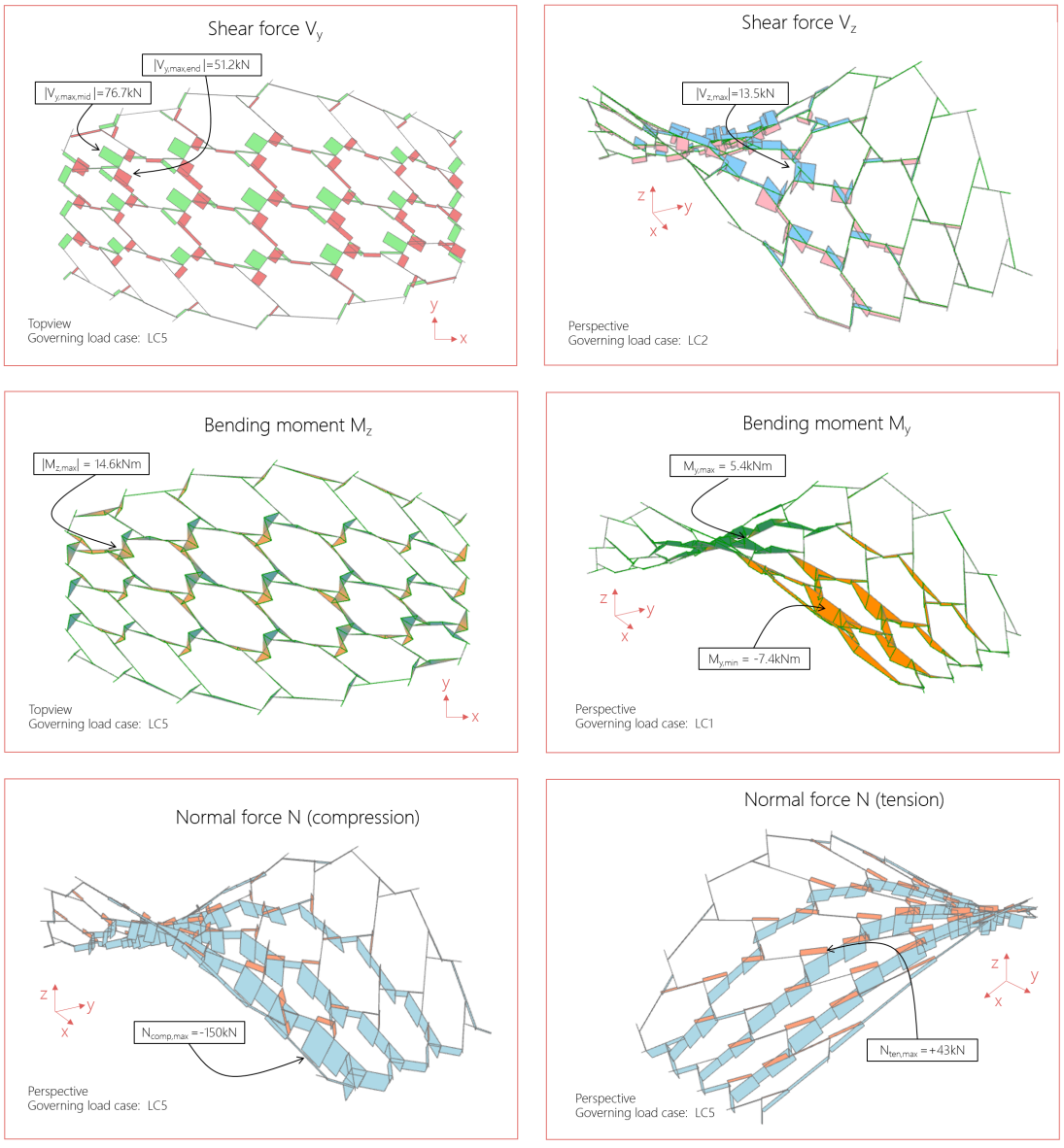

Figure 22.10: The maximum shear forces, bending moments and normal forces in the structure

Figure 22.11 shows the selection of beams and connections in which the maximum forces occur. The calculation of the unity checks that are related to these forces are discussed in Section 22.6.

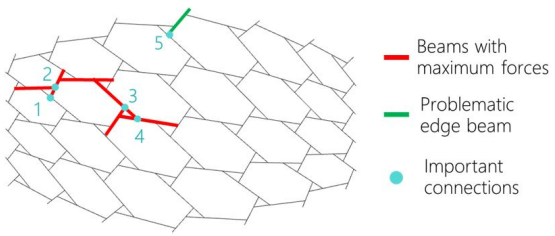

Figure 22.11: Selection of important connections based on the maximum forces that shown in Figure 22.10

22.5 Dimensions of the connections

Since for this case-study only one design iteration will be run through, it is decided to determine the dimensions of the connections by applying *Cross-section optimisation II* as described in Section 13.2 for all individual connections. This method is time-consuming but gives assurance that all connections fulfil the requirements. In order to speed up the process, the results of Cross-section optimisation I (COI), as described in section 9.1), are taken as starting point. The following discretisation for the seven parameters defining the dimensions of a connection is applied:

- a_1-ratio = [0.2, 0.3, 0.4, 0.5]
- a_2-ratio = [0.2, 0.3, 0.4, 0.5]
- b-ratio = [0.3, 0.4, 0.5, 0.6]
- h_1 = [$h_{1,COI}$, $h_{1,COI} + 50$, $h_{1,COI} + 100$]
- w_1 = [$w_{1,COI}$, $w_{1,COI} + 50$, $w_{1,COI} + 100$]
- h_2 = [$h_{2,COI}$, $h_{2,COI} + 50$, $h_{2,COI} + 100$]
- w_2 = [$w_{2,COI}$, $w_{2,COI} + 50$, $w_{2,COI} + 100$]

Every beam in the structure consists of three or four connection parts. Since all connection parts are designed independently, the possibility exists that the outer dimensions of the connecting beam parts do not match. It is decided to apply the maximum size that is present in one beam to the entire beam. The a_1-, a_2- and b-ratio remains unchanged.

Figure 22.12 shows the results of *Cross-section optimisation II* after the cross-section sizes are matched.

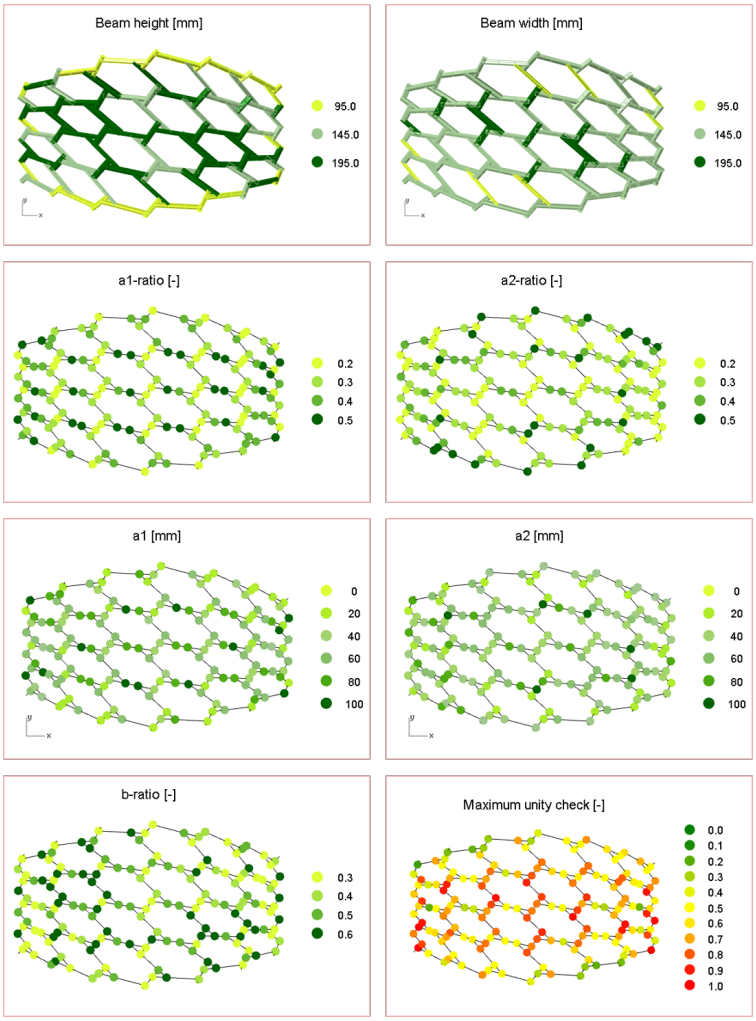

Figure 22.12: Result of *Cross-section optimisation II*

The following conclusions can be drawn:

- The beams with large heights can be found in the locations with high bending moments around the y-axis (M_y) and shear forces (V_y)
- Large widths are located at locations with high bending moments around the z-axis (M_z) and shear forces (V_y)
- Low a_1-ratios are located at locations with high compression forces. In this way the contact area at which the compression force is transferred is maximised
- Large values for a_1 are found at the locations with tensile forces in the beam.
- Low b-ratios are found at the locations where high bending moments occur, increases the bending moment capacity of the continuous beam

The figure on the bottom right shows the maximum unity check for each connection. It can be seen that the unity checks at the edges are low. This is the the fact that the minimum section size (95mm x 95mm) is restricted by the CNC-milling machine.

22.6 Verification of a set of connections

In this section, the calculation of the verification of four connections in which maximum forces occur is shown. The selection of these connection is shown in Figure 22.11. Additionally, the problem with a set of edge beams is discussed.

Verification of four important connections

Figure 22.13 and 22.14 show an example of the calculation of the the most important unity checks for four selected connections:

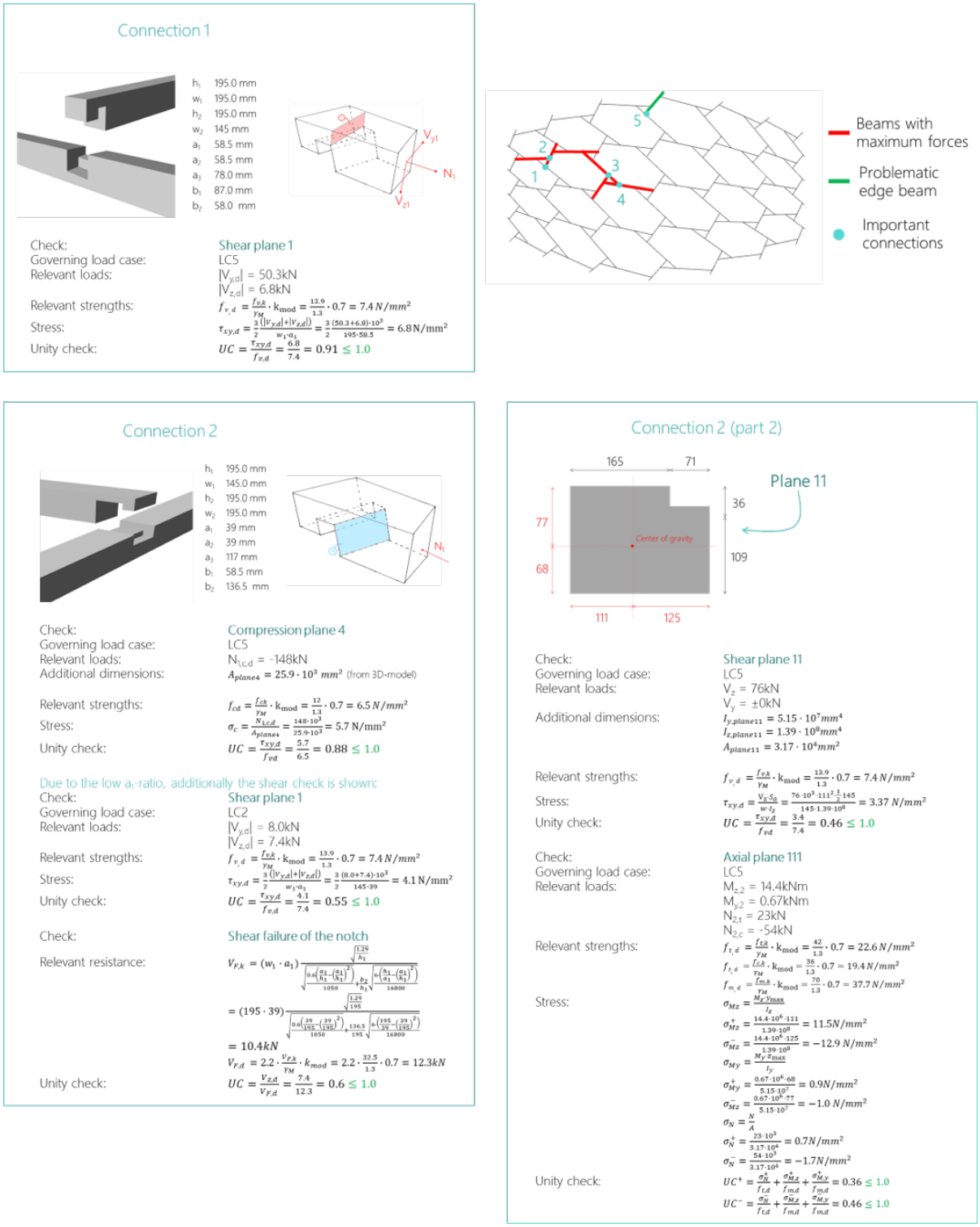

Figure 22.13: Verification of selected connection 1 and 2

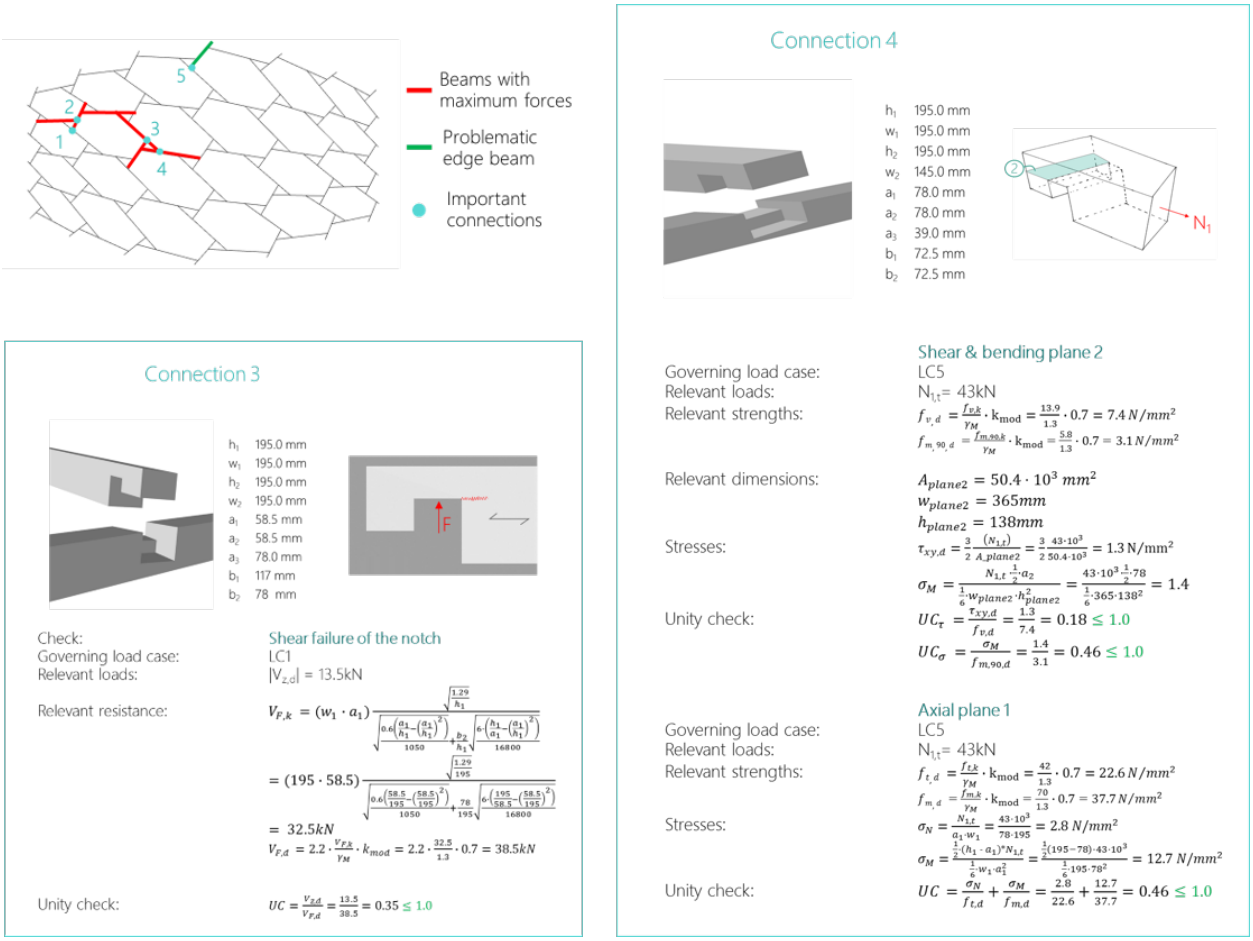

Figure 22.14: Verification of selected connection 3 and 4

Problematic edge beams

As discussed in Chapter 5, the beams can be modelled to be simply supported at the ends with two point loads along the span at the location of the connections. Nevertheless, a problem arises for a set of edge beams, see Figure 22.15. For the red marked beams, only one side of the beam is supported. Therefore, either the global design or the connection design should be adjusted. A few design options are given in Section 24.2.4. The design of the edges is out of the scope of the project. Despite, the order of magnitude of the loads in these problematic edge beams will be given to get an idea of the design situation.

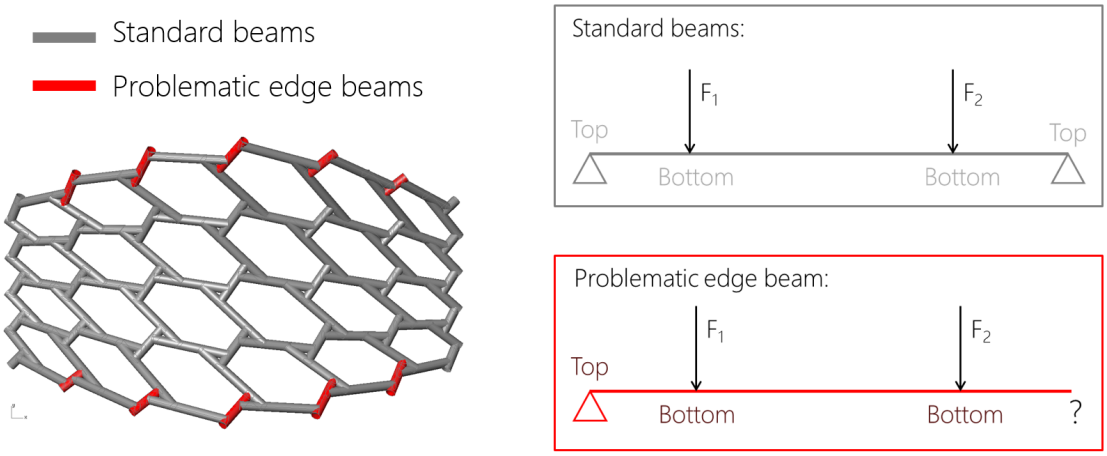

Figure 22.15: Problematic edge beams

In order to avoid a computational intensive model in the first design phase, a linear analysis is applied in which all connections can transfer both upward and downward loads. In reality this is not correct since the connection cannot transfer upward loads. For this reason, the loads in the problematic edge beams will in reality deviate from the forces that are presented. Nevertheless, for now this is disregarded. The following forces are found for the governing load case (LC1):

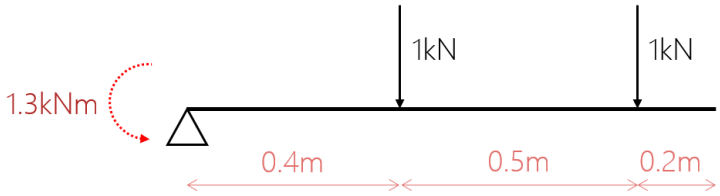

Figure 22.16: Order of magnitude of loads and sizes of the problematic edge beams

These forces induce a bending moment at the support of approximately 1.3kNm. Either the design of the connection should be adjusted for the concerning edge beams in order to transfer this bending moment or another measure should be taken to deal with the problem of the unsupported beams.

22.7 Deflections

In this research, focus was on the strength calculations of the structure. The serviceability and comfort criteria of the bridge are disregarded and would need to examined in further research. Nevertheless, Figure 22.17 shows the displacements that are found due to LC1 and LC5. A maximum displacement of 1.6 cm is found. Note that this is the displacement due to the design values of the loads. Normally the displacements are calculated with the characteristic values of the loads.

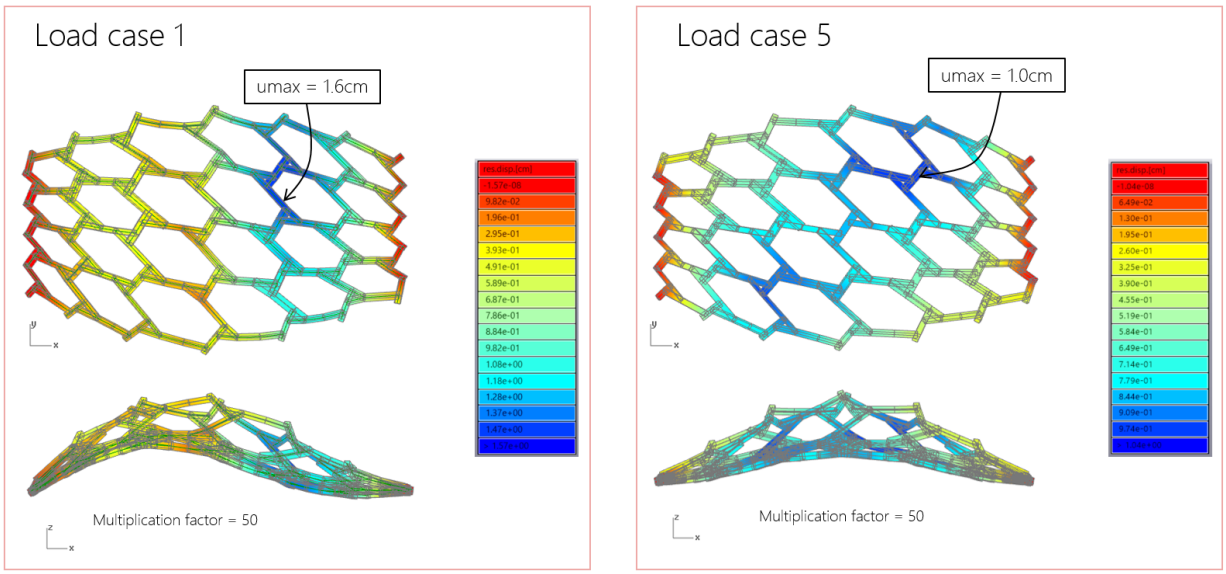

Figure 22.17: Displacements of the bridge due to LC1 (left) and LC5 (right)

22.8 Final design

Figure 22.18 shows the final design for the bridge, including the connections.

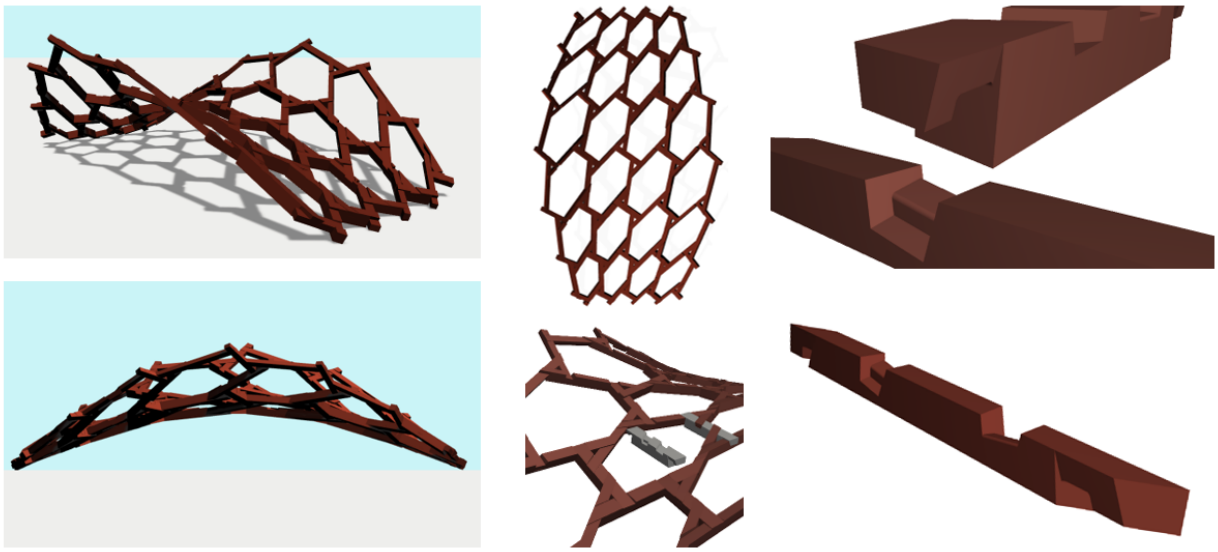

Figure 22.18: The final design for the case study

To give a clear overview, the specifications of the bridge that have already bean noted in in Section 22.3 are repeated:

Global dimensions	
Span:	± 9.4m
Clearance (mid):	± 1.2m
Edge height (mid):	± 1.3m
Width (deck):	± 2.5m
Width (mid):	± 6.0m
Weight of the structure	
Weight of the timber	± 2665kg
Weight of the steel (screws)	± 5kg
Weight per m^2 bridge deck	$89 kg/m^2$
Grid	
Type	Hexagonal reciprocal grid
Longitudinal divisions	6
Transverse divisions	4
Beams	
Maximum beam length:	± 2.0m
Minimum beam length:	± 0.5m
Number of beams:	93
Number of connections:	163

VIII

Conclusions & Recommendations

23

Conclusion

Rapid developments of both new (digital) fabrication techniques and innovative software facilitate the possibility to design, check and construct objects with great complexity and uniqueness without a large price tag. New fabrication techniques slowly enter the building sector through advanced architectural research institutes like the *Gramazio Kohler Research Group* of the ETH, Zürich [63] and the *Institute for Computational Design and Construction* of the University of Stuttgart [42]. Both focus on showcasing new computer-aided manufacturing processes through the design and construction of architectural structures like pavilions and art installations. The next step is to apply these new techniques in civil engineering to design structures with a load-bearing function in outdoor conditions, accompanied by strict safety requirements and a large number of load cases.

Furthermore, in current research only limited attention has been given to the design and optimisation of the connections, despite the fact that the connections are often critical in a structure. In existing free-form structures usually complex welded steel connections are applied, which obstruct the application of a completely digital fabrication and assembly process. In research projects on robotic timber fabrication a completely digital fabrication process is made possible by applying simple screwed, nailed and glued connections. [47] [63] [50] [25] However, these simple connections are unsuitable for application in structures with high loads and strict safety regulations. Therefore, in this research a strong emphasis is put on the design, structural calculation, detailing and integration of the connections into the global design.

To examine the above mentioned factors, in this research a case study is done on the design of a timber pedestrian bridge, fabricated using CNC-milling techniques. The case brings together the challenges that are accompanied by the design of a structure with a load-bearing function, and the advantages of digital fabrication techniques: the ability to design a free-form structure and to optimise all individual elements in a structure.

This research demonstrates that the inventive combination of a reciprocal gridshell structure with interlocking joints is suitable for a complete digital fabrication and assembly process. Lap joints, mostly known from traditional woodworking in for example ancient Japanese architecture, have lost their popularity over the past century due to a labour intensive fabrication process. With new fabrication techniques like CNC-milling this type of connection could make a revival. They allow for the connection of beams with different sizes, approaching from different angles and can accommodate the eccentricity required to create a double-curved free-form surface with straight beams. Additionally, they have a higher strength and stiffness than the conventional glued and screwed connections in digital timber fabrication projects, which makes them more convenient for a structure with a load-bearing function.

Although lap joints have been applied since thousands of years, there is only limited knowledge about the structural calculation of such connections since the design process was mainly based on trial and error. Something that is nowadays not possible anymore due to the strict safety regulations. Current research on the structural behaviour of interlocking joints is much focused on numerical modelling of one specific type of interlocking joint, resulting in a computational intensive model with limited applicability to designs that deviate from the examined design. [4] [16] Engineering firms that currently apply CNC-milling techniques like *Wijma Kampen B.V.* use calculation methods from codes and guidelines that are valid for standard shapes and traditional building methods. However, these methods are not suitable for the verification of non-standard geometries and cannot be integrated into a parametric workflow. For the application of lap joints in parametric free-form structures, simple calculation methods are required with applicability to a wide range of design parameters to allow for constantly changing connections and quick analysis. Therefore, in this research a simple calculation method is developed in which the stresses in all critical planes of a connection

are calculated and subsequently used to determine the relevant unity checks as stated in EC5. This method is integrated into the parametric design workflow.

When lap joints are applied in combination with a reciprocal structure, a stable system can be obtained without the application of any fastening materials, benefiting the assembly process, aesthetics and sustainability of the structure. Furthermore, the connections in a reciprocal structure are relatively simple since only two beams meet in one node and no bending moments and upward shear forces occur.

The great design freedom which is obtained with digital fabrication also comes at a price: a large complexity of design. The uniqueness of all beams and connections in a free-form structure demand an entirely parametric design. Because of the statical indeterminacy of the structure, the force-flow through the structure is dependent on the stiffness of each individual beam. This means that when the size of one single beam is adjusted, the forces in all beams change. Furthermore, since the connection of an interlocking joint is integrated in the beam, the size of the connection is limited by the size of the connecting beams. Therefore, global and connection design cannot be uncoupled. However, designing on global and connection level simultaneously is a complex task due the the lack of starting points. This problem can be solved by applying an iterative workflow in which first a feature of the global design is addressed, using reduction factors to account for the lower capacity at the connections. Subsequently the focus is shifted to the connection design, using the global design as starting point. After this, the two designs are integrated.

A new challenge occurs during the integration of the design at global and connection level. The large number and strong dependency of parameters influencing the optimal dimensions, the large amount of connections in one design and the static indeterminacy of the structure make it difficult to directly link parameters from the global design to suitable connection dimensions. Using machine learning to predict suitable dimensions is proven to speed up the connection design process in the first design phase in which still a lot of design changes are made. When the global design is adjusted, the algorithm can instantaneously predict the dimensions of the changed connections based on the new force distribution. Nevertheless, this algorithm requires input of a database with training input which is time consuming to construct. An alternative is to apply the same dimensions to all connections and spend more time to determine the dimensions of the connections that do not fulfil the requirements during the entire design process.

The application of new fabrication techniques is often associated with a lack of knowledge on the structural behaviour of the new material or type of design. In this case the largest source of uncertainty is the shear capacity of the notched beam. The Eurocode prescribes a calculation method for shear failure of notched members based on the fracture energy of softwoods. Previous research has indicated that this method is not suitable in case hardwood is applied. For this reason lab tests have been carried out at the TU Delft as part of this research. The tests confirm that the calculation method described in the Eurocode does not adequately predict the shear capacity of the notched beam and that additional research on the fracture energy of hardwoods is still required to make a more accurate prediction.

Rounded edges and screws were expected to improve the results. This was confirmed by lab tests. The tests showed an increase of shear capacity with a factor 1.6 when rounded edges instead of sharp edges were applied. Applying rounded edges in combination with three screws as reinforcement resulted in an increase with a factor 3.0. Additionally, both increase the ductility of the connection. It is therefore recommended to always apply rounded edges, since a higher capacity is obtained without increasing the costs and fabrication time. Screws perform even better, but the increase in capacity should be weighed against the increase in fabrication costs and time. This applies to all types of structures with notched members, including for example lock gates or timber roof structures.

This thesis has shown that the great design freedom that is made possible by applying digital fabrication techniques is accompanied by large complexity of design. The complexity is dealt with through the application of a completely parametric iterative workflow in combination with digital design tools like evolutionary solvers and machine learning algorithms. Additionally, it has been demonstrated that it is possible to use Azobé to fabricate connections with the required freedom of shape and as confirmed by lab tests, structural function. This together paves the way to apply digital fabrication of timber structures in civil engineering.

24

Recommendations

In this chapter, all recommendations are discussed. Firstly, a number of general recommendations are stated, followed by recommendations concerning the bridge design.

24.1 General Recommendations

Wider applicability

In this research project, the design process for the design of (partly) digitally fabricated structures was analysed through a very specific case study: digital fabrication of a timber bridge. Despite this clear focus, both the conclusion regarding the workflow, as well as the applied structural system and connection design are wider applicable.

First of all, the described workflow can be applied to different digital fabrication techniques, using different materials. For example 3D printing, laser cutting, CNC-milling, robotic sawing and laser sintering with materials like steel, polymers, timber, concrete or foam.

Furthermore, the application of a reciprocal grid shell with digitally fabricated interlocking joints is not only applicable for bridge structures but maybe even more suitable for roof structures.

Consideration of optimisation objective

It is important to make a well-considered decision regarding the design objectives for optimisation. Commonly structures or structural elements are optimised for minimum material use for sustainability reasons. However, other factors might have a bigger impact.

Take the timber bridge that is designed as part of this research as example. Since a sustainable material is used (timber), minimisation of the number of connections possibly has a bigger impact on the sustainability than the minimisation of material due to the reduction of machine operations.

Besides, the weight of the structure contributes to the functioning of the structural system. In case of wind uplift, the structural weight has to counterbalance the upward loading. When the structure is too light, beams can loosen leading to failure of the complete structure, in case no mitigation measures are taken.

Furthermore, a disadvantage of optimising all elements in the structure is that when during the lifetime of the bridge changes are made to the loading or verification regulations, the structure has no abundant capacity.

These facts point out that minimising material usage might not be the best optimisation objective.

24.2 Recommendations Bridge Design

Although many aspects are addressed in this research project, there is still an extensive amount of research that should be done in order to come to a final design of the bridge. This includes both points of improvement in the current design and model, as well as aspects that have not been dealt with yet.

First of all, advice regarding the design and modelling of the whole bridge is given (Section 24.2.1), followed by recommendations for (modelling of) the connection design (Section 24.2.2). Next, a few practical issues that require attention are appointed (Section 24.2.3). Finally, a number of parts of the bridge that are not designed yet are listed (Section 24.2.4).

24.2.1. Improvements to the global design

In this section first a number of improvements for the global design of the bridge are proposed. This includes improvements for the bridge shape, grid and shape and cross section optimisation. Thereafter, a advice is given regarding the modelling of the bridge (loads, load cases, stiffness and checks).

Height at start of the bridge

A feasibility study was carried out to check the results of the first cross section optimisation. For the calculation of all unity checks, an effective height of $h_{eff} = \frac{1}{2}h$ was applied. The resulting cross-section sizes can be seen in Figure 24.1 (top left). In the areas marked red, the largest cross-sections are applied. This is a result of the high bending moments (M_y) (bottom left). An explanation for the high bending moments close to the supports compared to the bending moments at mid span is the lack of structural height. At mid-span, a bending moment can be taken up by normal forces in the beam elements, see Figure 24.1 (right). The closer you get to the supports, the lower the structural height of the grid shell. In this area the bending moments should be taken by the beams themselves. Therefore sections with a larger height are required.

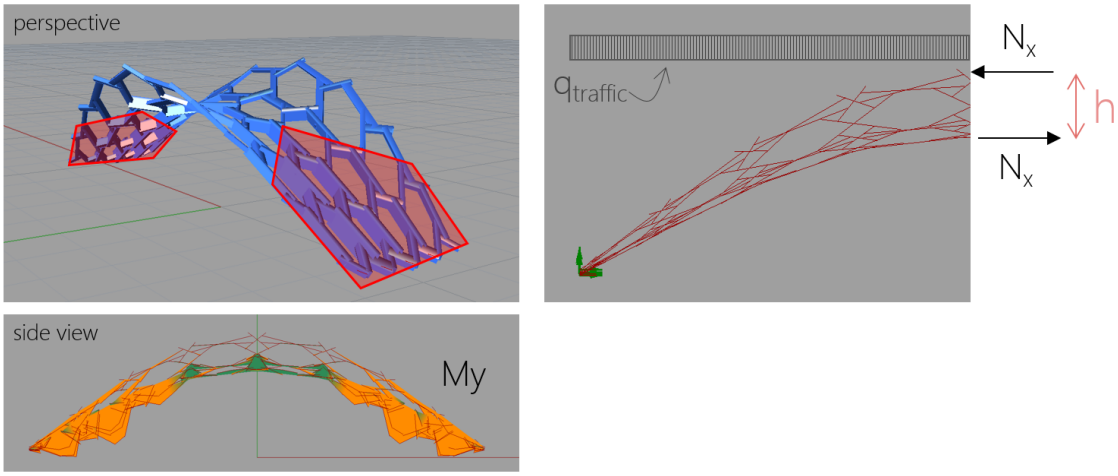

Figure 24.1: Design of the bridge after applying a cross section optimisation (top left), bending moment (M_y) results (bottom left) and schematization of the bending moment transfer at mid-span by normal forces (right)

Adjusting the shape of the bridge accordingly might both decrease the bending stresses close to the supports, as well as increase the resistance of the bridge to global buckling.

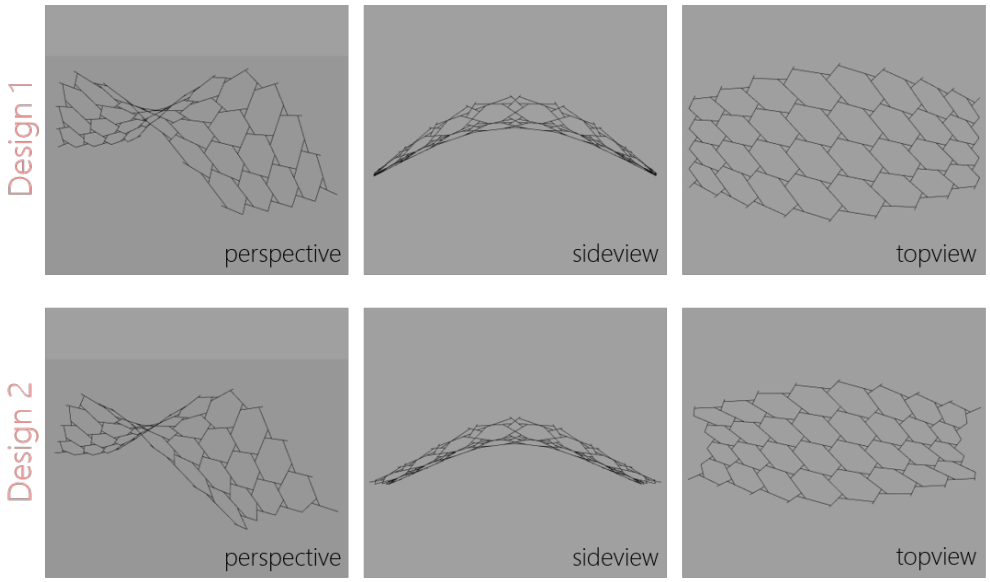

Figure 24.2: Current design (*Design 1*) and adjusted global design to create structural height at both ends of the bridge (*Design 2*)

Grid optimisation

Currently the design of the grid (spacing and radius size) is determined on engineering judgement. In order to optimise the structure, the different parameters defining the layout of the grid should be varied and the structural performance of the different designs compared. A number of parameters that could be analysed

are listed below.

Grid spacing

First of all, the number of divisions can be varied both in x-direction (n) and y-direction (m), see Figure 24.3. Furthermore, the size of the divisions can either be constant, or can be varied. In this way the grid can be made denser at locations with higher forces (e.g. close to the supports) and less dense at locations with lower forces in order to decrease self weight, see Figure 24.3 (right).

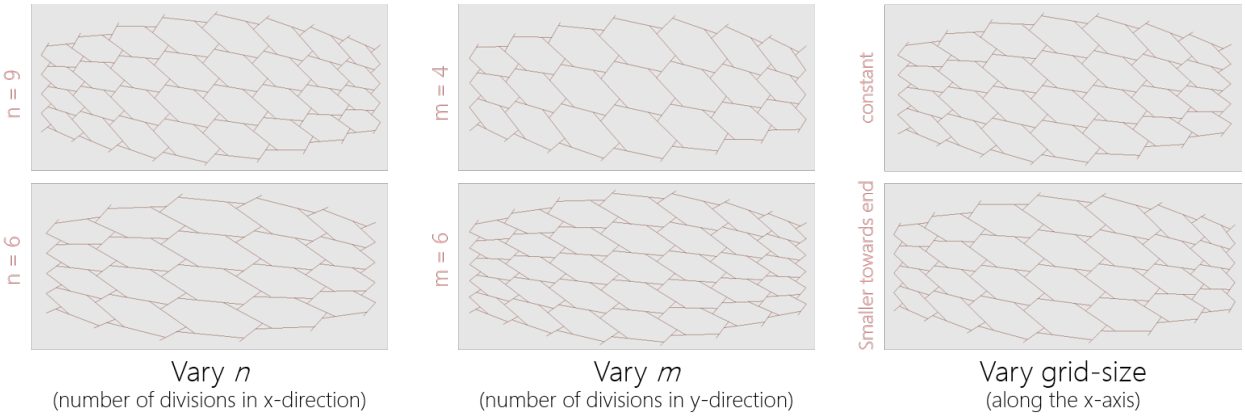

Figure 24.3: Parameters that can be varied that define the spacing of the grid

Second of all, the radius, r, of the circumscribed circle of three neighboring connections can be varied, see Figure 24.4. As well as for the grid spacing, the size can be varied locally. It is for example logical to apply a bigger radius where the grid size is larger.

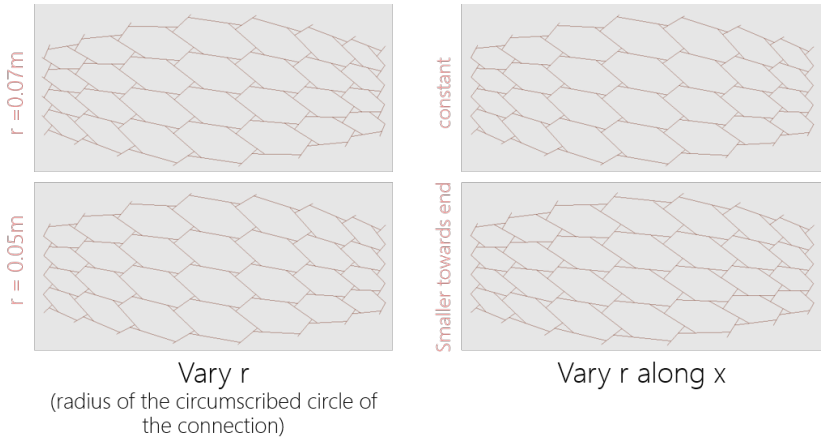

Figure 24.4: Variation of the radius of the circumscribed circle of three neighboring connections

Grid radii

At the moment, the radii are not linked to the section sizes of the beams. Nevertheless, this is advisable in order to prevent clashes between beams. The following expression could be used:

$$r_i \geq c \cdot w_{i,max} \tag{24.1}$$

Where:

r_i	is the radius of the circumscribed circle of connection pair i
c_j	is a constant accounting for the increase of the projected width due to rotation θ_3 of Beam 1 j
$w_{i,max}$	is the maximum width of the beams in connection pair i

Direction of the grid

Currently, the direction of the grid is kept constant constant (all anti-clockwise), see Figure 24.5a.

The physical model of the reciprocal grid shows on the other hand that a combination between clockwise and anti-clockwise connection pairs is possible, see Figure 24.5b. Combining the two directions might have a positive influence on the global buckling resistance of the structure.

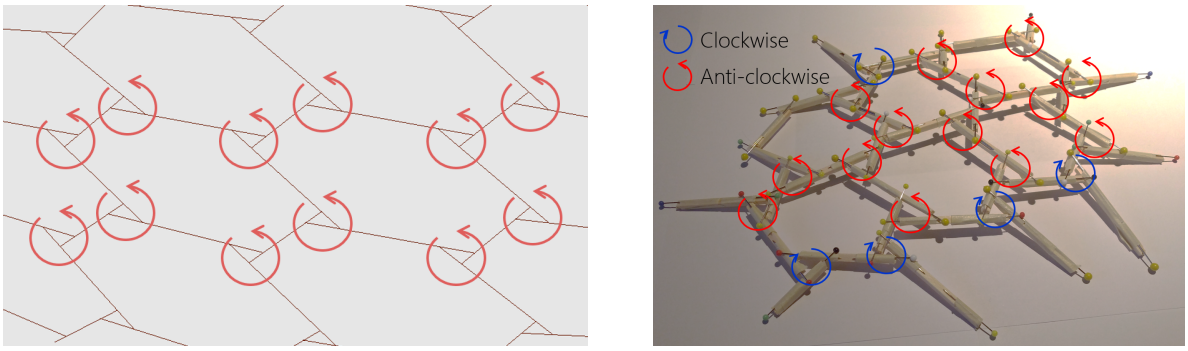

(a) (b)

Figure 24.5: Current direction of the grid (24.5a) and directions in the physical model (24.5b)

Grid type

In addition to improvements to the current reciprocal grid pattern, other grid types could be taken into consideration, see Figure B.1 and 3.16.

Cross section and shape optimisation

Two-directional cross-section optimisation

In the current cross section optimisation model as described in Section 9.1 the cross-section optimisation loop is *'one-directional'*. This means that only bigger cross-sections will be chosen during the loop. Since during an iteration simultaneously multiple section sizes are increased, it is possible that a number of sections are oversized since the structure is statically indeterminate. It could therefore be beneficial to add the possibility to decrease the section sizes of sections with a unity check underneath a certain upper limit (e.g. UC $\leq$ 0.8).

Shape optimisation

At the moment, only two parameters are varied (height at mid span and the height of the edges). The shape is actually defined by more parameters, among which the width at the supports and at the top, steepness at supports. It would be interesting to include more parameters into the optimisation.

Loads and load cases

Wind load

Two simplifications are implemented for the application of the wind load. First of all, the velocity pressure is a function of the height: $q_p(z)$. At the moment, in all cases a height of z = 5m is applied, which is a safe assumption. Either a more realistic height could be applied ($\pm$ 2m) or the wind load could be calculated using the exact height of each beam.

Secondly, currently the wind load is applied as a line load. This line load is calculated by multiplying the wind pressure (in kN/m^2) by the height of the beam. It would be more exact to calculate the projected height of the beam instead of the actual height of the beam, see Figure 24.6. The projected height could be larger than the actual height.

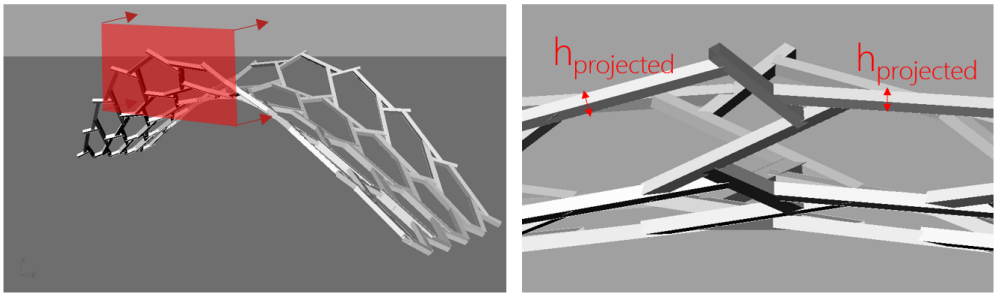

Figure 24.6: Projected height of the beams that should be used to calculate the wind load for each beam

Load Cases

At the moment, only 12 load cases are applied, combining self weight, wind load and crowd load. In all load cases, the crowd load is applied to the whole deck of the bridge. This is not necessarily the governing load case. By composing an influence plane of the bridge deck, the relevant load cases for crowd loading could be determined.

It should be considered in what design stage to implement this. When still a lot of changes are made to the layout of the bridge, it is too computational intensive to construct the influence plane over and over. An option would be to construct the influence plane for a small number of designs and from this derive the load cases to be used for the first design stage. In a later stage, when the shape and layout of the bridge is fixed, the actual influence plane should be determined.

Stiffness of connections in global model

Presently, all connections between Beam 1 and Beam 2 are modelled as hinged connections ($M_y = M_z = 0$). However, the connections will have some bending moment resistance. When the resistance of each connection is approximately the same, the is won't have a large influence on the force flow in the structure. Though, when there are large differences in stiffness, which is possible since the design of each connection is different, this could have a considerable effect. In order to verify this, a sensitivity study should be carried out to see what the influence of different stiffness's is. Prior to this it should be determined if the stiffness differences between connections is considerable. In case these two studies prove that the stiffnesses should be taken into account, rotational springs should be added at the connection between Beam 1 and 2. When effect of the stiffness is large, tests should be performed to gain insight in the rotational stiffness of the connections.

Dynamics check

It should be prevented that forces induced by pedestrians result in resonance of the bridge. To verify this, the Eurocode requires the calculation of relevant eigen-frequencies of the bridge. These eigen-frequencies should be higher than the frequencies that can be produced by pedestrians, see Section 6.2.4. Currently the check has not been implemented yet.

Local and global stability

Currently, no local buckling check is performed due to the short buckling length of the members. In a later design stage it should be verified if the hypothesis that local buckling is irrelevant is correct.

More important is the global stability of the structure. Shell structures are prone to global buckling. It is therefore of great importance to perform a global buckling check in the next design iteration and if required make adjustments to the design to improve the buckling behaviour.

24.2.2. Verification of the connections

This section summarises a number of areas for improvement in the current verification of the connections.

Simplified calculation model

At the moment, a simplified model of the connection is used for the verification, see Figure 24.7. In this model, all detailing (radii/slopes) are disregarded. The detailing is designed to have a positive influence on the structural performance. Nevertheless, for some planes, the area of the plane is overestimated leading to a non-conservative result for the stresses. Especially when a large slope is applied, the difference can be considerable. It could therefore be considered to either adjust the model used to determine the dimensions of the relevant planes or to add a reduction factor to account for this difference.

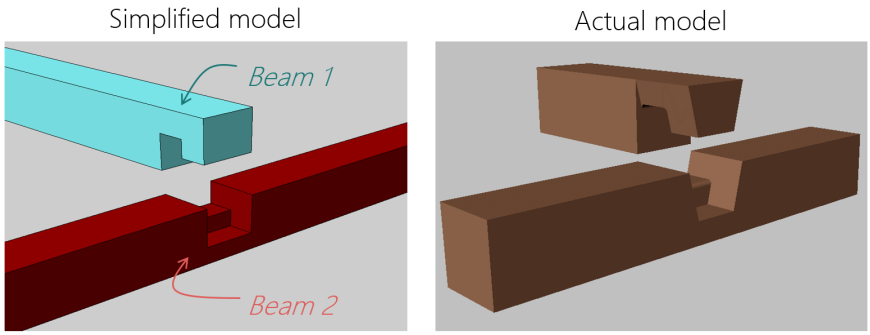

Figure 24.7: Simplified model used for the calculation of stresses in relevant planes (left) and the actual model of the connection (right)

Torsion check

Due to the eccentric load transfer at the connection from Beam 1 to Beam 2, torsion stresses are induced, see Figure 24.8. These stresses are currently not taken into consideration, despite that the Eurocode prescribes a torsion check that should be carried out for timber structures, see Equation 7.9 in Section 7.3.3.

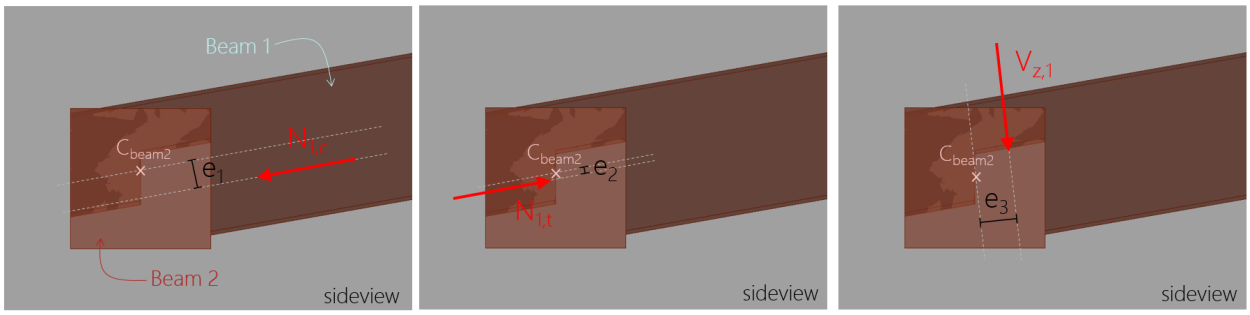

Figure 24.8: Eccentric loading inducing torsion in *Beam 2*

Bending moment induced by normal forces

The bending moment induced by the normal forces in *beam 2* is left out of consideration, see Figure 24.9. The order of magnitude of this bending moment should be defined. In case the order is considered to be relevant, the bending stresses due to the bending moment should be included in the check for axial stresses in plane 11.

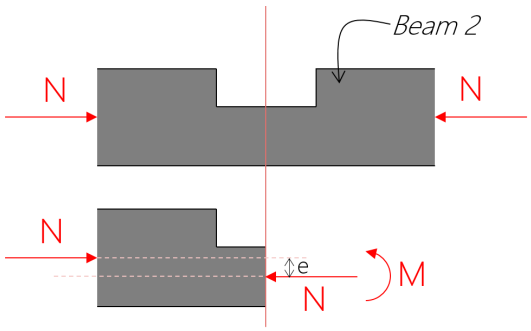

Figure 24.9: Bending moment due to eccentric application of normal forces

Simplifications in stress calculations calculations

Currently, a few simplifications are made when calculating the stresses in the relevant planes. The two most important ones are pointed out and a suggestion how to improve the calculation is given.

Bending moment capacity

As discussed in Section 12.2.5, the presence of Beam 1 is disregarded for the calculation of bending stresses in Beam 2. However, Beam 1 will likely have a positive influence on the bending moment resistance

of the connection. A test as described in Section 18.2.3 could validate if the two beams work together when loaded in bending. When performing the test with and without the presence of Beam 2, see Figure 24.10 the relevance of including Beam 1 in the calculation could be determined.

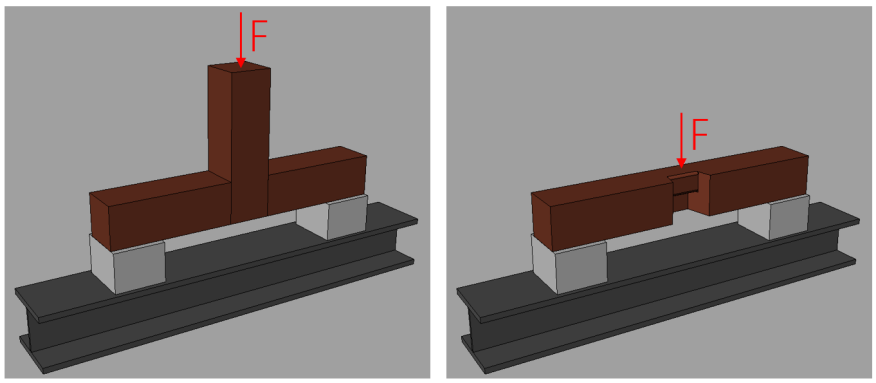

Figure 24.10: Bending test of beam 2 with and without the presence of Beam 1

Capacity of beam 2 when beam 1 is in tension

As mentioned in Section 12.2.4, for simplicity the capacity of the plane marked blue in Figure 24.11a is disregarded due to the relatively low strength (rolling shear). It is hard to estimate the the part of the load that will be transferred through the red marked planes (10.1 and 10.2) and the blue planes. Either tests or a 3D FEM model could give an idea of the actual behaviour of the this part of the connection.

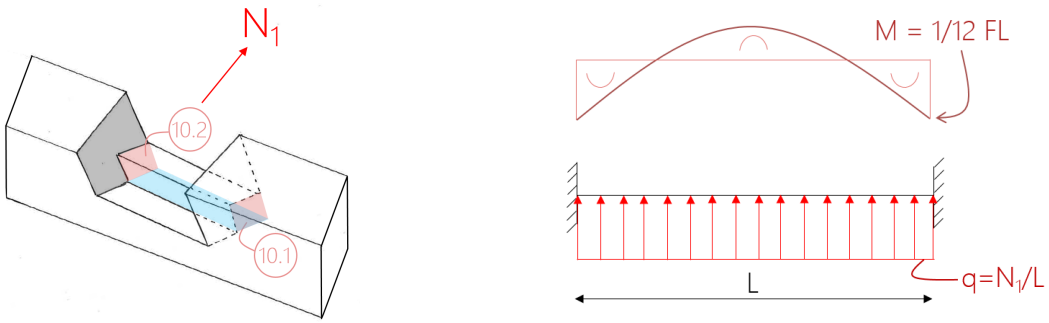

(a) (b)

Figure 24.11: Plane 10 and relevant forces(24.11a) and the assumed bending moment in plane 10 induced by the axial force N_1 (24.11b)

Load cases

Currently, to determine conservative dimensions of the connection, the envelope of all load cases is used. This is not a realistic situation since stresses that are not acting simultaneously are combined. Nevertheless, it is computationally intensive to perform every optimisation for all load cases. It should be verified if this is nevertheless a good method or if there is a better solution to deal with the large number of load cases.

24.2.3. Practical issues

This section some practical issues regarding the construction and operation phase of the bridge are discussed.

Deformation of the bridge

In this project, the design of the bridge is based on the strength calculations (Ultimate Limit State). The stiffness and stability of the bridge (Serviceability Limit State) is disregarded due to time-constraints.

Nevertheless, the deformation of the bridge needs some special attention since not only displacements will occur due to the forces in the beams but also due to potential spacing at the connection. First of all, depending on the type of machine or robot used for the processing of the beams at the connection, the connections will have a certain tolerance. Secondly, differential shrinkage of the two connecting beams due

to different grain-directions can result in a spacing at the connection. It should be verified what the influence of the displacements at all individual connections is on the total displacement of the bridge In case the displacements are large, the second-order effects should be taken into account.

Misfit due to dimensional deformations

Depending on the fabrication technique, small deviations between the actual connection design and the modelled design can occur. A plan should be composed how to deal with those deviations to prevent that beams don't fit.

A possibility is to apply a tolerance at all connections. As described above, it should then be verified that these tolerances don't result in a too large displacement of the whole bridge.

Research carried out by the *Gramazio Kohler* Research Group of the *ETH, Zürich* has shown development in real-time monitoring of structures, see Section A.1.3. In the future it might therefore be possible to scan the structure during construction and directly adjust the fabrication model of the elements that are not assembled yet accordingly. In this case the fabrication and assembly process should be performed simultaneously.

Construction of the bridge

One aspect that requires still some thought is the construction of the bridge. One of the drawbacks of a reciprocal structure is that the system is only stable when all beams are in place. This means that the beams should be supported (temporarily) during construction.

Robustness

Another drawback of a reciprocal structure is that the structure has almost no redundancy. Since all beams are supported by each other, the whole structure will collapse in case of failure of one single element. A bridge structure should have a certain level of robustness. Figure 3.14 in Section 3.2.2 shows design strategies that could be applied to achieve this. Ways to deal with accidental load combinations are either by applying strategies to avoid them (e.g. by choosing a location where no ships are passing), by limiting the risk of failure (e.g. by inserting screws) or a combination of both.

protection of the end of the beams

When solid timber is exposed to outside conditions, the ends of the beams should be protected against weather conditions. Part of the beams could be protected by the bridge deck. The remaining beams should be protected, for example by:[60]

- Priming and painting the timber
- Finish the end of the beams with caps
- Using metal, fibro or plastic shields on exposed faces
- Using damp proof membranes

24.2.4. Parts that should still be designed

Edges

In Section 5.3, the structural system of one beam was described as a simply supported beams with two concentrated loads. Despite this is a good representation for the beams in the middle of the structure, this does not apply to all beams at the edges, see Figure 24.12.

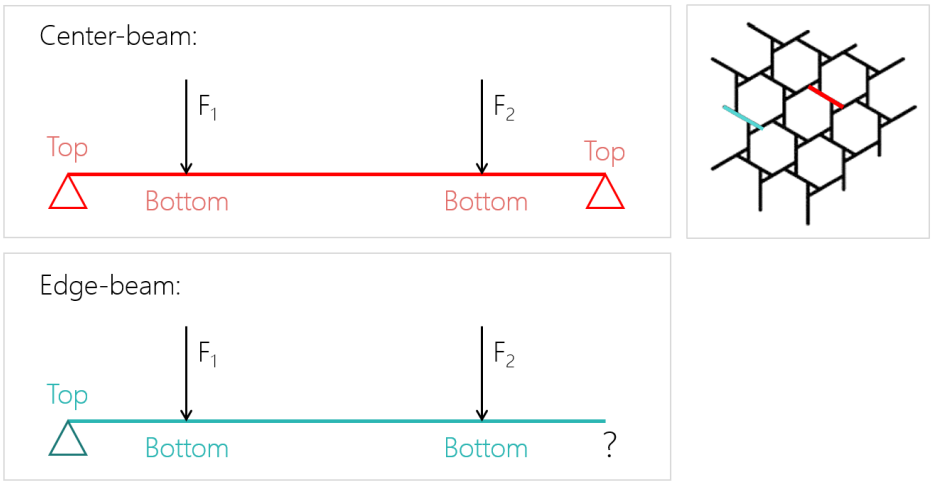

Figure 24.12: Supporting schemes for center- and edge-beams

There should be found a solution to this problem. A few options are:

- Design a different connection for the edge beams which can take bending moments. This results in the scheme shown in Figure 24.13 (left). In Section 22.6 the order of magnitude of the bending moment is estimated to be 1.3kNm.
- Change the grid pattern locally. Figure 24.13 (middle) shows the physical model (earlier presented in Section 5.3). The long stick designated by the red arrow enables omitting one of the supports. A drawback is that this will strongly influence the appearance of the bridge.
- The application of special edge beams that run along the entire edge of the bridge, see Figure 24.13 (right). This requires a whole design for the edge beams (connection between edge beams and (slicing joints) connection between the existing beams and the edge beams (connection joints)).

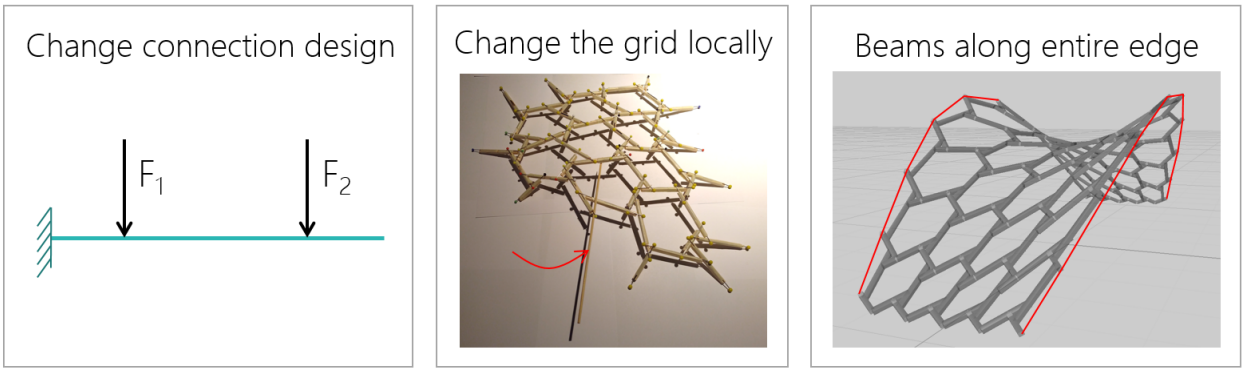

Figure 24.13: Two possible solutions to solve the problem at the edges

Deck

Currently the deck has not been designed yet. The assumed location the deck is shown. First of all, the material of the bridge deck should be chosen. Some options are:

- Recycled plastic
- Wooden slats
- Steel plate

Preferably, a sustainable material is used. Furthermore, in order to fit into the digital manufacturing work-flow, a design without requirement for complex fabrication and assembly process is preferred.

Thereafter, it should be decided how to fasten the deck or deck elements. Note that a few adjustments should be made to the loads on the bridge:

- The self weight of the deck should be added
- Currently the traffic loads are applied at the connections. Depending on the the location where the deck is fastened, this should be adjusted.

Railings

It is mandatory to have handrails on footbridges.

Supports

A design of the end of the bridges should be made. It should be decided were to cut off the grid and how to support the ends of the beams. The supports should resist considerable horizontal forces. A design for the foundation should be made accordingly.

25

Secondary objectives

In addition to the main research question, a number of secondary objects were defined. In this section a short overview of the findings regarding the sub-questions is given.

How to minimise the amount of secondary materials used for connections

A way to minimise the secondary material usage is by applying interlocking joints. A relatively strong and stiff connection can be obtained without the addition of steel plates. In combination with the application of a reciprocal grid, a connection can be made without any fasteners.

The tests that have been done show that the application of screws can increase the shear capacity of the connection significantly. When three screws per connection are applied, a total amount of steel of approximately 5kg for the entire bridge shown in Figure 22.18 is required. Given that the timber in the bridge has a weight of 2665kg, only 0.2% of the weight of the bridge is composed of steel.

How to minimise material usage

A way to minimise the material usage is by carrying out a cross-section optimisation and shape optimisation. Due to the statically indeterminacy of the structure, the cross-section optimisation is an iterative procedure. A customised python script can be used to determine the unity checks for each beam and if necessary increase the section size. After each change made, the force-flow in the structure is updated and the unity checks renewed until all beams fulfil the requirements.

Finding the optimal shape of the bridge is difficult due to the complex relationship between the parameters defining the shape of the bridge and the amount of material required. A way to deal with this is by using an evolutionary solver. For each design alternative the minimum cross-section sizes can be determined according to the aforementioned cross-section optimisation procedure.

The fitness landscape as shown in Section 22, Figure 22.8 shows the effectiveness of the combination of the cross-section and shape optimisation. Designs in the range of 2665 up to above 10,000kg were found.

How to make an integrated design on global and detail level

The fact that the grid shell structure is statically indeterminate makes that the dimensions of the individual beams have an influence on the force flow in the structure. For this reason, the global design of the bridge and the detail design cannot be uncoupled. A way to deal with this is by applying a simple cross section optimisation, using effective values for dimensions to take into account the reduced section size at the connections, to determine the force flow in the structure. This force flow can subsequently be used to find the dimensions of the connections.

Finding the dimensions is a complex task due to the strong relation with the global design, the large number of parameters defining the shape and size of the connection and the uniqueness of each connection. Nevertheless, with the help of design tools evolutionary solvers and machine learning algorithms it is possible to deal with this complex relation and a large number of parameters.

How to include the limitations of the digital fabrication process into the design work-flow

As mentioned before, digital fabrication is often associated with design without restrictions. Nevertheless, every type op manufacturing has its restrictions. For CNC-milling, the following restrictions have been taken into account:

- The minimum feasible beam size: 95x95mm

- The CNC drilling head should be able to approach all areas that needs to be removed. In some cases remaining material obstructs the course of the drill. See for example the areas marked red in Figure 25.1 of the preliminary design of the connection.

In corporation with timber designers of *Wijma*, the preliminary designs of the connections were reviewed and adjusted where necessary in order to obtain a feasible design for CNC-milling.

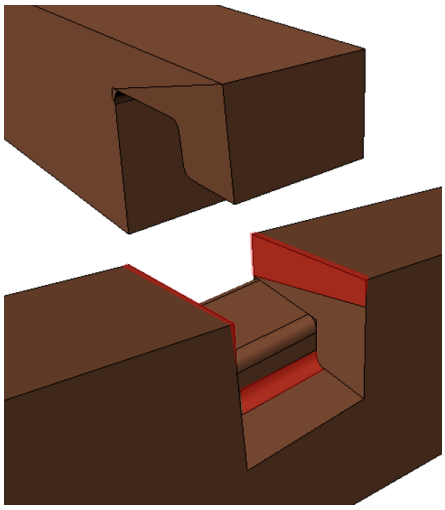

Figure 25.1: Preliminary connection design. Parts of the design that are not feasible for CNC-milling are marked red

IX

Appendices

A

Robotic Timber Fabrication

In this chapter, a number of projects related to robotic fabrication will be discussed. Four research groups that are leading in the field of robotic timber fabrication are the *Gramazio Kohler Research group* from the ETH Zürich, Switzerland, the *IBOIS Laboratory for Timber Construction* from EPFL, Switzerland, the *Institute for Computational Design* from the University of Stuttgart, Germany and the *Design & Make Hooke Park* from the Architectural Association, England. In the following sections, a short outline will be given of the progress made by those four research groups.

A.1 Gramazio Kohler Research

The Gramazio Kohler Research group mainly focuses on the application of additive digital fabrication techniques in architecture.

In this section, an overview will be given of the progress made by the research group in the field of robotic timber fabrication during the past 10 years.

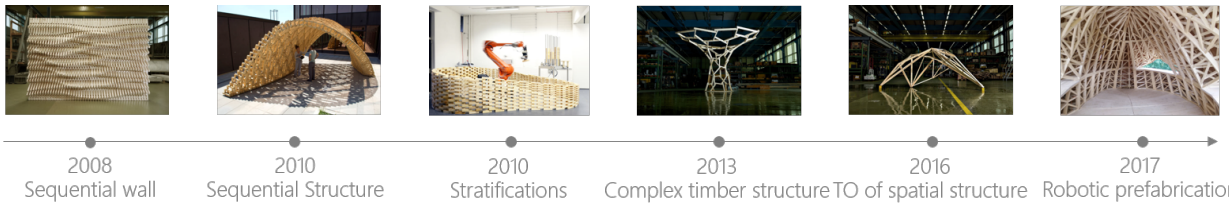

Figure A.1: Time-line of the projects by the Gramazio Kohler Research discussed in this chapter [63]

A.1.1. The Sequential Wall (2008)

The Sequential Wall is a structure developed by the Gramazio Kohler Research group at the ETH Zürich, see Figure A.2.

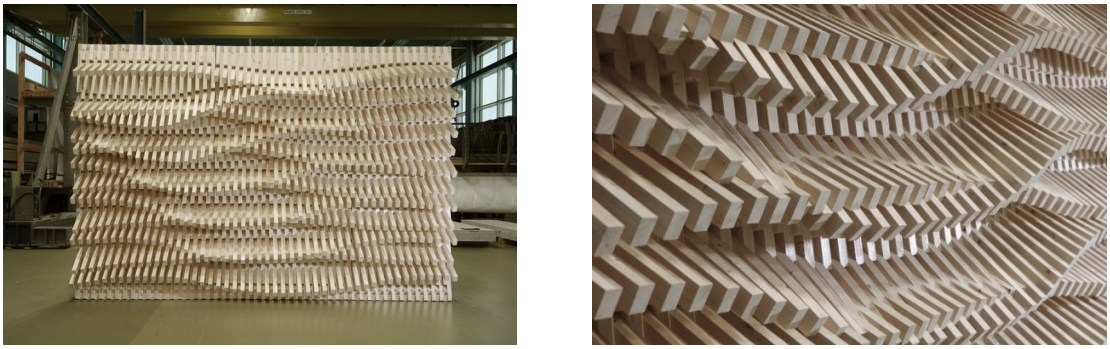

Figure A.2: The Sequential Wall (2008), ETH Zürich [47]

It is one of the first structures that has been constructed by means of additive robotic timber fabrication. The timber elements are positioned by meas of a machine, see Figure A.3. The fabrication of such a complex design with a great number of irregularly placed elements previously required a excessive amount of labour.

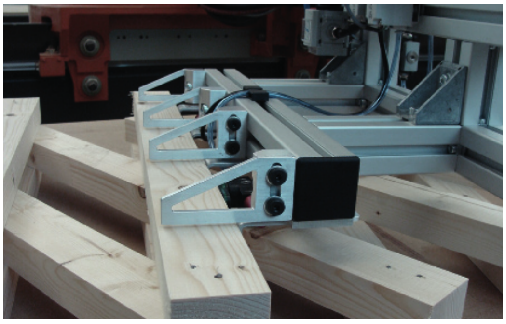

Figure A.3: Robotic positioning of timber elements [35]

A.1.2. The Sequential Structure (2010)

The next step for the Gramazio Kohler Research group was to go from a layered constructive system, like applied in *The Sequential Wall*, towards a spatial constructive system. In 2010, the team introduced *The Sequential Structure*, see Figure A.4.

The structure consists of 26 individual elemetns, connected into 11 arches which are mounted on site whithout the use of heavy machinery. The design is based on a hanging chain model. The diagonal grid allows for a multi-directional load transfer, making the structure act like a shell.

Figure A.4: The Sequential Structure (2010), ETH Zürich [63]

Figure A.5: Stratifications (2011), London [63]

A.1.3. Stratifications (2010)

Despite that the appearance of this structure does seem less advanced than *The Sequential Structure*, the project *Stratifications* was an important advancement in the field of digital fabrication. The structure consists of 1330 wood elements, all with a different thicknesses. Due to the variance in thickness, a feedback loop is required between a scanner which scans the top layer and the additive assembly strategy. This is the first step in identifying design strategies for adaptive robotic fabrication.

A.1.4. Complex Timber Structures (2013)

The project *Complex Timber Structure* is a result of a four-week workshop carried out by students of the ETH, Zürich. The structure has a span of 4.5m and consists of 93 beams. The beams where cut, drilled and positioned robotically, as can be seen in Figure A.6. The planning phase including the assembly sequencing was embedded in the design phase leading to a feasible design.

Prior to starting to design the overall structure, a study was done on both traditional and contemporary timber structures. As a result of the study, a suitable node design was defined which was suitable for robotic fabrication. It was decided to connect the coinciding bars eccentrically as can clearly be seen in Figure A.6c. This type of connection has the following advantages compared to a node where the bars connect at one single point [35]:

- Members can be connected one by one instead of all at once. This can easily be handled by a robotic

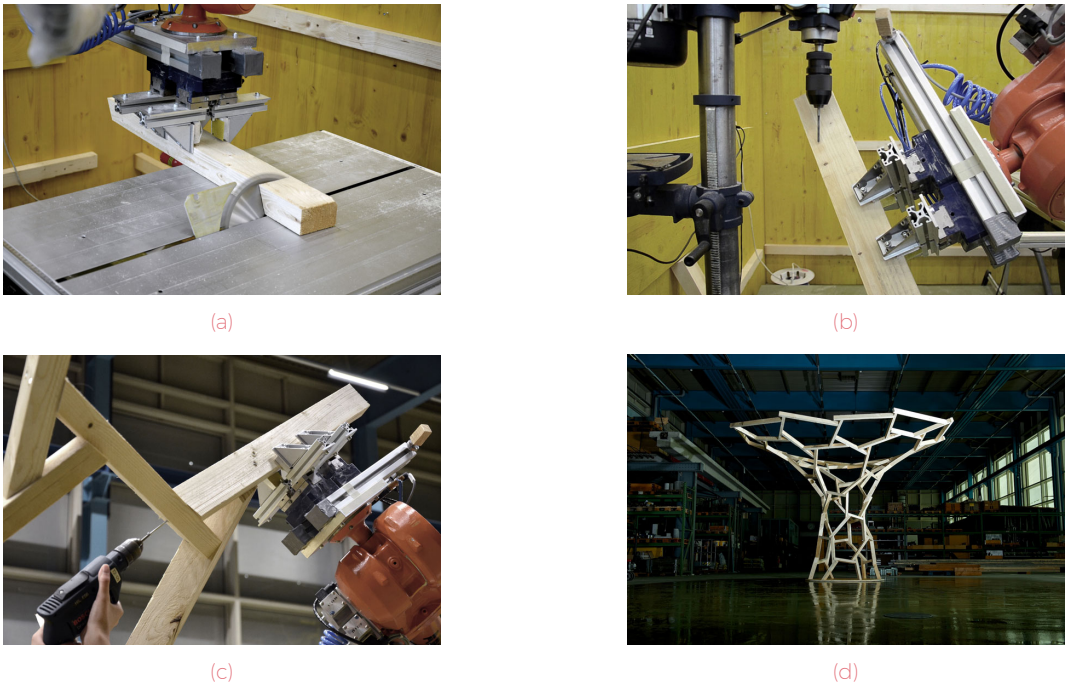

(a) (b)

(c) (d)

Figure A.6: The robotic sawing (A.6a), robotic drilling (A.6b), robotic positioning process (A.6c) and the final structure (A.6d) [63]

arm

- Since only one angled cut at both ends is required, the cutting procedure can be integrated into the assembly process

- The stiffness of the connection can be controlled by varying the eccentricity of the connected members

Besides, the triangular configuration provides both bending resistance and shear resistance, even though it is considered a pin-jointed connection in the structural system, see A.7. It should be taken into account that due to the flexural rigidity of the grid, bending stresses will be present in the members.

A.1.5. Topology optimisation of Spatial Timber Structures (2016)

In this project, research was done on the application of topology optimisation (TO) in the design of a spatial timber structure and the realisation of this design by applying robotic timber fabrication strategies.

First of all, the structural optimisation was carried out. A design space was generated and discretized by applying a set of nodes. Next, the nodes were connected by a set of potential bars. The requirement that should be met by the ground structure is that the structure should be able to transfer the loads from point of application to points of supports without forming a mechanism. Then, a sizing optimisation is carried out to find the optimal cross-sections for all bars. Unnecessary bars are removed by allocating a zero cross-sectional area. In the most basic form there will be searched for the solution with the maximum stiffness for a certain upper limit of volume used, under the condition that structural equilibrium is satisfied.

The output of the optimisation process is a design for the topological configuration and the cross-sectional area of all individual members. Nevertheless, it does not address the design at node (connection) level. Therefore, a procedure has been developed which gives for any topological configuration the necessary bar orientation and cutting sequence, taking into account the limitations of the robotically sawing process.

One of the greatest challenges in robotic fabrication is the generation of a processor for auto-generated sequencing. The processor should determine the chronological order of member placement without collision with the structure under construction. The workflow diagram for this project is shown in Figure A.9. There will be searched for the insertion sequence for which the least amount of collisions occurs. Furthermore, if possible, there will be searched for a build-up through triangulation, in order to ensure physical stability during assembly.

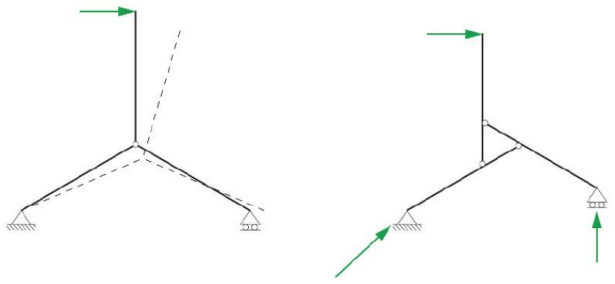

(a)

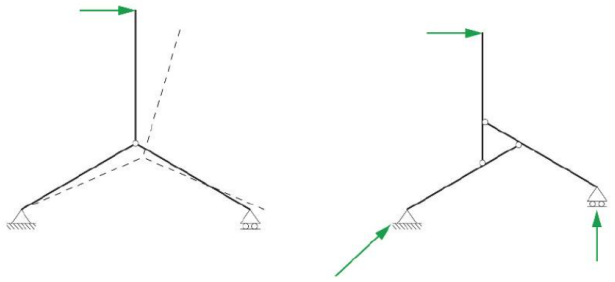

(b)

Figure A.7: Load bearing behaviour perpendicular to plane (A.7a) and in plane (A.7b): on the left a concentrated node and on the right an eccentric node [35]

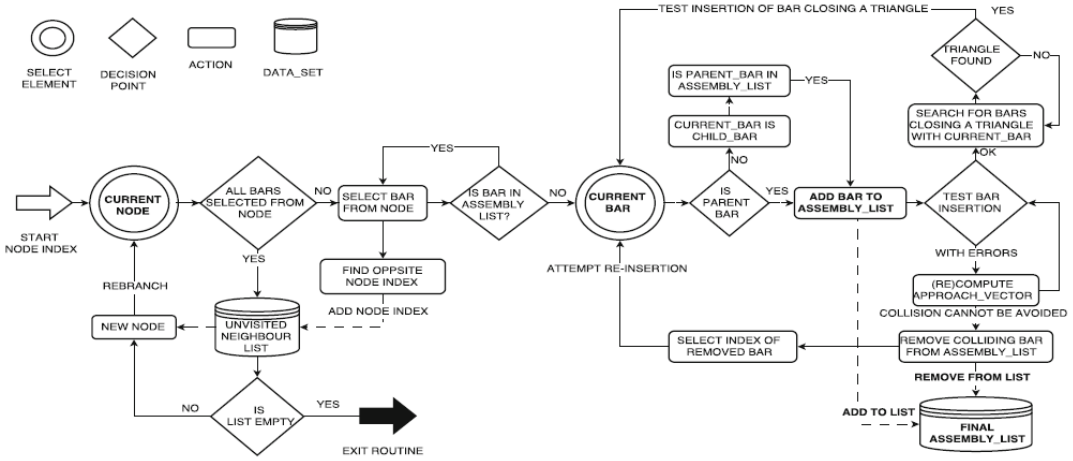

Figure A.9: Workflow diagram of the assembly procedure [50]

For the fabrication a KR 150 L110-2 KUKA robot on a 7m linear axis in combination with a Mafell Erika 85 circular table saw were used. The robot has a parallel gripper which can hold the beam stiff enough for the cutting process. During the process, the following steps are repeated:

1 Gripping of a wooden beam

2 Positioning of the wooden beam for cutting (repeated for all cutting planes)

3 Robot reaches the final assembly position

4 Multiple beams prepared for gluing

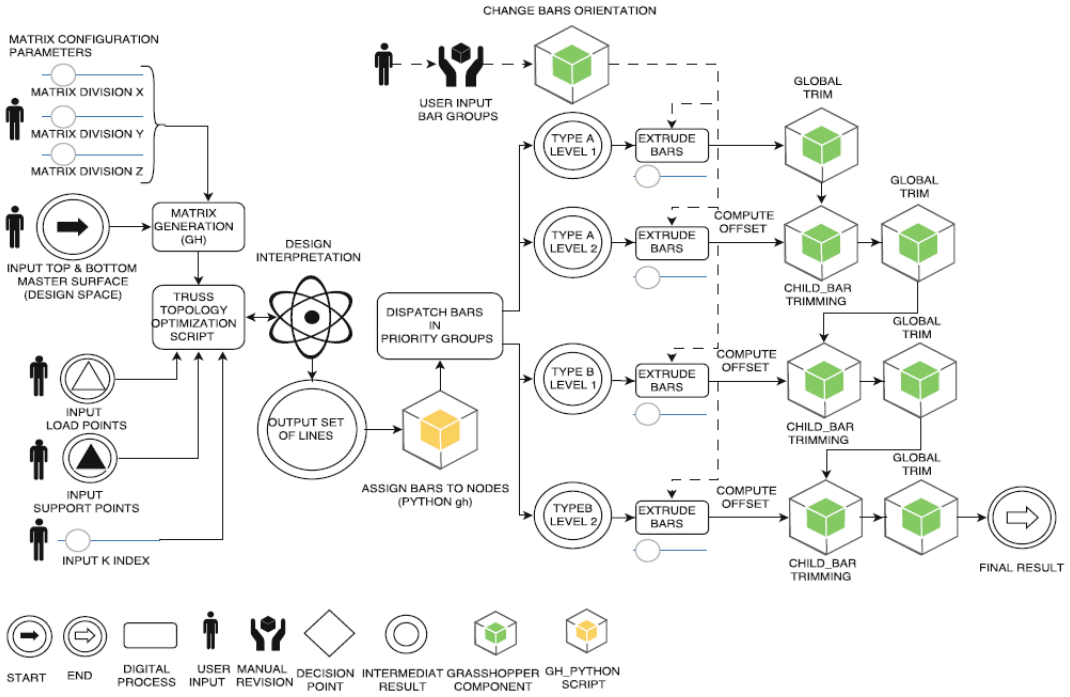

Figure A.8: Workflow diagram of the rationalisation procedure [50]

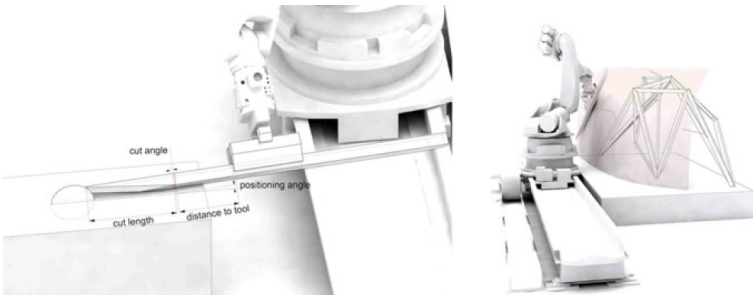

Figure A.10: Robotic setup [50]

Figure A.11 shows the prototypical structure. Tests on the structure showed that the prototype was very stiff due to its optimises configuration. Due to rapture of the connected metal braces the actual stiffness of the structure could not be determined though.

Figure A.11: Topology optimisation of Spatial Timber Structures (2015), Zurich [63]

A.1.6. Robotic prefabrication of timber structures (2017)

As part of a course of the Master of Advanced Studies program in Digital Fabrication at the ETH Zürich, a complete digital work-flow is realised using additive robotic fabrication techniques. As a case-study, a robotic fabrication system for a two-story structure was developed.

Robotic setup

The robotic setup that was used for the project is shown in Figure A.12. Two indistural robots were used and place on a 5m long linear axis. Both robots were able to communicate to each other in order to work synchronously. The two robots were equipped with the following tools:

- Left robot:
  - Measurement tool
  - Scanning tool
  - Vacuum gripping tool
  - Atuomatic nailing tool
- Right robot:
  - Two parallel electronic grippers

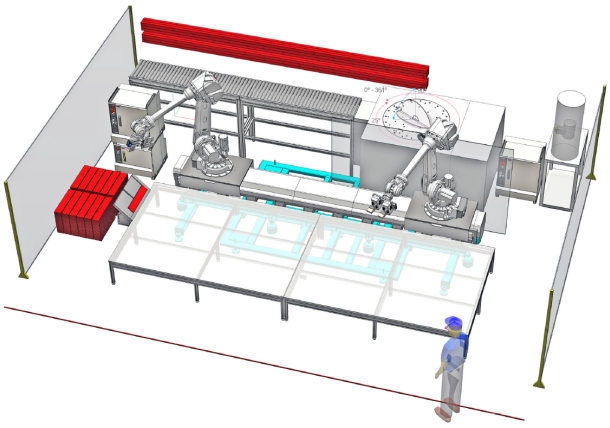

Figure A.12: Robotic setup [25]

Work-flow

The programming work-flow that was applied is shown in Figure A.13.

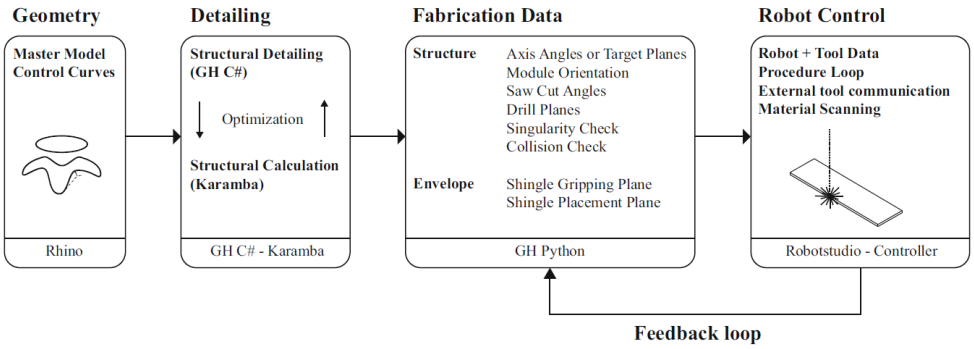

Figure A.13: Programming work-flow [25]

The geometry was defined with a *C# programming* script, which was connected to a structural calculation and optimisation tool, *Karamba*. Next, the fabrication data was generated in *Python*. Finally, the robot control, procedures and operations were written in *Robotstudio*.

Geometry and optimization

For the geometry generation, an adjustable cuboid was used, see Figure A.14. Combining multiple cuboids constitute a large spacial braced structure. The size and shape of the elements was determined by the functional, fabrication and assembly constraints.

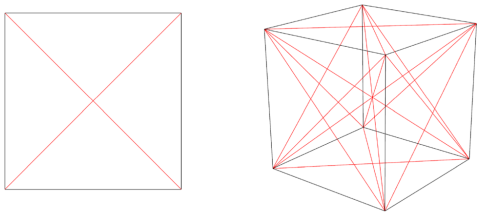

Figure A.14: The cuboid that was used as basic element [25]

Two optimisation strategies were used in order to reduce the amount of material usage.

1 Using an algorithm, braces were oriented in a way that they were mainly loaded compression. For this, the the principal stress lines were used, see A.15.

2 A costom-scripted cross section optimisation was carried out, using four different cross-section sizes. This resulted in a reduction of amount of material of more than 30%.

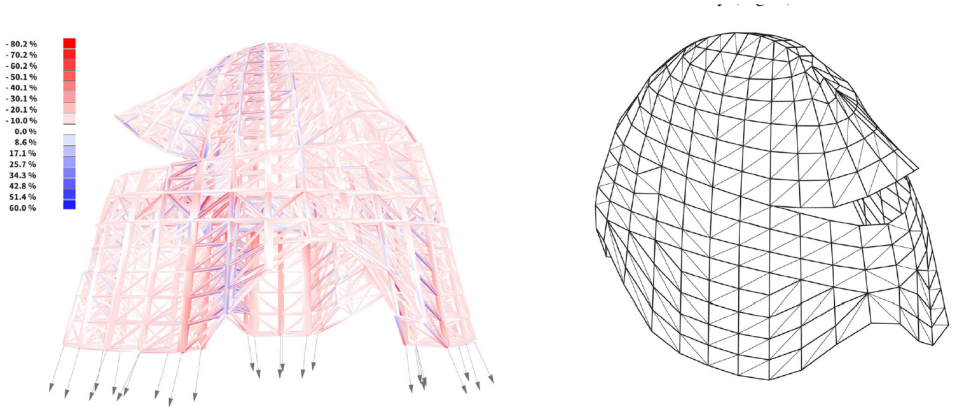

Figure A.15: The structural design of the double-story structure with Left: the FE analysis result for the utilisation of the members and Right: the orientation of the bracings following the stress-lines from the FE results [25]

Connections

For the connection between timber bars was made by using full-threaded carbon steel screws. The length and orientation of the crews was determined from the bar's thickness, orientation and direction of the fibers. An optimisation was used using four different bolt sizes with a similar diameter, see A.16. The model that was used for this could decompose the forces on the bolts in shear- and axial forces. With this, the bolted connections could be verified.

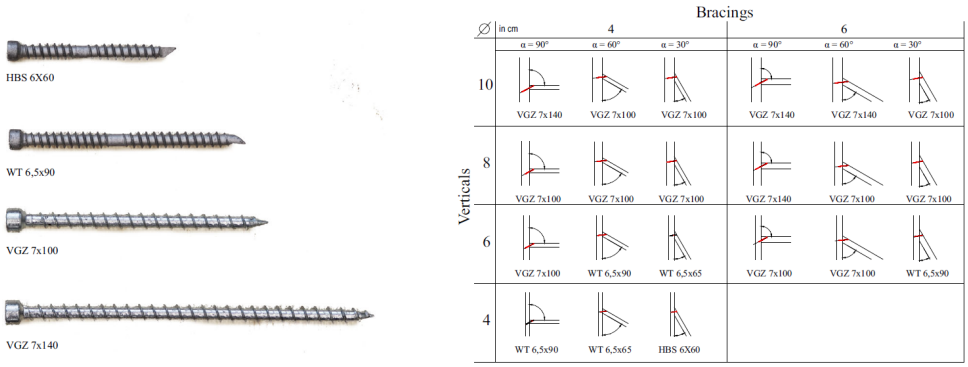

Figure A.16: Left: Type of bolts used for the optimisation procedure, Right: Calculation of required bolt type, angle and length depending on the the geometry and material thickness [25]

Robotic fabrication

For each beam, an array is constructed which contains the information about the procedures (e.g. drilling, cutting, placing, etc.) that should (1) or should not (0) be carried out. For every procedure another array is constructed containing specific information regarding the procedure (e.g. saw angle, approach planes etc.). This data work-flow is shown in the diagram in Figure A.17.

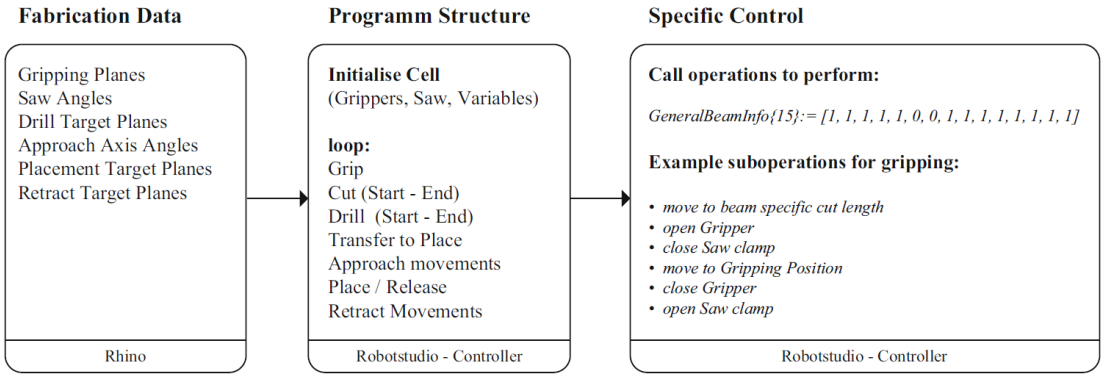

Figure A.17: Data work-flow for the robotic fabrication [25]

Following fabrication steps are performed:

1 Placement of wood slat on the roller rack

2 Wood slat is centred by closing the saw gripper to the reference position for robotic gripping

3 The saw gripper releases, allowing the robot to move to the beam's first programmed cutting position

4 The beam is held 5mm above the table while the beam is rotated in the right position

5 When the right orientation is obtained, the slat is pushed on the table in order to give additional stability

6 The cutting is performed

7 Step 4 until 6 are repeated for the second cut

8 The work-piece is lifted for additional operations like pre-drilling

9 The work-piece is mount on the structure

Sequencing

A path planning algorithm was developed in order to organise the positions to grip, move, approach and place the elements. Due to the simple geometric principle it was not necessary to solve the path planning for each part separately. The approach movements could be determined by the topological features (orientation, length and position).

(a) (b) (c)

Figure A.18: Placement of slat in home position at the assembly table (A.18a), placement in sawing position and moving towards saw (A.18b) and placement in the truss (A.18c) [25]

On-site assembly

The beams are robotically assembled into small modules. Next the modules are pre-assembled into large transportable modules. The large prefabricated modules were thereafter assembled on-site, see Figure A.19.

(a) (b) (c)

Figure A.19: Pre-assembly (A.19a), On-site assembly of large prefabricated modules (A.19b) and the final structure (A.19c) [25]

Conclusions from the project

The following conclusions were be drawn from this project:

- In the case-study project, 4000 differently shaped elements were assembled in 5 weeks (including testing and on-site assembly). This shows that, despite the irregular character of the structure, it is possible to attain a suitable construction time when using robotic fabrication techniques.

- The most efficient fabrication lengths of timber slats is between 400 and 1500 mm. Shorter elements were challenging for cutting and assembling and larger elements caused tolerance issues.

A.2 Workshop Intelligent Fabrication 2017 - Digital Bridges

In the workshop *Intelligent Fabrication 2017 - Digital Bridges* at the *Ecole nationale supérieure d'architecture de Versailles* students were assigned to design a bridge using digital fabrication techniques. The students made in groups of four bridge design using parametric tools like *Karamba* and *Grasshopper*. Three designs were selected to be fabricated at full scale, see Figure A.20. The other bridge designs were modelled at either 1:10 or 1:5 scale using 3D printing and/or laser cutting techniques, see Figure A.21.

A.2.1. Full scale models

(a)

(b)

(c)

Figure A.20: Constructed bridges on full scale as part of the *Intelligent Fabrication 2017 - Digital Bridges* workshop at the *Ecole nationale supérieure d'architecture de Versailles*

Hyperbolic Paraboloid

Figure A.20a shows a bridge in the shape of a hyperbolic paraboloid. Despite that the overall shape of the structure is double-curved, the structure consists of straight elements only. The grid was first formed flat and thereafter put in there final position by lifting the edges and bolted together. the bridge was kept in position by cables connecting the start and end of the bridge.

Domestical Wildness

In this design of the bridge shown in Figure A.20b the goal was to construct a frame which appears highly irregular but is structurally viable and well though out. The bridge consists of two irregular trusses. The visually random but optimised configuration was found by using a parametric algorithm in *Karamba*.

Triangle Reciprocal Structure

The bridge design is inspired by the reciprocal bridge design by Leonardo da Vinci, see Section 3.2.2. The bridge consists of two reciprocal structures which are horizontally connected. The design deviates from the design of Leonardo da Vinci by the application of triangular elements instead of straight beams, increasing the horizontal stability of the bridge.

A.2.2. Scale models

In Figure A.21, a number of the scale models made during the workshop is shown.

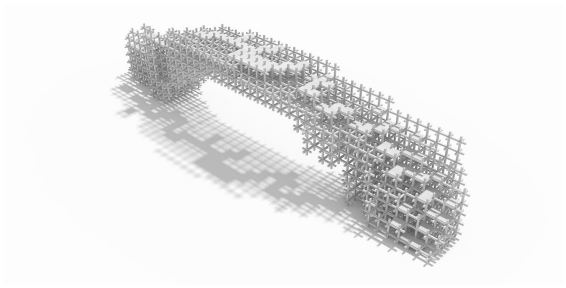

(a)

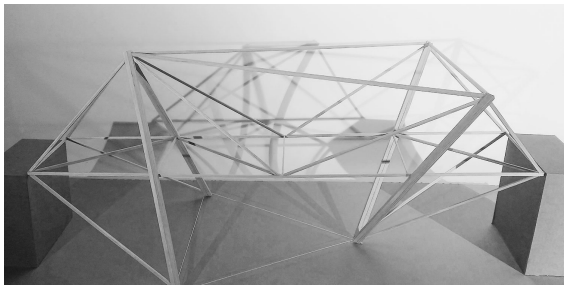

(b)

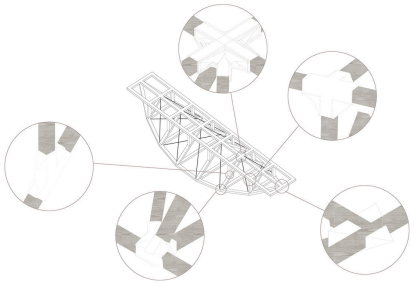

(c)

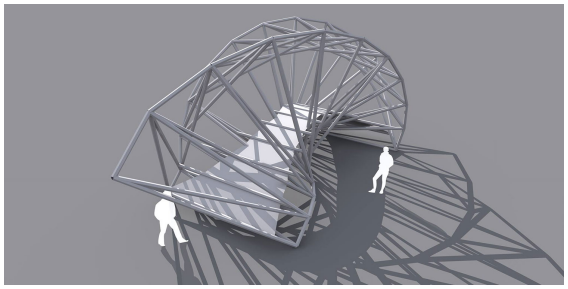

(d)

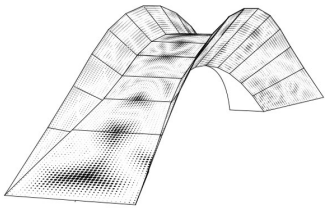

(e)

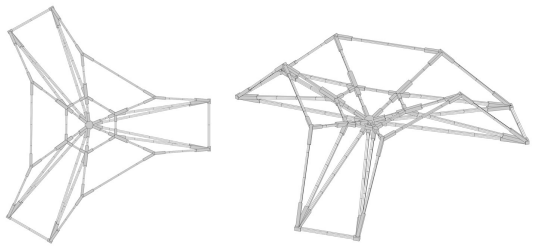

(f)

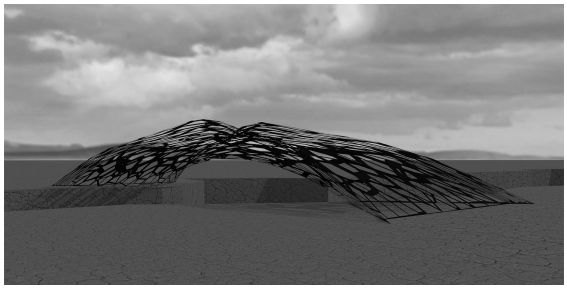

(g)

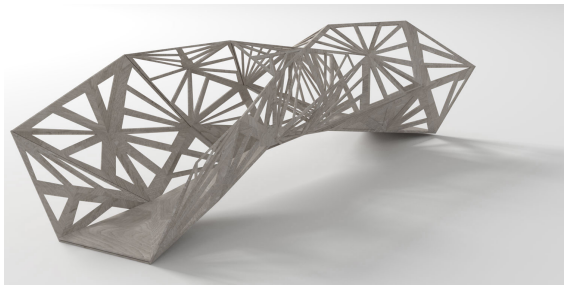

(h)

Figure A.21: Bridge designs by students of the workshop *Intelligent Fabrication 2017 - Digital Bridges* at the *Ecole nationale supérieure d'architecture de Versailles*

B

Japanese Joinery

Where Europe and China were front runners in the development of masonry structures, Japan walked ahead in the field of timber structures. The main reason for the almost exclusive concentration on timber structures in Japan is the abundance of timber. Another factor that influenced the choice for this type of material is the ability of timber structures to resist earthquakes and typhoons. Both the relatively low mass and the flexibility of joints in timber structure have a positive effect on the behaviour of a timber structure subjected to dynamic loading. [49]

B.1 Types of connections

The joints can be split up into two joint systems which contain plentiful different types:

- *Tsugite*: Splicing Joints, used to augment length where materials are insufficient in length
- *Shiguchi*: Connection Joints, used to connect materials at an angle

Figure B.1: A selection of traditional Japanese joinery

B.1.1. Tsugite - Splicing Joints

The joints from the category named *Tsugite* are defined as joints allowing for elongate elements that are too short. In case the joints are slightly modified, they could enable the transition to another cross-sectional dimension or a slight change in direction. The figures below show some examples of splicing joints. The

performance of the joint types subjected to compression, tension and shear load in two directions is reviewed using colour codes:

- Green: Good resistance

- Orange: Some resistance or resistance in only one direction (for shear forces)

- Red: No resistance

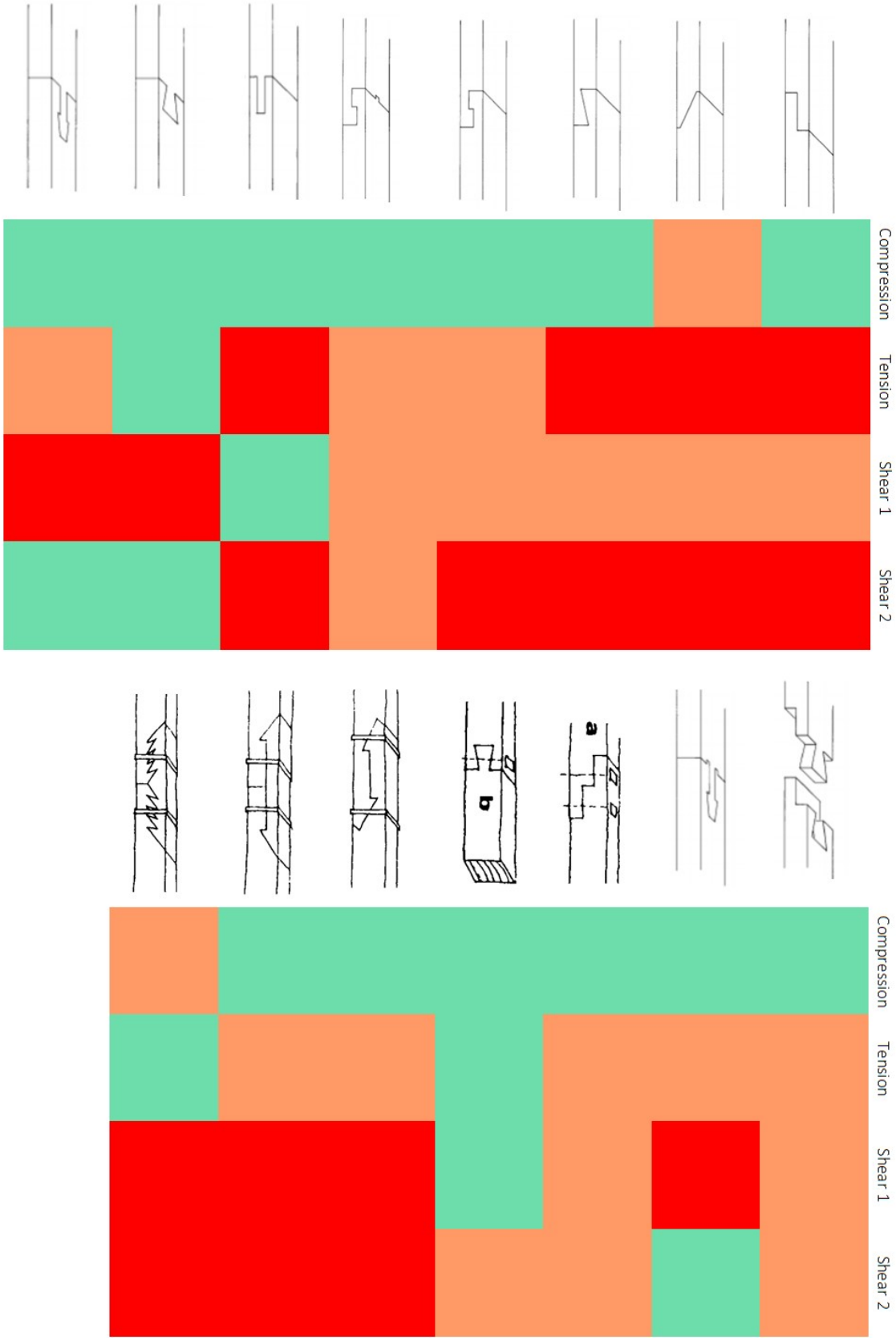

Figure B.2: A selection of Tsugite joints (Part 1) [64] [24]

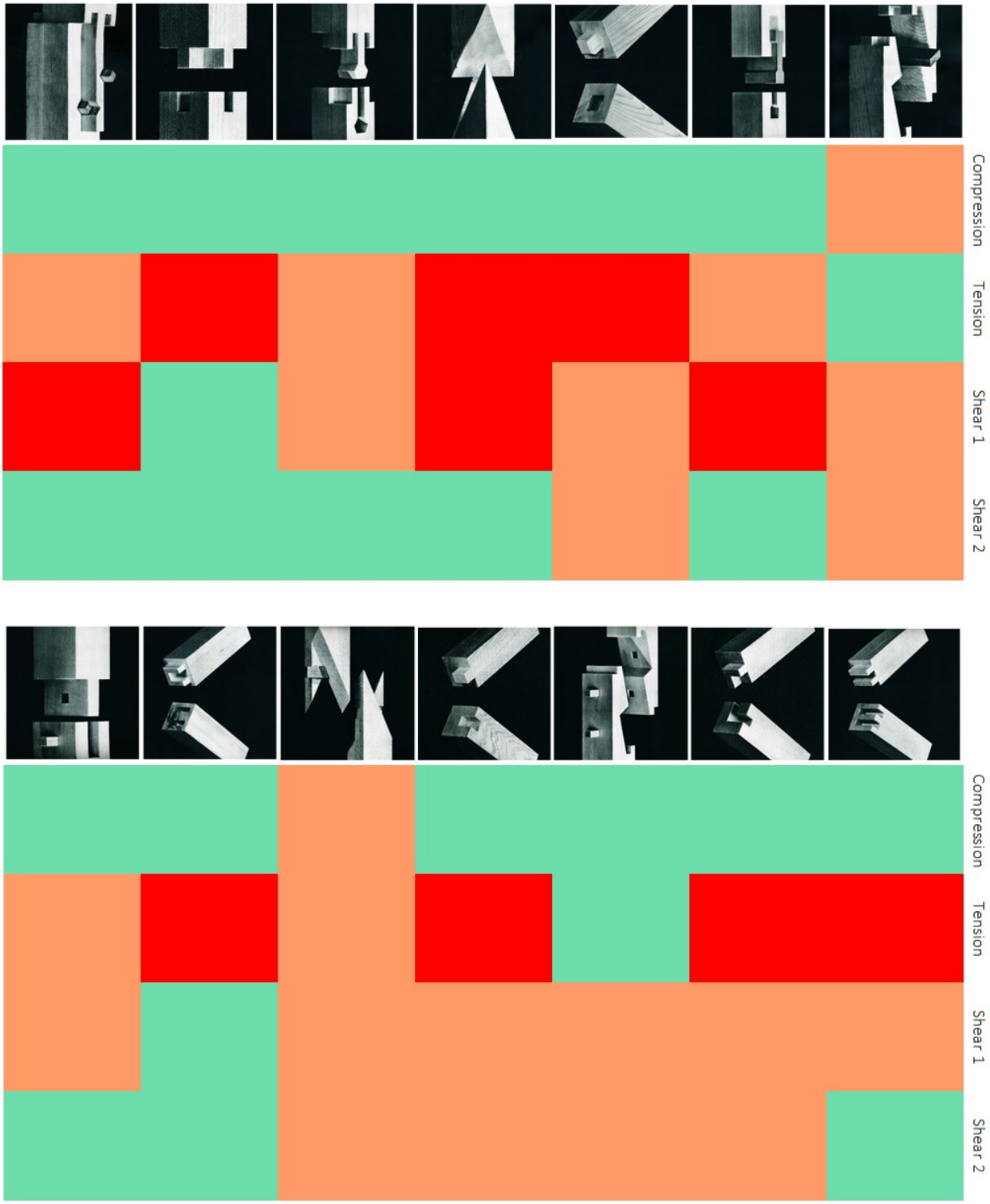

Figure B.3: A selection of Tsugite joints (Part 2) [49]

B.1.2. Shiguchi - Connection Joints

Corner joints

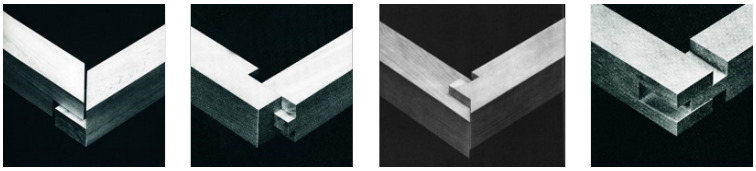

Figure B.4: Various types of corner joints [49]

T-joints

Figure B.5 shows various different types of T-joints. What the joints have in common is that they provide resistance to a tension force on the not-continuous member only by the application of a fastener.

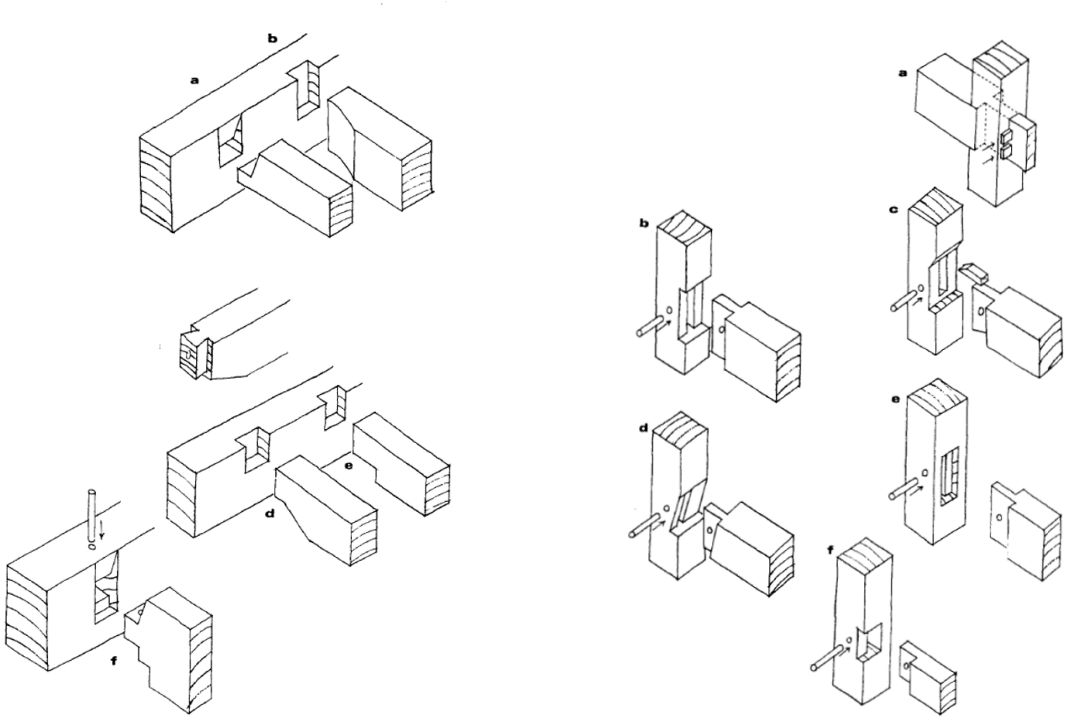

(a) (b)

Figure B.5: Various types of T-joints (Part 1) [24]

The T-joints shown in Figure B.6 on the other hand have some resistance to a tension force by means of interlocking.

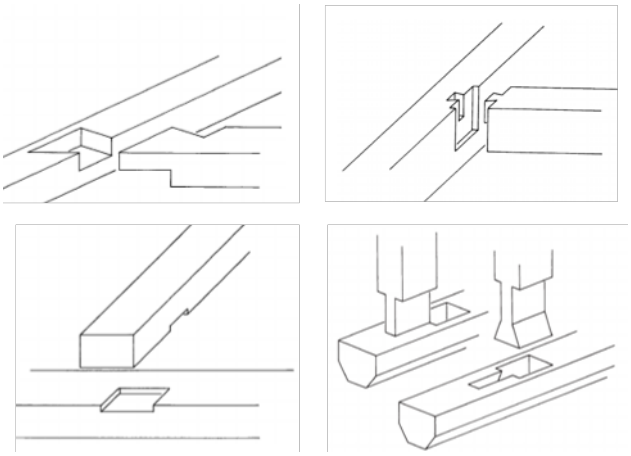

Figure B.6: Various types of T-joints (Part 2) [64]

Complex joints

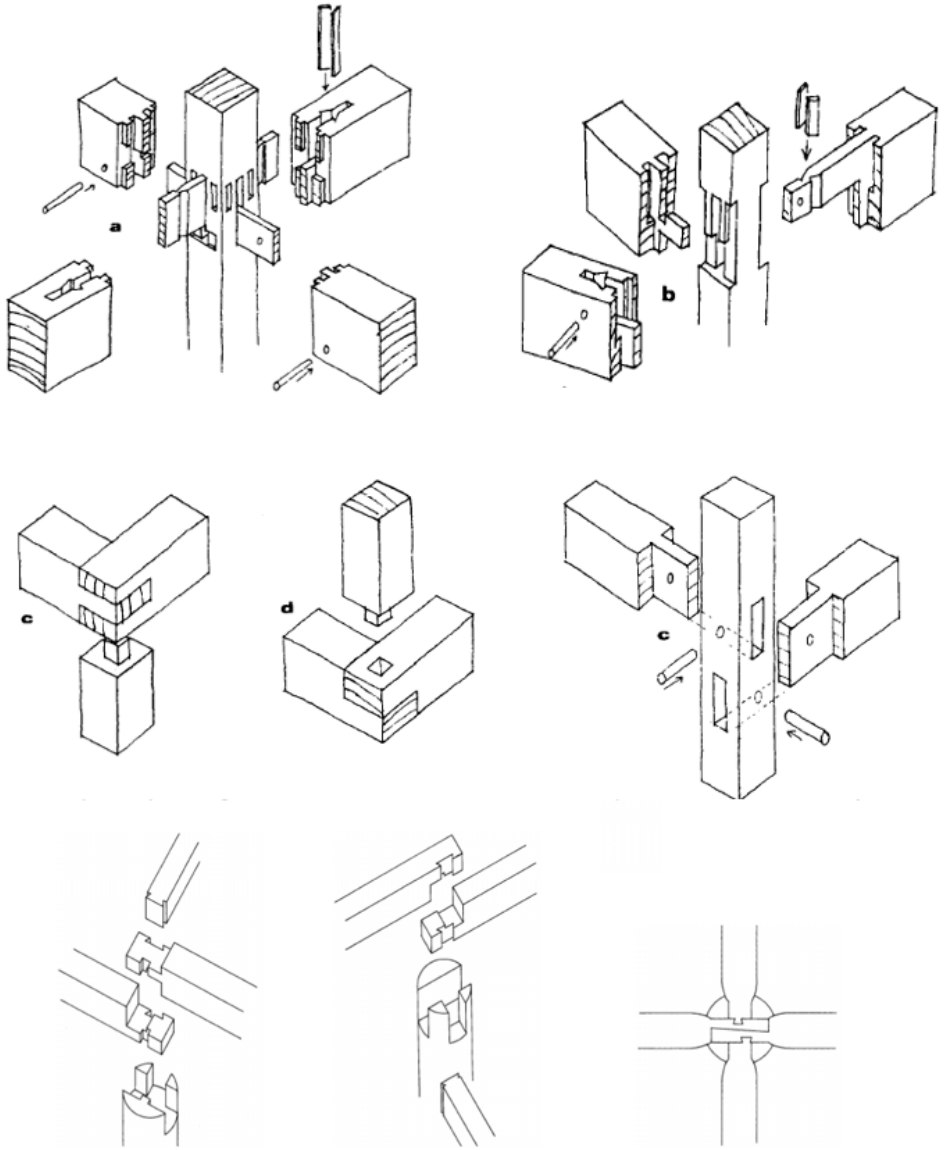

Figure B.7: Various types of complex joints [24] [64]

B.2 Research done on strength calculations of interlocking joints

The introduction of new (digital) manufacturing techniques like CNC, robotic milling and 3D printing has enabled the recurrence of interlocking joints. Unless the new manufacturing techniques show great potential in the field of fabrication, there is still a lack of scientific understanding of this type of joints. In the following sections two research projects will be discussed which focus on the modelling of the mechanical behaviour and optimisation of traditional interlocking joints.

B.2.1. Theoretical modeling and experimental study of Japanese "Watari-ago" joints

A study was carried out by Keita Ogawa, Yasutoshi Sasaki and Mariko Yamasaki on the mechanical behaviour of Japanese *Watari-ago* joints, see Figure B.8 [43]. The joint consists of two continuous beams which obtain resistance against in-plane shear forces by interlocking notches. No additional fasteners are used. Joints that obtain their strength mainly through embedment can be loaded far over their elastic limit. This ductile behaviour is beneficial for avoidance of brittle failure and can be favourable when a structure is subjected to dynamic loads like earthquakes or wind.

Figure B.8: A *Watari-ago* joint in horizontal roof members [43]

A predicting model of the mechanical behaviour of the joint was developed using wooden embedment theory. Inayama M from the University of Tokyo, Japan already made a theory that describes the mechanical behaviour of embedment joints in the elastic region. In order to describe the deformation behaviour after yielding, the theory should be expended, which was done in this research.

To verify the model, lab tests were carried out. The experimental results demonstrated that the mechanical behaviour of the joint depends on the notch size and shape. Furthermore it indeed showed that the joint can retain resistance after reaching the yield strength.

When comparing the test results to the results of the theoretical model, it could be concluded that the model reflects the behaviour of the watari-ago joint really accurately. Therefore it can be inferred that the mechanical behaviour of Watari-joints can be modelled by using the embedment theory. Additionally a model was made that could be used to find the shape and size of the notch that gives optimal structural performance. The results of this simulation showed that an increase of 50% in terms of the bending moment resistance of the joint could be obtained.

B.3 Application of Japanese joinery in modern structures

Due to the development of techniques to modify timber products with robots, a revival of the application of the traditional joinery techniques can be seen. Two architects that are famous for their striking timber structures are Kengo Kuma and Shigeru Ban. Both originating from Japan, which shows how persistently the application of timber structures is embedded in the Japanese culture. Both of them applied the traditional Japanese joinery in their modern architectural designs.

B.3.1. Kengo Kuma

An architect that applies the traditional Japanese joinery in contemporary architecture is Kengo Kuma, born in Yokohama, Japan in 1956. He aims to design eye catching architecture that is still connected to the area in which it's built by applying (manipulated) traditional architectural elements and using local materials.

Figure B.9 shows an example of one of his projects: the *GC Prostho Museum Research Center* in Kasugai-Shi, Japan (2010). The structure consist of wood members with small sections (6cm x 6cm) which are assembled without the use of glue. The joints are inspired by a traditional timber toy from the Hida Takayama region in Japan. The two traditional joints that are used are shown in Figure B.10.

Figure B.9: *GC Prostho Museum Research Center*, Kasugai-Shi, Japan by Kengo Kuma [10]

B.3.2. Shigeru Ban

Another architect famous for his timber structures is Shigeru Ban, mentioned before in Section 3.1.1 regarding his cardboard bridge. One of his projects that is noticeable for it's timber connections is *The Seine Misicale* in the west of Paris, France. The facade structure consists of 1,300 laminated CNC-machined beam segments. The timber structure was implemented in a fully parametric 3D CAD model, containing all information regarding fabrication and assembly. The model was used as basis for the structural calculations, the digital planning process, the fabrication data for lamination and CNC-milling and to simulate the assembly situations.

Shigeru Ban was assigned to use as little steel as possible within the timber structure. Therefore all cross joints and the longitudinal joints in the compression ring were executed as traditional lap joints, see Figure B.12a. For the joints in the tension rings, a splice joint was developed, see Figure B.12b. Lateral forces are taken by screws and beech dowels assure precise positioning.

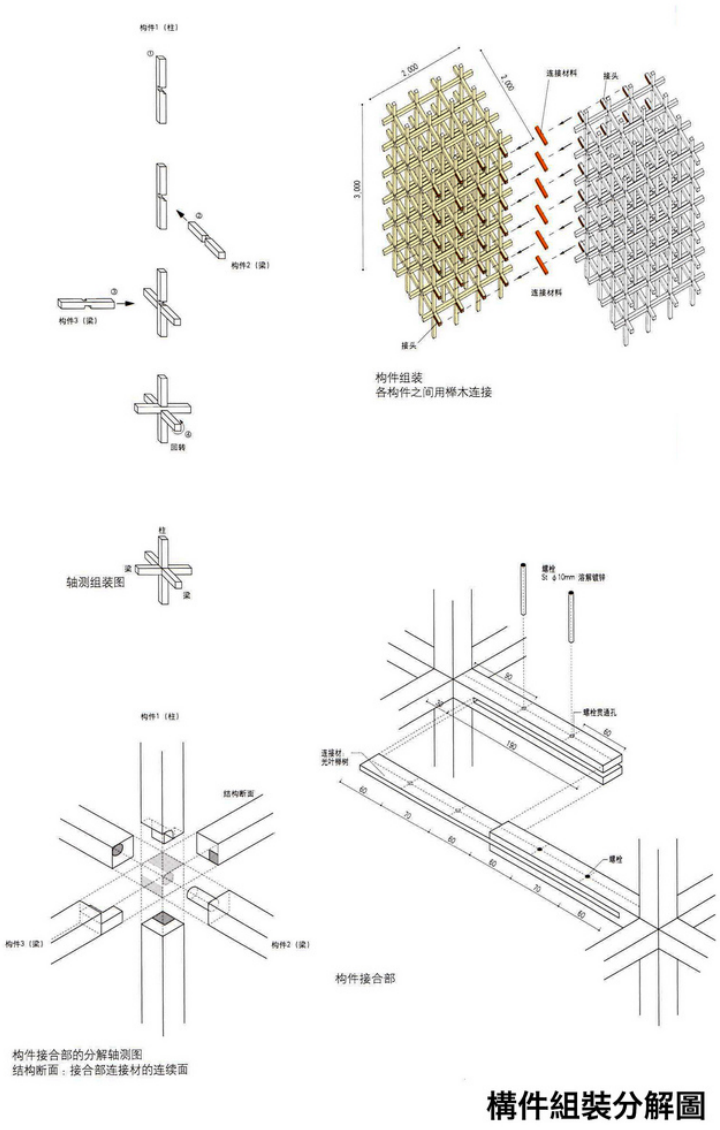

Figure B.10: Traditional joints in the *GC Prostho Museum Research Center*, Kasugai-Shi, Japan by Kengo Kuma [10]

Figure B.11: *The Seine Musicale* in Paris, France by Shigeru Ban [27]

(a)

(b)

Figure B.12: (Modified) traditional timber connection in *The Seine Musicale* in Paris, France by Shigeru Ban: a lab joint (B.12a) for joints in compression and splice joint (B.12b) for joints in tension [36]

C

Interlocking joint calculation research

C.1 Parametric Finite Element Contact Analysis for Topologically Interlocking Joinery

At Singapore University of Technology and Design, research was carried out Topologically Interlocking Joinery's (TIJs) [4]. The aim of the research was to increase the understanding and designs of TIJs with new simulation and fabrication methods. In order to predict the mechanical behaviour of the joints, full 3D finite element (FE) models were created. This requires a solid modelling of the geometry, FE mesh, assignment of contact interactions and selection of parameters.

A parametric study was carried out in order to identify the relation between geometric parameters and the stiffness of TIJs. For this, a parametric 3D finite element Contact Analysis was applied. As a case study, two types of joints were analysed: the *Basara Splice* and *Shihou-Ari Splice*, see Figure C.1.

(a) (b)

Figure C.1: Basara Splice (C.1a) and Shihou-Ari Splice (C.1b) [4]

C.1.1. Settings for the FE Contact Analysis

The following geometry loading and boundary conditions were used for the analysis:

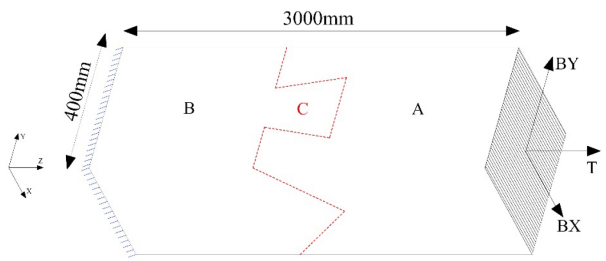

Figure C.2: Dimensions, loads and boundary conditions of the model [4]

The model was built up of two liner parts (A and B) connected by a joint in the middle (C). The bottom surface of part B was fixed in all six degrees of freedom. This kind of joint generally performs well under compression but relatively poor under tension loading and bending. In order to study if this performance can

be improved by changing the geometry, each joint was analysed under three loading conditions: a tension force T = 20kN and a horizontal bending moment in both directions (Bx = By = 5kN) at the top surface of element A, combined with a self-weight load.

An orthotropic representation of the material properties was used which is commonly used in numerical analysis:

Density [kg/m^3]	Ex [MPa]	Ey [MPa]	Ez [MPa]	Gxy [MPa]	Gxz [MPa]	Gyz [MPa]	Nu_{xy}	Nu_{xz}	Nu_{yz}
450	900	500	12000	40	700	700	0.558	0.038	0.015

Figure C.3: Mechanical properties of the wood used for the study [4]

The model was made using *ABAQUS* software. Between the parts *"general contact interaction"* was assumed. The Coulomb friction contact algorithm which is available in ABAQUS was used for the interface with a friction coefficient Îij = 0.5 and the contact pressure-over-closure was set to *âÄIJHardâÄİ*.

The efficiency and accuracy of the model depends on the FE discretization method, mesh size and numerical integration scheme. For this model Hexahedral discretization and the Newmark method for time integration, Newton-Raphson for linearization of nonlinear equations, and Gauss- Seidel relaxation for contact condition was used. A mesh refinement study carried out that the the stress distribution around sharp corners requires special attention and therefore a finer mesh was used at that location, see Figure C.4.

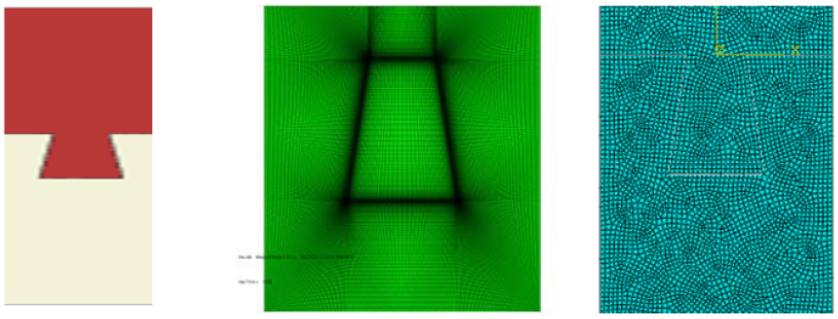

Figure C.4: 3D joint (left), fine mesh around the joint (middle), coarse mesh around the joint (right)

Basara Splice Joint

Next, a parametric study on the proportions of the connection was carried out. The following three parameters are varied: W_t, h and W_b, see Figure C.5. The study showed that the angle α, see Figure C.5, had the biggest impact on the minimisation of the displacement.

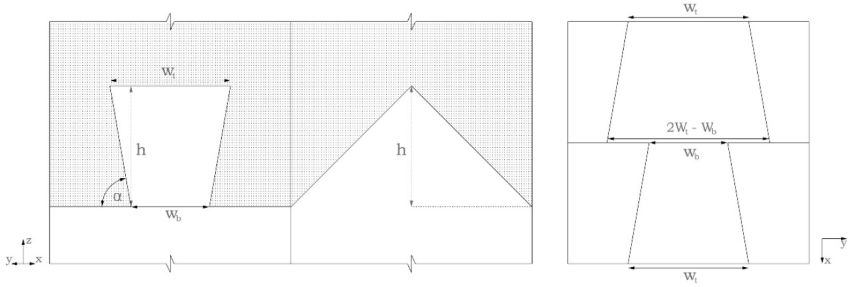

Figure C.5: Geometric parameters of the Basara Splice Joint

After, a study on the effect of the friction coefficient was done. The study indicated that, as expected, a higher friction coefficient reduces the displacement. Because of this it is suggested to increase the surface friction to increase the stiffness of the joint.

Shihou-Ari Splice Joint

Like for the Basara Splice Joint, a parametric study of the geometric parameters of the Shihou-Ari Splice Joint was carried out, with the goal to minimise the displacements. The angle α was varied by analysing different values for W_p and W_t.

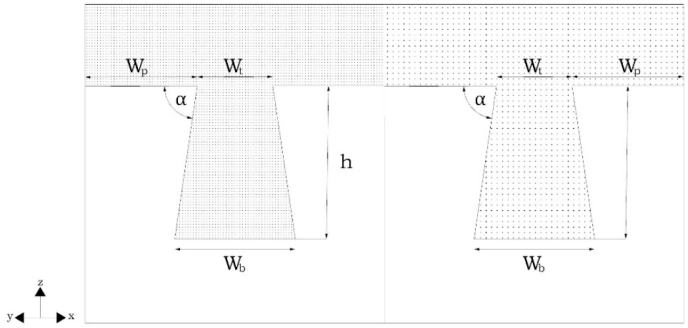

Figure C.6: Geometric parameters of the Shihou-Ari Splice Joint

In contrast to the Basara Spice Joint, the angle α did not have a big impact on the displacements. The dimension W_p appeared to be the dominant parameter for the stiffness of the joint.

Conclusion

From the parametric study it could be concluded that increasing the friction coefficient had a bigger impact on the stiffness than change the parametric parameters. Further research should be done on methods to increase the contact surface friction.

C.2 Flexural behaviour of timber dovetail mortise-tenon joints

In Section C.1, attention has already been paid to research done on the strength calculations of interlocking joints. The research mentioned mainly focused on both testing results and numerical simulations. A numerical simulation is unfortunately out of the scope of this project. The strength of the connections will be estimated by an analytically calculation. Hopefully, the testing of a prototype of one connection can show the *"proof of concept"*. The research that is treated in this section focuses on analytical calculations of interlocking joints.

In research carried out by Chunchao Chen, Hongxing Qiu and Yong Lu, the flexural behaviour of two types of dovetail mortise-tenon joints have been analysed, see Figure C.7 [16].

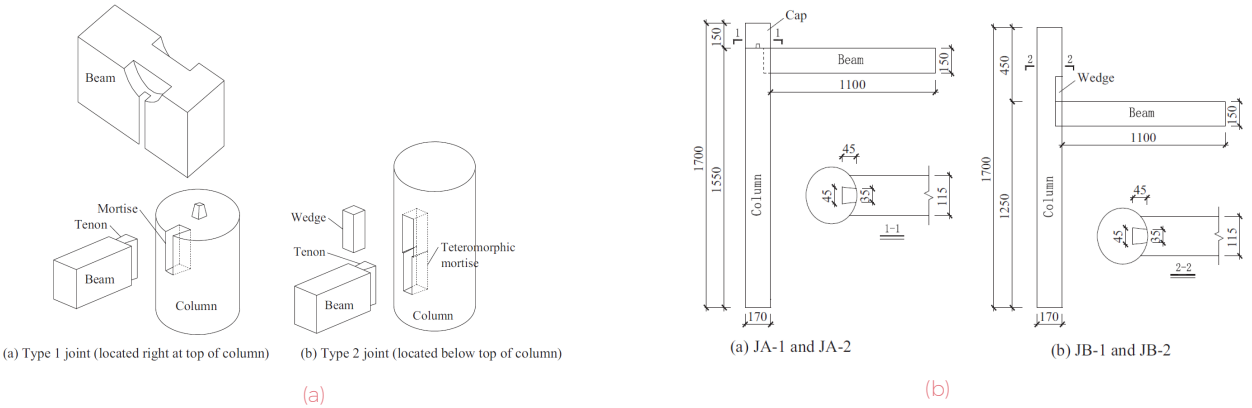

Figure C.7: Two types of dovetail mortise-tenon joint: Configuration of the joint (C.7a) and dimensions of the specimens [mm] (C.7b)

The research consists of three parts:

1. Experiment study: Analysis of the of the flexural behaviour on the basis of observations and load-deformation relationship
2. Numerical simulation: Finite element analysis using ABAQUS software

3. Theoretical analysis: Derivation of a simplified analytical model for the calculation of the moment-rotation relationship of the joint

Since the focus of the project is on simple analytical calculation methods, the focus will be on the last part.

Assumptions

For the derivation of the simplified analytical model for the calculation of the moment-rotation relationship, the following basic assumptions are made [16]:

- The bending deformation of the tenon is neglected. Only rigid body motion is taken into account. Therefore, the displacement of every point in the tenon can be expressed in the rotation, θ, and pull out displacement, δ_0, of the tenon
- When extrusion happens between longitudinal and transverse timber areas, the deformation takes place only in the transverse timber area
- When the intersection on the two side interfaces between tenon and mortise are both under compression in the timber transverse direction, the compression deformation of the tenon is equal to the expanding deformation of the mortise at the same point

Geometric conditions

Figure C.8 shows the geometric conditions of the mortise-tenon joint. The dimensions of the tenon are marked as:

- l = length
- h = height
- a = width of the tenon apex
- b = width of the tenon neck

The gaps in the connection between both members are denoted with l', a' and h'. It is assumed that the tenon will abut and therefore rotate around point 'A', see Figure C.8. Furthermore two angels are defined: $'\alpha'$ and $'\beta'$, also see Figure C.8. The origin of the axis is defined at the centre-line of the tenen, at the intersection point of the mortise and tenon neck. The displacement at the location of the origin, $'o'$, can be expressed in the rotation of the tenon:

$$\delta_0 = 0.5h\theta \tag{C.1}$$

This gives a compression deformation at the bottom:

$$\delta_b = l \cdot sin(\alpha + \theta)/cos(\alpha) - 0.5h - \delta_0 \cdot sin(\theta) - h' \tag{C.2}$$

The length of the contact area, see Figure C.8, is:

$$l_b = \delta_b \cdot cos(\theta) \tag{C.3}$$

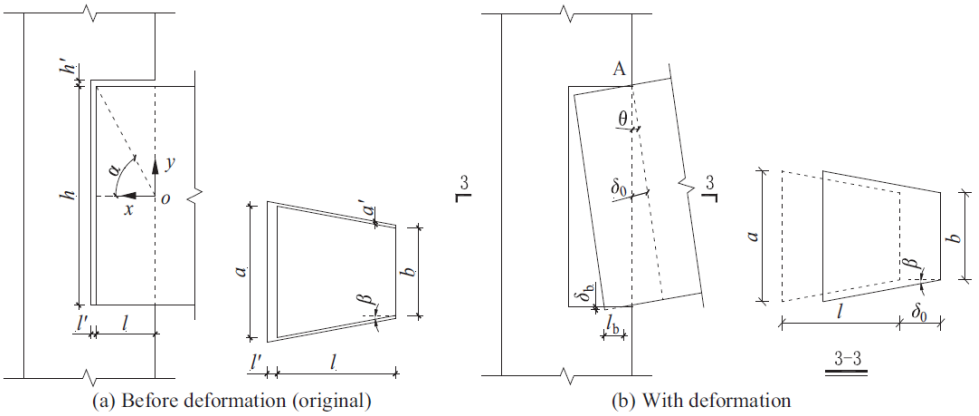

(a) Before deformation (original) (b) With deformation

Figure C.8: Dimensions of the connection

The compressive deformation of the sides of the tenon can be simplified as a uniform distribution along the length of the tenon as shown in Figure C.9a. Assuming this, the compression deformation at the bottom is:

$$\delta_s = [(l - l \cdot cos(\alpha + \theta)/cos(\alpha) + \delta_0 \cdot cos(\theta)) \cdot tan(\beta) - a']/4 \tag{C.4}$$

The height of the contact area on the side is:

$$h' = 4 \cdot \delta_s \cdot h/(4 \cdot \delta_s + a') \tag{C.5}$$

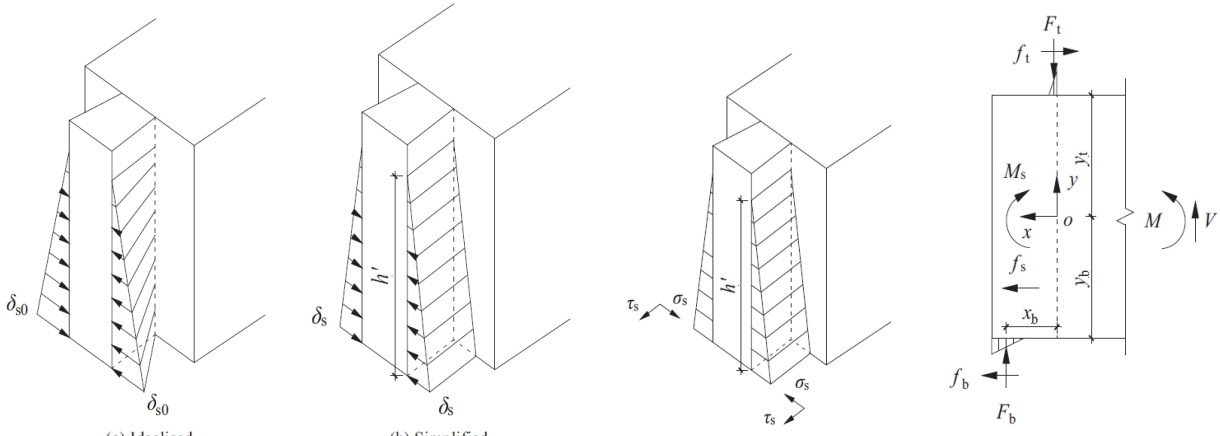

Figure C.9: Assumed stress compression deformation distribution and moment equilibrium

Equilibrium conditions

Two equilibrium equations can be defined:

- Equilibrium of horizontal forces: $\Sigma F_h = 0$

$$f_t = f_b + f_s \tag{C.6}$$

- Moment equilibrium around 'o': $\Sigma T|^o = 0$

$$M = F_b x_b + f_b y_b + f_t y_t + M_s \tag{C.7}$$

When the stresses enter the elastoplastic stage as shown in Figure C.10, Equation C.6 and C.7 still apply.

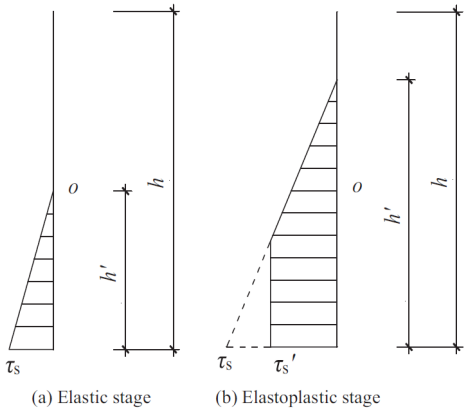

Figure C.10: Stress distribution on the side faces along the height of the tenon

Physical conditions

Now the distinction between the elastic stage and elastoplastic stage should be made. In the research carried out by Chunchao Chen, Hongxing Qiu and Yong Lu both stages are elaborated. Since for this project only the elastic stage linear elastic theory will be applied, the elastoplastic stage will be disregarded.

The vertical compressive stain, ϵ_b, can be expressed in terms of the vertical deformation δ_b:

$$\delta_b = 0.5 \cdot h \cdot \epsilon_b \tag{C.8}$$

This gives the following maximum compressive stress: e

$$\sigma_b = E_{c,R} \cdot \epsilon_b = 2 \cdot E_{c,R} \delta_b / h \tag{C.9}$$

This leads to the following resulting forces at the bottom of the tenon:

$$F_b = 0.5 \cdot a \cdot l_b \cdot \sigma_b \tag{C.10}$$

$$f_b = \mu \cdot F_b \tag{C.11}$$

The lever arms with respect to point $'o'$ is:

$$x_b = l - l_b/3 \tag{C.12}$$

$$y_b = y_t = 0.5h \tag{C.13}$$

The maximum shear force and normal force along the two side faces are:

$$\sigma_s = \epsilon_s \cdot E_{c,T} = \frac{2\delta_s}{0.5(a+b)} \cdot E_{C,t} = 4 \cdot E_{c,T} \cdot \delta_s / (a+b) \tag{C.14}$$

$$\tau_s = \mu \cdot \sigma_s \tag{C.15}$$

Assuming the stress-distribution in the elastic stage as shown in Figure C.10 gives the following horizontal resultant force:

$$f_s = 2 \cdot 0.5 \cdot \tau_s \cdot h' \cdot (l - \delta_0) = \tau_s h' (l - \delta_0) \tag{C.16}$$

Now, the resulting bending moment due to f_s around point $'o'$ can be expressed as:

$$M_s = \tau_s h' (l - \delta_o) \cdot (h/2 - h'/3) \tag{C.17}$$

C.2.1. Simplified calculation

A simplified calculation approach is proposed that can be used to only calculate the moment-rotation relationship at a few key points:

1. The settling point at which the bending moment starts to develop with an initial rotation θ_i and a zero moment ($M_i = 0$)
2. The initial yield point at which the timber starts to reach the plastic range at the two side faces at a rotation θ_y and bending moment M_y
3. The peak moment, M_p and the corresponding rotation (θ_p)
4. The failure or ultimate point where the tenon is on the onset of pull-out from the mortise, with a rotation θ_u and bending moment M_u

Since linear-elasticity theory will be used for this research, point 2 is most important. At this point it can be assumed that $\sigma_T = f_{c,T}$ in Equation C.14. The rotation and bending moment at the initial yield point can be calculated as follows:

$$\theta_y = \frac{-h + \sqrt{h^2 + 2l[a' \frac{(a+b) f_{c,T}}{E_{c,T}}] cot(\beta)}}{l} \tag{C.18}$$

When this equation is substitute into Equation C.7, the yield moment can be expressed as:

$$M_y = \frac{4\mu E_{c,T} (l - 0.5h\theta_y) h^2 k_1}{a+b} \frac{4k_1}{4k_1 + a'} [1 - \frac{4k_1}{3(4k_1 + a')}] \tag{C.19}$$

Where:

$$k_1 = [(0.5l\theta^2 + h\theta) tan(\beta) - a']/4 \tag{C.20}$$

Verification

The simplified method is verified by comparing the results to the experimental results. Both the theoretical and experimental results are graphed in Figure C.11.

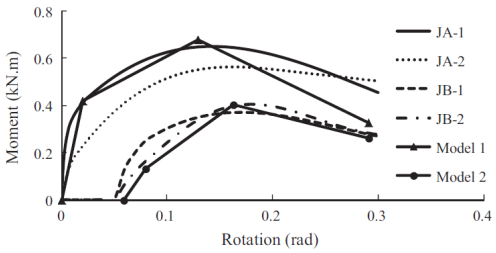

Figure C.11: Comparison between experimental results and predicted results using the simplified method

It can be seen that the simplified method gives a fairly good prediction for the flexural behaviour of the connections at the four key points.

C.3 Calculation of dovetail joints according to the DIBt

The Deutsches Institut für Bautechnik, *DIBt*, prescribes a formula to calculate the capacity of dovetail joints based on the Eurocode and National Annex DIN EN 19995-1-1 and DIN EN 1995-1-1/NA:

$$R_{90,d} = min \begin{cases} k_{ab} \cdot \frac{h_z}{h_z - r}(6.5 + \frac{18(h_H - h_z + r)^2}{h_H^2}) \cdot (t_{ef} \cdot h_H)^{0.8} \cdot f_{t,90,d} \\ \frac{k_v \cdot b_N \cdot (h_Z - r)}{1.5} \cdot f_{v,d} \end{cases} \tag{C.21}$$

All dimensions are pictured in Figure C.12 and C.13. Furthermore:

t_{ef} is the effective depth in mm: $t_{ef} = min(b_H, 100)$

$t_{t,90,d}$ is the design tensile strength perpendicular to the grain: $f_{t,90,d} = f_{t,90,k} \cdot k_{mod}/\gamma_M$, where $\gamma_M = 1.3$ and k_{mod} should be calculated according to the EC

k_{ab} is a factor that takes into account one- or two-sided connections:

$$k_{ab} = \begin{cases} 1, \text{for one-sided connections} \\ min \begin{cases} 1 \\ b_H/200 \end{cases}, \text{for two-sided connections} \end{cases} \tag{C.22}$$

k_v Can be calculated using Equation C.23

α can be calculated as follows: $\alpha = cod(\delta) \cdot (h_Z - r)/h_N$

δ See Figure C.13

k_n

$$\begin{cases} = 5, \text{for solid wood and laminated softwood} \\ = 6.5, \text{for glulam} \end{cases}$$

$$k_v = min \begin{cases} 1 \\ \frac{k_n}{\sqrt{h_N} \cdot (\sqrt{\alpha \cdot (1-\alpha)} + 0.4 \cdot \frac{l_Z}{h_N} \cdot \sqrt{\frac{1}{\alpha} - \alpha^2})} \end{cases} \tag{C.23}$$

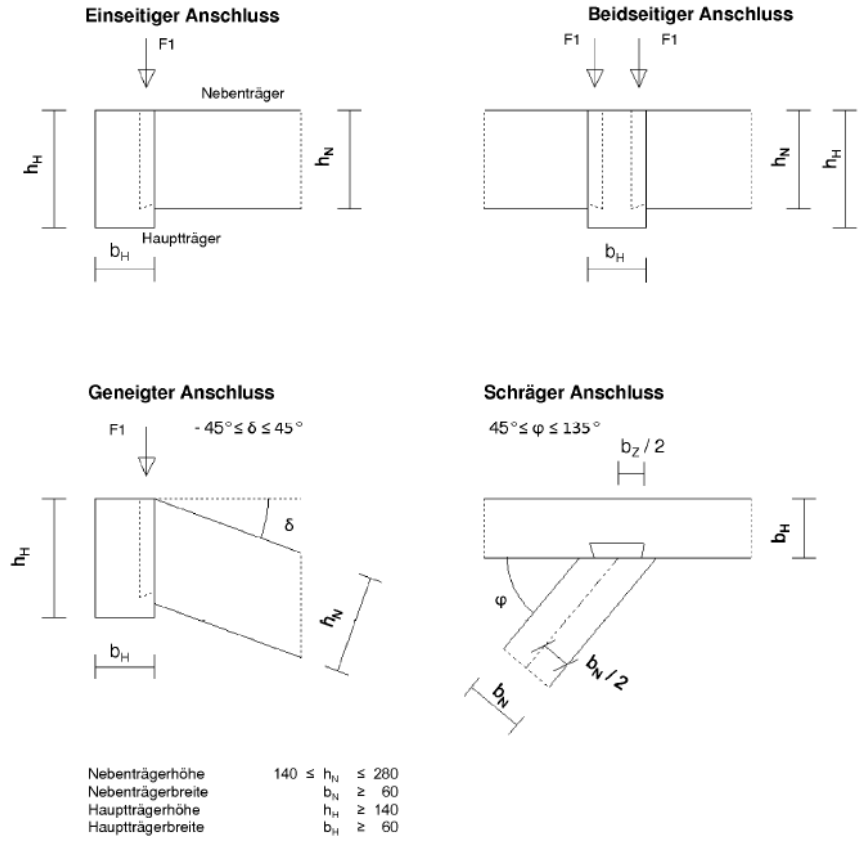

Figure C.12: Dimensions of the dovetail joint (Part 1)

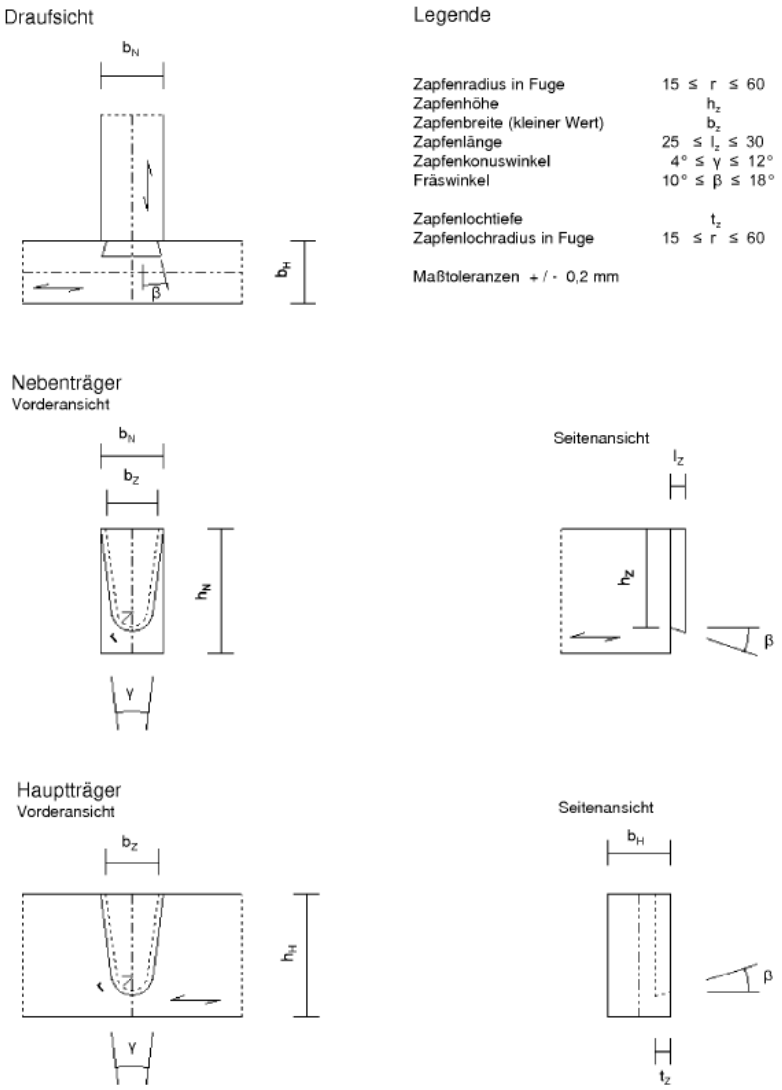

Figure C.13: Dimensions of the dovetail joint (Part 2)

D

Optimisation

D.1 Optimisation principles

E. Ramm describes structural optimisation as: âĂİParameters defining the layout of structures and material, the shape, the dimensions are taken as the unknown primary design variables; we define objectives, equality and inequality constraints, bounds for the design parameters and enter the world of mathematical optimisation. In more or less automated iterative process we loop through the three basic modules of structural optimisation: geometry, mechanics, mathematics.âĂİ Furthermore, he divides the field of layout optimisation in four categories, see Figure D.1:

1. Size optimisation
2. Shape optimisation
3. Topology optimisation
4. Material optimisation

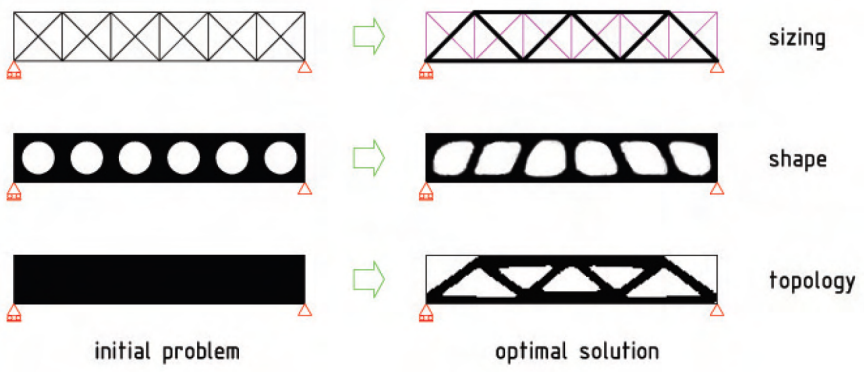

Figure D.1: Representation of the three layout optimisation principles: size, shape and topology optimisation [17]

In order to obtain an integrated design, a combination of multiple optimisation principles can be applied consecutively. Figure D.2 shows a flowchart for an integrated design including both topology and shape optimisation.

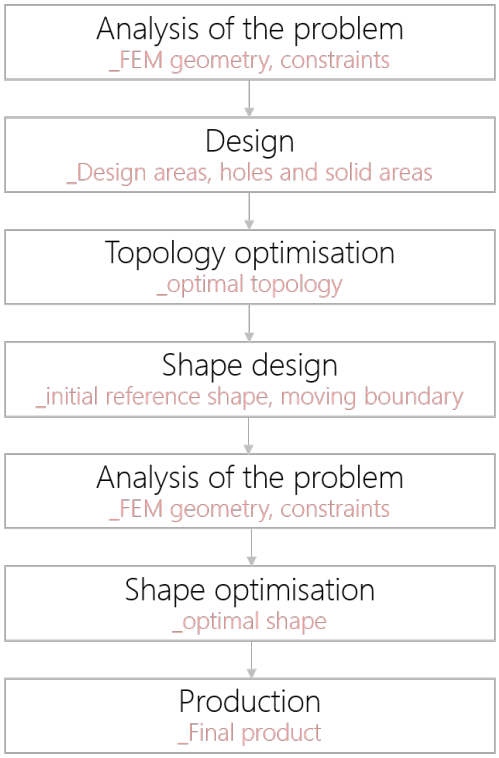

Figure D.2: Flowchart of an integrated design system including topology and shape optimisation [17]

Size optimisation

For this type of optimisation, the domain of the design model is known beforehand and fixed throughout the optimisation process. The shape and topology remain the same and only the size of the elements is varied. In this way, the optimal set of cross-sections can be found in a truss or frame structure or the optimal thickness distribution in a plate structure. The goal of the optimisation is to maximise the structural performance of the structure in terms of weight and overall stiffness of strength while satisfying the equilibrium conditions and design constraints.

Shape optimisation

The goal of the shape or geometry optimisation is to find the optimal geometry of the design domain. The shape is, in contrary to a size optimisation method, not fixed but a design variable. In a shape optimisation, only the boundaries of the design domain are varied but not the topology of the domain.

Topology optimisation

The goal of a topology optimisation is to find the optimal layout of a structure within certain boundaries. The only parameters that are known during a topology optimisation are the applied loads, possible support conditions, the volume of the structure to be constructed and possibly some additional design restrictions. In this case the physical size, the shape and the connectivity of the structure are unknown beforehand.

D.2 Evolutionary Algorithm (Galapagos)

Grasshopper includes an Evolutionary Solver or Genetic Algorithm called *Galapagos* that can be used to solve optimisation problems. In this section, a short outline of this computational method will be given.

D.2.1. Advantages and disadvantages

Evolutionary Algorithms have a number of important advantages and disadvantages, which are listed below:

- Advantages:
  - Evolutionary Algorithms are slow
  - A solution is not guaranteed. There is for example the risk of finding a local optimum instead of a a global optimum
- Disadvantages:

- Evolutionary Algorithms are really flexible. They are able to solve a large variation of problems
- Evolutionary Algorithms are forgiving. They can solve problems that are under- or over-constraint or poorly formulated
- The run-time is progressive, meaning that even when the solver is prematurely aborted, usually a result with a higher quality than the original will be obtained
- The solver allows for a high degree of interaction with the user

The process

The process of an Evolutionary Solver will be explained on the basis of a few figures.

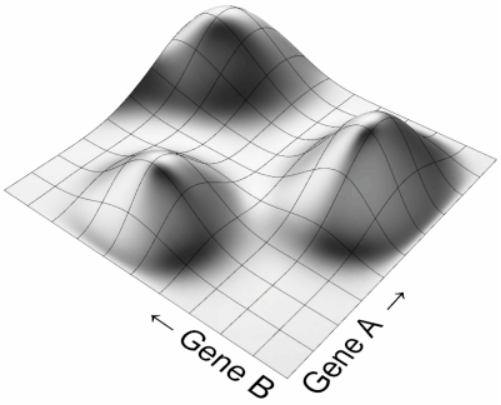

Figure D.3: *Fitness Landscape* for a particular model containing two variables [45]

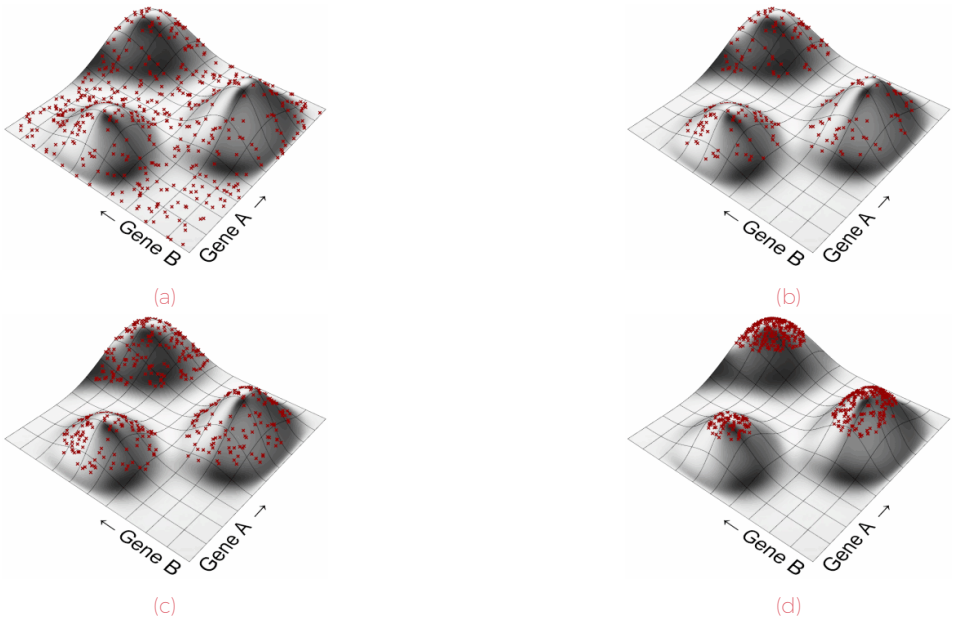

Figure D.4: Evolutionary progress shown in a few pictures. An extensive description of the figures can be found in the table below [45]

Figure D.3 A *Fitness Landscape* expresses the fitness of a certain combination of variables (genes) as the height of the landscape. The goal is to find the highest peak in this landscape. In the simple case of two variables with a 2D fitness plane, this results in an easy to visualise 3D plot as shown in Figure D.3. A model with for example 12 genes would result in a 12-dimensional fitness volume, deformed in 13 dimensions, which is complex to visualise. Therefore, the simple example with only 2 genes will be used for the explanation of the process.

Figure D.4a Since the Fitness Landscape is not know in advance, first a random combination of individuals, called *genomes*, are generated (Generation 0). A genome is a specific value for each and every gene, so for example {A = 0.2, B = 0.5}. The solver will then evaluate the fitness for each random genome, giving the distribution as shown in Figure D.4a

Figure D.4b After this, the genomes are sorted from fittest to lamest. The assumption will be made that the genomes with a high fitness are closer to a potential peak than the low ones. Since the goal is to find the genome with the highest fitness, the worst performing genomes will be disregarded and the focus will be on the remainder.

Figure D.4c Since the genomes in Generation 0 is a result form randomly picked genomes, it cannot be assumed that the best performing genome is among them. Therefore a Generation 1 will be created. When two genomes are bred, the offspring will be in the intermediate model-space, see Figure D.4c.

Figure D.4d Now a new generation is obtained which is not completely random but clustered around the fitness 'peaks'. When repeating the previous two steps, (killing the worst genomes and breeding with the best performing ones), the highest peak will be reached, see Figure D.4d.

An Evolutionary Solver requires the following five interlocking parts in order to perform the above mentioned process:

- Fitness Function (Section D.2.2)
- Selection Mechanism (Section D.2.3)
- Coupling Algorithm (Section D.2.4)
- Coalescence Algorithm (Section D.2.5)
- Mutation Factory (Section D.2.6)

D.2.2. Fitness Function

In biological evolution, the quality known as *'Fitness'* is hard to determine, whereas for Evolutionary Computation the fitness is an easy concept since it can be whatever you want it to be. En example of an application where Evolutionary Computation can be used for is the search for the position of a certain shape so that it can be milled with the least material waste, see Figure D.5. Figure D.5a shows that by rotating the bounding-box, an area B can be found which is smaller than area A and is therefore fitter. When finding the optimum bounding box for a 3D-object (see Figure D.5a), at least three rotation axes are required. For now, it will be restricted to two axis (X and Y).

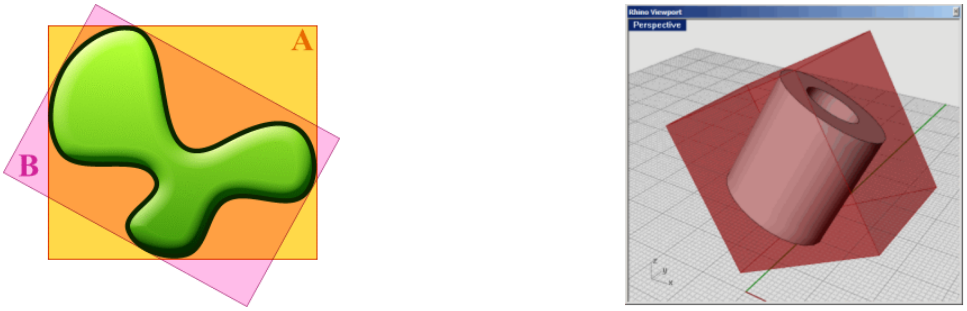

(a) (b)

Figure D.5: [45]

When a random genome is picked at the bottom of the fitness scale, the path of the genetic descendents will be generally be the steepest slope up, see Figure D.6a. The steepest uphill climb is the fastest towards high fitness.

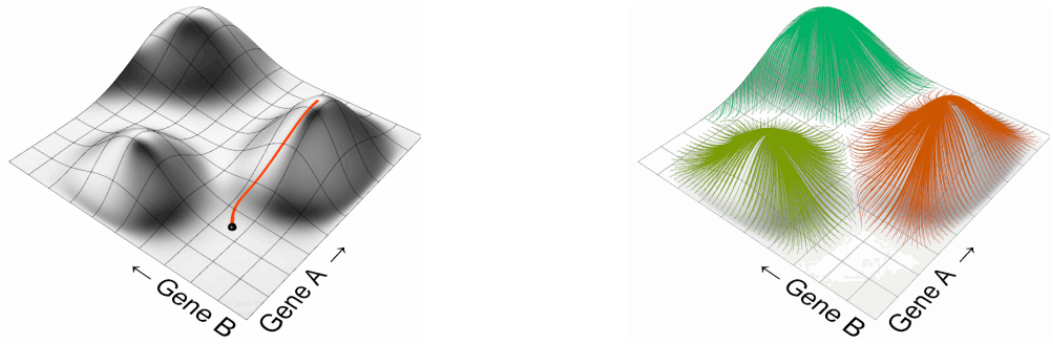

(a) (b)

Figure D.6: Path of random genomes with a low fitness to the top during the evolutionary process[45]

Since every genome want to climb uphill, every peak in the fitness landscape has is own basin of interaction (see Figure D.6b). The size of the basin of interaction cannot directly say something about the quality of the peak. A typical problem is that the solution reaches a local optimum. The Fitness Landscape of the model that seeks the smallest orthogonal box covering the cylinder shown in Figure D.5b is shown in Figure D.7.

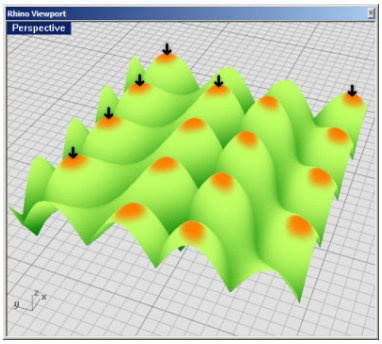

Figure D.7: *Fitness Landscape* for a particular model containing two variables [45]

The Landscape has a highly repetitive pattern. When the landscape is generalised to a 2D-graph Figure D.8a is obtained. Since all minima are of the same scale, there is no risk for finding a local minimum.

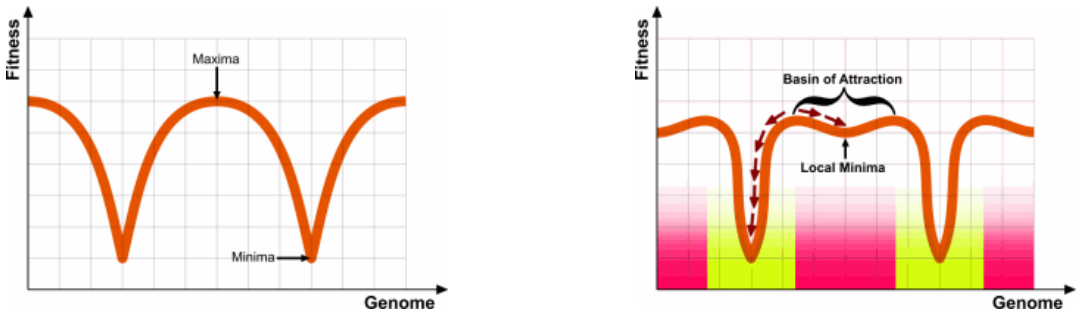

(a) (b)

Figure D.8: Risk for local maximum or minimum [45]

When looking at the Fitness graph in Figure D.8b, it can be seen that the landscape has two solutions: a local and a global one. The Basin of Attraction for both solutions is shown (yellow = high quality, yellow = low quality). It can be concluded that about half of the model space is attracted by a low quality solution. This is

a big drawback of this method. Three more examples of problematic Fitness Landscapes are shown in Figure D.9.

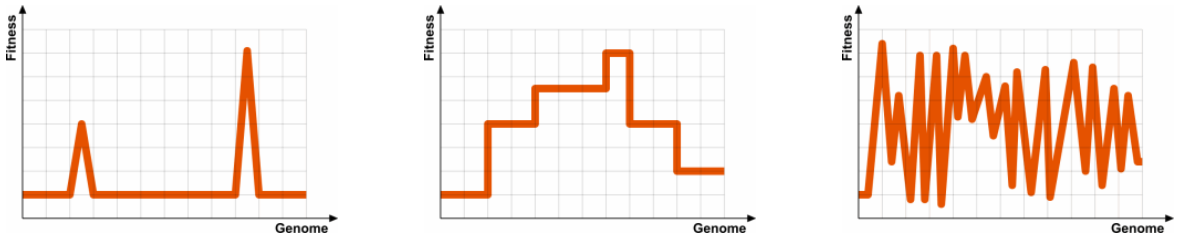

(a) (b) (c)

Figure D.9: Problematic Fitness landscapes [45]

Figure D.9a In this case there will be searched for a maximum. Since the Basin of Attraction for both peaks is really small, there will be a large risk of missing the peaks. The smaller the basin for a solution, the harder to solve the solution for an Evolutionary Algorithm

Figure D.9b Although there are no real local minima, there is no improvement at the plateaus. Therefore, a genome won't 'know' what path to follow

Figure D.9c This Fitness Landscape has a high degree of chaos

D.2.3. Selection Mechanism

There are three main types of artificial selection available in Galapagos, as shown in Figure D.10

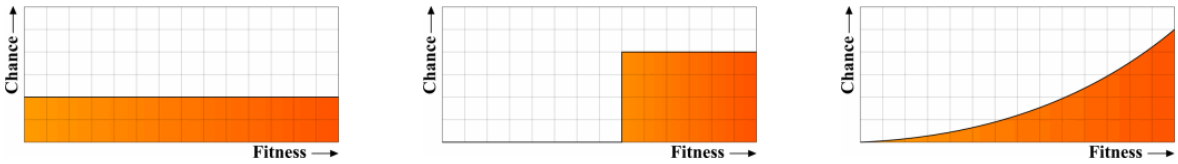

(a) (b) (c)

Figure D.10: Mechanisms for parent selection available in Galapagos, see description below [45]

Figure D.10a *Isotropic Selection*: Is in fact the absence of a selection algorithm. Independently of where the genome is located inside the fitness graph, the chances of mating are constant

Figure D.10b *Exclusive Selection*: Only the top N% of the population gets to mate. If the genome is in the top N%, the chance of having multiple offspring is high

Figure D.10c *Biased Selection*: the chance of mating increases when the fitness increases

D.2.4. Coupling Algorithms

Coupling is the process of finding mates. Once a genome is selected during by the Selection Algorithm, it has to pick a mate from the population. Galapagos (currently) only allows selection by genomic distance. Figure D.11a shows a Genome Map: it shows all genomes in a certain population as dots on a grid. The distance between dots is approximately the same as the distance between genomes in gene-space. The distance is an N-dimensional value, where N is the number of genes. Figure D.11b shows a specific genome that has been selected for mating.

(a) (b)

Figure D.11: [45]

Now there are three options:

Figure D.12a *In-breeding:* Search for a partner in the immediate neighbourhood. The disadvantage is that this would result in a low diversity, leading to a smaller chance of finding alternate solution basins and therefore a higher risk of ending up in a local optimum

Figure D.12b *Out-breeding:* Another extreme is excluding all near genomes. The disadvantage of this is that partners at a large distance will be so different that that they become incompatible

Figure D.12c The best option is a balance between in-breeding and out-breeding

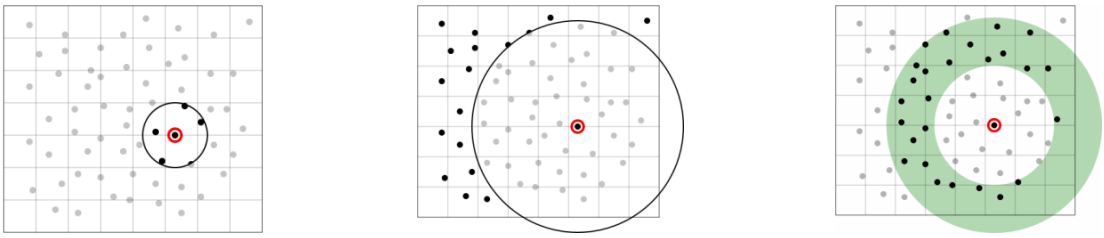

(a) (b) (c)

Figure D.12: [45]

D.2.5. Coalescence Algorithm

When two genomes are mate, it should be decided what values should be assigned to the genes of the offspring. Figure D.13 shows a visualisation of the two 'parent' genomes, each with four genes.

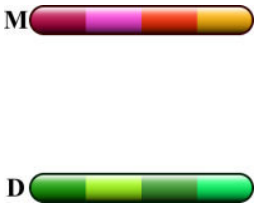

Figure D.13: Two parent genomes for mating [45]

Again there are three options:

Figure D.14a *Crossover Coalescence*: the offspring inherits a random number of genes from both parents. In this way gene value is maintained

Figure D.14b *Blend Coalescence*: New values are computed based on the genes from both parents. The values are basically averaged

Figure D.14c It is possible to add blending preference based on the relative fitness of both parents. For example, if genome M has a higher fitness than genome D, the genes of genome M will be more prominent in the offspring

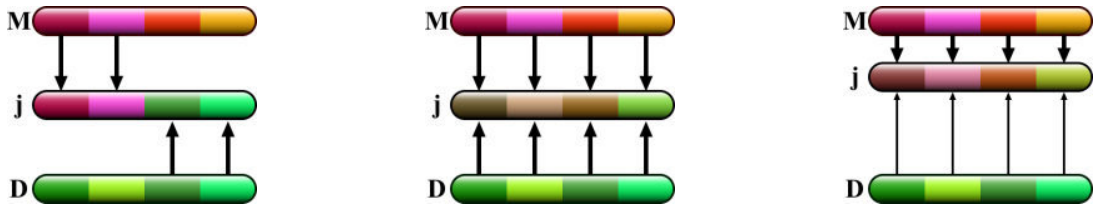

(a) (b) (c)

Figure D.14: Different types of coalescence [45]

D.2.6. Mutation Factories

The three mechanisms discussed before (Selection, Coupling and Coalescence) are designed to improve the solutions on a generation to generation bases. Nevertheless, they all decrease the bio-diversity of the population. The only mechanism that can improve the bio-diversity is mutation. There are multiple types of (Point-)mutations available in Galapagos.

Figure D.15 shows an example of a *Genome Graph*. It is a way to display multi-dimensional points on a two-dimensional medium by drawing them as a series of lines that connect different values on a set of vertical bars, each representing a single dimension. In this way not only points with any number of dimension can be displayed this way, but also points with different number of dimensions in the same graph. In Figure D.15, a genome consisting of 5 genes is shown. The genome is therefore a point in 5-dimensional space. When for example G0 is drawn at $\frac{1}{3}$, this means that the value is at $\frac{1}{3}$ between the minimum and maximum allowed limits.

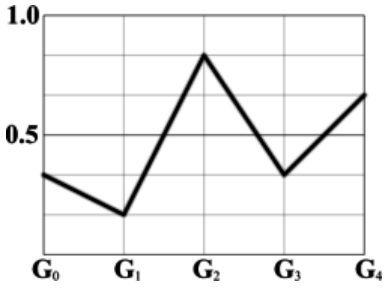

Figure D.15: Genome Graph [45]

The figure below shows four different types of mutations.

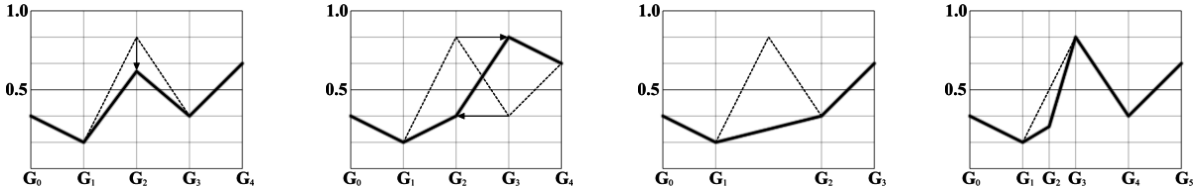

(a) (b) (c) (d)

Figure D.16: Different types of mutations [45]

Figure D.16a *Point Mutation*: Only a single gene value is changed. This is the only mutation possible in Galapagos at the moment

Figure D.16b *Inversion Mutation*: Swapping two adjacent gene values. This is only useful when the genes have a specific relationship

Figure D.16c *Addition Mutations*: this can only be applied to species which don't require a fixed number of genes

Figure D.16d *Deletion Mutations*: like Addition Mutations, this can only be applied to species which don't require a fixed number of genes

D.2.7. Conclusion

Galapagos is an user friendly tool that can be used to solve relatively small problems relatively quick. Nevertheless, it needs a lot of work to make the solver more robust and usable for complex problems.

E

Physical Modelling

E.1 Physical model of a reciprocal structure

In order to get a feeling of the behaviour of a reciprocal structure, a physical model has been made. The model is made from wooden sticks with a pin with a head at the end, representing the connection. The connection can take some tension by the hooking of the pin-head behind the timber bar. There is no glue or other fastening material used.

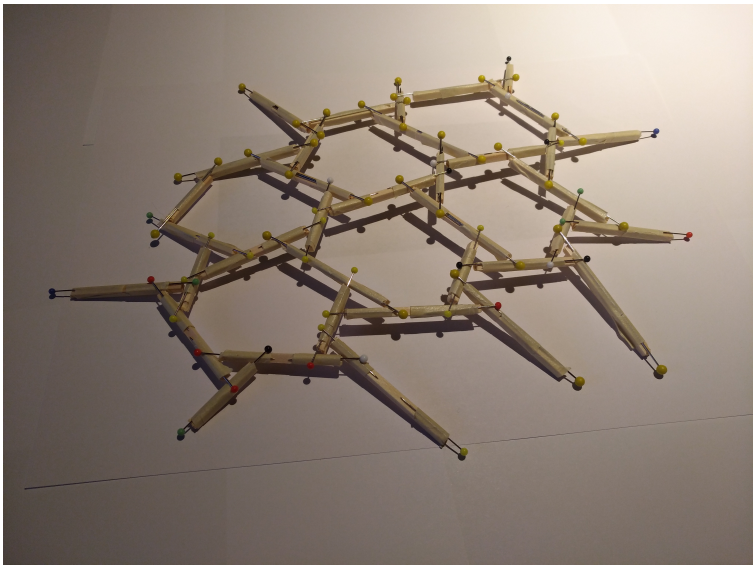

Figure E.1: Physical model of a reciprocal structure

When experimenting with this model the following conclusions were made:

- The structure behaves well under a downward load (in the gravitational direction)
- The beam elements can barely take any upward load. The upward load has to balanced by the downward self-weight load since the connections cannot take any upward shear forces.
- When applying the reciprocal pattern as shown in Figure E.1, all beams at the edges need to be vertically supported. Adjustments to this pattern should be made at the edges

E.1.1. Reciprocal pattern edge

As mentioned above, the beams at the edges of a reciprocal structure are usually vertically supported. This is problematic when designing a 2D-structure like a bridge, where you prefer to have two free edges. Figure E.2 shows a solution that could be used. Further research should evaluate other possibilities with maybe a better aesthetic value.

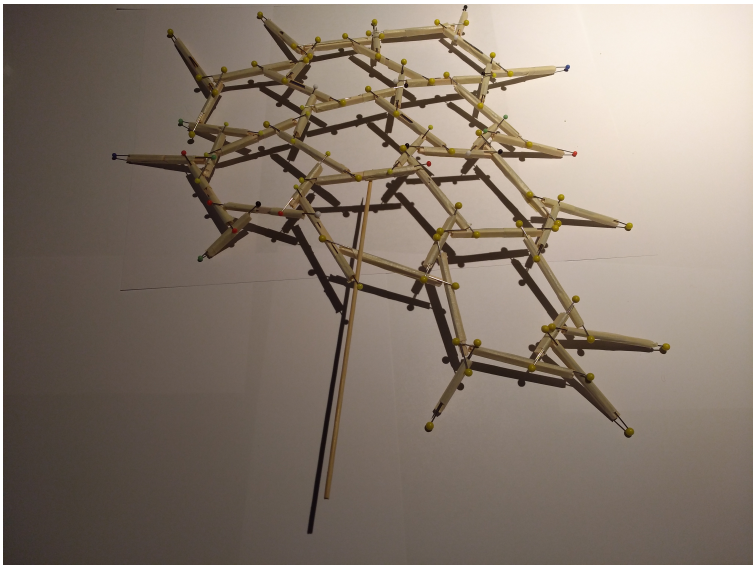

Figure E.2: Physical model of a reciprocal structure with an alternative edge

E.1.2. Grid parameters

Since for this physical model no shear constraints are made at the connection, it is easy to play with the size ratio between the hexagons and triangles in the grid. Figure E.3 shows how the configuration can be easily changed, entailing a change of the stiffness of the structure, without changing the length of the beams.

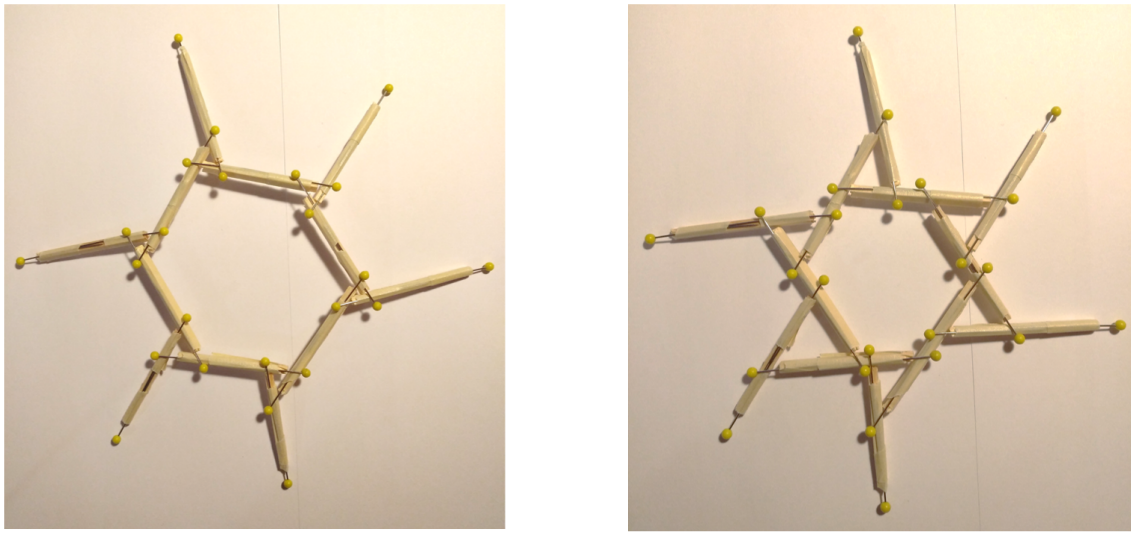

Figure E.3: Adjustable grid configuration without changing the beam sizes

F

Peak Velocity Pressure

The peak velocity pressure can be calculated using equation F.1

$$q_p(z) = [1 + 7 \cdot I_v(z)] \cdot \frac{1}{2} \cdot \rho \cdot v_m^2(z) \tag{F.1}$$

Where:

- ρ is the air density, depending on altitude, temperature and barometric pressure to be expected in the region during wind storms. According to the Dutch Annex $\rho = 1.25 kg/m^3$ in the Netherlands
- $I_v(z)$ is the turbulence intensity which can be determined using Equation F.2
- $v_m(z)$ is the mean wind velocity at a height z above the terrain, see Equation F.3

$$I_v(z) = \begin{cases} \frac{\sigma_v}{v_m(z)} = \frac{k_I}{c_o(z) \cdot ln(z/z_0)}, & \text{for } z_{min} \leq z \leq z_{max} \\ I_v(z_{min}), & \text{for } z < z_{min} \end{cases} \tag{F.2}$$

Where:

- k_I is the turbulence factor. The recommended value for k_I is 1.0
- $c_o(z)$ is the orography factor. This factor takes into account the increased wind velocity by orography (e.g. hills, cliffs etc.) In this case a flat terrain will be assumed whereby the effects of orography may be neglected, so c_o = 1.0
- z_0 is the roughness length, which can be found in Table F.1
- z_{max} is 200m according to the Dutch Annex (NEN-EN 1991-1-4 nb, Section 4.3.2)
- z_{min} is dependent on the terrain category and can be found in Table F.1

$$v_m(z) = c_r(z) \cdot c_o(z) \cdot v_b \tag{F.3}$$

Where:

- $c_r(z)$ is the roughness factor and can be determined using Equation F.4
- $c_o(z)$ is the orography factor taken as 1.0 as discussed above
- v_b is the basic wind velocity and can be calculated using Equation 6.2

Table F.1: Terrain categories and terrain parameters (Table NB.3 - 4.1 from NEN-EN 1991-1-4 nb)

Terrain category		z_0 [m]	z_{min} [m]
0	Sea or coastal area	0.005	1
II	Uncultivated area	0.2	4
III	Cultivated area	0.5	7

$$c_r(z) = \begin{cases} k_r \cdot ln(\frac{z}{z_0}), & \text{for } z_{min} \leq z \leq z_{max} \\ c_r(z_{min}), & \text{for } z < z_{min} \end{cases} \tag{F.4}$$

Where:

- z_0 is the roughness length, defined in Table F.1 for the Netherlands
- k_r is terrain factor depending on the roughness length z_0 and can be calculated using Equation F.5
- z_{max} is 200m according to the Dutch Annex (NEN-EN 1991-1-4 nb, Section 4.3.2)
- z_{min} is dependent on the terrain category and can be also be found in Table F.1

$$k_r = 0.19 \cdot (\frac{z_0}{0.05})^{0.07} \tag{F.5}$$

G

Timber properties

Table 3 — Strength classes for hardwoods based on edgewise bending tests – strength, stiffness and density values

	Class	D18	D24	D27	D30	D35	D40	D45	D50	D55	D60	D65	D70	D75	D80
Strength properties in N/mm²															
Bending	$f_{m,k}$	18	24	27	30	35	40	45	50	55	60	65	70	75	80
Tension parallel	$f_{t,0,k}$	11	14	16	18	21	24	27	30	33	36	39	42	45	48
Tension perpendicular	$f_{t,90,k}$	0,6	0,6	0,6	0,6	0,6	0,6	0,6	0,6	0,6	0,6	0,6	0,6	0,6	0,6
Compression parallel	$f_{c,0,k}$	18	21	22	24	25	27	29	30	32	33	35	36	37	38
Compression perpendicular	$f_{c,90,k}$	4,8	4,9	5,1	5,3	5,4	5,5	5,8	6,2	6,6	10,5	11,3	12,0	12,8	13,5
Shear	$f_{v,k}$	3,5	3,7	3,8	3,9	4,1	4,2	4,4	4,5	4,7	4,8	5,0	5,0	5,0	5,0
Stiffness properties in kN/mm²															
Mean modulus of elasticity parallel bending	$E_{m,0,mean}$	9,5	10,0	10,5	11,0	12,0	13,0	13,5	14,0	15,5	17,0	18,5	20,0	22,0	24,0
5 percentile modulus of elasticity parallel bending	$E_{m,0,k}$	8,0	8,4	8,8	9,2	10,1	10,9	11,3	11,8	13,0	14,3	15,5	16,8	18,5	20,2
Mean modulus of elasticity perpendicular	$E_{m,90,mean}$	0,63	0,67	0,70	0,73	0,80	0,87	0,90	0,93	1,03	1,13	1,23	1,33	1,47	1,60
Mean shear modulus	G_{mean}	0,59	0,63	0,66	0,69	0,75	0,81	0,84	0,88	0,97	1,06	1,16	1,25	1,38	1,50
Density in kg/m³															
5 percentile density	ρ_k	475	485	510	530	540	550	580	620	660	700	750	800	850	900
Mean density	ρ_{mean}	570	580	610	640	650	660	700	740	790	840	900	960	1020	1080

NOTE 1 Values given above for tension strength, compression strength, shear strength, char. modulus of elasticity in bending, mean modulus of elasticity perpendicular to grain and mean shear modulus, have been calculated using the equations given in EN 384.

NOTE 2 The tabulated properties are compatible with timber at moisture content consistent with a temperature of 20 °C and a relative humidity of 65 %, which corresponds to a moisture content of 12 % for most species.

NOTE 3 Characteristic values for shear strength are given for timber without fissures, according to EN 408.

NOTE 4 The edgewise bending strength may also be used in the case of flatwise bending.

Figure G.1: Timber properties according NEN-EN 338:2016 for hardwoods based on edgewise bending tests (strength, stiffness and density values)

H

ML Training Validation Graphs

1

V_{y1}, V_{z1}, $[N_{21,c}, N_{22,c}]_{max}$, M_{y2}, M_{z2}

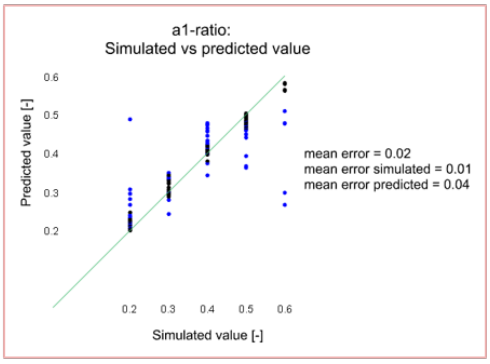

2

$N_{1,c}$, V_{y1}, V_{z1}, $[N_{21,c}, N_{22,c}]_{max}$, M_{y2}, M_{z2}

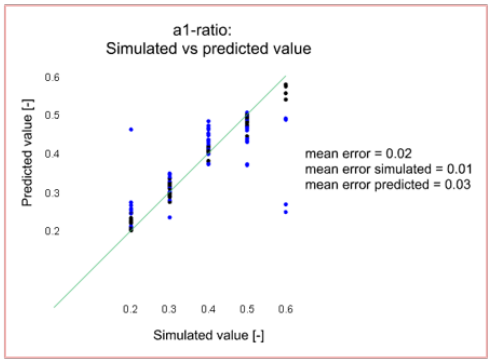

3

$N_{1,comp}$, V_{y1}, V_{z1}, M_{y2}, M_{z2}

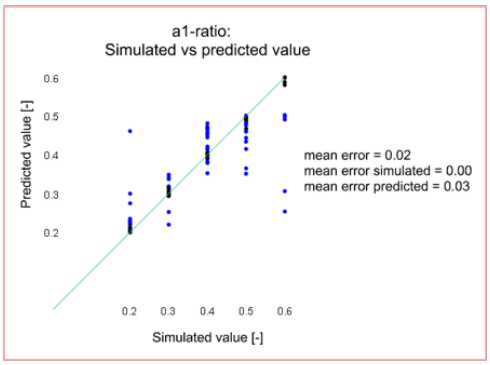

4

$N_{1,c}$, V_{y1}, V_{z1}, $[V_{y,21}, V_{y,22}]_{max}$, $[V_{z,21}, V_{z,22}]_{max}$, M_{y2}, M_{z2}

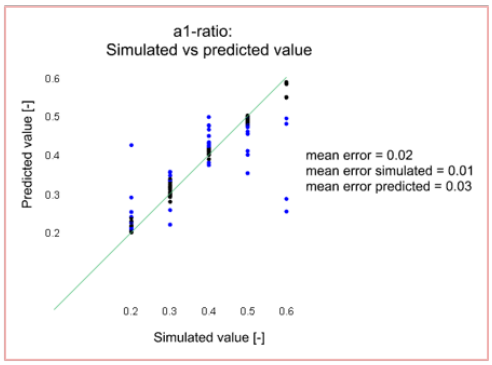

5

$N_{1,c}$, V_{y1}, V_{z1}, $[V_{y,21}, V_{y,22}]_{max}$, M_{y2}, M_{z2}

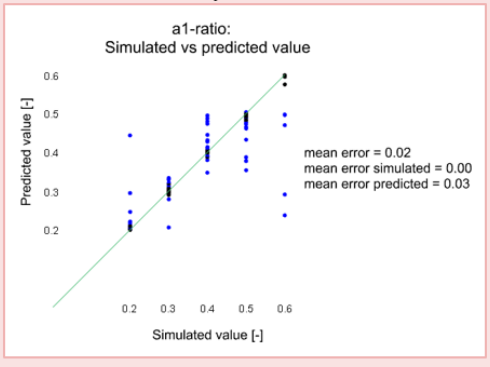

6

V_{y1}, V_{z1}, $[V_{y,21}, V_{y,22}]_{max}$, M_{y2}, M_{z2}

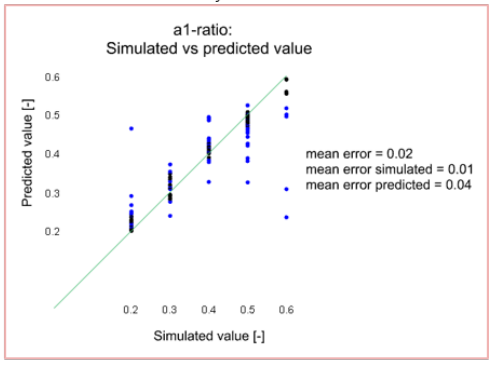

Figure H.1: Simulated values plotted against the predicted values for the a_1-ratio when different combinations of forces are used as training input

1 V_{y1}, V_{z1}, $[N_{21,c}, N_{22,c}]_{max}$, M_{y2}, M_{z2}

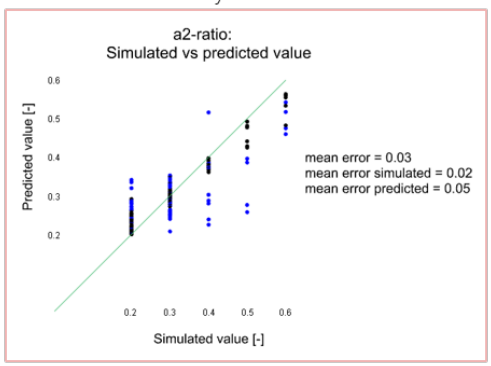

2 $N_{1,c}$, V_{y1}, V_{z1}, $[N_{21,c}, N_{22,c}]_{max}$, M_{y2}, M_{z2}

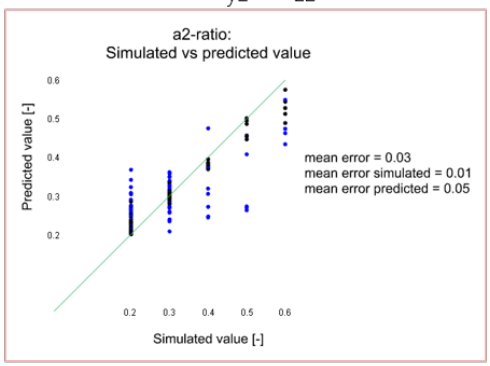

3 $N_{1,comp}$, V_{y1}, $V_{z1,}$ M_{y2}, M_{z2}

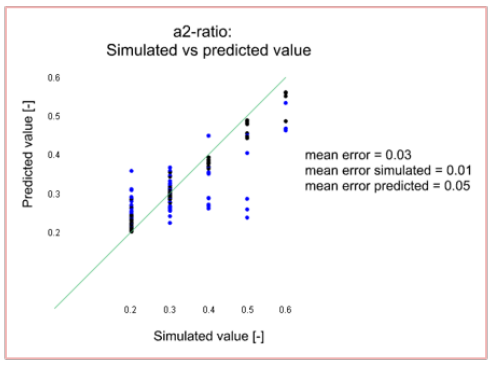

4 $N_{1,c}$, V_{y1}, V_{z1}, $[V_{y,21}, V_{y,22}]_{max}$, $[V_{z,21}, V_{z,22}]_{max}$, M_{y2}, M_{z2}

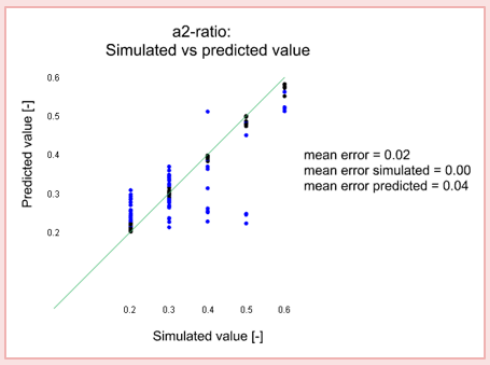

5 $N_{1,c}$, V_{y1}, V_{z1}, $[V_{y,21}, V_{y,22}]_{max}$, M_{y2}, M_{z2}

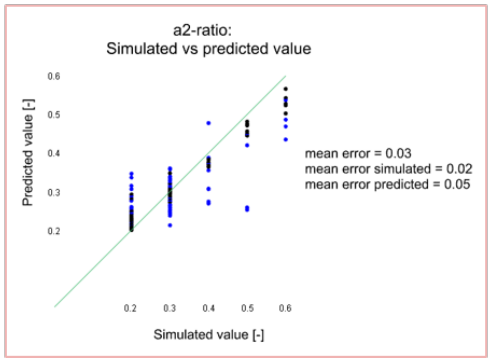

6 V_{y1}, V_{z1}, $[V_{y,21}, V_{y,22}]_{max}$, M_{y2}, M_{z2}

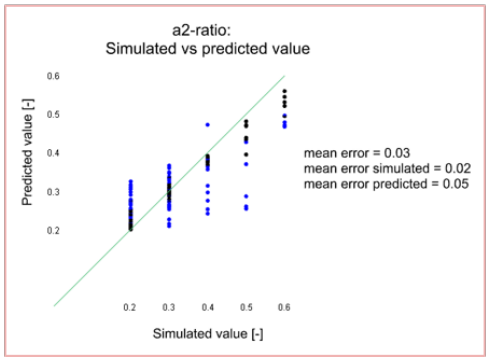

Figure H.2: Simulated values plotted against the predicted values for the a_2-ratio when different combinations of forces are used as training input

1 V_{y1}, V_{z1}, $[N_{21,c}, N_{22,c}]_{max}$, M_{y2}, M_{z2}

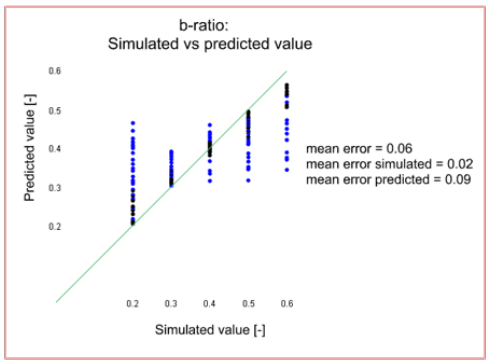

2 $N_{1,c}$, V_{y1}, V_{z1}, $[N_{21,c}, N_{22,c}]_{max}$, M_{y2}, M_{z2}

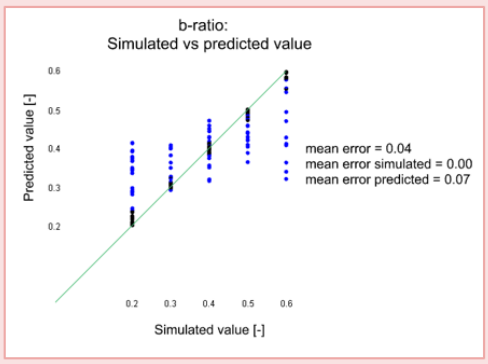

3 $N_{1,comp}$, V_{y1}, V_{z1}, M_{y2}, M_{z2}

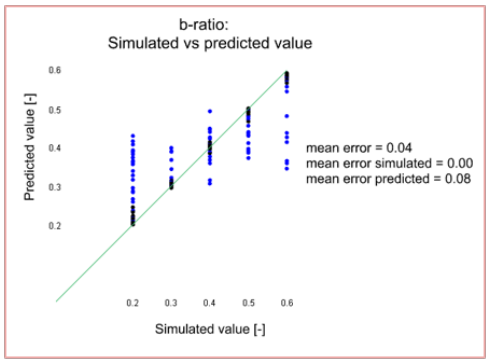

4 $N_{1,c}$, V_{y1}, V_{z1}, $[V_{y,21}, V_{y,22}]_{max}$, $[V_{z,21}, V_{z,22}]_{max}$, M_{y2}, M_{z2}

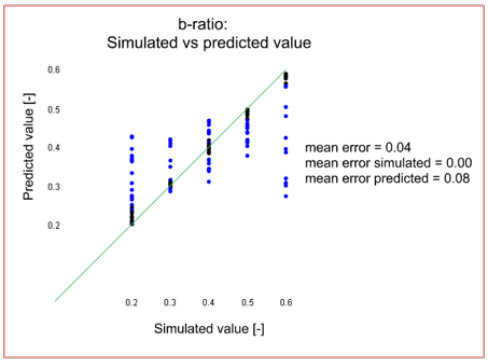

5 $N_{1,c}$, V_{y1}, V_{z1}, $[V_{y,21}, V_{y,22}]_{max}$, M_{y2}, M_{z2}

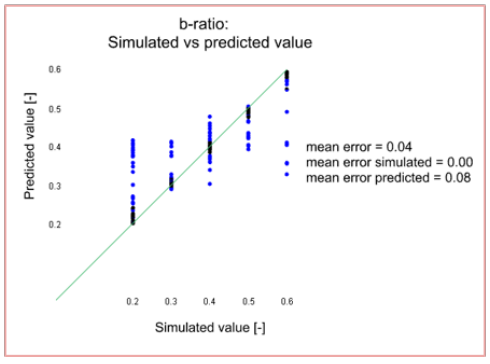

6 V_{y1}, V_{z1}, $[V_{y,21}, V_{y,22}]_{max}$, M_{y2}, M_{z2}

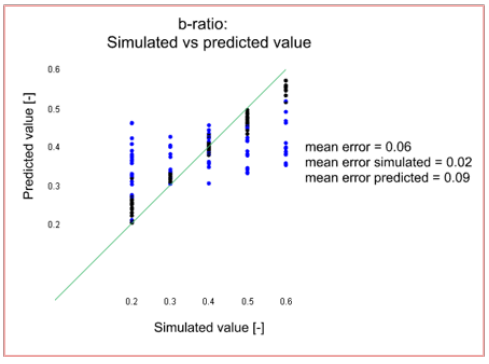

Figure H.3: Simulated values plotted against the predicted values for the *b*-ratio when different combinations of forces are used as training input

Bibliography

[1] *Shear strength values for soft- and hardwoods, Official publication of the INTER conference.*

[2] *Enhanced Design Approach for Reinforced Notched Beams (46th CIB-W18 Meeting, Vancouver, Canada, August 2013)*, 2013.

[3] *Species independent strength grading of structural timber*, 2015.

[4] *Proceedings of the International Association for Shell and Spatial Structures (IASS) Symposium 2015: Future Visions (Amsterdam, The Netherlands, August 2015)*, 2015.

[5] *A beam theory fracture mechanics approach for strength analysis of beams with a hole (in International Network on Timber Engineering Research - Proceedings Meeting 48)*, 2015.

[6] European technical assessment eta-11/0030 of 2016-04-07. Technical report, ETA-Denmark, 2016.

[7] Structural Awards 2017. University of exeter forum. URL https://www.istructe.org/.

[8] Water Street Academy. Leonardo's self supporting bridge. URL https://waterstreetacademy.wordpress.com/.

[9] Alchetron. Savill building. URL https://alchetron.com/.

[10] Daici Ano. Gc prostho museum research center / kengo kuma & associates. URL https://www.archdaily.com/.

[11] Neri Architects. The contortion movement. URL http://www.neriarchitects.com/.

[12] Architekture.info. Pritzker 2012. URL http://www.architektura.info/.

[13] Wood Awards. Marlowe academy. URL http://woodawards.com/.

[14] G. Biau and E. Scornet. A random forest guided tour. *Test*, 25:197–227, 2016. doi: 10.1007/s11749-016-0481-7.

[15] H.J. Blaß and C. Sandhaas. *Timber Engineering, Principles for Design*. KIT Scientific Publishing, 2017.

[16] C. Chen, H. Qui, and L. Yong. Flexural behaviour of timber dovetail mortise and tenon joints. *Elsevier - Construction and Building Materials*, pages 366 – 377, 2016. doi: https://doi.org/10.1016/j.conbuildmat.2016.02.074.

[17] J.L. Coenders. *CT5251: Structural Design - Special Structures*. Delft University of Technology, 2008.

[18] MC2 Estudio de Ingenieria. Palafolls sports hall. URL http://www.mc2.es/.

[19] TU Delft. The glass bridge to the green village. URL https://www.tudelft.nl/.

[20] Diversare. Kengo kuma and associates. URL https://divisare.com/.

[21] Niklas Donges. The random forest algorithm. URL https://towardsdatascience.com/.

[22] Egorlin. Japanese woodworking joints with original innovation. URL https://egorlin.com/.

[23] Format Engineers. Kreod pavilion (2012). URL http://formatengineers.com/.

[24] E. Erman. Demountable Timber Joints for Timber Construction Systems. *Architectural Science Review*, pages 133 – 243, 2002. doi: 10.1080/00038628.2002.9697501.

[25] Philipp Eversmann, Fabio Gramazio, and Matthias Kohler. Robotic prefabrication of timber structures: towards automated large-scale spatial assembly. *Construction Robotics*, Aug 2017. ISSN 2509-8780. doi: 10.1007/s41693-017-0006-2. URL https://doi.org/10.1007/s41693-017-0006-2.

[26] Formakers. Pritzker prize 2014 / shigeru ban wins. URL http://www.formakers.eu/.

[27] Colleen Hawkes. Solar sail for seine musicale music and cultural centre in paris. URL https://www.stuff.co.nz/.

[28] Lunds Tekniska Hogskola. Limtraehandbok. URL http://www.kstr.lth.se/.

[29] The Architects' Journal. Working detail: Herbert museum and art gallery by pringle richards sharratt architects. URL https://www.architectsjournal.co.uk/.

[30] Karamba. Intelligent fabrication 2017 âĂŞ digital bridges. URL https://www.karamba3d.com/.

[31] City Form Lab. Sutd gridshell. URL http://cityform.mit.edu/.

[32] Patrick Lynch. These mesmerizing gifs illustrate the art of traditional japanese wood joinery. URL https://www.archdaily.com/.

[33] MCDC. Reciprocal structures. URL http://m-cdc.de/.

[34] Compagnie Meco. Testing a cardboard pedestrian bridge. URL http://www.compagniemeco.com/.

[35] A. Menges. *Advancing Wood Architecture: A Computational Approach*. Taylor and Francis, 2016.

[36] A. Menges, B. Sheil, R. Glynn, and M. Skavara. *Fabricate 2017*. UCL Press, 2017.

[37] C.M. Moerbeek. Stresses in the mortise and tenon joint. Master thesis, Delft University of Technology, 2017.

[38] Hiroshi Murata. The da vinci dome. URL http://www.hiroshi-murata.com/.

[39] K.P. Murphy. *Machine Learning: A Probabilistic Perspective*. MIT Press, 2014.

[40] Nationaal Militair Museum. Nationaal militair museum. URL https://www.nmm.nl/.

[41] University of Exeter. Univercity of exeter gallery. URL http://www.exeter.ac.uk/.

[42] University of Stuttgart. Institute for computational design and construction. URL icd.uni-stuttgart.de.

[43] K. Ogawa, Y. Sasaki, and M. Yamasaki. Theoretical modeling and experimental study of Japanese âĂIJWatari-agoâĂİ joints. *Journal of Wood Science : Official Journal of the Japan Wood Research Society*, 61:481–491, 2015. doi: 10.1007/s10086-015-1498-3.

[44] B. Prayudhi. 3f3d: Form follows force with 3d printing. Master thesis, Delft University of Technology, 2016.

[45] David Rutten. Evolutionary principles applied to problem solving. URL http://www.grasshopper3d.com/.

[46] T. Sandy, M. Giftthaler, K. DÃűrfler, Kohler, and J. M., Buchli. Autonomous Repositioning and Localization of an In situ Fabricator. *IEEE Conference Publications*, pages 2852 – 2858, 2016. doi: 10.1109/ICRA.2016.7487449.

[47] New York Schools of Architecture. Digital design and fabrication. URL http://digitaldesignfabrication.blogspot.co.uk/.

[48] Timothy A. Schuler. Umass amherst design building zipper trusses. URL http://www.architectmagazine.com/.

[49] K. Seike, Y. Yobuko, and R.M. Davis. *The Art of Japanese Joinery*. Weatherhill, 1977.

[50] A. Sondergaard, O. Amir, P. Eversmann, L. Piskorec, F. Stan, F. Gramazio, and M. Kohler. Topology Optimization and Robotic Fabrication of Advanced Timber Space-Frame Structures. *Robotic Fabrication in Architecture, Art and Design, Springer*, pages 191 – 203, 2016. doi: 10.1007/978-3-319-26378-6_14.

[51] P Song and C. Fu. Reciprocal Frame Structures Made Easy. *ACM Transactions on Graphics (32)*, page 10, 2013.

[52] Staalmakers. Nationaal militair museum - soesterberg. URL http://www.staalmakers.nl/.

[53] SteelConstruction.info. Structural robustness. URL https://www.steelconstruction.info/.

[54] Landwirtschaftsmuseum Schloss Steinz. Geheimnis holz. URL https://www.museum-joanneum.at/.

[55] Feilden Clegg Bradley Studios. The earth centre and solar canopy. URL https://fcbstudios.com/.

[56] Svetlanatam. Shigeru ban impression. URL https://svetlanatam.wordpress.com/.

[57] M.A. Taj, S.K. Najafi, and G. Ebrahimi. Withdrawal and lateral resistance of wood screw in Beech, Hornbeam and Poplar. *European Journal of Wood and Wood Products : Holz Als Roh- Und Werkstoff*, pages 135 – 140, 2009. doi: 10.1007/s00107-008-0294-9.

[58] James Taylor-Foster. Monocle 24 explores women in architecture. URL https://www.archdaily.com/.

[59] Tekla. Exeter university forum: No room for error in a challenging multi-material project. URL https://www.tekla.com/uk/.

[60] Hyne Timber. Working with weather exposed timber. URL https://www.hyne.com.au/.

[61] Eco Web Town. The toledo gridshell. URL http://www.ecowebtown.it/.

[62] J.R. van Otterloo. Force distribution and connection strength in timber lock gates. Master thesis, Delft University of Technology, 2013.

[63] ETH Zürich. *Gramazio Koher Research*. http://dfab.arch.ethz.ch/.

[64] K Zwerger. *Wood and Wood Joints : Building Traditions of Europe, Japan and China*. Walter de Gruyter GmbH, 2015.